Delft University of Technology

Innovative Permeable Materials for Broadband Trailing-Edge Noise Mitigation

Rubio Carpio, A.

DOI
10.4233/uuid:fd3d84a7-c162-4cd4-8b19-bee53e00505f

Publication date
2021

Document Version
Final published version

Citation (APA)
Rubio Carpio, A. (2021). *Innovative Permeable Materials for Broadband Trailing-Edge Noise Mitigation*. [Dissertation (TU Delft), Delft University of Technology]. https://doi.org/10.4233/uuid:fd3d84a7-c162-4cd4-8b19-bee53e00505f

INNOVATIVE PERMEABLE MATERIALS FOR BROADBAND TRAILING-EDGE NOISE MITIGATION

INNOVATIVE PERMEABLE MATERIALS FOR BROADBAND TRAILING-EDGE NOISE MITIGATION

Dissertation

for the purpose of obtaining the degree of doctor
at Delft University of Technology
by the authority of the Rector Magnificus, Prof.dr.ir. T.H.J.J. van der Hagen,
chair of the Board for Doctorates
to be defended publicly on
Wednesday 14 July 2021 at 17:30

by

Alejandro RUBIO CARPIO

Ingeniero Aeronáutico,
Universidad Politécnica de Valencia, Spain,
born in Valencia, Spain.

This dissertation has been approved by the promotors

Promotor: Prof.dr.ir. M. Snellen
Promotor: Dr. D. Ragni
Copromotor: Dr. F. Avallone

Composition of the doctoral committee:

Rector Magnificus,	chairperson
Prof.dr.ir. M. Snellen,	Delft University of Technology, promotor
Dr. D. Ragni,	Delft University of Technology, promotor
Dr. F. Avallone ,	Delft University of Technology, copromotor
Independent members:	
Prof.dr. S. J. Watson,	Delft University of Technology
Prof.dr.ing. E. Sarradj,	Technical University of Berlin, Germany
Prof.dr.ir. C. Schram,	von Kármán Institute for Fluid Dynamics, Belgium
Dr. M. Herr,	German Aerospace Center, Germany
Prof.dr.ir. D. von Terzi,	Delft University of Technology, reserve member

Keywords: Trailing-Edge Noise, Aeroacoustics, Noise Control, Porous Materials

Printed by: Ipskamp

Front & Back: Thesis cover layout beautifully crafted by Diego Serna Valverde; wind turbine picture by Sergii Kozak; metal foam microscopy picture by Alejandro Rubio Carpio.

ISBN 978-94-6384-240-2

CONTENTS

Summary **ix**

Preface **xi**

1 Introduction **1**
- 1.1 Demand for Quieter Wind Turbines . . . 2
- 1.2 Wind Turbine Noise . . . 2
  - 1.2.1 Inflow Turbulence Noise . . . 2
  - 1.2.2 Turbulent Boundary Layer Trailing-Edge (TBL-TE) Noise . . . 4
  - 1.2.3 Laminar Boundary Layer Trailing-Edge (LBL-TE) Noise . . . 4
  - 1.2.4 Blunt Trailing-Edge Noise . . . 4
  - 1.2.5 Separation/Stall Noise . . . 4
  - 1.2.6 Tip Vortex Noise . . . 5
- 1.3 Wind Turbine Noise Mitigation Approaches . . . 5
- 1.4 Motivation and Objectives . . . 5
- 1.5 Outline . . . 6
- References . . . 7

2 Trailing-Edge Noise **11**
- 2.1 Introduction . . . 12
- 2.2 Trailing-Edge Noise Characteristics . . . 12
  - 2.2.1 Acoustic Analogy . . . 12
  - 2.2.2 Trailing-Edge Noise: Characteristic Scales and Source Nature . . . 13
- 2.3 Trailing-Edge Noise Prediction . . . 15
  - 2.3.1 Diffraction Theory - 2D Formulation . . . 15
  - 2.3.2 3D Gust Scattering Extension . . . 19
  - 2.3.3 Leading-Edge Back-Scattering Extension . . . 21
  - 2.3.4 Wavenumber-Frequency Wall Pressure Spectrum - Statistical Description . . . 22
- 2.4 Trailing-Edge Noise Mitigation Strategies . . . 26
  - 2.4.1 Serrations . . . 27
  - 2.4.2 Optimization of the Airfoil Shape . . . 27
  - 2.4.3 Porous Metamaterials . . . 28
- References . . . 30

3 Experimental Methodology **35**
- 3.1 Introduction . . . 36
- 3.2 Models and Aeroacoustic Research Facility . . . 36
  - 3.2.1 Models . . . 36
  - 3.2.2 Wind Tunnel . . . 37

3.2.3 Open-jet Wind Tunnel Correction . . . 39
3.3 Trailing-Edge Inserts . . . 40
3.3.1 Geometry . . . 41
3.3.2 Porosity . . . 44
3.3.3 Tortuosity . . . 44
3.3.4 Permeability and Form Drag Coefficient . . . 46
3.4 Measurement Techniques. . . . 49
3.4.1 Particle Image Velocimetry. . . . 49
3.4.2 Hot-Wire Anemometry. . . . 52
3.4.3 Unsteady Wall-Pressure Measurements . . . 53
3.4.4 Acoustic Measurements . . . 54
3.5 Data Processing and Reduction . . . 55
3.5.1 Kinematic Quantities . . . 55
3.5.2 Pressure-Based Boundary Layer Description. . . . 58
References . . . 62

4 Flow Field over Metal Foam Trailing Edges and Acoustic Scattering 69
4.1 Introduction . . . 70
4.2 Results and Discussion . . . 70
4.2.1 Far-field Acoustic Pressure . . . 70
4.2.2 Velocity Field. . . . 72
4.2.3 Surface Pressure . . . 79
4.2.4 Prediction using Amiet's Analytical Model . . . 84
4.3 Conclusions. . . . 85
References . . . 87

5 Mechanisms of broadband noise generation on metal foam edges 91
5.1 Introduction . . . 92
5.2 Results . . . 92
5.2.1 Far-field Noise . . . 92
5.2.2 Mean and Root-Mean-Square Velocity . . . 93
5.2.3 Correlation of Velocity Fluctuations . . . 94
5.2.4 Acoustic Source Maps . . . 98
5.3 Conclusion . . . 102
References . . . 104

6 Noise Mitigation with Perforated Trailing Edges 105
6.1 Introduction . . . 106
6.2 Results . . . 107
6.2.1 Scaling Laws for Noise Mitigation . . . 107
6.2.2 Effect of Tortuosity on Noise Mitigation . . . 113
6.2.3 Scaling of Far-Field Acoustic Pressure with Free-Stream Velocity. . . . 114
6.2.4 Effect of the Relative Permeable Chord Length on Noise Abatement . 116
6.2.5 Appearance of Shedding-Related Tones . . . 118
6.3 Conclusions. . . . 121
References . . . 122

7 Inserts with Tailored Permeability Gradients for Noise Mitigation 125
7.1 Introduction 126
7.2 Trailing-Edge Inserts with Streamwise Permeability Gradients 127
7.3 Results 133
7.3.1 Influence of the Permeability Gradient on Noise Scattering 133
7.3.2 Change in Noise Mitigation Performance with Reynolds Number and Loading 137
7.3.3 Remarks on Roughness Noise 139
7.4 Conclusions. 140
References 142

8 Conclusions and Recommendations 143
8.1 Conclusions. 143
8.2 Recommendations 145

Acknowledgements 147

A Acoustics: definitions 149

B Schwarzschild's Solution 151

C Additional Scaling Laws 153

Curriculum Vitæ 155

List of Publications 157

SUMMARY

Permeable trailing edges are experimentally investigated in this thesis as a mean to mitigate aeroacoustic noise. The first part of the study is devoted to deciphering the mechanisms of noise generation involved in these devices. To this aim, trailing-edge inserts are manufactured employing commercially-produced open-cell metallic foams with different material properties, i.e., permeability and pore size.

It is found that permeable inserts distribute noise scattering along the entire permeable surface, creating noise sources with decreased radiation efficiency, and minimizing coherent noise emission. This process, requiring flow communication between both sides of the airfoil through the porous medium, is controlled by the local permeability of the material. For instance, for metal foams with higher permeability (of 3.2×10^{-9} m^2), the intensity of the noise emission at the trailing edge is decreased, and the solid-permeable junction becomes the main contributor to far-field sound; for metal foams with lower permeability (of 5×10^{-10} m^2), the main noise source still lays along the trailing edge, although its intensity is lower compared to a fully solid edge. Other likely mechanisms such as the overall variation of the turbulent flow field in the vicinity of the trailing edge, or the absorption of acoustic waves, barely contribute to noise abatement for metal foam trailing-edge inserts.

In the second part of the thesis, these findings are further exploited by the design and 3D-printing of permeable inserts with a simplified pore topology, i.e., with cylindrical channels normal to the chord and homogeneous hole distribution. These perforated inserts allow flow at the suction and pressure sides to communicate, hence abate noise similarly to those manufactured with metal foams. Yet, inserts fabricated with additive manufacturing are more suitable for industrial and research applications as their final topology can be fully controlled in the design phase, and is barely altered by subsequent manufacture or shaping steps.

The comparison between inserts with different pore topologies allows to define optimal permeability thresholds of 3.5×10^{-9} m^2 and 1×10^{-9} m^2 for perforated and metal-foam inserts, respectively. Below these values, decreasing the local permeability of the material significantly reduces the maximum noise mitigation potential. Above them, further increasing the permeability does not produce additional noise mitigation benefits. The differences in acoustic performance of inserts with different pore topologies but similar permeability demonstrates that this parameter is insufficient to fully characterize their performance. Hence, the tortuosity, a measure of how tortuous pore paths are, is proposed as an additional parameter to the local flow permeability for noise abatement control. Results obtained for perforated inserts with varying chordwise extent allow to establish an optimal threshold of 5% of the total airfoil chord. As for permeability thresholds, further increasing the permeable chordwise extent above this value does not yield significant gains in terms of maximum noise abatement. Given that longer or more permeable inserts entail decreasing lift and increasing drag, an insert with permeability of

1×10^{-9} m^2, a tortuosity of 1.15 and a length of 5% of the chord is identified as an optimal trade-off between acoustic and aerodynamic performance. In spite of the benefits in terms of broadband noise mitigation, it is found that, as for models with a fully blunt trailing edge, permeable inserts with high permeability and ordered pore arrangement trigger vortex-shedding. Hence, they provoke loud low-frequency tones that penalize their overall noise mitigation performance.

Finally, the noise mitigation potential of perforated inserts with locally varying permeability is assessed. Graded inserts have lower permeability at the solid-permeable junction, and monotonically increase their permeability towards the edge by increasing their hole density. The gradual match of the acoustic impedance jump along the permeable surface brings additional benefits with respect to fully homogeneous inserts. Mock-ups with tailored permeability gradients allow to control the magnitude of low-frequency noise abatement by varying the permeability of the insert at its root, and to overcome the maximum noise mitigation of homogeneous variants. Moreover, they also minimize vortex-shedding, hence removing loud tones in the acoustic spectra, as they confine the regions of higher permeability to the very aft end of the airfoil.

PREFACE

I still remember the day I was introduced to the discipline of Aeroacoustics clearly. It was September 2015 and professor C. Schram invited me to his office at VKI to discuss the possibility of carrying out a study on shock-cell noise in the framework of my Research Master project. As I am usually overcautious, the first thing I told him the moment I went into his office was: "Christophe, I never took a course on Aeroacoustics, I have no idea about the subject". "Well, nobody really does, but you will learn" was the answer, which at the time seemed equally shocking and appealing. Five years and a half later I am about to hold a PhD in the discipline, so I guess I did learn something in the way. I have tried to condense most of it in this book, clarifying as much as possible the somewhat abstract concepts that vertebrate the topic. I hope you (the reader) have as much pleasure reading this thesis as I had during the research. Enjoy the read.

Alejandro Rubio Carpio
Delft, March 2021

1

INTRODUCTION

Rising awareness of the human impact on the environment has increased the popularity of clean energy sources such as wind. During the past few decades, extensive wind farms have been created around the globe, turning what initially was a marginal energy production mean into a real alternative to fossil-fuel based technologies. Yet, as humans get acquainted to be surrounded by wind turbines, certain aspects might challenge their embracement as a clean, cheap, energy source. One of these aspects is wind turbine noise. For this reason, efficient noise mitigation techniques have been sought by both industry and academia. This chapter underlines the necessity for quieter wind turbines, and presents a summary of the most relevant noise sources present in modern wind turbines. Moreover, noise control techniques that are currently applied or have been proposed for application in wind turbines are explained. Finally, an overview of the thesis objectives and an outline is given.

1.1. DEMAND FOR QUIETER WIND TURBINES

Wind turbines produce renewable energy, hence contributing to sustainable development. As of 2019, the global installed wind power capacity amounts to 650 GW, more than thirty times the values reported in 2000 [1]. As a consequence of such a rapid expansion, the wind power outcome is now similar to that of other consolidated energy sources such as nuclear (420 GW) or solar (600 GW) energy. However, it is still far from those derived from fossil-fuel based technologies, such as gas- (1800 GW) or coal-based (2200 GW) power plants. To meet the Paris Agreement [2] and keep the increase in global temperatures below 2°C with respect to those of 2015, energy outlooks estimate that wind energy generation should be tripled by 2040 [3].

Noise disturbance is a potential barrier to scale up on-shore wind power: surveys of residents near wind farms in European countries such as The Netherlands,[4], Sweden [5], United Kingdom [6] or Poland [7] report that wind farm noise is perceived as annoying for population living as far as 2 km away from the nearest wind turbine. Perceived nuisance seems to be aggravated by the low-frequency nature (within 20 and 400 Hz) and the swishing quality of the sound [8]. Annoyance may result in sleep deprivation and other adverse health effects such as cardiovascular disease or cognitive impairment for human population nearby [9]. Higher awareness of harmful noise effects results in more restrictive legislations, which protect public health by establishing upper boundaries for noise exposure, as well as delimiting areas where wind turbines are allowed. This has negative implications for wind energy competitiveness against other energy sources. Among others, high wind power density areas might be discarded for wind turbine installation due to the presence of residences nearby; furthermore, to comply with noise regulations wind turbines might work under partial loading, hence limiting the power output. Noise control is thus a fundamental aspect of modern wind turbines design, and must be taken into account to guarantee that wind energy becomes a key player in the new global energy scenario.

1.2. WIND TURBINE NOISE

Noise generated by operating wind turbines is usually divided in mechanical and aerodynamic noise. The former originates from mechanical components such as the gearbox, generator, cooling or hydraulic systems [10]. The latter is produced by the interaction between atmospheric air and the different parts of the turbine. Mechanical noise is characterized by the presence of loud tones, hence is highly penalized by environmental regulations. Yet, this source of noise can be effectively reduced by acoustically treating the nacelle raft and avoiding vibration of machinery parts [11]. Wind turbine manufacturers managed to reduce mechanical noise in such a way that aerodynamic noise has become the main contributor to the overall noise scattered by modern wind turbines [12]. For this reason, a more exhaustive description of the different sources of aerodynamic noise present in wind turbines is presented below.

1.2.1. INFLOW TURBULENCE NOISE

Turbulence is intrinsically present in atmospheric flows, and interacts with the wind turbine blade causing broadband noise radiation (figure 1.1 (a)). The characteristics of the

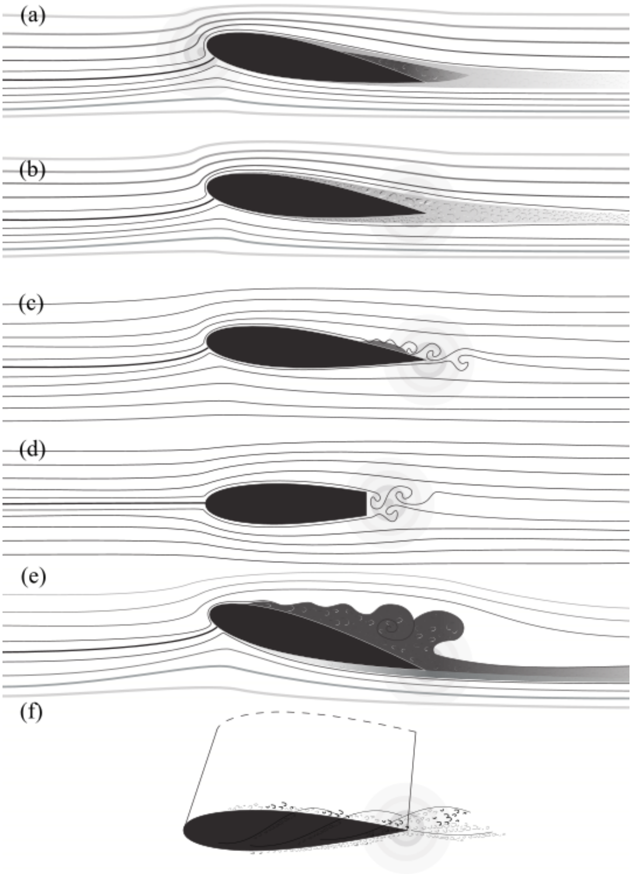

Figure 1.1: Different types of airfoil self-noise. (a) Inflow turbulence noise. (b) Turbulent boundary layer trailing-edge noise. (c) Laminar boundary layer trailing-edge noise. (d) Blunt trailing-edge noise. (e) Separation/stall noise. (f) Tip vortex noise. Adapted from Brooks *et al.* [13].

emitted noise are highly dependent on the properties of the inflow turbulence. For eddies that are much larger than the chord of the blade, noise is radiated into the far-field due to a variation in the total blade loading; the wavelength of the acoustic wave is much larger than the chord of the blade, hence the blade can be regarded as a point source with acoustic intensity proportional to the sixth power of the local flow velocity [12]. On the other hand, for eddies smaller than the blade chord, noise is radiated due to the local change in blade loading, and the acoustic wave is of a high-frequency nature; the blade cannot be considered as a point source, and the directivity pattern will depend on the blade geometry. In this case, the acoustic intensity scales with the fifth power of the local flow velocity [14]. Inflow turbulence noise can be a large contributor to the total far-field noise for highly turbulent inflow conditions. Yet, it represents a marginal contribution to the overall noise scattering of a wind turbine under typical operational conditions [15].

1.2.2. TURBULENT BOUNDARY LAYER TRAILING-EDGE (TBL-TE) NOISE

When the air inflow interacts with a wind turbine blade, a boundary layer, i.e. a region where viscosity effects are relevant, develops over the surface (figure 1.1 (b)). Transition from a laminar to a fully turbulent state occurs naturally at sufficiently high Reynolds numbers ($\geq 10^6$) at a certain chord position, or can be triggered due to the presence of inhomogeneities on the blade surface (dirt, blade damage). Turbulent eddies induce unsteady pressure fluctuations beneath the boundary layer. These are inefficient sound radiators in subsonic conditions; yet, when convected over a sharp edge, they are radiated efficiently into the far-field as acoustic pressure waves. Turbulent eddies populating the boundary layer are intrinsically random and chaotic, hence their acoustic signature is broadband. Turbulent boundary layer-trailing edge (TBL-TE) noise is the most relevant contributor to the overall noise scattered by modern wind turbines [16], and its characteristics depend on the boundary layer structure near the edge, as well as on the trailing-edge geometry [17].

1.2.3. LAMINAR BOUNDARY LAYER TRAILING-EDGE (LBL-TE) NOISE

The boundary layer over the blade might remain laminar at lower Reynolds numbers or in presence of smooth and clean surfaces. Under these conditions, instability waves grow larger as they travel downstream, and, as for TBL-TE noise, they scatter noise as they are convected over the surface discontinuity (figure 1.1 (c)). A strong tonal noise often arises due to the appearance of a self-excited feedback loop whereby flow instabilities are triggered by the upstream travelling acoustic wave created by precedent instabilities [12]. The acoustic signature of such noise typology is hence tonal. Most modern turbines operate at much higher local Reynolds numbers ($\geq \times 10^6$); laminar-boundary-layer-trailing-edge (LBL-TE) noise is hence of minor importance, and contributes significantly to overall noise scattering only for small turbines [18].

1.2.4. BLUNT TRAILING-EDGE NOISE

For blades with a sharp rear end, the interaction between the boundary layer and the surface discontinuity constitutes the most relevant noise source [19]. For blades with blunt trailing edge, the noise generation mechanism is different; periodic Von Karman type vortex shedding forms at the trailing edge in case the ratio of trailing-edge to boundary layer thickness exceeds a critical value [20]. The pressure fluctuations associated to the periodic vortex roll-up interact with the trailing edge, resulting in a strong tonal noise (figure 1.1 (d)). This noise contribution can be eliminated with an adequate blade design that minimizes the trailing edge thickness [21].

1.2.5. SEPARATION/STALL NOISE

Flow separation might occur on the suction side when the blade is set at a large incidence, producing trailing-edge noise due to the shed vorticity. At very high angles of attack, large scale turbulence is convected past the trailing edge, radiating low-frequency noise [12, 13, 22]. Depending on the degree of stall, noise is either radiated from the trailing edge (figure 1.1 (e)) or from the chord as a whole. The occurrence of this noise mechanism is rare in modern pitch controlled wind turbines.

1.2.6. TIP VORTEX NOISE

For wind turbine blades, the pressure difference between suction and pressure side is compensated at the tip, creating a local 3D-flow area (figure 1.1 (f)). Tip noise is generated by the interaction of the tip vortex with the side edge and the trailing edge of the blade tip [12]. The noise generation mechanism is similar to that of TBL-TE noise [23] and, consequently, scattered noise levels depend on the characteristics of the tip vortex such as size, strength and convection velocity. Reduction of tip noise is principally focused on minimizing the interaction between tip vortex and blade edges by employing planform blades or winglets [24, 25].

1.3. WIND TURBINE NOISE MITIGATION APPROACHES

Due to its relevance for wind turbine applications, TBL-TE noise has been subjected to extensive research along the last three decades to understand the mechanisms of sound production and to develop effective noise control strategies, and some of them are currently in operation on industrial wind turbines. To date, the most successful approach for wind turbine noise mitigation is the use of trailing-edge serrations. These are usually integrated in already installed wind turbine systems as attachable add-ons that provide the rear end of the blade with a wavy edge. These devices not only reduce the amplitude of the acoustic pressure emitted by wind turbines, but also shift acoustic power towards higher frequency, whereby atmospheric attenuation is more effective. Field measurements on a 2.3 MW, 94 m-diameter turbine equipped with non-optimized serrations report an average acoustic source level reduction of 3.2 dB for a blade subject to variable loading [26]. Further research shows that an additional reduction of 1.1 dBA in overall A-weighted noise can be attained with optimized geometries [27]. Another approach explored by blade manufacturers is the optimization of the airfoil shape for aeroacoustic purposes. This concept produced remarkable noise attenuation levels on two-dimensional NACA 64418 [28] (2-4 dB) and NACA 63418 [29] (up to 3.5 dB) wings, commonly employed in commercial wind turbines. However, it has been translated to wind turbines with moderate success: an average noise reduction of only 0.5 dB was achieved on the same 2.3 MW turbine described above, and similar levels (0.6 dB) were obtained on a smaller, 0.85 kW turbine [30]. Besides these two more established approaches, other innovative concepts for TBL-TE noise mitigation include the application of surface treatments or finlets [31] (initially conceived for marine propeller applications) or the employment of partially porous wings [32, 33]. The latter is especially interesting given the outstanding levels of noise attenuation (more than 20 dB at specific frequencies) reported in wind tunnel experiments on scaled models [34].

1.4. MOTIVATION AND OBJECTIVES

The rapid growth of wind turbines as a source of renewable energy poses some technical challenges that might jeopardize an even more widespread implementation. One of these is noise, and as such, there exists an ongoing need to develop novel noise control strategies that overcome state-of-the-art approaches such as serrations. A possible alternative is the employment of semi-porous wings, which has been shown to significantly mitigate trailing-edge noise in controlled environments. However, in spite of extensive experimental research, little insight in the noise generation process on porous edges is available in the literature. Hence, the main goal of this thesis is to advance towards a more complete understanding of the underlying physical mechanisms behind sound production in permeable edges. Furthermore, commercially available cellular materials often rely in manufacturing processes such as casting over polymeric precursors or powder sintering, that create a three-dimensional, random pore distribution [35]. As will be shown along this thesis, materials with such a complex micro-structure often entail additional fluid-dynamic and acoustic features. Further aspects, such as the change of properties when subject to conventional machining processes, or repeatability and inhomogeneity problems also discourage their application. Novel manufacturing techniques such as additive manufacturing allow creating porous materials by spatially distributing unit cells with defined geometries, i.e. fully controlled, tailored properties. The second objective of this thesis is thus exploring the design and manufacturing of porous materials with optimized meso structures for wind turbine noise applications.

1.5. OUTLINE

This thesis contains eight chapters. The first chapter provides an overview on wind turbine noise, as well as the research motivation and objectives. Chapter 2 describes more in detail the characteristics of TBL-TE noise, as well as different approaches to model and mitigate it. Chapter 3 contains a detailed description of the experimental techniques and set-ups employed to obtain data described along the thesis. Chapters 4 and 5 are dedicated to discuss the mechanisms of noise generation present in a NACA 0018 airfoil equipped with trailing edges manufactured with metallic foams, with emphasis on describing the underlying mechanisms of low-frequency noise mitigation. Chapter 6 describes the acoustic performance of 3D-printed micro-perforated trailing edges with straight holes normal to the chord, and an homogeneous hole distribution. Finally, Chapter 7 analyses the acoustic scattering of edges with straight holes and varying hole distribution. The thesis ends with Chapter 8, that contains a summary of the main findings.

REFERENCES

[1] *Global Wind Report,* (2020).

[2] *Paris Agreement to the United Nations,* (2015).

[3] *Wind Energy Outlook,* (2019).

[4] E. Pedersen, F. van den Berg, R. Bakker, and J. Bouma, *Response to noise from modern wind farms in The Netherlands.* The Journal of the Acoustical Society of America **126**, 634 (2009).

[5] E. Pedersen and K. Persson Waye, *Perception and annoyance due to wind turbine noise—a dose–response relationship,* The Journal of the Acoustical Society of America **116**, 3460 (2004).

[6] F. Qu, *Impacts of wind turbine noise on health and well-being from the perspective of urban morphology*, Ph.D. thesis, University of Sheffield (2018).

[7] M. Pawlaczyk-Luszczyńska, K. Zaborowski, A. Dudarewicz, M. Zamojska-Daniszewska, and M. Waszkowska, *Response to noise emitted by wind farms in people living in nearby areas,* International Journal of Environmental Research and Public Health **15** (2018), 10.3390/ijerph15081575.

[8] C. Doolan, *A review of wind turbine noise perception, annoyance and low frequency emission,* Wind Engineering **37**, 97 (2013).

[9] *WHO Environmental Noise Guidelines for the European Region,* (2018).

[10] K. W. V. Treuren, *Wind Turbine Noise: Regulations, Siting, Perceptions and Noise Reduction Technologies,* (2018), 10.5281/zenodo.1345527.

[11] J. N. Pinder, *Mechanical Noise from Wind Turbines,* Wind Engineering **1614822518**, 158 (1992).

[12] S. Wagner, R. Bareiß, and G. Guidati, *Wind Turbine Noise* (Springer, 1996).

[13] T. F. Brooks, D. S. Pope, and M. A. Marcolini, *NASA Reference Publication*, Tech. Rep. (NASA Langley Research Center, 1989).

[14] R. Zamponi, S. Satcunanathan, S. Moreau, D. Ragni, M. Meinke, W. Schröder, and C. Schram, *On the role of turbulence distortion on leading-edge noise reduction by means of porosity,* Journal of Sound and Vibration **485**, 115561 (2020).

[15] S. Deshmukh, S. Bhattacharya, A. Jain, and A. Paul, *Wind turbine noise and its mitigation techniques: A review,* Energy Procedia **160**, 633 (2019).

[16] S. Oerlemans, P. Sijtsma, and B. Méndez López, *Location and quantification of noise sources on a wind turbine,* Journal of Sound and Vibration **299**, 869 (2007).

[17] C. J. Doolan and D. J. Moreau, *A review of airfoil trailing edge noise with some implications for wind turbines,* International Journal of Aeroacoustics **14**, 811 (2015).

[18] C. Hansen and K. Hansen, *Recent Advances in Wind Turbine Noise Research,* Acoustics **2**, 171 (2020).

[19] D. Shannon and S. C. Morris, *Trailing Edge Noise Measurements Using a Large Aperture Phased Array,* International Journal of Aeroacoustics **7**, 147 (2008).

[20] S. Pröbsting, M. Zamponi, S. Ronconi, Y. Guan, S. C. Morris, and F. Scarano, *Vortex shedding noise from a beveled trailing edge,* International Journal of Aeroacoustics **15**, 712 (2016).

[21] D. W. Shannon, S. C. Morris, and T. J. Mueller, *Radiated sound and turbulent motions in a blunt trailing edge flow field,* International Journal of Heat and Fluid Flow **27**, 730 (2006).

[22] G. Lacagnina, P. Chaitanya, T. Berk, J. Kim, P. Joseph, B. Ganapathisubramani, S. M. Hasheminejad, T. P. Chong, O. Stalnov, K. Choi, M. Shahab, M. Omidyeganeh, and A. Pinelli, *Mechanisms of airfoil noise near stall conditions,* Physical Review Fluids **4**, 123902 (2019).

[23] S. Oerlemans, *Wind turbine noise : primary noise sources*, Tech. Rep. (2011).

[24] R. E. Longhouse, *Control of tip-vortex noise of axial flow fans by rotating shrouds,* Journal of Sound and Vibration **58**, 201 (1978).

[25] T. F. Brooks and M. A. Marcolini, *Airfoil tip vortex formation noise,* AIAA Journal **24**, 246 (1986).

[26] S. Oerlemans, M. Fisher, T. Maeder, and K. Kögler, *Reduction of wind turbine noise using optimized airfoils and trailing-eratdge serions,* AIAA Journal **47**, 1470 (2009).

[27] S. Oerlemans, *Reduction of wind turbine noise using blade trailing edge devices,* in *22nd AIAA/CEAS Aeroacoustics Conference* (2016) pp. 1–18.

[28] G. Guidati and S. Wagner, *Design of reduced noise airfoils for wind turbines,* European Congress on Computational Methods in Applied Sciences and Engineering, ECCOMAS 2000 , 11 (2000).

[29] F. Bertagnolio, H. A. Madsen, and C. Bak, *Trailing edge noise model validation and application to airfoil optimization,* Journal of Solar Energy Engineering, Transactions of the ASME **132**, 0310101 (2010).

[30] M. F. Barone, *SandiaTechnical Report*, Tech. Rep. August (2011).

[31] I. A. Clark, *Bio-Inspired Control of Roughness and Trailing Edge Noise Bio-Inspired Control of Roughness and Trailing Edge Noise*, Ph.D. thesis, Virginia Polytechnic Institute and State University (2017).

[32] T. Geyer, *Trailing Edge Noise Generation of Porous Airfoils*, Ph.D. thesis (2011).

[33] M. Herr and J. Reichenberger, *In Search of Airworthy Trailing-Edge Noise Reduction Means,* in *17th AIAA/CEAS Aeroacoustics Conference*, June (2011) pp. 1–25.

[34] T. Geyer, E. Sarradj, and C. Fritzsche, *Porous airfoils: noise reduction and boundary layer effects,* International Journal of Aeroacoustics **9**, 787 (2010).

[35] J. Banhart, *Manufacture, characterization and application of cellular materials and metal foams,* Progress in Material Science (2001).

2

TRAILING-EDGE NOISE

-"Look there, Sancho Panza, my friend, and see those thirty or so wild giants, with whom I intend to do battle and kill each and all of them, so with their stolen booty we can begin to enrich ourselves."
-"What giants?" Asked Sancho Panza.
-"The ones you can see over there," answered his master, "with the huge arms, some of which are very nearly two leagues long."
-"Now look, your grace," said Sancho, "what you see over there aren't giants, but windmills, and what seems to be arms are just their sails, that go around in the wind and turn the millstone."
-"Obviously," replied Don Quixote, "you don't know much about adventures."

Miguel de Cervantes Saavedra, The Ingenious Gentleman Don Quixote of La Mancha (1605).

This chapter contains a description of the main characteristics of turbulent-boundary-layer trailing-edge noise. Among others, the directivity and scaling laws for the acoustic power radiated due to the interaction between a solid edge and turbulent flow are addressed. The process of noise generation and an analytical solution for the diffraction of wall-pressure waves at the trailing edge are also described. This model allows to identify the flow properties that drive noise generation on solid edges. This analysis serves as a basis to discuss the physical principle behind the three trailing-edge noise mitigation strategies detailed in Chapter 1.

2.1. INTRODUCTION

In the previous chapter, relevant sources of aerodynamic and mechanical noise within industrial windmills have been described, and trailing-edge noise has been identified as the most important contributor to the overall noise scattered by modern wind turbines.

The present chapter is intended to detail the main features of such a source of noise. To this aim, besides an introduction, the chapter contains three different sections. Section 2.2 addresses fundamental aeroacoustic concepts such as those of acoustic analogy or acoustic compactness, which are subsequently employed to define general scaling laws for trailing-edge noise; these relate the radiated acoustic power to turbulent length scales, flow speed or the size of the wing. Section 2.3 details an analytical model [1] for solid trailing-edge noise scattering, which allows to estimate the sound production employing as input a simplified statistical representation of the boundary layer. The analytical solution allows to identify the characteristics of the turbulent boundary layer that drive noise generation on a solid edge, as well as to introduce further aeroacoustic concepts such as those of subcritical and supercritical gusts. These are used in section 2.4 to deliver a more detailed description of the noise mitigation mechanisms involved in the three noise control techniques presented in section 1.3, namely the optimization of the airfoil shape, serrations and the employment of porous meta-materials at the aft end of the blade. A summary of relevant conclusions resulting from research prior to this PhD project research is included, and the likely noise generation processes taking place at a porous edge are discussed.

2.2. TRAILING-EDGE NOISE CHARACTERISTICS

2.2.1. ACOUSTIC ANALOGY

The process of sound generation by air flow may be regarded as a phenomenon in which part of the energy of a system is converted in acoustic energy that propagates as waves and causes nuisance to people nearby [2].

Despite the great impact that has in daily life, the prediction of aerodynamically generated noise still represents a daunting task, since it usually entails modelling complex physical phenomena (turbulent flow at high Reynolds number, i.e. non-linear governing equations) and complicated geometries. Both the high level of detail required to accurately describe the acoustic field, and the complexity of the physics explain why aeroacoustics is a relatively young discipline, whose origins date back to the seminal work of Sir Michael J. Lighthill [3, 4] in the 1950s.

These works introduce the idea of acoustic analogy, a rearrangement of the governing (full, non-linear) mass and momentum conservation equations into a linearised wave equation with source terms. The analogy is based on the restatement of the real problem as a region where sound is generated, i.e. a source region, and an uniform medium at rest, where sound is propagated. Different elementary solutions to the wave equation, each one with a specific radiation directivity and scaling of the acoustic intensity with flow velocity, are identified depending on the source term. Specifically, the presence of fluctuating volume flow injection, unsteady forces or Reynolds stresses produce solutions that are respectively referred to as monopoles, dipoles and quadrupoles.

Lighthill developed the concept of acoustic analogy to study jet noise, i.e. noise produced by unbounded turbulence, intrinsically related to the latter type of elementary solution. The fundamental result of his work is the well-known Lighthill's eight power law, derived on the basis of dimensional analysis. The law states that free turbulence with characteristic length scale of the order of the jet diameter D, being convected at a characteristic velocity U, and in a medium with density ρ_0, radiates noise whose power W (defined in Appendix A) is proportional to

$$W \propto \rho_0 c_0^3 D^2 M_0^8 \tag{2.1}$$

where M_0 is the Mach number $M_0 = U/c_0$ and c_0 is the speed of sound. The law was experimentally verified a posteriori [5]. Such a result had a remarkable impact on the design of subsequent propulsive units as it underlined that in order to achieve quieter jets without losing thrust, larger jet diameters were necessary.

The derivation of this law assumes compactness of the source region, which applies when the characteristic length scale of the flow is small compared to the acoustic wavelength. If this condition applies, one can assume incompressible potential flow within the finite source region and replace it by a point source [6]. This concept is formally expressed in terms of the Helmholtz number $\mathrm{He} = 2\pi D/\lambda_0 = k_0 D$ as $\mathrm{He} \ll 1$, where λ_0 and $k_0 = 2\pi/\lambda_0$ are the acoustic wavelength and wavenumber respectively. Note that this approximation implies subsonic flow conditions ($D/\lambda_0 \sim M_0$) [7]. Lighthill's eight power law addresses sound generated by the interaction between free vortices, but it no longer holds in the presence of solid boundaries. This problem is representative of the noise generated at the rear end of a lifting surface, and is addressed in the following.

2.2.2. TRAILING-EDGE NOISE: CHARACTERISTIC SCALES AND SOURCE NATURE

The effect of introducing solid boundaries on the scattered sound field was firstly studied by Curle [8]. He extended Lighthill's analogy to account for unsteady flow interaction with a surface of length c and span L. In this case, the solid surface is replaced by equivalent external forces acting on the fluid, i.e. dipoles. The power of the radiated acoustic waves is then found to scale as

$$W \propto \rho_0 c_0^3 c^2 \frac{L}{c} M_0^6 \tag{2.2}$$

Hence, the presence of a solid surface increases the radiation efficiency by a factor M_0^2. Physically, this result points out that, compared to jet noise, the noise production at low Mach numbers is higher since the solid boundary partially prevents the compensation of local fluid inhomogeneities with reciprocal flow motions [9]. From this result it also stems that, for instance, doubling the span will result in double the acoustic power (i.e. an increase of 3 dB). Furthermore, from the fact that the source of noise can be regarded as an equivalent acoustic dipole, it stems that noise is radiated along an axis perpendicular to the surface (figure 2.1 for lower U). Formally, this radiation pattern can be described as $p^2 \propto \sin^2(\theta)$, where p is the scattered acoustic pressure and θ is the angle between the chord line and the source-observer line.

Ffowcs-Williams and Hall [11] further addressed the problem of noise generation in the vicinity of a semi-infinite (i.e. non-compact) surface edge. Considering Lighthill's

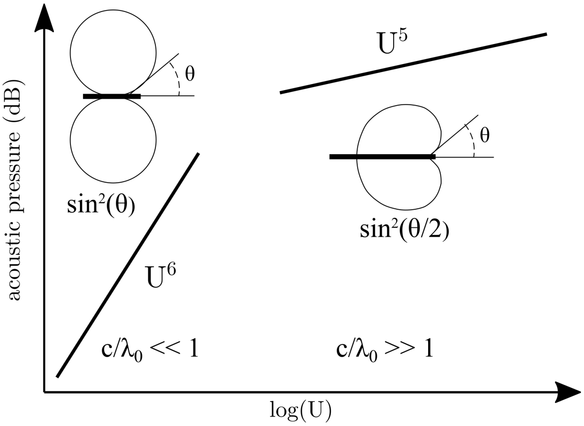

Figure 2.1: Scaling laws and directivity for unsteady flow intearcting with a solid surface with chord c. Adapted from Oerlemans [10].

equation, Ffowcs-Williams and Hall employ a generalized Fourier transform to rewrite it as an inhomogenous Helmholtz equation. The latter is solved employing a tailored Green's function, whose normal derivative vanishes on the surface. The power of the radiated sound is estimated as

$$W \propto \rho_0 c_0^3 \delta^2 \frac{L}{\delta} M_0^5 \tag{2.3}$$

with δ being a turbulence length scale.

The acoustic power is thus proportional to the fifth power of the fluid velocity, i.e. it increases the radiation efficiency with respect to that of a compact surface by a factor M_0. As with the span, the acoustic power scales linearly with the size of the eddy, i.e. an eddy twice as large will result in an increase of 3 dB. Ffowcs-Williams and Hall [11] argued that for turbulent eddies far-away from the surface the scaling laws for unbounded turbulence are retrieved. In other words, the closer the eddies are to the edge, the louder the associated acoustic pressure disturbance is. Specifically, a reduction of 9 dB in the scattered acoustic intensity is estimated for an eddy that doubles the effective distance from the edge.

Furthermore, it is shown that the non-compactness approximation changes significantly the radiation directivity; specifically, noise is now mainly radiated towards the leading edge, resulting in the so-called cardioid directivity pattern ($p^2 \propto \sin^2(\theta/2)$). This directivity pattern, depicted in figure 2.1 for higher U, is responsible for the strong asymmetry observed in the acoustic power scattered by the different blades of a wind turbine [12]; for an observer placed in the ground, the noise perceived has a strong amplitude modulation since it is mainly produced by the blade moving downwards [13].

From the afore described aeroacoustic analogies, it stems that the properties of the noise emitted by the interaction between wall-bounded flow and the trailing edge are strongly dependent on flow speed and turbulent length scales. As a matter of fact, transition from a compact to a non-compact regime will occur for increasing flow speed. It should also be noted that both suction and pressure side of the airfoil contribute to the scattered noise field. Hence, given that turbulence length scales at the suction side are larger than at the pressure side (figure 2.2), the contribution of the suction side to the overall sound emitted is louder, and lower in frequency ($f \sim u/\delta$). The total noise radiation from an edge, with separate contributions from suction and pressure sides, is sketched in figure 2.2.

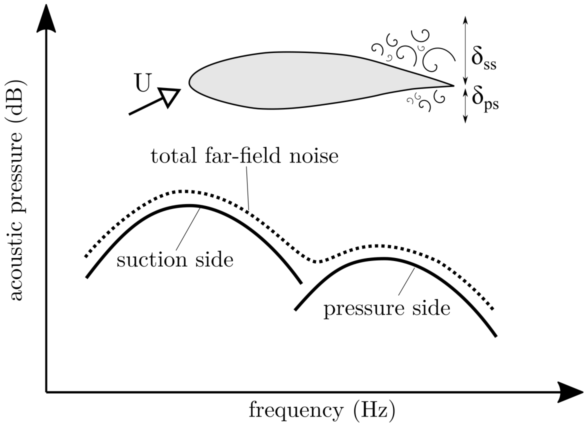

Figure 2.2: Combined contributions of suction and pressure sides to the overall scattered pressure. Adapted from Oerlemans [10].

2.3. TRAILING-EDGE NOISE PREDICTION

The analytical solution derived by Ffowcs-Williams and Hall for a semi-infinite scattering plate can be employed to obtain noise predictions on the basis of kinematic data [11]. This solution requires as input time-resolved information on the three velocity components evaluated in the source region [14]. These data might be retrieved using modern experimental techniques such as tomographic Particle Image Velocimetry (PIV) [15]. However, Tuinstra *et al.* [16] shows that this approach leads to a large overprediction (12 dB) of the scattered sound. The disagreement between measurements and prediction is attributed to the lack of spatial resolution, as well as the presence of measurement noise, which lead to an incorrect computation of local source cancellations.

A second class of solutions for trailing-edge noise prediction is that produced by diffraction theory [17], which relates the scattered far-field acoustic pressure to the surface pressure field measured in the vicinity of a radiating edge. To compute the aeroacoustic transfer function that relates both, thin-airfoil linearized theory [18] is employed. This approach, referred to as diffraction theory, was originally formulated by Amiet [1, 19, 20]; a summary of the derivation is reproduced here for completeness.

2.3.1. DIFFRACTION THEORY - 2D FORMULATION

A surface that interacts with unsteady flow is subject to time variations of both lift and drag forces. Following the Lighthill-Curle formulation, from which equation 2.2 stems, unsteady forces act as equivalent sources of noise. In other words, the acoustic response of the airfoil can be estimated by replacing these forces by equivalent dipoles distributed over the surface. For lifting surfaces the unsteady drag component is much smaller than the lifting one, hence the former can be ignored [21]. The unsteady lift component can then be estimated by solving an equivalent problem, i.e. the response of a plate with chord c, infinitely small thickness and camber (i.e. wall-normal wavenumber $k_y = 0$), no incidence, and parallel flow at a free-stream velocity U_∞, to an incident (compressible) two-dimensional gust. The incident disturbance is assumed to be frozen, i.e. the decaying time is much larger than the time to traverse the chord length [22]. Physically, it is a reasonable assumption for turbulent structures whose dissipation and diffusion time scales are larger than that associated to advection. The coordinate system employed in the following is placed at the trailing edge, with the x and y axes being aligned with stream and spanwise directions (figure 2.3).

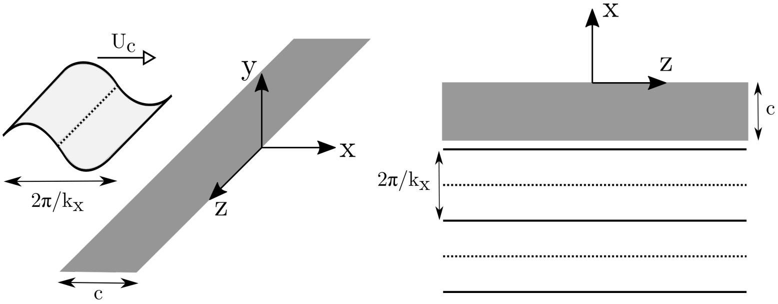

Figure 2.3: Sketch depicting a flat plate with a two-dimensional incident gust.

Assuming a two-dimensional incident pressure gust $p_0(x, y, t)$ with wave fronts parallel to the trailing edge (i.e. spanwise wavenumber $k_z = 0$)

$$p_0(x, y, t) = P_0(x, y)e^{-i(kx-\omega t)} \tag{2.4}$$

with $\omega = 2\pi f$ being the angular frequency, $k = \omega/U_\infty = k_0/M_\infty$ the hydrodynamic wavenumber, $k_0 = \omega/c_0$ the acoustic wavenumber and M_∞ the free-stream Mach number. The gust satisfies the convective wave equation, which is derived from the mass conservation and linearized Euler equations (adiabatic, inviscid flow):

$$\frac{\partial^2 p_0}{\partial x^2} + \frac{\partial^2 p_0}{\partial y^2} - \frac{1}{c_0^2}\left(\frac{\partial}{\partial t} + U_\infty \frac{\partial}{\partial x}\right)^2 p_0 = 0 \tag{2.5}$$

In order to find a solution to this gust-airfoil interaction problem, Amiet employs Schwarschild's technique [23] (detailed in Appendix B). To comply with the technique, equation 2.5 is turned into a canonical Helmholtz equation employing a series of coordinate transformations detailed in the following. Employing the definition of p_0, the convected wave equation reads as follows

$$\beta^2 \frac{\partial^2 P_0}{\partial x^2} + \frac{\partial^2 P_0}{\partial y^2} - 2ik_0 M_\infty \frac{\partial P_0}{\partial x} + k_0^2 P_0 = 0 \tag{2.6}$$

with $\beta^2 = 1 - M_\infty^2$ being the Prandtl-Glauert factor. Further applying the change of variable $P_0(x,y) = p_0^*(x,y)e^{i(k_0 M_\infty/\beta^2)x}$ and using the product rule, one obtains the following expression:

$$\beta^2 \frac{\partial^2 p_0^*}{\partial x^2} + \frac{\partial^2 p_0^*}{\partial y^2} + \left(\frac{kM_\infty}{\beta}\right)^2 p_0^* = 0 \tag{2.7}$$

where $k = \omega/U_\infty = k_0/M_\infty$ is the hydrodynamic wavenumber. Further applying Riessner's transformation $\hat{x} = 2x/c$, $\hat{y} = 2y\beta^2/c$ and $\hat{\mu} = kM_\infty c/2\beta^2$, one retrieves a canonical Helmholtz equation:

$$\frac{\partial^2 p_0^*}{\partial \hat{x}^2} + \frac{\partial^2 p_0^*}{\partial \hat{y}^2} + \hat{\mu}^2 p_0^* = 0 \tag{2.8}$$

Note that in transformed variables the airfoil extends along $-1 \le \hat{x} \le 0$. The trace of the incident gust on the surface of the airfoil can be written as $p_0(x,0,t) = P_0(x,0)e^{i\omega t}$. Solving equation 2.8 requires two boundary conditions. The first stems from the Kutta condition, i.e. pressure must be continuous at the trailing edge. Note that the validity of the assumption for high-frequency disturbances is a matter of on-going discussion (see Satyanarayana and Davisj [24], Taha and Rezaei [25] for further details). The Kutta condition is satisfied by adding a pressure disturbance $P_1(x,0)$ in such a way that the initial one is cancelled at the wake:

$$P_0(x,0) + P_1(x,0) = 0, \quad x \ge 0 \tag{2.9}$$

Let us further assume that the shed disturbances convect at a speed U_c such that $U_c < U_\infty$[1]; hence $p_1(x,0,t) = P_1(x,0)e^{i\omega t} = e^{-i(k_x x - \omega t)}$, with $k_x = \omega/U_c$. Equation 2.9 in transformed coordinates then reads

$$p_1^*(\hat{x},0) = -p_0^*(\hat{x},0) = -e^{-i\frac{\hat{x}c}{2}\left(\frac{U_\infty}{U_c} + \frac{M_\infty^2}{\beta^2}\right)}, \quad \hat{x} \ge 0 \tag{2.10}$$

The second boundary condition states that the airfoil is perfectly rigid:

$$\frac{dP_1}{dy}(x,0) = 0, \quad x < 0 \tag{2.11}$$

In order to comply with the Schwarzschild's technique one must extend the leading edge of the airfoil to infinity. This intrinsically translates into a scattering problem for non-compact surfaces, i.e. high frequencies. The latter boundary condition in transformed coordinates reads

$$\frac{dp_1^*}{d\hat{y}}(\hat{x},0) = 0, \quad \hat{x} < 0 \tag{2.12}$$

Employing Schwarzschild technique on equation 2.8 with boundary conditions 2.10 and 2.12, the airfoil surface pressure jump $\Delta P = P_0(\hat{x},0) - P_1(\hat{x},0)$ reads as follows

---

[1] Note that this assumption conflicts with the assumed initial speed of U_∞ for the incident gust and the frozen turbulence assumption.

$$\Delta P(\hat{x},\omega) = \left[(1+i)E^*\left(-\hat{x}\left[(1+M_\infty)\hat{\mu}+\frac{ck_x}{2}\right]\right)-1\right]e^{-\frac{ik_xc\hat{x}}{2}}P_0(\hat{x},\omega), \quad \hat{x}<0 \tag{2.13}$$

where $k_x = \omega/U_c$ is the streamwise wavenumber and $E^*(x)$ is the complex error function

$$E^*(x) = \int_0^x \frac{e^{-i\xi_0}}{\sqrt{2\pi\xi_0}}d\xi_0 = C_2(x) - iS_2(x) \tag{2.14}$$

with $C_2(x)$ and $S_2(x)$ being Fresnel integrals. For an observer located at $\boldsymbol{x_O} = (x_O, y_O, z_O)$, the far-field acoustic pressure p_a generated by a point source source of strength ΔP submerged in flow at a speed U_∞ is given by Lighthill-Curle theory as [18]

$$p_a(\omega,\boldsymbol{x},\boldsymbol{x_O}) = \frac{-i\omega y_O \Delta P}{4\pi c_0\sigma^2}e^{\frac{i\omega}{c_0\beta^2}\left[\sigma - M_\infty(x_O-x)-\frac{x_Ox+\beta^2y_Oy}{\sigma}\right]} \tag{2.15}$$

where $\sigma^2 = x_O^2+\beta^2(y_O^2+z_O^2)$ is the flow-corrected distance between observer and trailing edge. Equation 2.15 refers to the acoustic pressure produced by a single wave component. The total acoustic pressure can be estimated by employing the overall pressure jump ΔP, contributed by all disturbances whose product $k_xU_c = \omega$ is constant. The incident turbulent pressure field is in practice better suited to a statistical description. For this reason, the cross-power spectral density of the surface pressure jump Φ_{pp} is introduced as

$$\Phi_{pp}(\xi,\omega) = \lim_{T\to+\infty}\left(\frac{\pi}{T}\mathscr{E}[\Delta P(x_1,\omega)\Delta P(x_2,\omega)]\right) \tag{2.16}$$

where $\mathscr{E}$ is the expected value operator, and $\xi = x_2 - x_1$, with the suffixes 1 and 2 referring to different points across the airfoil surface. The total far-field pressure is thus computed by integration of equation 2.15 along the airfoil planform area [20]. Expressing the acoustic pressure in terms of its auto-power spectral density S_{pp}, the derivation yields the following expression for an observer in the midspan plane z_O and wings with large span-to-chord ratio $L/c >> 1$:

$$S_{pp}(x_O,y_O,z_O=0,\omega) = \left(\frac{\omega c y_O}{4\pi c_0\sigma^2}\right)^2\frac{L}{2}\mid\mathscr{L}(k_x)\mid^2\Pi_0\left(\omega,k_x=\frac{\omega}{U_c}\right) \tag{2.17}$$

where $\mathscr{L}$ is the aeroacoustic transfer function[2], defined as

$$\mid\mathscr{L}(k_x)\mid = \frac{1}{\Theta}\left|(1+i)\left\{\Xi E^*\left[2\hat{\mu}\left(1+\frac{x}{\sigma}\right)\right]e^{-i2\Theta} - E^*\left[2((1+M_\infty)\hat{\mu}+\hat{k}_x)\right]\right\}+1\right| \tag{2.18a}$$

$$\Xi = \sqrt{\frac{1+M_\infty+\frac{\hat{k}_x}{\hat{\mu}}}{1+\frac{x_O}{\sigma}}} \tag{2.18b}$$

---

[2] Note that the definition of $\mathscr{L}$ provided by Amiet in the original publication describing the model [1] was later corrected in Amiet [20], following the review on trailing-edge noise modelling of Howe [26]

$$\Theta = \hat{k}_x + \hat{\mu}(M_\infty - \frac{x_O}{\sigma}) \tag{2.18c}$$

with $\hat{k}_x = k_x c/2$ being the dimensionless streamwise wavenumber. On the other hand, the wavenumber-frequency pressure spectrum Π_0, defined as

$$\Pi_0(\omega, k_x = \frac{\omega}{U_c}) = \frac{1}{2\pi}\int_{-\infty}^{\infty} S_{qq}(\xi,\omega)e^{ik_x\xi}\mathrm{d}\xi \tag{2.19}$$

acts as source term for acoustic scattering. The scattering term will be studied more in detail in section 2.3.4. Note that equation 2.17 accounts for the scattering of a single boundary layer; to account for identical boundary layers at both sides of the airfoil, a factor 2 must be included.

2.3.2. 3D GUST SCATTERING EXTENSION

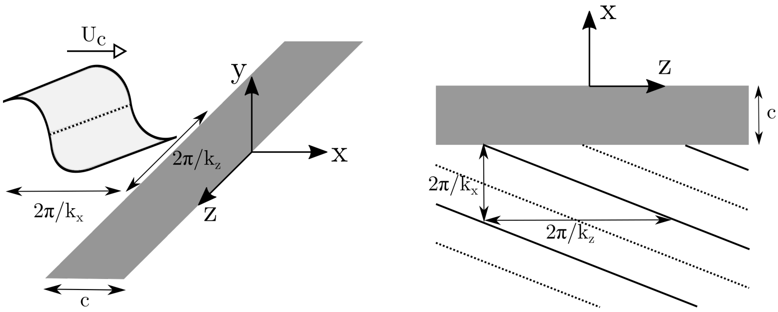

Figure 2.4: Sketch depicting a flat plate with an 3D incident gust.

The two-dimensional problem of the aeroacoustic response of an airfoil described above can be generalized for incident pressure disturbances whose wave fronts are not parallel to the trailing edge (figure 2.4), i.e. with spanwise wavenumbers $k_z \neq 0$ [27]. The skewed incident gust $p_0(x,y,z,t)$ is thus assumed to be of the form

$$p_0(x,y,z,t) = P_0(x,y,z)e^{-i(k_x x + k_z z - \omega t)} \tag{2.20}$$

The incident pressure disturbance now satisfies the three-dimensional convective wave equation that governs the problem. This can be defined analogously to equation 2.5 as

$$\frac{\partial^2 p_0}{\partial x^2} + \frac{\partial^2 p_0}{\partial y^2} + \frac{\partial^2 p_0}{\partial z^2} - \frac{1}{c_0^2}\left(\frac{\partial}{\partial t} + U_\infty\frac{\partial}{\partial x}\right)^2 p_0 = 0 \tag{2.21}$$

By employing a similar transformation as with equations 2.5-2.8 (the reader is referred to Graham [28] and Roger [21] for further details), we now obtain the following canonical Helmholtz equation

$$\frac{\partial^2 p_0^*}{\partial \hat{x}^2} + \frac{\partial^2 p_0^*}{\partial \hat{y}^2} + \left(\frac{M_\infty k_x c}{2\beta^2}\right)^2\left(1 - \frac{1}{\theta^2}\right)p_0^* = 0 \tag{2.22}$$

where $\theta = M_\infty k_x/(\beta k_z)$ is the so-called Graham's gust parameter [28]. This parameter is of paramount relevance for airfoil self-noise theory since the type of pressure response depends on its value. Specifically, for $\theta < 1$ (subcritical gusts) equation 2.22 becomes an elliptic partial differential equation (PDE), and the disturbance gust fades far away from the airfoil surface, i.e. it does not contribute to the acoustic pressure field. On the contrary, for $\theta > 1$ (supercritical gusts) the PDE becomes hyperbolic and the airfoil gust response propagates into the far field. For this reason, the aeroacoustic transfer function of an airfoil often includes exclusively the response to supercritical gusts, as they are the only ones scattered as sound. From the definition of Graham's gust parameter, it stems that in the limit of infinite spanwise wavenumber ($\theta \to 0$), i.e. highly subcritical gusts, these would have their wavefront practically perpendicular to the edge, while for highly supercritical gusts ($\theta \to \infty$) the wavefront would be parallel. Physically, the different scattering properties can be linked to the process of noise generation by the interaction between gust wavefronts and surface discontinuities. Parallel gusts, addressed in section 2.3.1, scatter noise efficiently as they radiate coherently from the entire edge. For oblique gusts, regions of noise generation with different phase alternate sinusoidally along the span, thus provoking source cancellation and radiating sound less efficiently. As will be shown later, this kind of gust scattering is promoted by serrations. Solving for supercritical gusts, the far-field pressure perceived by an observer in the midspan plane $z_O = 0$ is

$$S_{pp}(x_O, y_O, z_O = 0, \omega) = \left(\frac{\omega c y_O}{4\pi c_0 \sigma^2}\right)^2 \frac{L}{2} \mid \mathscr{L}(k_x, k_z) \mid^2 \Pi_0\left(\omega, k_x = \frac{\omega}{U_c}, k_z\right) \tag{2.23}$$

where the aeroacoustic transfer function $\mathscr{L}$ is now defined as

$$\mid \mathscr{L}(k_x, k_z) \mid = \frac{1}{\Theta}\left|(1+i)\left\{\sqrt{\frac{\Omega}{\Omega-\Theta}}E^*\Big[2(\Omega-\Theta)]e^{-i2\Theta}\Big] - E^*\left[2\Omega\right]\right\} + 1\right| \tag{2.24a}$$

$$\Omega = \hat{k}_x + M_\infty \hat{\mu} + \hat{\kappa} \tag{2.24b}$$

$$\hat{\kappa}^2 = \hat{\mu}^2 - \frac{\hat{k}_z}{\beta^2} \tag{2.24c}$$

with $\hat{k}_z = k_z c/2$ being the dimensionless spanwise wavenumber. For $k_z = 0$ the 2D expression (equation 2.18a) is retrieved. The pressure wavenumber-frequency spectrum is in turn modified to account for three-dimensionality

$$\Pi_0(\omega, k_x = \frac{\omega}{U_c}, k_z) = \frac{1}{(2\pi)^2}\int_{-\infty}^{\infty}\int_{-\infty}^{\infty} S_{qq}(\xi, \zeta, \omega) e^{i(k_x\xi + k_z\zeta)} \mathrm{d}\xi \mathrm{d}\zeta \tag{2.25}$$

Note that the analysis above holds strictly under the assumption of infinite aspect ratio ($L/c \to \infty$). For finite wings, subcritical gusts are also radiated into the far-field. For this reason, Roger and Moreau [27] derived a modified aeroacoustic transfer function accounting for subcritical gust scattering $\mid \mathscr{L}'(k_x, k_z) \mid$; they verified *a posteriori* that the subcritical aeroacoustic response has indeed significantly lower amplitude than the supercritical counterpart. However, subcritical disturbances are found to have a non-negligible contribution to the overall far-field pressure outside supercritical radiation lobes. In general, the contribution of subcritical gusts can be safely ignored when computing sound perceived within the midspan plane, although for observer positions closer to the airfoil plane subcritical scattering might become relevant [21]. Note that in order to account for this type of response it is convenient to interpolate between $\mid \mathscr{L}(k_x, k_z) \mid$ and $\mid \mathscr{L}'(k_x, k_z) \mid$ close to the singular condition $k_z = \beta\mu$, that bounds elliptic and hyperbolic solutions to equation 2.22. Given the additional implementation complexity, and the fact that within the framework of the present thesis noise calculations are restricted to an observer in the midspan plane of an isolated airfoil, the subcritical gust response is neglected. However, it should be noted that for rotating blade applications it must be accounted for to retrieve accurate sound levels.

Finally, it is interesting to point out that the infinite aspect ratio approximation not only affects the airfoil gust response but also allows to simplify the radiation integral that yields equation 2.22. Moreau and Roger [29] assessed the effect of this assumption by comparing the general formulation for arbitrary aspect ratio to the infinite aspect ratio formulation (equation 2.23). Results indicate that both agree within 1 dB for $L/c > 2$ and $k_0 c/\beta^2 > 1$. For the typical experimental set-up employed throughout the present work (free-stream velocity $U_\infty = 20$ m/s, chord $c = 0.2$ m and span $L = 0.4$ m), this corresponds to frequencies f above 270 Hz. As will be shown later, this range matches the measurements, hence the infinite aspect ratio formulation is employed.

2.3.3. LEADING-EDGE BACK-SCATTERING EXTENSION

The derivation of the aeroacoustic transfer function for the two-dimensional case (section 2.3.1) extends the leading edge infinitely in order to apply Schwarschild's solution. Hence, the unsteady pressure jump induced by the incident disturbance does not satisfy the condition of pressure continuity upstream the airfoil. Although physically incorrect, Amiet [1] argues that this approximation is valid as long as the scales of turbulence involved in the problem are small (i.e. frequency is high enough). To account for lower-frequency scattering, Roger and Moreau [27] derived a correction term that accounts for the back-scattering of acoustic pressure waves at the leading edge of the airfoil.

The first-order airfoil response derived above (equation 2.24a) is therefore corrected by iteratively applying Schwarschild's technique. In this way, a second-order aeroacoustic transfer function is computed by assuming that the trailing edge is placed at an infinite distance further downstream, and estimating a new solution that ensures the continuity of the pressure field upstream the leading edge. However, such a solution would not satisfy the Kutta condition alone, and successive higher-order leading and trailing edge corrections should be computed iteratively if a rigorous solution is needed. In practice, a second order correction yields accurate results [27]. To compute the far-field pressure accounting for leading edge back-scattering, the same expression detailed in equation 2.23 is employed; yet, the aeroacoustic transfer function is now the sum of the direct scattering term $\mathscr{L}$ defined in equation 2.24a, and a back-scattering term $\mathscr{P}$ [3]. As expected, the correction effectively vanishes at higher-frequencies ($k_0 c > 1$, i.e. $f > 270$ Hz), where only the direct scattering term contributes to far-field pressure [27]. For the

---

[3] The reader is referred to Roger and Moreau [27] for the detailed definition.

same reason detailed above, the leading-edge backscattering correction is not used in the remainder of the thesis.

2.3.4. WAVENUMBER-FREQUENCY WALL PRESSURE SPECTRUM - STATISTICAL DESCRIPTION

The afore described model for trailing-edge noise scattering employs the wall-pressure field in the vicinity of the surface discontinuity as source term. Specifically, the turbulent pressure is statistically described in terms of the wavenumber-frequency spectrum $\Pi(\omega, k_x = \omega/U_c, k_z)$. The characterization of this quantity is of major relevance not only for trailing-edge noise applications, but also for car/aircraft cabin comfort [30]. Yet, its modelling and measurement is still a matter of ongoing research since it involves temporally resolved multi-point measurements, typically with two-dimensional arrays (the reader is referred to Arguillat *et al.* [31], Salze *et al.* [32], Panda *et al.* [33] for recent developments on the topic); a large amount of information is therefore required to achieve a proper characterization.

In this section, two different approaches to model $\Pi(\omega, k_x, k_z)$ into more straightforward variables are described. Firstly, the wavenumber-pressure spectrum is decomposed into the product of a single-point energy spectrum and a characteristic length, which can be experimentally characterized employing a linear array of pressure transducers. Secondly, the relationship between pressure and velocity fluctuations within an incompressible turbulent boundary layer is described, and it is subsequently employed to write the wavenumber-frequency pressure spectrum in terms of readily measurable kinematic quantities.

PRESSURE-BASED DESCRIPTION

Assuming flow in the x direction over a flat surface (i.e. $k_y = 0$) delimited by the plane $x - z$, the wavenumber-frequency spectrum for an oblique incident gust can be formally defined as the time-space Fourier transform of the cross-correlation function R_p of the wall-pressure estimated at 2 points separated by streamwise ξ and spanwise η distances [34]

$$\Pi(\omega, k_x, k_z) = \frac{1}{(2\pi)^3} \int_{-\infty}^{\infty} \int_{-\infty}^{\infty} \int_{-\infty}^{\infty} R_p(\xi, \eta, \tau) e^{-i(\omega\tau - k_x\xi - k_z\eta)} \mathrm{d}\xi \mathrm{d}\eta \mathrm{d}\tau \tag{2.26}$$

where R_p is defined as

$$R_p(x+\xi, z+\eta, t+\tau) = \frac{\overline{p(x,z,t)p(x+\xi, z+\eta, t+\tau)}}{\sqrt{\overline{p^2(x,z,t)}}\sqrt{\overline{p^2(x+\xi, z+\eta, t+\tau)}}} \tag{2.27}$$

Upon integration over the time delay τ one would retrieve the wavenumber-frequency pressure spectrum as the spatial Fourier transform of the cross-spectral density Φ_{pp}, as defined in equation 2.25. Noise predictions require a representation of the wavenumber-frequency spectrum that accounts for the total energy contained at a specific frequency and spanwise wavenumber $\Pi_0(\omega, k_z)$, which can be defined as

$$\Pi_0(\omega, k_z) = \int_{-\infty}^{\infty} \Pi(\omega, k_x, k_z) \mathrm{d}k_x \tag{2.28}$$

Roger and Moreau [27] argue that chordwise statistics have a limited effect on trailing-edge noise; hence assuming that the pressure field is statistically homogeneous nearby the edge, and that the pressure field is measured along a line parallel to the edge, $\Pi_0(\omega, k_z)$ can be computed as [35]

$$\Pi_0(\omega, k_z) = \frac{\phi_p(\omega)}{2\pi} \int_{-\infty}^{\infty} \frac{\Phi_{pp}(\omega, 0, \eta)}{\phi_p(\omega)} e^{ik_z\eta} \mathrm{d}\eta \tag{2.29}$$

where $\phi_p(\omega) = \int_{-\infty}^{\infty} \Pi_0(\omega, k_z)\mathrm{d}k_z$ is the pressure auto-spectrum, that describes the total energy distribution as a function of frequency. The integrand in equation 2.29 is a measure of correlation between pressure measured at points separated spanwisely [36] and can be readily written in terms of the magnitude-squared coherence $\gamma^2(\omega, \eta)$, defined as

$$\gamma^2(\omega, \eta) = \frac{\mid \Phi_{pp}(\omega, \eta) \mid^2}{\phi_p(\omega)^2} \tag{2.30}$$

Taking the absolute value in equation 2.29 and employing the definition of the magnitude-squared coherence, $\Pi_0(\omega, k_z)$ can be described as

$$\Pi_0(\omega, k_z) = \frac{\phi_p(\omega)}{2\pi} \int_{-\infty}^{\infty} \sqrt{\gamma^2(\omega, \eta)} \cos\left(k_z\eta\right) \mathrm{d}\eta \tag{2.31}$$

Finally, introducing the corrected spanwise correlation length $\Lambda_{p|z}(\omega, k_z)$ as

$$\Lambda_{p|z}(\omega, k_z) = \frac{1}{2} \int_{-\infty}^{\infty} \sqrt{\gamma^2(\omega, \eta)} \cos\left(k_z\eta\right) \mathrm{d}\eta = \int_{0}^{\infty} \sqrt{\gamma^2(\omega, \eta)} \cos\left(k_z\eta\right) \mathrm{d}\eta \tag{2.32}$$

the wavenumber-frequency pressure spectrum $\Pi_0(\omega, k_z)$ can be described as the product of the auto power spectral density of the wall-pressure fluctuations $\phi_p(\omega)$ and the spanwise correlation length $\Lambda_{p|z}(\omega, k_z)$

$$\Pi_0(\omega, k_z) = \frac{1}{\pi} \phi_p(\omega) \Lambda_{p|z}(\omega, k_z) \tag{2.33}$$

These two quantities therefore act as source term for the scattering of pressure waves into the far-field (equation 2.17), and suggest that flows with higher turbulent energy and larger flow structures yield higher sound generation. Given their relevance for noise production, semi-empirical models that allow for a fast computation of these quantities based on boundary layer statistics are available in the literature. A brief summary of these is included in the following.

Wall-pressure Power Spectra Eddies of different size contribute the pressure spectrum beneath a turbulent layer [37, 38]. Chase [39] argues that high frequency spectra are influenced by near-wall eddies, while lower frequencies are dominated by larger-scale outer boundary-layer motions. In line with this observation, Keith *et al.* [40], studying experimental data obtained for zero pressure gradient flows, found that distinct sets of boundary layer scales collapse specific frequency ranges within the pressure spectra. On one hand, higher-frequency spectra collapse when normalized by inner boundary layer scales: wall shear stress $\tau_w = \rho u_\tau$ (where u_τ is the friction velocity) as pressure scale, and the ratio ν/u_τ^2 (where ν is the kinematic viscosity) as time scale; on the other hand, lower-frequency spectra collapse using the edge velocity U_e as velocity scale and the boundary layer thickness δ or displacement thickness δ^* as length scale. This implies that there is no universal set of parameters that yield a collapse of wall-pressure spectra within the entire frequency range [41]. More recently, Hwang *et al.* [42] proposed specific boundaries for the regions whereby these different sets of scales can be applied: the low frequency region has a high-frequency bound of $\omega\delta/u_\tau = 100$, the high-frequency region has a low-frequency bound of $\omega\delta/u_\tau^2 = 100$, and there exists an overlap region between both. Furthermore, specific frequency decays were also identified in each region: ω^2 for the lower-frequency region (outer scales), $\omega^{-7/3}$ and ω^{-5} for the higher frequency region (inner scales), and $\omega^{-(0.7-1.1)}$ in the overlap region between both.

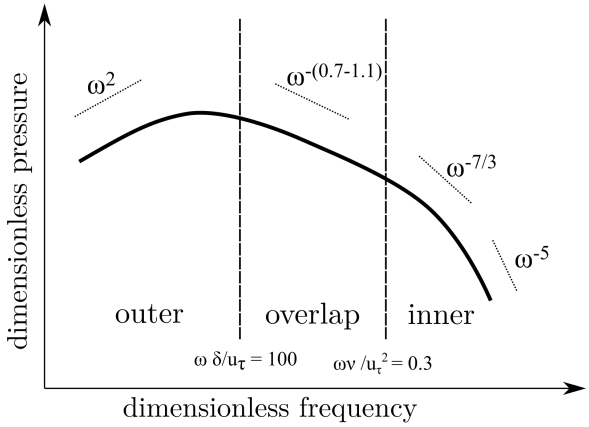

Figure 2.5: General spectral characteristics of wall-pressure spectra. Adapted from Hwang *et al.* [42].

The study of the wall-pressure power spectra is a matter of on-going research due to the complexity of the subject, and several semi-empirical models can be found in the literature as a result of more than 60 years of research [43]. These are created on the basis of the fit of experimental data measured for specific flow conditions (flows subjected to zero/adverse/favourable pressure gradients, and different Reynolds number ranges), as well as tailored object functions that comply with the afore described scalings. For instance, remarkable modelling attempts derived for trailing-edge noise research are those of Amiet [1], Chase-Howe [44, 45] and Graham [36], all relying on zero-pressure gradient turbulent-boundary-layer data. However, wall-pressure spectra measured in the vicinity of the trailing edge of an airfoil are expected to match more accurately Rozenberg's semi-empirical model [46], which relies on adverse-pressure gradient data. This models the pressure power spectrum as

$$\frac{\phi_p(\omega)U_e}{\tau_{\max}^2\delta^*} = \frac{\left(2.82\Delta^2(6.13\Delta^{-0.75}+F_1)^{A_1}\right)(4.2(\Pi/\Delta)+1)\,\tilde{\omega}^2}{\left(4.76\tilde{\omega}^{0.75}+F_1\right)^{A_1}+(C_3\tilde{\omega})^{A_2}} \qquad (2.34)$$

where $\tilde{\omega} = \omega\delta_*/U_e$, $\Delta = \delta/\delta^*$, $A_1 = 3.7+1.5\beta_C$, $A_2 = \min(3, 19/\sqrt{R_T})+7$,$C_3 = 8.8R_T^{-0.57}$,

$F_1 = 4.76(1.4/\Delta)^{0.75}(0.375A_1 - 1)$ and Clauser's parameter $\beta_c = (\theta/\tau_w)(dp/dx)$ [47]. The wake strength parameter Π is found by solving the law of the wake [48], defined as

$$2\Pi - \ln(1+\Pi) = \kappa\frac{U_e}{u_\tau} - \ln\left(\frac{\delta^* U_e}{\nu}\right) - \kappa C^+ - \ln\kappa \tag{2.35}$$

with $\kappa = 0.41$ and $C^+ = 5.1$. This model will be employed to validate pressure data measured nearby the trailing edge of a fully solid airfoil.

Spanwise Correlation Length Corcos [49] modelled the coherence function γ assuming that spanwise and chordwise separations can be treated as independent variables, i.e. that γ can be expressed as a function of the form

$$\gamma(\omega,\xi,\eta) = F_1\left(\frac{\omega\xi}{U_c}\right)F_2\left(\frac{\omega\eta}{U_c}\right)e^{i\frac{\omega\xi}{U_c}} \tag{2.36}$$

where F_1 and F_2 are unknown functions. On the basis of experimental data reported by Willmarth and Wooldridge [50], Corcos [51] argues that these two functions should take the form of exponental decays. Hence, the spanwise coherence function $\gamma(\omega,0,\eta)$ is computed as

$$\gamma(\omega,0,\eta) = e^{-\alpha_1\frac{\omega\eta}{U_c}} \tag{2.37}$$

with α_1 being a fitting parameter with values within 0.48 [1] and 0.71 [49]. Substituting equation 2.37 into equation 2.32, a general expression for the spanwise correlation length $\Lambda_{p|z}(\omega,k_z)$ is attained

$$\Lambda_{p|z}(\omega,k_z) = \frac{\alpha_1\omega/U_c}{k_z^2 + (\alpha_1\omega/U_c)^2} \tag{2.38}$$

and for $k_z = 0$, the correlation length has the form

$$\Lambda_{p|z}(\omega,k_z=0) = \frac{U_c}{\alpha_1\omega} \tag{2.39}$$

VELOCITY-BASED DESCRIPTION

The following pressure wavenumber-frequency spectrum decomposition is usually referred to in the literature as the TNO-Blake model [52, 53]. Here a summary of the derivation is presented. The reader is referred to the original articles for further details. The wall-pressure field generated beneath an incompressible fully turbulent boundary layer is governed by the Poisson equation, which can be derived from the continuity equation and the divergence of the momentum equation

$$\nabla^2 p = -2\rho_0\frac{\partial u_j}{\partial x_i}\frac{\partial U_i}{\partial x_j} - \frac{\partial^2}{\partial x_i x_j}(u_i u_j - \overline{u_i u_j}) \tag{2.40}$$

where ∇^2 stands for the Laplacian operator, U and u refer respectively to time-averaged and fluctuating velocity components following Reynolds decomposition $\hat{u}(t) = U + u(t)$, and $u_1 \equiv u$ and $u_2 \equiv v$ represent streamwise and wall-normal velocity components. The first term on the right hand side of equation 2.40 indicates that pressure unbalances take place due to mean shear-turbulence interaction, and the second term describes the contribution to the pressure field of the interaction between turbulent eddies. For wall-bounded flows, the latter is at least one order of magnitude lower [43], it can thus be neglected. Hence, for a two-dimensional boundary layer over a rigid wall the Poisson equation takes the following form

$$\nabla^2 p = -2\rho_0 \frac{\partial v}{\partial x} \frac{\partial U}{\partial v} \tag{2.41}$$

The solution to equation 2.41 in the free-field involves integrating the convolution of the simplified term on the right hand side with a free-field Green's function [52]. The presence of a rigid wall is then introduced employing the method of images, i.e. the amplitude of the hydrodynamic pressure fluctuation generated by flow over a wall is exactly twice the level of fluctuations generated by the flow in the free-field [6]. The wavenumber-frequency spectrum can be therefore expressed as [54]

$$\Pi(\omega, k_x, k_z) = -2\rho_0 \int_0^{\infty} \frac{\partial U}{\partial y} \frac{k_x}{k} \mathscr{V}(\omega, k_x, k_z, y) e^{-yk} \mathrm{d}y \tag{2.42}$$

where $\mathscr{V}$ stands for the wavenumber-frequency spectrum of the vertical velocity fluctuations, defined analogously to equation 2.26. Assuming that pressure and velocity fields are stationary and homogeneous in the vicinity of the edge, and employing the frozen turbulence assumption, the wavenumber-spectrum for parallel gusts $\Pi_0(\omega, k_z = 0)$ is estimated as [52, 53]

$$\Pi_0(\omega, k_z = 0) = 4\rho_0^2 \int_0^{\delta} \Lambda_{v|y}(\mathrm{y}) U_c(\mathrm{y}) \phi_v(\mathrm{y}, \omega) \left(\frac{\partial U(\mathrm{y})}{\partial y}\right)^2 \frac{\overline{v^2}(\mathrm{y})}{U_c(\mathrm{y})^2} e^{-2k_x y} \mathrm{d}y \tag{2.43}$$

where $\phi_v(y,\omega)$ is the power spectral density of the wall-normal velocity fluctuations, $\Lambda_{v|y}(y)$ is the vertical correlation length of the wall-normal velocity fluctuations and $U_c(y)$ is the streamwise convection velocity of the turbulent structures. As with the pressure-based description (equation 2.33), equation 2.43 indicates that turbulent flows with a higher level of fluctuations or containing larger coherent structures increase noise radiation. Interestingly, the integrand in equation 2.43 is weighted by the exponential term $e^{-2k_x y}$; hence, flow features close to the wall contribute more significantly to the overall scattering of pressure waves, in line with the analytical result obtained by Ffowcs-Williams and Hall [11] (see section 2.2.2).

2.4. TRAILING-EDGE NOISE MITIGATION STRATEGIES

In this section, the noise mitigation mechanisms exploited by the noise mitigation approaches detailed in Chapter 1 are addressed. Specifically, the process of noise generation for serrated, partially porous and optimized edges is described employing concepts and quantities specified in sections 2.2 and 2.3. For edges manufactured with porous materials, a summary of the state of research at the beginning of the present study is also included.

2.4.1. SERRATIONS

Serrations are already a standard noise control technique for industrial wind turbine blade manufacturers such as Siemens Gamesa (Dino-Tails©), Nordex-Acciona (Xtended Power©) or LM Wind Power. This geometrical modification of the edge was devised as a way to promote subcritical gust scattering at the expense of supercritical modes [55], decreasing their overall radiation efficiency (see section 2.3.2). Serrations have received significant attention along the last decade, with a great body of research dedicated to shed light on their working principle, and find geometrical solutions that maximize their noise mitigation performance under specific design conditions. Detailed experimental studies [56–58] reveal the complex flow field in the vicinity of a sawtooth edge, featuring small-scale tip vortices, as well as a modification of the effective angle between flow and edge line. These features might limit noise attenuation with respect to theoretical maxima predicted by analytical models [55], and might also be related to an increase in high-frequency noise scattering. To minimize these issues, researchers at Delft University of Technology have recently conceived an iron-shaped tip [59], that minimizes the three-dimensionality of the flow while promoting interference between sources distributed along the edge [60]. As a result, a noise attenuation of up to 8 dB is achieved with the optimized design, against 6 dB for a baseline sawtooth serration. Similarly, the application of combs between serrations [61] yields further acoustic benefits with respect to a baseline serration. An additional noise attenuation of up to 2 dB is reported, and is attributed to an improved capability to distribute the noise sources along the serrated edge.

2.4.2. OPTIMIZATION OF THE AIRFOIL SHAPE

As seen in Chapter 1, the use of airfoils whose shape has been adapted to maximize noise mitigation has been widely considered as an alternative to serrations in the wind turbine industry. For this reason, several optimization schemes have been proposed by different research groups. Marsden *et al.* [62] employed a derivative-free optimization coupled to a numerical solver to find a local minimum for noise scattering. The procedure is applied to a generic flat plate with beveled trailing-edge, and a more streamlined airfoil with smaller trailing-edge angle is attained as a result. Acoustic data show a complete suppression of shedding-related tonal noise, as well as a decrease of higher-frequency broadband noise. Differences in sound generation with respect to the baseline model are ascribed to a reduction of turbulence intensity (related to the terms $\overline{v^2}$ and Φ_v in equation 2.43) and Reynolds stresses in the vicinity of the aft end. Bertagnolio *et al.* [63] followed a similar approach employing a NACA 63418 airfoil as baseline. In this case, the iterative design cycle includes the characterization of the flow field employing a RANS solver, and an evolutionary algorithm that varies the airfoil shape to minimize the quantities involved in the integrand of equation 2.43. The resultant airfoil has decreased camber and a quasi-constant thickness for the last 5% of the airfoil. As a result, a noise reduction of up to 3.5 dB is achieved. As in the study above, this is mainly attributed to a decrease in turbulent kinetic energy nearby the edge, and to a lesser extent, a reduction in the boundary layer thickness δ, which determines the integration limit in equation 2.43. Volkmer and Carolus [64] also employed evolutionary algorithms to iteratively optimize a baseline Somers S834 airfoil for noise mitigation purposes. In this case, noise radiation is computed employing a pressure-based description of the source term for acoustic scattering, i.e. $\phi_p(\omega)$ and $\Lambda_{p|z}$ (equation 2.33) are minimized. The optimized airfoil is significantly thinner than the baseline and yields up to 5 dB noise mitigation, which is produced by a reduction in the energy of the wall-pressure field $\phi_p(\omega)$. It can be therefore concluded that this noise control strategy aims at decreasing energy and size of turbulent structures within the boundary layer as a mean to decrease sound scattering at the edge.

2.4.3. POROUS METAMATERIALS

An extensive experimental data-base showing the great noise mitigation potential of porous edges was already available at the beginning of the current doctoral work. Geyer *et al.* [65–67] performed acoustic measurements on fully permeable SD7003 airfoils showing more than 20 dB noise attenuation with respect to a solid baseline counterpart. However, this solution also caused a decrease of up to 80% in lift, compared to the baseline airfoil, and up to ten times more drag. To mitigate the loss in aerodynamic performance, Geyer and Sarradj [68] restricted the use of porous materials to the trailing edge. A far-field noise abatement of up to 8 dB was measured even when the permeable fraction was restricted to the last 5% of the chord. With this configuration, only a 6% increase in drag was measured while the decrease in lift was negligible. Different studies [68, 69] also showed a high dependence of the flow field above the trailing-edge insert on the characteristics of the porous material. Specifically, the turbulence intensity in the vicinity of the porous edge was shown to decrease or increase with respect to the solid case for porous materials with similar properties. Such a behaviour indicates that the noise reduction level and mechanism not only depend on the material but also on set-up characteristics such as the model, length of porous insert or angle of attack. Moreover, noise attenuation was measured for porous edges that featured an increase in boundary layer thickness and turbulence intensity with respect to the reference case. As can be seen in section 2.3, these factors should result in noise increase according to the theory for noise scattered from solid edges.

Herr *et al.*[70, 71] also tested different permeable materials on a DLRF16 airfoil with a porous insert length equal to 10% of the chord. Noise reduction with respect to the solid case was reported up to a frequency of 10 kHz depending on the porous material, while above this limit an increase in noise levels was measured. The noise increase, attributed to a surface roughness contribution, was linked to the pore size, while the noise reduction was linked to the permeable nature of the foams, with foams with a higher permeability showing more noise abatement. However, no boundary layer data were reported in this investigation. A comparison between experiments carried out in different facilities [67, 72] also showed scalings of the far-field acoustic pressure with the flow speed ranging between the 5^{th} and the 7^{th} power, indicative of changes in the nature of the acoustic source.

According to Geyer and Sarradj [65], the employment of porous edges might reduce noise due to acoustic absorption, a decrease in turbulent energy nearby the porous extent or a decrease of the radiation efficiency of the edge caused by the modification of the pressure mismatch. A simplified numerical analysis of the acoustic scattering of a single gust convecting over a partially permeable airfoil [73] suggested that the latter mechanism might indeed have a role in the sound scattered at porous edges. Given the many inconclusive aspects described above, the first steps of the project were directed towards clarifying the contribution of each of these mechanisms to the overall noise mitigation of porous edges. This part of the research, described in Chapters 4 and 5, was carried out with porous variants manufactured with metallic foams. Once the mechanism of noise generation was somewhat clarified, it was exploited by the design of permeable edges that link suction and pressure sides of the airfoil with straight channels normal to the chord. These trailing-edge variants are described in Chapters 6 and 7 for variants with homogeneous and varying hole arrangement, respectively.

REFERENCES

[1] R. K. Amiet, *Noise due to turbulent flow past a trailing edge,* Journal of Sound and Vibration **47**, 387 (1976).

[2] M. Roger, *Experimental Aeroacoustics,* edited by M. L. Riethmuller and M. R. Lema (von Karman Institute for Fluid Dynamics, Rhode-Saint-Genese, Belgium, 2006) pp. 1–31.

[3] J. Lighthill, M, *On sound generated aerodynamically I. General theory,* Proceedings of the Royal Society of London. Series A. Mathematical and Physical Sciences **211**, 564 (1952).

[4] M. J. Lighthill, *On sound generated aerodynamically II. Turbulence as a source of sound,* Proceedings of the Royal Society of London. Series A. Mathematical and Physical Sciences **222**, 1 (1954).

[5] M. J. Fisher, P. A. Lush, and M. Harper Bourne, *Jet noise,* Journal of Sound and Vibration **28**, 563 (1973).

[6] S. W. Rienstra and A. Hirschberg, *An Introduction to Acoustics* (2018).

[7] J. Delfs, *Basics of Aeroacoustics,* Lecture Notes (Technische Universitat Braunschweig, 2016).

[8] N. Curle, *The influence of solid boundaries upon aerodynamic sound,* Proceedings of the Royal Society of London. Series A. Mathematical and Physical Sciences **231**, 505 (1955).

[9] C. Schram, *Advances in Aeroacoustics and Thermoacoustics,* edited by C. Schram (von Karman Institute for Fluid Dynamics, Rhode-Saint-Genese, Belgium, 2010) pp. 1–16.

[10] S. Oerlemans, *Airfoil and Wind Turbine Noise.* (2017).

[11] J. E. Ffowcs-Williams and L. H. Hall, *Aerodynamic sound generation by turbulent flow in the vicinity of a scattering half plane,* Journal of Fluid Mechanics **40**, 657 (1970).

[12] S. Oerlemans, P. Sijtsma, and B. . Méndez -López, *Location and quantification of noise sources on a wind turbine,* Journal of Sound and Vibration (2007), 10.1016/j.jsv.2006.07.032.

[13] K. Yoon, D. Y. Gwak, Y. Seong, S. Lee, J. Hong, and S. Lee, *Effects of amplitude modulation on perception of wind turbine noise,* Journal of Mechanical Science and Technology **30**, 4503 (2016).

[14] M. Wang and P. Moin, *Computation of trailing-edge flow and noise using large-eddy simulation,* AIAA journal **38**, 2201 (2000).

[15] G. E. Elsinga, F. Scarano, B. Wieneke, and B. W. Van Oudheusden, *Tomographic particle image velocimetry,* Experiments in Fluids **41**, 933 (2006).

[16] M. Tuinstra, S. Pröbsting, and F. Scarano, *On the use of Particle Image Velocimetry to predict trailing edge noise,* 19th AIAA/CEAS Aeroacoustics Conference , 237 (2013).

[17] K. L. Chandiramani, *Diffraction of evanescent waves, with applications to aerodynamically scattered sound and radiation from unbaffled plates,* The Journal of the Acoustical Society of America **55**, 19 (1974).

[18] R. K. Amiet, *Acoustic radiation from an airfoil in a turbulent stream,* Journal of Sound and Vibration **41**, 407 (1975).

[19] R. K. Amiet, *High frequency thin-airfoil theory for subsonic flow,* AIAA Journal **14**, 1076 (1976).

[20] R. K. Amiet, *Effect of the incident surface pressure field on noise due to turbulent flow past a trailing edge,* Journal of Sound and Vibration **57**, 305 (1978).

[21] M. Roger, *Noise Sources in Turbulent Shear Flows: Fundamentals and Applications,* edited by R. Camussi (Springer, 2013) p. 432.

[22] G. I. Taylor, *The Spectrum of Turbulence,* Proceedings of the Royal Society A: Mathematical, Physical and Engineering Sciences **164**, 476 (1938).

[23] K. Schwarzschild, *Die Beugung und Polarisation des Lichts durch einen Spalt. I,* Mathematische Annalen **55**, 177 (1901).

[24] B. Satyanarayana and S. Davisj, *Experimental Studies of Unsteady Trailing-Edge Conditions,* AIAA Journal **16**, 125 (1978).

[25] H. Taha and A. S. Rezaei, *Viscous extension of potential-flow unsteady aerodynamics: the lift frequency response problem,* Journal of Fluid Mechanics , 141 (2019).

[26] M. S. Howe, *A Review of the Theory of Trailing Edge Noise,* Journal of Sound and Vibration **75**, 239 (1978).

[27] M. Roger and S. Moreau, *Back-scattering correction and further extensions of Amiet's trailing-edge noise model. Part 1: Theory,* Journal of Sound and Vibration **286**, 477 (2005).

[28] J. M. Graham, *Similarity rules for thin aerofoils in non-stationary subsonic flows,* Journal of Fluid Mechanics **43**, 753 (1970).

[29] S. Moreau and M. Roger, *Back-scattering correction and further extensions of Amiet's trailing-edge noise model. Part II: Application,* Journal of Sound and Vibration **323**, 397 (2009).

[30] D. Juve, M. Beron, and E. Salze, *Spectral Properties of Wall-Pressure Fluctuations and Their Estimation from Computational Fluid Dynamics*, edited by E. Ciappi, S. De Rosa, F. Franco, J.-L. Guyader, and S. A. Hambric (Springer International Publishing, 2015).

[31] B. Arguillat, D. Ricot, C. Bailly, and G. Robert, *Measured wavenumber: Frequency spectrum associated with acoustic and aerodynamic wall pressure fluctuations,* The Journal of the Acoustical Society of America **128**, 1647 (2010).

[32] É. Salze, C. Bailly, O. Marsden, E. Jondeau, and D. Juvé, *An experimental characterisation of wall pressure wavevector-frequency spectra in the presence of pressure gradients,* 20th AIAA/CEAS Aeroacoustics Conference (2014), 10.2514/6.2014-2909.

[33] J. Panda, N. H. Roozeboom, and J. C. Ross, *Wavenumber-frequency spectra on a launch vehicle model measured via unsteady pressure-sensitive paint,* AIAA Journal **57**, 1801 (2019).

[34] A. Caiazzo, R. D. Amico, and W. Desmet, *A Generalized Corcos model for modelling turbulent boundary layer wall pressure fl uctuations,* Journal of Sound and Vibration , 1 (2016).

[35] B. A. Singer, *Turbulent Wall-Pressure Fluctuations : A New Model for Off-Axis Cross-Spectral Density,* Journal of Fluids Engineering **1**, 9 (2017).

[36] W. R. Graham, *A Comparison Of Models For The Wavenumber-Frequency Spectrum Of Turbulent Boundary Layer Pressures,* Journal of Sound and Vibration **206**, 541 (1997).

[37] M. K. Bull, *Wall-pressure fluctuations beneath turbulent boundary layers: some reflections on forty years of research,* Journal of Sound and Vibration **190**, 299 (1996).

[38] G. Schewe, *On the structure and resolution of wall-pressure fluctuations associated with turbulent boundary-layer,* Journal of Fluid Mechanics **134**, 311 (1983).

[39] D. M. Chase, *Modeling the wavevector-frequency spectrum of turbulent boundary layer wall pressure,* Journal of Sound and Vibration **70**, 29 (1980).

[40] W. L. Keith, D. A. Hurdis, and B. M. Abraham, *A comparison of turbulent boundary layer wall-pressure spectra,* Journal of Fluids Engineering, Transactions of the ASME **114**, 338 (1992).

[41] T. M. Farabee and M. J. Casarella, *Spectral features of wall pressure fluctuations beneath turbulent boundary layers,* Physics of Fluids A **3**, 2410 (1991).

[42] Y. F. Hwang, W. K. Bonness, and S. A. Hambric, *Comparison of semi-empirical models for turbulent boundary layer wall pressure spectra,* Journal of Sound and Vibration **319**, 199 (2009).

[43] R. H. Kraichnan, *Pressure Fluctuations in Turbulent Flow over a Flat Plate,* The Journal of the Acoustical Society of America **28**, 378 (1956).

[44] D. M. Chase, *The character of the turbulent wall pressure spectrum at subconvective wavenumbers and a suggested comprehensive model,* Journal of Sound and Vibration **112**, 125 (1987).

[45] M. S. Howe, *Acoustics of Fluid-Structure Interactions* (Cambridge University Press, 1998).

[46] Y. Rozenberg, G. Robert, and S. Moreau, *Wall-pressure spectral model including the adverse pressure gradient effects,* AIAA Journal **50**, 2168 (2012).

[47] F. H. Clauser, *The turbulent boundary layer,* in *Advances in applied mechanics* (Elsevier, 1956) pp. 1–51.

[48] D. Coles, *The law of the wake in the turbulent boundary layer,* Journal of Fluid Mechanics **1**, 191 (1956).

[49] G. M. Corcos, *Resolution of Pressure in Turbulence,* The Journal of the Acoustical Society of America **35**, 192 (1963).

[50] W. W. Willmarth and C. E. Wooldridge, *Measurements of the fluctuating pressure at the wall beneath a thick turbulent boundary layer,* Journal of Fluid Mechanics **14**, 187 (1962).

[51] G. M. Corcos, *The structure of the turbulent pressure field in boundary-layer flows,* Journal of Fluid Mechanics **18**, 353 (1964).

[52] W. K. Blake, *Mechanics of flow-induced sound and vibration, volume 2* (Elsevier Science Publishing Co Inc, 2017).

[53] R. R. Parchen, *Progress Report DRAW: A Prediction Scheme for Trailing Edge Noise Based on Detailed Boundary Layer Characteristics*, TNO report (TNO Institute of Applied Physics, 1998).

[54] O. Stalnov, P. Chaitanya, and P. F. Joseph, *Towards a non-empirical trailing edge noise prediction model,* Journal of Sound and Vibration **372**, 50 (2016).

[55] M. S. Howe, *Aerodynamic noise of a serrated trailing edge,* Journal of Fluids and Structures **5**, 33 (1991).

[56] M. Gruber, P. Joseph, and T. Chong, *On the mechanisms of serrated airfoil trailing edge noise reduction,* in *17th AIAA/CEAS Aeroacoustics Conference (32nd AIAA Aeroacoustics Conference)*, June (American Institute of Aeronautics and Astronautics, Reston, Virigina, 2011) pp. 1–23.

[57] T. P. Chong and A. Vathylakis, *On the aeroacoustic and flow structures developed on a flat plate with a serrated sawtooth trailing edge,* Journal of Sound and Vibration **354**, 65 (2015).

[58] F. Avallone, S. Pröbsting, and D. Ragni, *Three-dimensional flow field over a trailing-edge serration and implications on broadband noise,* Physics of Fluids **28**, 117101 (2016).

[59] F. Avallone, W. C. P. van der Velden, and D. Ragni, *Benefits of curved serrations on broadband trailing-edge noise reduction,* Journal of Sound and Vibration **400**, 167 (2017).

[60] F. Avallone, W. C. P. van der Velden, D. Ragni, and D. Casalino, *Noise reduction mechanisms of sawtooth and combed-sawtooth trailing-edge serrations,* Journal of Fluid Mechanics **848**, 560 (2018).

[61] S. Oerlemans, *Reduction of wind turbine noise using blade trailing edge devices,* in *22nd AIAA/CEAS Aeroacoustics Conference* (2016) pp. 1–18.

[62] A. L. Marsden, M. Wang, J. E. Dennis, and P. Moin, *Trailing-edge noise reduction using derivative-free optimization and large-eddy simulation,* Journal of Fluid Mechanics **572**, 13 (2007).

[63] F. Bertagnolio, H. A. Madsen, and C. Bak, *Trailing edge noise model validation and application to airfoil optimization,* Journal of Solar Energy Engineering, Transactions of the ASME **132**, 0310101 (2010).

[64] K. Volkmer and T. H. Carolus, *Aeroacoustic airfoil shape optimization utilizingsemi-empirical models for trailing edge noise prediction,* 2018 AIAA/CEAS Aeroacoustics Conference , 1 (2018).

[65] T. Geyer and E. Sarradj, *Noise generation by porous airfoils,* 13th AIAA/CEAS Aeroacoustics Conference (2007), 10.2514/6.2007-3719.

[66] T. Geyer, E. Sarradj, and C. Fritzsche, *Porous airfoils: noise reduction and boundary layer effects,* International Journal of Aeroacoustics **9**, 787 (2010).

[67] T. Geyer, E. Sarradj, and C. Fritzsche, *Measurement of the noise generation at the trailing edge of porous airfoils,* Experiments in Fluids **48**, 291 (2010).

[68] T. Geyer and E. Sarradj, *Trailing edge noise of partially porous airfoils,* 20th AIAA/CEAS Aeroacoustics Conference (2014), 10.2514/6.2014-3039.

[69] S. A. S. Ali, M. Azarpeyvand, and C. R. I. da Silva, *Experimental Study of Porous Treatment for Aerodynamic and Aeroacoustic Purposes,* in *23rd AIAA/CEAS Aeroacoustics Conference* (2017).

[70] M. Herr and W. Dobrzynski, *Experimental Investigations in Low-Noise Trailing Edge Design,* AIAA Journal **43**, 1167 (2005).

[71] M. Herr, K. S. Rossignol, J. Delfs, N. Lippitz, and M. Moßner, *Specification of Porous Materials for Low-Noise Trailing-Edge Applications,* in *20th AIAA/CEAS Aeroacoustics Conference* (2014) pp. 1–19.

[72] M. Herr and J. Reichenberger, *In Search of Airworthy Trailing-Edge Noise Reduction Means,* in *17th AIAA/CEAS Aeroacoustics Conference*, June (2011) pp. 1–25.

[73] J. Delfs, B. Faßmann, N. Lippitz, M. Lummer, M. Mößner, L. Müller, K. Rurkowska, and S. Uphoff, *SFB 880: aeroacoustic research for low noise take-off and landing,* CEAS Aeronautical Journal **5**, 403 (2014).

3

EXPERIMENTAL METHODOLOGY

"A good rule for rocket experimenters to follow is this: always assume that it will explode."

Astronautics Magazine, Issue 38, October 1937

This chapter describes the experimental methods employed to obtain data analysed in the remaining of the thesis. Specifically, the wind tunnel, airfoil models, permeable trailing-edge inserts, measurement techniques and data reduction procedure are detailed.

3.1. INTRODUCTION

The present chapter is divided into four different sections. Section 3.2 describes the A-Tunnel, the aeroacoustic research facility at Delft University of Technology, as well as the airfoil models used during the tests. Section 3.3 details the different types of porous and permeable meta-materials employed at the rear end of the wings. The procedures applied to characterize them, as well as a summary of their most relevant properties are also included here. Section 3.4 introduces the experimental techniques adopted to characterize both flow field and acoustic scattering for fully solid and partially permeable wings, namely Particle Image Velocimetry (PIV), Hot-Wire Anemometry (HWA), wall-pressure transducers and acoustic beamforming. Finally, the data processing employed to compute kinematic and pressure-related quantities is presented in section 3.5. The procedure is validated by comparing present data with benchmark literature.

3.2. MODELS AND AEROACOUSTIC RESEARCH FACILITY

3.2.1. MODELS

Experiments to be described are carried out primarily on a NACA 0018 airfoil with chord length c of 20 cm, span length L of 40 cm and a trailing-edge thickness of 0.3 mm (figures 3.1 (a-c)). This model is selected because of the availability of extensive aerodynamic [1, 2] and acoustic [3, 4] validation data. The high wing aspect ratio ($L/c = 2$) guarantees negligible three-dimensional flow effects in the midspan plane [5]. The wing section is mounted between two vertical side plates (height: 120 cm) flush-mounted to the nozzle inner lips. The angle of attack can be adjusted using a remote controlled turntable. A sketch of the wing mounted between the side plates is presented in figure 3.1 (a). The model is CNC-machined out of a single block of aluminium (surface roughness: 0.05 mm). The airfoil is modular, i.e. the last 20% of the chord (s = 4 cm) is exchangeable, allowing for testing of trailing edge inserts manufactured from different materials. A dovetail construction is applied to make sure the inserts were rigidly connected to the airfoil body, and vertical screws hold inserts and body together and impede any chordwise misalignment. A piece of 3M Scotch Crystal Tape (width: 19 mm; nominal thickness: 51 μm) is carefully applied at the junction between the solid body of the airfoil and the permeable/solid trailing-edge inserts in such a way that the tape covers 1 mm of the insert in the streamwise direction. This procedure ensures a smooth transition between both pieces. The thickness of the airfoil body at the main body-insert interface h is equal to 15.7 mm. The leading edge of the model is placed 50 cm away from the nozzle outlet.

The streamwise-vertical X-Y-Z coordinate system is also specified in figures 3.1 (a-c). The coordinate system has the origin at the intersection between the trailing edge and the mid-span plane of the airfoil; the X and Z-axis are respectively aligned with the chord and the trailing edge.

To guarantee the fully turbulent state of the boundary layer, transition is forced at 20% of the chord (X/c = -0.8) on both sides using a 10 mm strip with 0.84 mm-diameter carborundum particles randomly distributed along the span. The homogeneity of turbulence downstream the turbulator is assessed with an stethoscope probe [6], consisting of a *Brüel & Kjaer* (B&K) 4134 microphone and a B&K 2619 pre-amplifier [7].

To assess the pressure distribution along the chord, the model is equipped with 30 pressure taps (diameter: 0.4 mm) equally distributed on each side. The taps are distributed within X/c = -0.99 to -0.34 along a plane inclined 15 degrees and with an offset of 20 mm with respect to the midspan plane (figure 3.1 (c)). This configuration minimizes flow interference between consecutive holes.

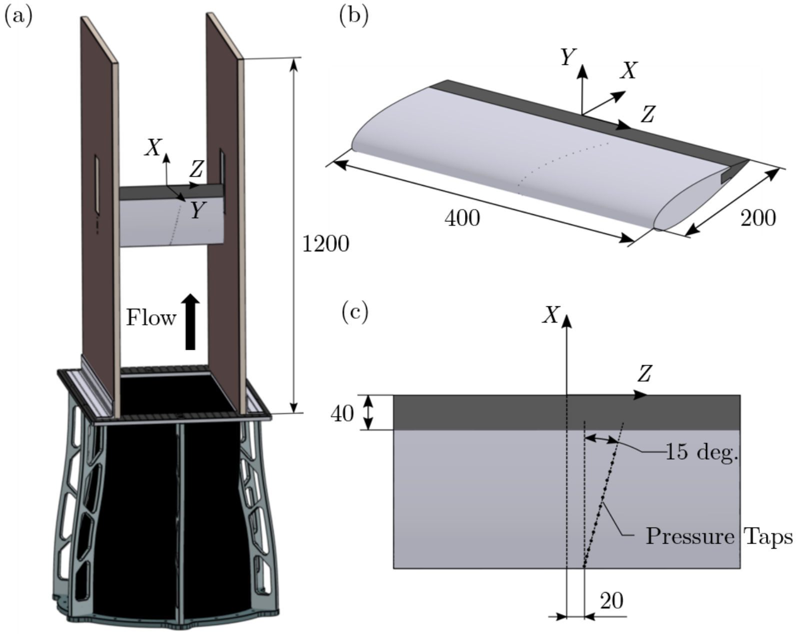

Figure 3.1: Sketch of the test section with the NACA 0018 airfoil and the 40×70 cm^2 nozzle. The aluminum body and the metal foam insert are depicted in light and dark grey respectively. (a) Isometric view. Airfoil and wooden plates mounted on the nozzle. (b) Detail isometric view of the NACA 0018 airfoil. (c) Top view. Lengths in mm.

Some of the results described in Chapter 7 are obtained employing a NACA 63018 airfoil, designed by Luesutthiviboon [8]. These data allow to obtain information about the effect of the partially permeable airfoil shape on the noise mitigation performance. The model has the same dimensions as the afore described NACA 0018 wing and is also modular. The same turbulator is employed for both models.

3.2.2. WIND TUNNEL

The present experimental work was performed in the A-Tunnel, the low-speed vertical wind tunnel at Delft University of Technology. The A-tunnel is an open-jet closed-circuit facility conditioned for aeroacoustic research. The test section is placed at the center of an anechoic plenum (size: 6.4×6.4×3.2 m^3), with walls, floor and ceiling covered with melamine foam wedges. These minimize sound reflections and set quasi far-field conditions over the frequency range from 200 Hz to 20 kHz [9].

The flow accelerates from the settling chamber with a larger baseline nozzle, with an outlet diameter of 0.6 m, height of 3.8 m and a contraction ratio of 15. The outlet

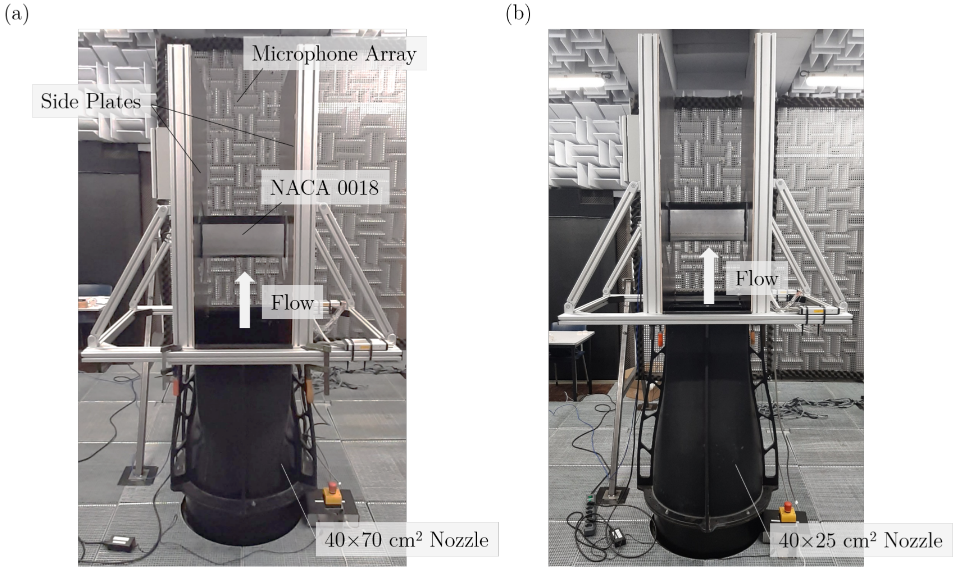

Figure 3.2: Pictures of the A-tunnel test section. The NACA 0018 model between the two side plates is shown in the foreground, while the microphone array is in the background. Air flows from bottom to top. (a) 40×70 cm^2 nozzle extension. (b) 40×25 cm^2 nozzle extension.

conditions can be further adapted by mounting smaller nozzle extensions on top of the baseline contraction. Results were obtained employing two different rectangular contractions: one is 40×70 cm^2 (figure 3.2 (a)) and imposes an overall contraction ratio at 15, while the other is 40×25 cm^2 (figure 3.2 (b)), and has a contraction ratio of 42. Consequently, maximum flow speeds of 34 and 75 m/s can be respectively obtained with each extension. Assuming a typical length of 5 equivalent area diameters [10], the model is well located in the potential core of the jet independently of the nozzle exit dimension. Small jet width-to-airfoil thickness ratios (equal to 0.05 and 0.14 respectively for larger and small cross-area sections) anticipate minor blockage effects [11], and high jet width-to-airfoil chord ratios (higher than 1 for both nozzles) suggest similar loading, hence acoustic scattering [12, 13].

Flow quality is periodically assessed in terms of velocity uniformity and turbulence intensity. The characterization is performed at free-stream velocities U_∞, defined as the velocity at the center of the nozzle outlet, ranging from 2.5 m/s to the afore defined maxima. The mean flow uniformity with respect to the free-stream $(U-U_\infty)/U_\infty$ is evaluated by traversing a Pitot tube across the outlet of the different nozzle extensions. Characteristic results for the 40×70 cm^2 nozzle exit, measured at U_∞ = 34 m/s, are shown in figure 3.3. Measurement positions are depicted as circles and contours are obtained by linear interpolation. Data show that the mean streamwise velocity distribution across most of the outlet section is uniform within 0.6% of the free-stream velocity, and only for outmost points the velocity is up to 0.8% lower than that at the center. Turbulence intensity $\sqrt{\overline{u^2}}/U_\infty$ is characterized employing HWA. The experimental set-up is described in de-

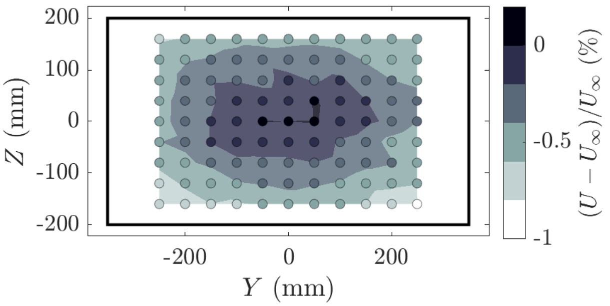

Figure 3.3: Flow uniformity with respect to the free-stream velocity U_∞, measured at the center of the nozzle-cross area section. Measurements are performed at a free-stream velocity of 34 m/s. The nozzle inner lip contour is depicted as a black solid line. Measurement positions are indicated as circles. Adapted from Merino-Martínez *et al.* [9]

tail in section 3.4.2. Data measured at the center of the nozzles are shown in figure 3.4, where turbulence intensity is plotted as a function of free-stream velocity. Results for both nozzles are similar; a maximum turbulence intensity level of approximately 0.2% below $U_\infty = 5$ m/s, and lower values of approximately 0.1% above. Similar results are also found at different points within the outlet cross-section. The high flow uniformity and low turbulence intensity levels encountered in the present facility are in line with other aeroacoustic research facilities [14–17]; hence, they are considered satisfactory.

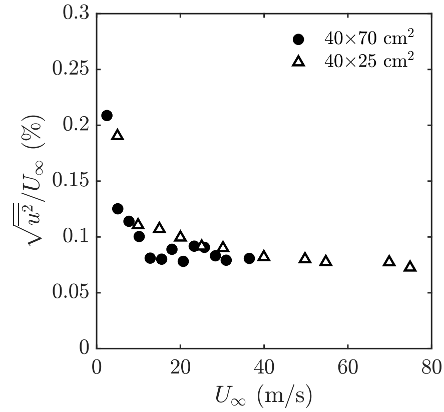

Figure 3.4: Turbulence intensity $\sqrt{\overline{u^2}}/U_\infty$ as a function of free-stream velocity U_∞ measured at the center of the 40×70 cm^2 and 40×25 cm^2 nozzles. Adapted from Merino-Martínez *et al.* [9].

3.2.3. OPEN-JET WIND TUNNEL CORRECTION

The test of finite wings in open-jet facilities entails artificial flow curvature and downwash deflection, effectively reducing the angle of attack seen by the model [18]. The static pressure distribution measured with the model set at a geometric angle α_g is matched to XFOIL predictions [19] to estimate the effective angle of attack α, lower than α_g. Static pressure measurements are obtained through 30 differential pressure Honeywell TruStability transducers (range: ±2.5 kPa; accuracy: 12.5 Pa), connected to the pressure taps. Pressure data are sampled for 15 s at a sampling rate of 50 Hz. The pressure coefficient C_p, defined as

$$C_p = \frac{P - P_\infty}{0.5\rho U_\infty^2} \tag{3.1}$$

where P and P_∞ stand for static and ambient pressure respectively, is plotted as a function of the chordwise position in figure 3.5 (a) for a wind tunnel angle of attack of 8 degrees. The measured suction peak matches the one predicted by XFOIL for an effective angle of attack α of 5.4 degrees, thus yielding a geometric-to-effective angle of attack ratio $\nu = \alpha_g/\alpha$ of 1.48. Brooks *et al.* [20] proposed the following expression, based on lifting surface theory, for ν:

$$\nu = (1+2\psi)^2 + \sqrt{12\psi} \tag{3.2}$$

where $\psi = (\pi c)^2/(48H^2)$ and $H = 70$ cm is the jet width [1]. This yields a value for the correction factor $\nu = 1.52$, in line with the one estimated from the measurements. Additionally, the suction peak close to the leading edge confirms that free-air conditions are adequately reproduced during the tests [12], as anticipated by the low airfoil-thickness-to-jet-width and chord-to-jet-width ratios. The measured lift polar $C_L = L/(0.5\rho U_\infty^2 c)$ (where L is the lift per unit span) is compared in figure 3.5 (b) with XFOIL data and classic thin airfoil theory [21], which yields $C_L = 2\pi\alpha$. Experimental data are plotted employing a geometric-to-effective angle of attack ratio ν of 1.48. Results are in good agreement with both XFOIL data and thin airfoil theory up to the stall regime. This occurs at $\alpha =$ 10 degrees approximately, in line with previously reported values obtained in closed-section facilities [1]. The post-stall overestimation of C_L is a widely-known limitation of XFOIL [22–24], and is due to the employment of empirical closure relations that cannot describe accurately the flow field in such conditions.

3.3. TRAILING-EDGE INSERTS

The NACA 0018 wing is retrofitted with permeable trailing-edge inserts. This feature allows to easily assess the noise mitigation performance of edges with different characteristics.

Specifically, two types of inserts are investigated: on one hand, metallic open-cell foam inserts (figure 3.6 (a)) are machined by electrical discharge machining blocks of material acquired from an external manufacturer; on the other hand, channelled inserts (figure 3.6 (b)), with straight cylindrical channels linking suction and pressure sides of the wing, are 3D-printed in-house. The latter process is intrinsically more suitable for experimental research, as it eliminates any likely change of properties when subjected

---

[1] Measurements at incidence are only performed with the 40×70 cm^2 nozzle; hence the correction is only illustrated for such nozzle geometry.

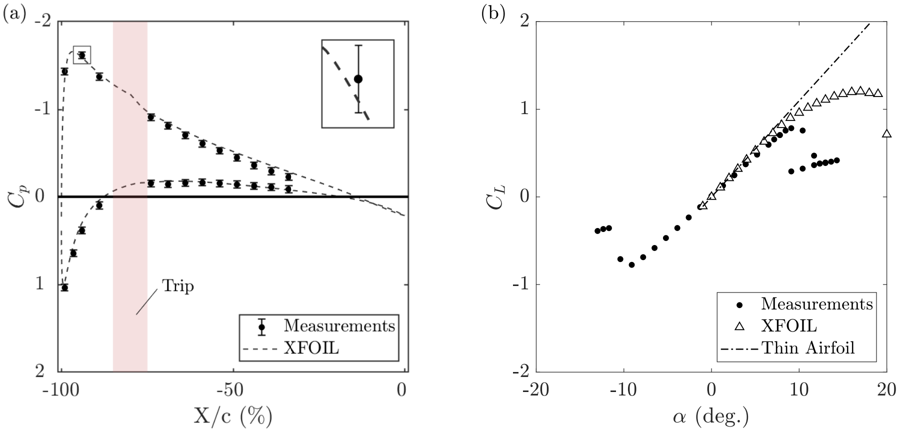

Figure 3.5: Pressure and lift coefficients for the baseline NACA 0018 model. (a) Pressure coefficient C_p along the chord of the baseline NACA 0018 airfoil at a wind tunnel angle of attack α_g of 8 degrees and $U_\infty = 15$ m/s. XFOIL data are obtained for an effective angle of attack α of 5.4 degrees. (b) Change of lift coefficient C_L with α. Experimental data are compared to XFOIL data and thin airfoil theory $C_L = 2\pi\alpha$.

to conventional machining processes, and increases repeatability and prevents inhomogeneity issues, often present in materials with random pore distribution such as metal foams.

Open-cell materials can be characterized in terms of quantities describing geometrical properties, such as cell size d_c, porosity σ or tortuosity τ, as well as on the basis of hydrodynamic properties such as permeability K or form coefficient C, that quantify fluid energy losses as air flows through them. In this section, metal foams and channelled inserts are characterized in terms of these properties. The link between these classifiers and the noise mitigation performance is investigated in the remainder of the thesis.

3.3.1. GEOMETRY

Metal foam inserts are fabricated with *Alantum* NiCrAl open-cell metal foams. In the following, these are referred to in terms of their cell size d_c, as indicated in the microscopy pictures shown in figures 3.7 (a) and (b). Specifically, four different types of foams, with cell sizes d_c of 450, 580, 800 and 1200 μm are extensively studied. All these foams are produced by electrodeposition of pure Ni on a polyurethane foam and subsequently coated with highly-alloyed reactive metal powder [25]. They share a homogeneous micro-structure consisting of the random, three-dimensional repetition of a dodecahedron-shaped cell. The inserts are in turn manufactured by shaping metal foam blocks using electrical discharge machining. Due to manufacturing constraints, two inserts with spanwise extent of 130 and one with 140 mm are assembled to produce a full length trailing edge. The total chordwise length of the inserts is 60 mm, of which only $s/c = 0.2 = 40$ mm is exposed to the flow.

Perforated trailing-edge inserts are manufactured with an *EnvisionTEC*'s Perfactory 4 Standard (resolution: 25 μm), a Digital Light Processing (DLP) printer. The inserts (surface roughness: 0.03 mm) are printed from root to tip using *EnvisionTEC*'s HTM 140

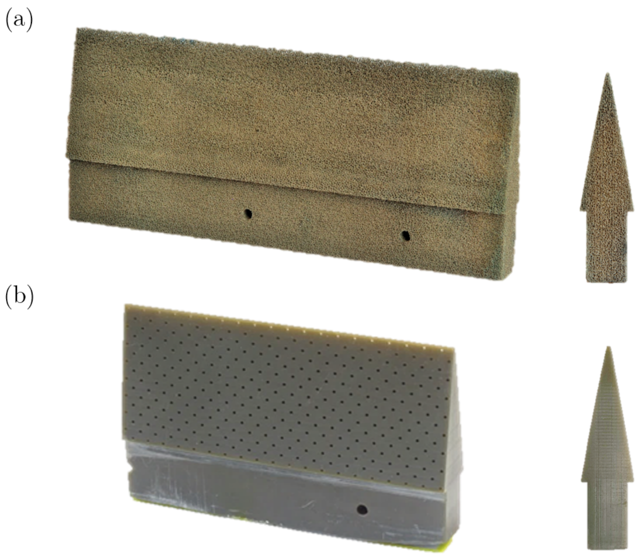

Figure 3.6: Pictures of trailing-edge inserts. Total chordwise extent is 60 mm (of which exposed to the flow s/c = 0.2 = 40 mm) (a) Metal foam with cell size $d_c = 800\,\mu m$. Total span is 130 mm. (b) Perforated insert with l_h = 5 mm. Total span is 100 mm.

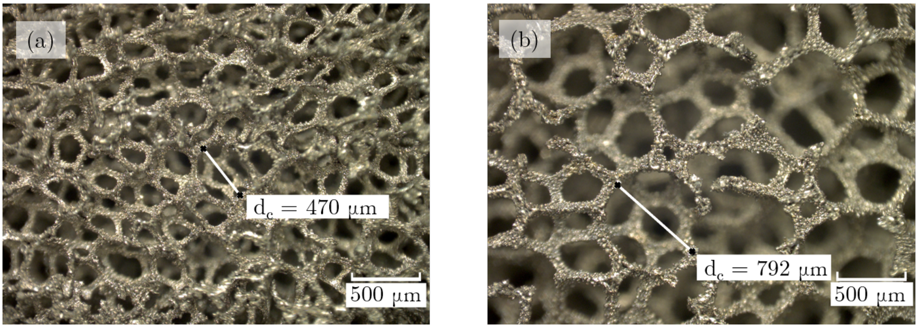

Figure 3.7: 2D microscopy images of the 2 metal foams used in the experiments. (a) $d_c = 450\,\mu m$. (b) $d_c = 800\,\mu m$. Total field of view in the images is 3.05×2.28 mm^2. Resolution: 525 px/mm.

V2, a high-temperature photopolymer [26]. The maximum span of each insert is limited by the build envelope of the printer (160×100×180 mm^3) to 100 mm; hence, 4 inserts are assembled to build the entire trailing edge. The inserts contain straight cylindrical channels normal to the chord connecting suction and pressure sides. Unless indicated differently, holes are distributed according to a staggered square lattice, as shown in figure 3.8. In this study, d_h is equal to 0.8 mm to ensure that the channels are open after the printing process and to avoid low-frequency acoustic tones [27]. The flow permeability

K of the inserts can be varied by changing the hole spacing l_h. Five different perforated inserts, with homogeneous hole spacing l_h of 1.5, 2, 2.5, 3 and 5 mm, are studied. As will be shown, hole spacings are chosen to attain perforated edges with permeability values comparable to those obtained with the metallic foams (the permeability characterization is discussed more in detail later in section 3.3.4). The smallest hole spacing (l_h = 1.5 mm) is determined by manufacturing constraints requiring 0.3 mm of solid material between orifices to yield a satisfactory outcome of the 3D-printing process.

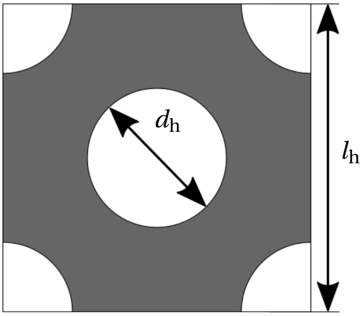

Figure 3.8: Sketch of the hole pattern for perforated inserts.

A post-manufacture quality evaluation reveals that holes are not perfectly round due to limitations in the printing process [28]; specifically, the most downstreamwise end of each hole is flattened, producing D-shaped channels. Optical microscopy (figure 3.9) shows that these holes have a major diameter of approximately 800 μm and a shortened side with length of 700 μm. To account for this feature, an equivalent hole diameter of 754 μm, that yields a circle with area equal to the measured open area (of 447,000 $\mu\mathrm{m}^2$), is employed in section 3.3.4.

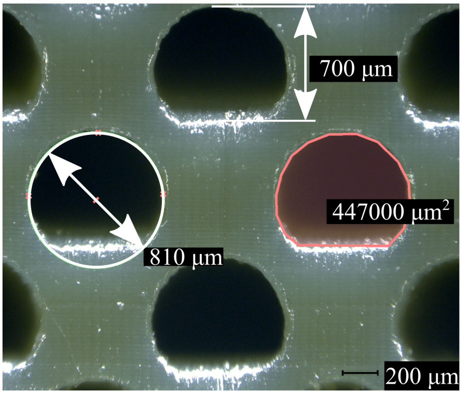

Figure 3.9: Microscope picture of the perforated plate with l_h = 1.5 mm employed to characterize the hydraulic properties of the hole pattern. Hole open area is shadowed in red. Printing layers are distributed horizontally. Printing direction goes from top to bottom. For trailing-edge inserts air flows from top to bottom. The total field of view in the image is of 2.56×2.23 mm^2. Resolution: 2 μm/px.

3.3.2. POROSITY

The porosity σ of a material is defined as:

$$\sigma = 1 - \frac{\rho_p}{\rho_b} \tag{3.3}$$

where ρ_p and ρ_b are respectively the density of porous and base materials (NiCrAl alloy for metal foams). For foams, the density ρ_p is calculated as the ratio between the weight and the volume of $10 \times 10 \times 5$ mm^3 samples. The samples are weighted using a *Mettler* Toledo AB204S analytical balance. In order to retrieve the density of the base alloy ρ_b, the approximate composition is obtained by energy-dispersive X-ray spectroscopy (EDS). The EDS analysis is carried out employing a *Jeol* JSM-7500F Field Emission Scanning Electron Microscope on the same samples used to calculate ρ_p. For perforated inserts, the porosity is computed as $\sigma = \pi d_h^2/(2l_h^2)$, derived from equation 3.3 employing geometrical relations. Porosity values computed for metal foam and channelled inserts are presented in table 3.3. As expected, perforated inserts with higher hole density are more porous, with minimum and maximum porosity of 4 and 40% being measured for channelled inserts with $l_h = 5$ and 1.5 mm respectively. The porosity variation among foams is much more limited; porosity values range between 89 and 92 %, with higher porosity being measured for foams with larger pore size. these values are in line with those reported by the manufacturer (85-90%).

3.3.3. TORTUOSITY

Tortuosity $\tau \equiv l_p/t$ is usually defined [2] as the ratio between the average pore length l_p and the thickness of the porous medium t [31]. From this definition, it follows that straight channels have $\tau_Y = 1$. For random porous media, a statistical description must be employed instead. Specifically, the tortuosity of the pore phase can be computed with random walk models [32]. This approach is specially suitable for research due to the relatively low computational cost and the availability of the open-source *Python* suite *pytrax* [33], which can be employed on CT-scanned samples (size: $10{\times}10{\times}0.5$ mm^3; resolution: 12 μm) shown in figures. 3.10 (a-c).

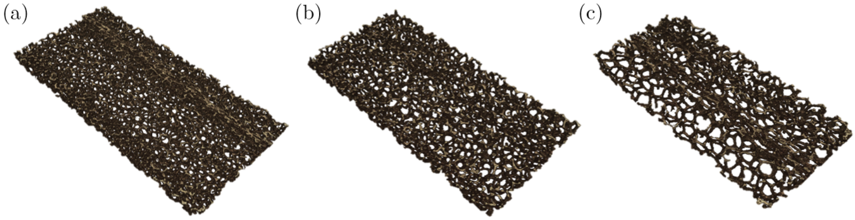

Figure 3.10: CT-scanned samples (resolution: 12 μm) of metal foams with different pore size and permeability. Size: $10{\times}5{\times}0.5$ mm^3.(a) $d_c = 450\,\mu m$. (b) $d_c = 580\,\mu m$. (c) $d_c = 800\,\mu m$.

---

[2] Note that a distinction between tortuosity τ, as defined in the present work, and tortuosity factor $\kappa = \tau^2$ should be made [29]. For more information about the physical interpretation of the latter quantity, the reader is referred to the excellent review of Tjaden *et al.* [30].

Random walk mimics the diffusion of walkers, randomly distributed within porous media [34]. The algorithm begins a time sequence in which each walker randomly selects a neighbouring voxel; if the chosen voxel is also void, the walker then migrates to that position; if not, the walker does not move at that time-step [30]. The mean squared displacement of the ensemble of random walkers $\overline{r(t)^2}$ is then computed as

$$\overline{r(t)^2} = \frac{1}{n_w} \sum_{i=1}^{n_w} \left(r_{X,i}(t)^2 + r_{Y,i}(t)^2 + r_{Z,i}(t)^2 \right) \tag{3.4}$$

where n_w is the total number of walkers, and $r_{X,i}$, $r_{Y,i}$ and $r_{Z,i}$ refer to the displacement of the walker i along X, Y and Z respectively. From equation 3.4, it can be inferred that considering only axial mean square displacements, the tortuosity in a specific direction (τ_X, τ_Y, τ_Z) can be also computed. The mean squared displacement within porous media $\overline{r(t)^2}_p$ is then lower than the one obtained in a fully void space $\overline{r(t)^2}_v$. The degree of reduction, i.e. τ, is then computed as [35]

$$\tau = \sqrt{\frac{\dot{\overline{r^2}}_v}{\dot{\overline{r^2}}_p}} \tag{3.5}$$

where $\dot{r}$ refers to the time derivative of r.

An accurate computation of τ is dependent on both the number of walkers and time-steps n_t. To obtain converged τ values, n_w and n_t should be determined by means of a parametric analysis. In this particular case, convergence is attained with 50,000 walkers and 50,000 time-steps.

Results, presented in table 3.1, are obtained from an ensemble of 100 simulations; reported values correspond to the ensemble average, and a high-bound for the relative uncertainty is estimated as 0.6% based on a 95% confidence level. From the results, it stems that metal foams are not perfectly homogeneous in the transverse flow direction (τ_Y), as can also be inferred from optical observations of cross-sections of the foams. The planar density fluctuations are attributed to the manufacturing process for the original foam blocks.

d_c (μm)	τ_X	τ_Y	τ_Z	τ
450	1.142±0.007	1.194±0.007	1.141±0.007	1.158±0.004
580	1.115±0.006	1.153±0.007	1.143±0.006	1.137±0.004
800	1.107±0.006	1.129±0.006	1.113±0.006	1.116±0.003
1200	1.079	1.061	1.088	1.076

Table 3.1: Tortuosity of metal foams (void phase) computed with random walk methods.

To limit the uncertainty on the aeroacoustic analysis derived from using materials with somewhat heterogeneous properties, the same batch of foam material is used for the tortuosity computation, permeability characterization and insert construction. Similarly, the permeability characterization is carried out in such a way that $K \equiv K_Y$ and $C \equiv C_Y$.

Tortuosity values of table 3.1 are in line with those previously reported in the literature [36–38] for open-cell metal foams with similar characteristics; due to the lack of availability of a CT-scan sample for the metal foam with $d_c = 1200\ \mu$m, its tortuosity is estimated by linear extrapolation of the tortuosity-cell diameter relationship.

3.3.4. PERMEABILITY AND FORM DRAG COEFFICIENT

The static pressure drop Δp across a sample of a homogeneous permeable material with thickness t is described by the Hazen-Dupuit-Darcy equation [39]

$$\frac{\Delta p}{t} = \frac{\mu}{K} v + \rho C v^2 \tag{3.6}$$

where ρ is the fluid density, μ the dynamic viscosity and v is the Darcian velocity, defined as the ratio between the volumetric flow rate and the cross-section area of the sample. The linear and quadratic velocity terms in equation 3.6 account for pressure losses due to viscous dissipation and inertial effects respectively, and are weighted by the permeability K and form coefficient C. These two properties are estimated by least-squares fitting of equation 3.6 to 20 pressure drop data, measured for Darcian velocities ranging between 0 and 2.5 m/s (figures 3.11 (a, b)).

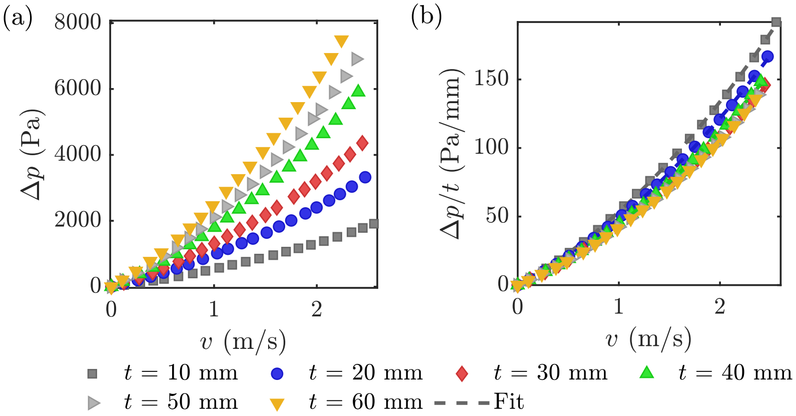

Figure 3.11: Characterization of hydrodynamic properties. (a) Pressure drop measured across samples of d_c = 450 μm metal foams with thickness ranging from 10 to 60 mm. (b) Ratio of pressure drop to thickness (left-hand side term in equation 3.6).

In order to have a precise characterization of the permeability of the metallic foams and the various printed insert configurations, the experimental rig shown in figure 3.12 is used where a pressure drop Δp is specified across a permeable specimen. The rig, supplied by air at 10 bar, allows to measure Δp between two pressure taps placed 5 cm upstream and downstream of the test section. The test section consists of an aluminium cylinder, into which 55 mm diameter sample disks are inserted. The pressure taps are connected to a Mensor 2101 differential pressure sensor (range: -1.2 to 15 kPa; accuracy: 2 Pa). The volumetric flow rate is controlled using an *Aventics* pressure regulator and measured by a *TSI* 4040 volumetric flow meter (range: 0 to 2.5 m/s; accuracy: 2 % of reading) located upstream the pipe. Measurements are performed for 4 s with the static pressure stable within 1% of the read value.

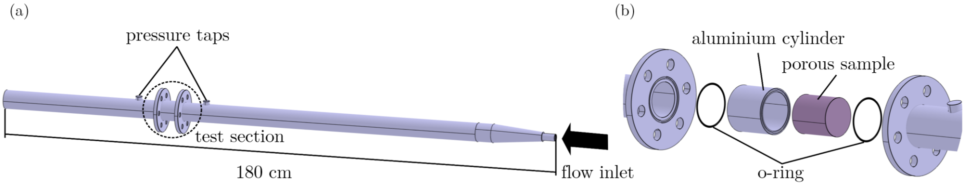

Figure 3.12: (a) Sketch of the rig used to characterize the permeability/resistivity of the metal foams used during the experiments. (b) Detail of the test section.

Previous studies [40, 41] showed that hydraulic properties measured on thin samples are biased due to the prevalence of entrance/exit effects on the measured pressure drop. To study the effect of the sample thickness, t, on K and C, samples with t ranging from 10 mm to 60 mm are tested. Results are shown in figures 3.13 (a) and (b) for metal foams with d_c of 450, 580 and 800 μm. Uncertainty bounds are computed as the 95% confidence levels of the fit. K and C values obtained on samples thicker than 40 mm are similar, i.e. entrance/exit effects are practically negligible. Measured values are in agreement with nominal data reported by the manufacturer, as well as previously published data for open-cell metal foams with similar pore arrangement [42, 43].

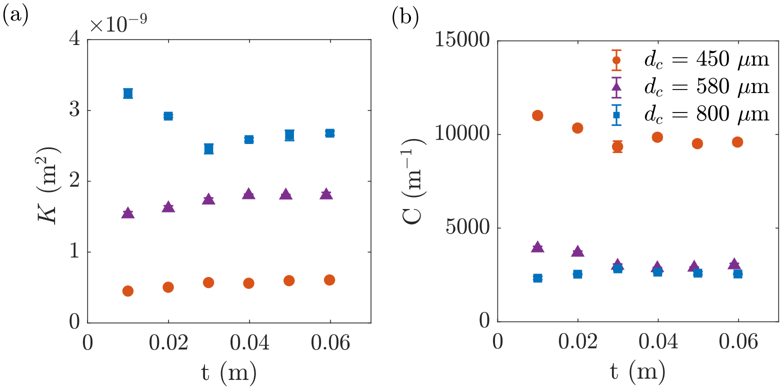

Figure 3.13: Change of hydraulic properties with metal foam specimen thickness t. (a) Permeability K. (b) Form coefficient (C).

Hole patterns employed in the channelled inserts are only characterized for samples with thickness $t = 10$ mm. 3D-printing thicker samples yielded irregular channel diameters, with some of them being closed. Similarly, the characterization of stacked $t = 10$ mm specimens produced inconsistent results due to the impossibility of guaranteeing an adequate channel alignment. The cylindrical samples have hole patterns with l_h = 1.5, 2.8, 4.5 and 6 mm and the same outer diameter of 55 mm. To yield the same D-shaped hole feature, samples are printed as the trailing-edge inserts, i.e., the printing direction is perpendicular to the channels' axes. Hydraulic properties for the specific hole distributions employed in the trailing edges are then estimated using equations 3.7 (a) and (b),

$$K = \frac{\sigma\, d_h^2\, t}{\beta_1 t + \beta_2 d_h} \tag{3.7a}$$

$$C = \beta_3 \frac{1-\sigma}{\sigma^2 t} \tag{3.7b}$$

Study	β_1	β_2	β_3	R^2
Ref. [44]	32	15	0.75	0.98
Present	40	15	0.73	0.95

Table 3.2: Fitting coefficients for equations 3.7 (a) and (b).

These empirical correlations are defined by Bae and Kim [44] for perforated plates with a similar hole arrangement and fully cylindrical holes. The original fit coefficients β_1, β_2 and β_3, as well as the ones retrieved with present data, are reported in table 3.2. To validate the results, correlations based on measured data are compared to the ones presented by Bae and Kim [44] in figures 3.14 (a) and (b). For completeness, K and C values computed from equation 3.6 (referred to as "Measurements"), and the ones interpolated at l_h employed in trailing-edge inserts (referred to as "Interpolation") are shown. The relative error for the original correlations stated by the authors (equal to 3%) is also depicted as a grey shadowed area. Results show that both correlations are in good agreement, confirming the goodness of the permeability characterization.

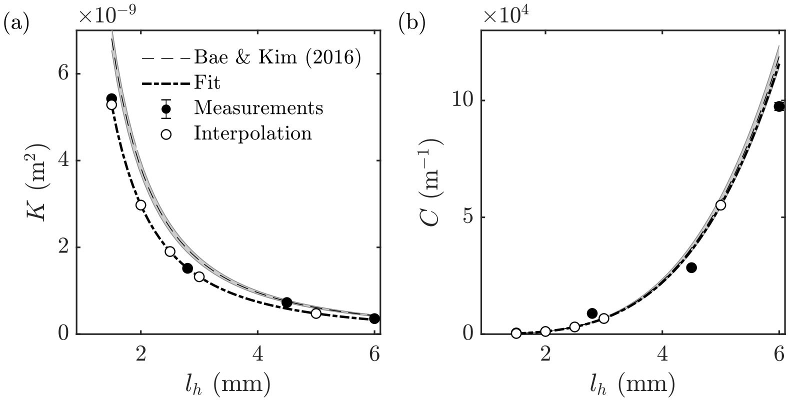

Figure 3.14: Flow permeability K (a) and form coefficient C (b) as a function of the hole spacing. Measurements (diamond markers) are compared to empirical correlations (dashed line) reported in [44], together with the 3% relative error stated by the authors (grey shadowed area).

In previous research on trailing edge noise reduction using porous media [27, 45, 46], the air flow resistivity $R = \Delta p/(t\ v_d)$ was used to characterize the flow-porous material interaction. This property, estimated here as $R = \mu/K$, is also presented in table 3.3 for comparison. Since the noise scattering analysis includes a comparison with inserts manufactured with metal foams, a summary of relevant parameters previously measured [47, 48] for metal foams with d_c = 450, 580 and 800 μm, is also included. For the metal foam with d_c = 1200 μm, the nominal permeability values as reported by the manufacturer is included due to the lack of availability of a cylindrical sample at the time the permeability characterization was performed.

Type	d_c (mm)	d_h (mm)	l_h mm)	σ (-)	K (m^2)	C (m^{-1})
CH	-	0.8	1.5	0.40	54×10^{-10}	279
CH	-	0.8	2	0.22	31×10^{-10}	1138
CH	-	0.8	2.5	0.14	20×10^{-10}	3065
CH	-	0.8	3	0.10	14×10^{-10}	6681
CH	-	0.8	5	0.04	5×10^{-10}	55189
MF	1.20	-	-	-	64×10^{-10}	-
MF	0.80	-	-	0.92	32×10^{-10}	2333
MF	0.58	-	-	0.91	15×10^{-10}	3939
MF	0.45	-	-	0.89	5×10^{-10}	10335

Table 3.3: Characteristics of permeable micro-structures measured on samples with t = 0.01 m. C stands for channelled and MF stands for metal foam. K and C values are interpolated from equations 3.7 (a) and (b) employing the corresponding l_h value. The porosity σ is computed with the corrected d_h of 754 μm to account for D-shaped holes.

3.4. MEASUREMENT TECHNIQUES

In this section, the experimental techniques employed to measure flow field and acoustic scattering for the afore described porous materials, as well as a fully solid baseline insert are introduced. Specifically, the set-ups used to collect PIV, HWA, unsteady surface-pressure and far-field acoustic data are described.

3.4.1. PARTICLE IMAGE VELOCIMETRY

PIV is a versatile non-intrusive technique employed to characterize the local velocity field within a measurement plane or volume. Tracer particles are injected into a fluid flow (often air or water) and are illuminated with a light sheet produced by a source that emits pulses of the order of nanoseconds. Tracers scatter light, which is captured by camera sensors (generally CCD or sCMOS). Pictures of a typical PIV set-up employed in the present project are shown in figures 3.15 (a) and (b). Particle images (figure 3.15 (c)) are then acquired within time intervals of the order of microseconds to seconds, and the particle movement is statistically computed by correlating image pairs. As a result, two or three components vector fields are determined within the measurement region. The reader is referred to the excellent reviews of Raffel *et al.* [49], Westerweel [50] or Scharnowski and Kähler [51] for further information about fundamentals and application.

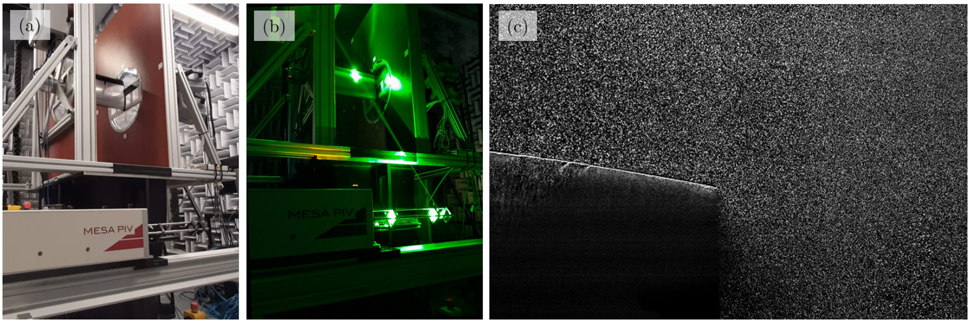

Figure 3.15: PIV set-up pictures. (a) Set-up for a time-resolved PIV experiment. (b) Same set-up during image acquisition. (c) Particle image showing tracers and approximately the last 30% and the wake of the NACA 0018 model.

A series of experiments featuring two-dimensional two-component (2D2C) PIV measurements have been performed in the wall-parallel/normal plane (x-y) at the midspan of the airfoil. For all tests, seeding is produced by a *SAFEX* Twin-Fog Double Power fog generator using a glycol-based solution with mean droplet diameter of 1 μm. Laser optics are used to turn the laser beam into a laser sheet of approximately 1 mm thickness.

The choice of illumination and cameras depends on the required spatial and time resolution. For time resolved experiments, illumination is provided by laser pulses generated either by a *Quantronix* Darwin Duo 527-80-M double cavity Nd:YLF (laser wavelength: 527 nm; energy: 30 mJ/pulse) or a *Continuum* MESA PIV 532-120-M Nd:YAG (wavelength: 532 nm; energy: 18 mJ/pulse) system. Images are recorded using *Photron* Fastcam SA-1 CMOS cameras (1024×1024 pixel^2, 12 bit, pixel size 20 μm), placed at approximately 30 cm from the measurement plane. Cameras are equipped with *Nikon* NIKKOR 105 mm focal distance macro-objectives set at $f_\#$ around 5.6. Time-resolved data are acquired at sampling rates ranging from 10 to 20 kHz depending on the experiment. 5457 (sensor size: 1024×512 pixels) and 10914 (512×512 pixels) image pairs are respectively acquired for each set-up.

For lower image acquisition rates, illumination is provided by laser pulses generated at 3 Hz by a *Quantel* Evergreen 200 II (laser wavelength: 532 nm; energy: 180 mJ/pulse) system. In this case, *Imager* Pro LM 16M cameras (4872×3248 pixel^2, 12 bit, pixel size 7.4 μm) cameras are employed to acquire 1200 image pairs. The different fields of view (FOV) are shown in figure 3.16, and are detailed in table 3.4.

Processing of the images is carried out using *LaVision* DaVis 8.4 software. A multi-pass cross-correlation algorithm [52] with window deformation [53] is applied. Finally, spurious vectors are discarded by applying a universal outlier detector [54] and are replaced by interpolation based on adjacent data. The main characteristics of cameras and acquisition parameters are summarized in table 3.4.

UNCERTAINTY ANALYSIS

Random and systematic (bias) errors are accounted for in the PIV uncertainty estimation. Random errors are due to uncertainty on the cross-correlation analysis and the

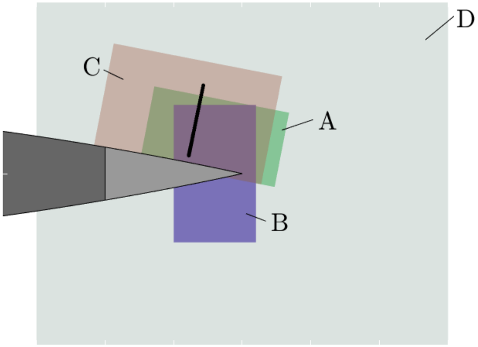

Figure 3.16: Sketch detailing the different FOVs characterized along the doctoral work. HWA measurements are indicated by circles.

Configuration	A	B	C	D
Camera (num.)	Photron (1)	Photron (2)	Photron (2)	Imager (1)
Acq. frequency (kHz)	10	20	20	3
Sep. time (μs)	100	50	50	15
Acq. sensor (px^2)	512×1024	512×512	512×512	4872×3248
FOV (mm^2)	20×40	32×14	30×50	90×130
Dig. resolution (px/mm)	25	25	15	37
Mag. factor	0.51	0.51	0.34	0.25
Int. window (px^2)	24×24	24×24	12×12	12×12
Overlap factor (%)	75	75	75	50
Vec. per field	88×172	136×60	150×250	250×380
Vec. spacing (mm^2)	0.24×0.24	0.24×0.24	0.2×0.2	0.34×0.34
Max. pixel disp. (px)	40	20	15	10
Max. unc. mean velocity (%U_∞)	1	0.5	0.3	0.3
Max. unc. r.m.s. velocity (%U_∞)	0.4	0.4	0.6	0.2

Table 3.4: PIV acquisition parameters.

stochastic description of quantities associated to random processes, which depends on the number of samples. The most important systematic errors are typically peak-locking, particle slip, calibration errors and lack of spatial resolution. Peak-locking consists of a bias of the correlation peak position towards integer displacement. In order to minimize this source of error, the particle image is kept larger than 2 pixels, as suggested in Raffel *et al.* [49]. The histogram of the round-off residual of the particle displacement $\Delta x_i - [\Delta x_i]$, where $[\cdot]$ refers to the rounding function, is depicted in figure 3.17(a); it shows that no bias towards integer values is present on the instantaneous PIV snapshots. In figure 3.17(b), the cumulative sum of the measured decimal particle displacement, used to quantify this source of error, is shown. The error due to peak-locking is found to be always around one order of magnitude smaller than the cross-correlation error.

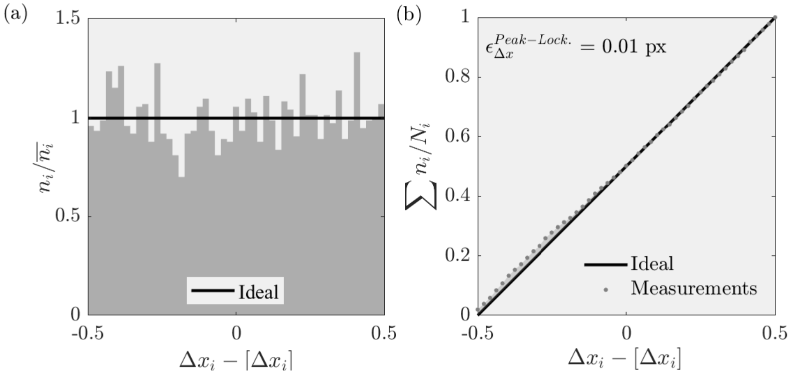

Figure 3.17: Estimation of peak-locking error. (a) Histogram binning $\Delta x_i - [\Delta x_i]$. (b) Cumulative sum of $\Delta x_i - [\Delta x_i]$ values in each bin. The dark grey area between the black line and the dark grey circle markers gives an estimation of peak-locking error. n_i and N_i refer to the number of values inside each bin and the total number of vectors within a instantaneous PIV snapshot, respectively.

Ultimate uncertainty values are determined with the method introduced by Wieneke [55], which measures the correlation between image pairs, once the second frame is projected back accounting for the computed particle displacement. Considering a 95% confidence interval, the latter yields the uncertainty values reported in table 3.4.

3.4.2. HOT-WIRE ANEMOMETRY

HWA is a technique to measure the fluid velocity. A hot wire probe is composed of a thin wire, with diameter of the order of microns, stretched between two prongs. In constant-temperature anemometry (CTA), the operating mode employed for these measurements, flow velocity can be related to the output voltage of a electric circuit that compensates for any deviation from the reference temperature. The system must be therefore calibrated employing accurate sensors such as Pitot tubes as reference. In comparison with PIV, HWA experiments often have higher time and spatial resolution, at the expense of being limited to single point measurements.

Present HWA measurements are carried out with a single-wire *Dantec Dynamics* 55P11 probe (platinum-plated tungsten wire; diameter: 5 μm; length: 1.25 mm) aligned with the Z-axis. The probe is connected to a *TSI IFA-300* system and is operated at an overheat ratio of 0.8 [56]. The analog output voltage signal is sampled at 51.2 kHz for 2 s. The calibration is performed setting both the hot-wire probe and a Pitot tube within the potential core of the jet at the nozzle outlet cross-section. Output voltage and flow speed are related using a fourth-order polynomial fit [57]. In order to correct for any potential deviation from calibration conditions, flow temperature and ambient pressure values are recorded for each measurement [58]. Hot-wire signals are band-pass filtered within 50 Hz and 20 kHz employing a third order Butterworth filter. Measurements are carried out travelling the probe perpendicularly to the wall at X/c = -0.08. A total of 48 wall-normal positions are scanned over a distance of 22 mm. The distance between scans is 0.2 mm closer to the wall, and it is increased gradually up to 0.7 mm in the free-stream region. The probe is mounted on a *Zaber* Traverse System with an positioning accuracy of 15 μm. Wall-normal sweeps are performed above the spanwisely distributed microphones (their specific locations are described below in section 3.4.3.

The uncertainty due to the statistical convergence error on computed velocity quantities is of 0.001% and 0.3% on mean and r.m.s. velocity respectively, and of ±0.1 dB on spectra. To account for any possible Z-axis-wire misalignment, as well as inaccuracies on the positioning, the uncertainty is further estimated as the standard deviation of the values retrieved for different wall-normal runs. This yields relative uncertainty levels of 1 and 2%U_∞ on mean and r.m.s. quantities, respectively, and of ±0.2 dB on spectra.

3.4.3. UNSTEADY WALL-PRESSURE MEASUREMENTS

An L-shaped microphone array consisting of 8 *Sonion* 8010T microphones (nominal phase spreading: ±5°) is clustered inside both solid and metal foam edges to characterize the wall-pressure field above them. The microphones have a sensing diameter of 0.76 mm, total diameter of 2.56 mm and height of 3 mm. The nominal noise level and maximum input are 28 and 112 dB SPL (ref. 20 μPa) respectively. The transducers are installed inside solid and metal foam mock-ups parallel to the surface, and are equipped with pinhole-caps (wall-thickness of 0.4 mm) that decrease the sensing diameter to 0.3 mm. The spacing between inner pinhole wall and sensing diameter is 0.1 mm. This geometry yields an estimated resonant frequency of the cavity of approximately 25 kHz [59], well outside the measurement range.

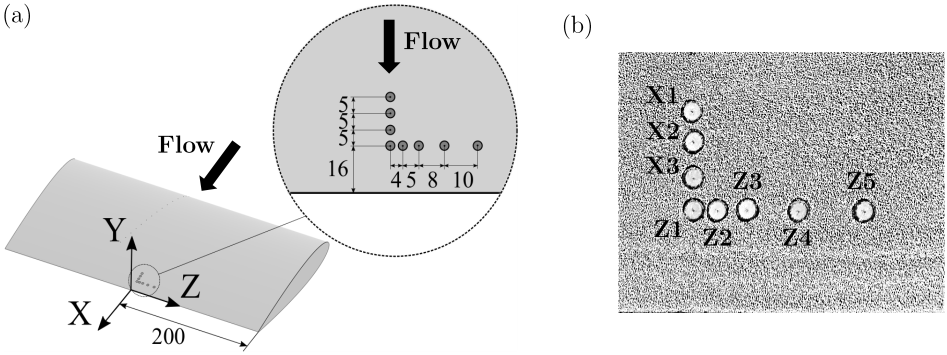

Figure 3.18: (a) Sketch of the NACA 0018 model with *Sonion* 8010T microphone distribution. Lengths are specified in mm. (b) Detail picture of the d_c = 450 μm with microphone nomenclature. Total field of view in the picture is 49×38mm^2.

A sketch of the mock-up is shown in figure 3.18 (a). Three microphones are streamwisely distributed along the midspan plane of the airfoil ($Z/L = 0$), with positions X/c = -0.155, -0.13 and -0.105; these are referred to as X1, X2 and X3 respectively and are employed to compute the mean wall-pressure convection velocity U_c. Five microphones, referred to as Z1, Z2, Z3, Z4 and Z5, are located along the span at X/c = -0.08; transducer Z1 is aligned with microphones X1-X3 ($Z/L = 0$), while the rest are placed at $Z/L = 0.01$, 0.0125, 0.02 and 0.025 respectively. These are employed to calculate the spanwise correlation length $\Lambda_{p|z}$. A detail picture of the instrumented $d_c = 450$ μm mock-up, that includes the microphone terminology, is presented in figure 3.18 (b). A detailed description of the procedure employed to compute U_c and $\Lambda_{p|z}$ is given in section 3.5. The transducers are supplied with 0.9 Vdc. They are calibrated using a *Linear X* M51 electret condensor microphone (maximum input: 150 dB SPL, ref. 20 μPa) as reference [60]. Data are acquired at 51.2 kHz with a *National Instruments* (*NI*) cDAQ 9179 chassis and 4 *NI* 9234 analog-to-digital modules.

Measured spectra are limited by the flat response (±1 dB) of the sensor between 100 Hz and 10 kHz. Power spectra measured by transducers Z1-Z5 yield similar results; hence, wall-pressure spectra included in the present manuscript are obtained by averaging their signals in the frequency domain. A separate data-set is acquired synchronously with the hot-wire probe to assess the coherence between wall-pressure and velocity fluctuations. Similarly to HWA data, the uncertainty (equal to ±0.8 dB) is estimated as the standard deviation of the ensemble.

3.4.4. ACOUSTIC MEASUREMENTS

Far-field acoustic measurements are performed with a phased microphone array consisting of 64 G.R.A.S. 40 PH free-field microphones (frequency response: ±1 dB; frequency range: 10 Hz to 20 kHz; max. output: 135 dB ref. 20 μPa; nominal phase spreading: ±3 deg.) with integrated CCP preamplifiers. The microphone distribution within the antenna, shown in figure 3.19, is optimized to reduce both the main lobe width and the maximum sidelobe level [61]. To improve the resolution in the streamwise direction, microphones are distributed over an ellipse with major-to-minor axis ratio of 2, and a streamwise effective diameter of 2 m. Results have been corrected for a distance from the antenna plane to the airfoil trailing edge of 1 m. The planar array is parallel to the streamwise-spanwise X-Z plane. The center of the array is 3 cm upstream the airfoil trailing edge for the 40×70 cm^3 nozzle, and 10 cm downstream for the 40×25 cm^3 one.

Data are sampled for 20 s at a sampling rate of 50 kHz. Acoustic data are divided in time blocks of 5000 samples ($\Delta t = 0.1$ s), thus resulting in a frequency resolution of 10 Hz, and windowed using a Hanning weighting function with 50% overlap. The cross-spectral matrix of the acoustic pressure is obtained by averaging spectra computed for each sample block [62]. The refraction of sound waves through the shear layer of the jet is corrected using the method proposed by Sijtsma [63]. Conventional frequency domain beamforming [64–66] is performed on a square grid ranging between $-2 < X/c < 2$ and $-2 < Z/c < 2$ and distance between grid points of 10 mm. In order to minimize the effect of extraneous noise sources, integration of the source map within $-0.3 < Z/c < 0.3$ and $-0.6 < X/c < 0.4$ (red area in figure 3.19) is performed. These parameters are optimized for trailing-edge noise research on the basis of a parametric study where the integration region is varied [67]. The high-bound frequency depends on the free-stream velocity due to signal-to-noise ratio issues, and is determined by the presence of the characteristic line source at the trailing edge within beamforming maps (figures 3.20 (a-f)). The lower-bound is limited by background noise levels and the resolution of the array, i.e. the capability to separate different noise sources. The aforedescribed acoustic data reduc-

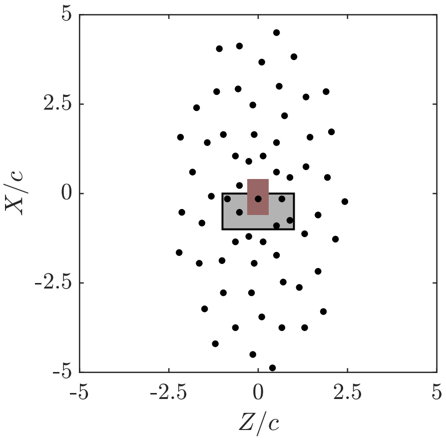

Figure 3.19: Microphone distribution within the array (as seen from the back). The airfoil is marked by the grey area. The distance between trailing edge and microphone array plane is 1.01 m. The trailing edge is approximately 30 mm downstream the center microphone. The integration area is shadowed in red. Flow goes from bottom to top.

tion is typically employed in trailing-edge noise research, with satisfactory results [68]. Uncertainty is estimated in ±1 dB based on a reported comparison with synthetic data [69].

Given the low-frequency nature (below 200 Hz) of some of the fundamental tones described in Chapters 6 and 7, the resolution of the array is too low to distinguish trailing-edge noise from other noise sources. For this reason, far-field acoustic data are obtained by averaging spectra acquired by the 64 microphones [70]. To accurately resolve tones, the number of samples in each data block is increased to 65536, thus yielding a frequency resolution of 0.76 Hz. Acoustic data corrupted by tones also present in background noise measurements are removed from spectra and replaced by linear interpolation based on adjacent points. Noise levels are not corrected for sound wave reflections; therefore their magnitude is not analysed. Acoustic data will be explicitly labelled depending on their origin.

3.5. DATA PROCESSING AND REDUCTION

In this section, the procedure employed to compute kinematic and pressure flow quantities of interest for sound production is detailed. In addition, validation of measurements and data reduction is carried out by comparing data computed for the baseline model with previous studies.

3.5.1. KINEMATIC QUANTITIES

As described in Chapter 2, the sound production at a solid edge can be linked to the following boundary layer kinematic quantities: the power spectral density ϕ_v, the wall-normal correlation length of the wall-normal velocity fluctuations $\Lambda_{v|y}$, the streamwise convection velocity of the turbulent eddies U_c and the boundary layer thickness δ. Moreover, in Chapter 5 correlation maps are extensively employed to analyse the presence of flow communication in permeable edges. The methodology used to estimate these quantities is described below.

POWER SPECTRA

The power spectral density of the vertical velocity fluctuations $\phi_v(\omega)$ is defined as:

$$\phi_v(x,y,\omega) = 2\int_0^{\infty} R_v(x,y,\tau)e^{\mathrm{j}\omega\tau}\mathrm{d}\tau \tag{3.8}$$

where the auto-correlation function R_v is defined as:

$$R_v(x+\xi, y+\zeta, \tau) = \frac{\overline{v(x,y,t)v(x+\xi,y+\zeta,t+\tau)}}{\sqrt{\overline{v^2(x,y)}}\sqrt{\overline{v^2(x+\xi,y+\zeta)}}} \tag{3.9}$$

with τ being the time delay and $\boldsymbol{\xi} = (\xi,\zeta)$ the separation vector. Accordingly to the definition presented in equation 3.8, power spectra reported in the current work follow the single-sided convention $\overline{v^2} = \int_0^{\infty}\phi_v(\omega)\mathrm{d}\omega$. To calculate $\phi_v(\omega)$, Hanning windows of 128 elements and 50% overlapping were used, thus resulting in a frequency resolution of 78 Hz.

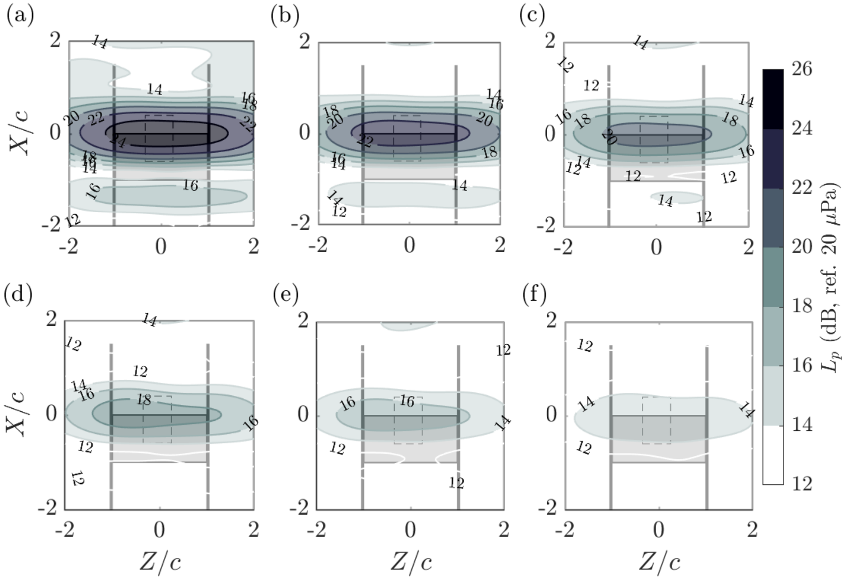

Figure 3.20: Acoustic source maps measured at U_∞ = 25 m/s for solid and channelled trailing edges. Source maps correspond to a frequency of 1400 Hz. Integration area is marked by the dashed line. Dynamic range is 14 dB. Permeable inserts cover 20% of the chord length. (a) Solid. (b) l_h = 5 mm. (c) l_h = 3 mm. (d) l_h = 2.5 mm. (e) l_h = 2 mm. (f) l_h =1.5 mm.

VERTICAL CORRELATION LENGTH

The length scale $\Lambda_{v|y}(x,y)$ is linked to the wall-normal length of turbulence structures. This quantity is defined as:

$$\Lambda_{v|y}(x,y) = \int_0^{\infty} R_v(x, y+\zeta, \tau=0)\mathrm{d}y \tag{3.10}$$

Convergence of the $\Lambda_{v|y}(x,y)$ values within the number of acquired samples is verified. The integration is performed within the range $y \in [0.2\delta, 1.7\delta]$ similarly to Kamruzzaman *et al.* [71] and Arce León *et al.* [4].

CONVECTION VELOCITY

The streamwise convection velocity $U_c(x+\xi, y, \omega)$ is calculated following the method proposed by Romano [72]:

$$U_c(x+\xi, y, \omega) = \xi \frac{\partial\omega}{\partial\phi(x+\xi, y, \omega)} \tag{3.11}$$

where $\phi(x+\xi, y, \omega)$ refers to the phase of the cross-spectra of the wall-parallel fluctuations u between two points separated by a wall-parallel distance ξ. The measured slope $d\phi/d\omega(x+\xi, y, \omega)$ is practically constant within the low frequency range. Deviation from linearity takes place at higher frequencies due to loss of correlation. In order to avoid mislead on the calculation of $U_c(x+\xi, y, \omega)$, measured $\phi(x+\xi, y, \omega)$ are fitted with a line considering data up to cut-off frequency f_{co} = 500 Hz, similarly to Avallone *et al.* [73]. The dependence of the calculated convection velocity on f_{co} is also studied, being assessed that the fit of data up to f_{co} = 1 kHz yields similar results. Due to the employed measurement technique, a wide range of different separation lengths ξ is available. The ultimate $U_c(x+\xi, y, \omega)$ value is estimated as the mean of the ensemble of $U_c(x+\xi, y, \omega)$ values corresponding to different ξ.

BOUNDARY LAYER INTEGRAL PARAMETERS

For PIV data, the boundary layer edge δ_e is estimated with the analysis of the integral of the out-of-plane vorticity along the vertical, as described in Spalart and Watmuff [74]. As the upwash velocity is required to apply this methodology, for HWA data δ_e is instead determined with the diagnostic plot method [75], based on the universal scaling of $\sqrt{\overline{u^2}}$ with U within the outer boundary layer region described by Alfredsson *et al.* [76]. The boundary layer thickness δ is then estimated as the wall-normal distance where $U = 0.99U_e$, with the edge velocity U_e being calculated as the velocity at δ_e.

Experimental PIV and XFOIL data measured for the baseline case are compared against XFOIL data [19] and previous experiments [2, 4] in table 3.5. The agreement with previously published experimental data is good. XFOIL and current data are also in line. Yet, XFOIL underestimates integral boundary layer length scales; this result is consistent with the employment of large carborundum particles within the trip to guarantee turbulent flow at the trailing edge. The shape factor $H = \delta_*/\theta$ is also reported for completeness.

Study	X/c	δ (mm)	δ_* (mm)	θ (mm)	H
Present (HWA)	-0.08	8.3±0.1	2.5±0.1	1.25±0.01	2
Present (PIV)	-0.08	8.1±0.2	2.8±0.3	1.3±0.1	2.2
XFOIL	-0.08	-	1.49	0.87	1.7
Present (PIV)	0	9.2±0.2	3.5±0.3	1.5±0.1	2.3
Ref. [2]	0	9.5	3.3	1.5	2.2
Ref. [4]	0	9.4	2.1	1.3	1.6
XFOIL	0	-	2.3	1.2	2

Table 3.5: Comparison of edge velocity U_e, boundary layer thickness δ, displacement thickness δ_*, momentum thickness θ and shape factor H for the solid edge at $U_\infty = 20$ m/s with values reported in previous studies [2, 4] and XFOIL [19].

CORRELATION MAPS

In Chapter 5 the presence of correlation between turbulent fluctuations at both sides of the airfoil will be addressed. To this aim, the two-point spatial cross-correlation function of the wall-normal velocity fluctuations $R_v(x+\xi, y+\zeta, \tau=0)$ is employed [77].

The normalization of the covariance employed in equation 3.9 provokes an artificial increase of $R_v(x+\xi, y+\zeta)$ at locations where the r.m.s. velocity has low values, i.e., close to the outer boundary layer edge [78]. To avoid this issue, in the present analysis the spatial cross-correlation is computed as:

$$R_v^*(x+\xi, y+\zeta) = R_v(x+\xi, y+\zeta)\sqrt{\frac{\overline{v(x+\xi, y+\zeta)^2}}{\overline{v(x,y)^2}}} = \frac{\overline{v(x,y)\,v(x+\xi, y+\zeta)}}{\overline{v(x,y)^2}}. \tag{3.12}$$

In this way, statistic quantities measured at the separation point are removed from the denominator of equation 3.9. This definition is usually employed in trailing-edge noise research [79, 80].

3.5.2. PRESSURE-BASED BOUNDARY LAYER DESCRIPTION

As explained in section 2.3.4, the power spectral density of the far-field acoustic pressure scattered by the interaction between turbulent flow and an edge can be expressed as the product of the power spectra $\phi_p(\omega)$ and the spanwise correlation length $\Lambda_{p|z}(\omega)$.

POWER SPECTRA

The power spectral density of the surface pressure fluctuations ϕ_p is defined analogously to ϕ_v as:

$$\phi_p(x,z,\omega) = 2\int_0^\infty R_p(x,z,\tau)e^{-\mathrm{j}\omega\tau}\mathrm{d}\tau \tag{3.13}$$

where τ refers to time delay and $R_p(x,z,\tau)$ to the auto-correlation function of the wall-pressure fluctuation signal measured by the microphones, defined in equation 2.27. This quantity is computed employing Welch's spectral estimate [62] (chunks of 2048 data samples; Hanning weighting function; 50 % overlap).

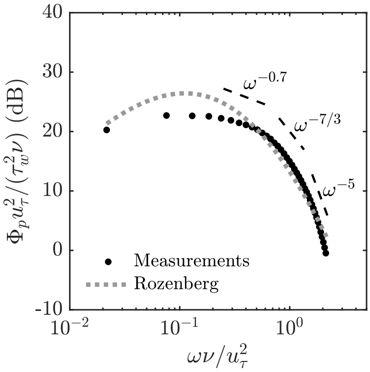

Figure 3.21: Comparison of wall-pressure power spectral density Φ_p with the prediction of Rozenberg's [81] empirical model.

As described in Chapter 2, present ϕ_p data are expected to accurately match Rozenberg's empirical model [81], defined in equation 2.34. Specifically, the wall-pressure spectrum measured at $U_\infty = 20$ ms^{-1} for the baseline model is compared to Rozenberg's model prediction, using boundary layer data presented in table 3.5 as input. The wall shear stress $\tau_w = \rho u_\tau = 0.44$ Pa (where u_τ is the friction velocity) value obtained with PIV is employed. The mean pressure gradient dP/dx, required to compute Clauser's parameter $\beta_c = 5.46$ [82] is obtained from XFOIL data and the Cole's strength parameter $\Pi = 2.46$ is found by solving equation 2.35. The comparison between measurements and predictions is presented in figure 3.21. Wall-pressure spectra are scaled with inner boundary layer quantities u_τ and τ_w. Experimental data agrees with Rozenberg's model prediction within the measured frequency range. Furthermore, experimental data follows the well-established decays corresponding to different frequency regions detailed in Chapter 2.

CONVECTION VELOCITY

The average convection velocity U_c is estimated by analyzing the phase ϕ of the cross-spectra between pressure signals measured by sensors X3 and Z1, separated by a streamwise distance ξ of 5 mm. As with kinematic data, the wall-pressure convection velocity is computed employing equation 3.11. In figure 3.22, ϕ data measured for free-stream velocities of 10, 15 and 20 ms^{-1} are plotted as a function of frequency f. The slope $d\phi/d\omega$ is constant up to a free-stream velocity dependent high-bound frequency ranging between 2 (for $U_\infty = 10$ ms^{-1}) and 4 kHz (for $U_\infty = 20$ ms^{-1}). To avoid deviation from linearity at higher frequencies due to loss of coherence, the mean convection velocity U_c is computed by least-squares fit of a line to experimental data up to 1.5 kHz. For the baseline configuration, U_c ranges between 0.55-0.6 of the free-stream velocity U_∞, in line with values reported by previous experimental trailing-edge noise research [83].

SPANWISE LENGTH SCALE

The spanwise coherence length of the surface-pressure waves $\Lambda_{p|z}$ is estimated employing signals from transducers Z1-Z5, distributed spanwisely at X/c = -0.08, employing

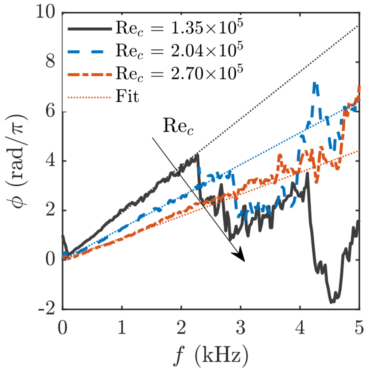

Figure 3.22: Phase ϕ of the cross-spectra between wall-pressure signals acquired by probes X3-Z1 as a function of frequency for the baseline configuration at free stream velocities of 10, 15 and 20 ms^{-1}. Lines are fitted employing data up to 1.5 kHz.

equation 2.32. For validation, $\Lambda_{p|z}(\omega)$ is compared to the afore described semi-empirical relationship introduced by Corcos [84] with fitting constant $\alpha_1 = 0.71$. In figure 3.23, the magnitude squared coherence computed employing signals acquired by transducers Z1 and Z2 ($\eta = 4$ mm) for Re_c ranging from 1.35×10^5 to 2.70×10^5 ($U_\infty = 10$ to 20 ms^{-1}) are compared to equation 2.37. Note that f is normalized by U_c, as determined from the streamwise cross-spectra measurements, and the chord c. Experimental coherence data match the semi-empirical model above $fc/U_c \geq 8$ independently of Re_c, in agreement with previous trailing-edge noise research [85, 86]. Below, the semi-empirical model overestimates experimental coherence data: this is a well-known limitation of the model [87, 88].

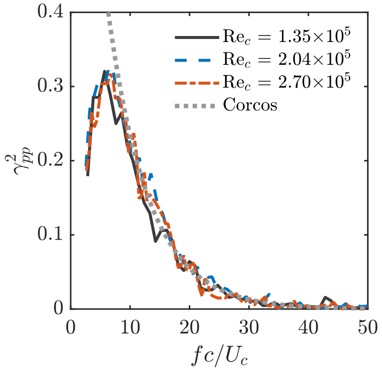

Figure 3.23: Magnitude-squared coherence between pressure signals measured by transducers Z1 and Z2 (η = 4 mm) for chord-based Reynolds numbers Re_c between 1.35×10^5 and 3.40×10^5 (U_∞ = 10, 15, 20 and 25 ms^{-1}) with the semi-empirical relation introduced by Corcos [89].

PRESSURE-VELOCITY CORRELATIONS

The magnitude-squared coherence between pressure and hot-wire data is usually defined as

$$\gamma^2_{u,p}(f) = \frac{\mid \Phi_{u,p}(f) \mid^2}{\phi_p(f)\phi_u(f)} \tag{3.14}$$

where $\Phi_{u,p}$ refers to the cross-spectra between pressure and hot-wire signals acquired synchronously. However, this definition artificially raises coherence values measured outside the boundary layer due to the small values of the velocity spectra, present in the denominator. For this reason, the normalization of the cross-spectra proposed by Zang *et al.* [90] is preferred. This modified pressure-velocity squared-coherence $\tilde{\gamma}^2_{u,p}(f)$ reads as follows

$$\tilde{\gamma}^2_{u,p}(f) = \gamma^2_{u,p}(f)\left(\frac{\sqrt{\overline{u^2}}}{U_\infty}\right)^2 \tag{3.15}$$

Note that due to the change in normalization coherence values are not bounded by [0, 1].

REFERENCES

[1] W. A. Timmer, *Two-dimensional low-Reynolds number wind tunnel results for airfoil NACA 0018,* Wind Engineering **32**, 525 (2008).

[2] F. Avallone, W. C. P. van der Velden, R. Merino-Martínez, and D. Ragni, *Near-wall pressure fluctuations over noise reduction add-ons,* in *23rd AIAA/CEAS Aeroacoustics Conference* (American Institute of Aeronautics and Astronautics, 2017).

[3] C. A. Leon, F. Avallone, S. Pröbsting, and D. Ragni, *PIV Investigation of the Flow Past Solid and Slitted Sawtooth Serrated Trailing Edges,* in *54th AIAA Aerospace Sciences Meeting* (American Institute of Aeronautics and Astronautics, 2016).

[4] C. Arce León, R. Merino-Martínez, D. Ragni, F. Avallone, and M. Snellen, *Boundary layer characterization and acoustic measurements of flow-aligned trailing edge serrations,* Experiments in Fluids **57**, 182 (2016).

[5] M. Mizoguchi and H. Itoh, *Effect of aspect ratio on aerodynamic characteristics at low Reynolds numbers,* AIAA Journal **51**, 1631 (2013).

[6] J. H. M. Gooden, *Experimental low-speed aerodynamic characteristics of the Wortmann FX66-S-196 V1 airfoil,* in *XVI OSTIV Congress* (Chateauroux, France, 1978) pp. 1–11.

[7] D. Lentink and R. de Kat, *Gliding Swifts Attain Laminar Flow over Rough Wings,* PLoS ONE **9**, e99901 (2014).

[8] S. Luesutthiviboon, D. Ragni, F. Avallone, and M. Snellen, *Assessment of the thin-airfoil method for predicting steady pressure distribution on partially-porous airfoils,* 25th AIAA/CEAS Aeroacoustics Conference, 2019 , 1 (2019).

[9] R. Merino-Martínez, A. Rubio Carpio, L. T. Lima Pereira, S. van Herk, F. Avallone, D. Ragni, and M. Kotsonis, *Aeroacoustic design and characterization of the 3D-printed, open-jet, anechoic wind tunnel of Delft University of Technology,* Applied Acoustics **170** (2020), 10.1016/j.apacoust.2020.107504.

[10] P. Upadhyay, G. Valentich, R. Kumar, and F. Alvi, *Flow and acoustic characteristics of non-axisymmetric jets at subsonic conditions,* Experiments in Fluids **58**, 0 (2017).

[11] R. I. Lewis, *Theoretical simulation of open jet wind tunnels for testing wind generator blade profiles,* Wind Engineering **14**, 98 (1990).

[12] S. Moreau, M. Henner, G. Iaccarino, M. Wang, and M. Roger, *Analysis of Flow Conditions in Freejet Experiments for Studying Airfoil Self-Noise,* AIAA Journal **41**, 1895 (2003).

[13] S. Moreau and M. Roger, *Effect of Airfoil Aerodynamic Loading on Trailing Edge Noise Sources,* AIAA Journal **43**, 41 (2005).

[14] T. P. Chong, P. F. Joseph, and P. O. Davies, *Design and performance of an open jet wind tunnel for aero-acoustic measurement,* Applied Acoustics **70**, 605 (2009).

[15] E. Sarradj, C. Fritzsche, T. Geyer, and J. Giesler, *Acoustic and aerodynamic design and characterization of a small-scale aeroacoustic wind tunnel,* Applied Acoustics **70**, 1073 (2009).

[16] W. J. Devenport, R. A. Burdisso, A. Borgoltz, P. A. Ravetta, M. F. Barone, K. A. Brown, and M. A. Morton, *The Kevlar-walled anechoic wind tunnel,* Journal of Sound and Vibration **332**, 3971 (2013).

[17] K. Pascioni, R. Reger, A. Edstrand, and L. Cattafesta, *Characterization of an aeroacoustic wind tunnel facility,* INTERNOISE 2014 - 43rd International Congress on Noise Control Engineering: Improving the World Through Noise Control , 1 (2014).

[18] T. F. Brooks, D. S. Pope, and M. A. Marcolini, *NASA Reference Publication*, Tech. Rep. (NASA Langley Research Center, 1989).

[19] M. Drela, *XFOIL: an analysis and design system for low Reynolds number airfoils,* in *Low Reynolds Number Aerodynamics* (1989) pp. 1–12.

[20] T. F. Brooks, M. A. Marcolini, and D. S. Popet, *Airfoil Trailing-Edge Flow Measurements,* AIAA Journal **24** (1986).

[21] J. D. Anderson, *Fundamentals of Aerodynamics*, 5th ed. (Mcgraw-Hill Education, 2011).

[22] E. Lasauskas and L. Naujokaitis, *Analysis of three wing sections,* Aviation **13**, 3 (2009).

[23] L. F. de Oliveira, H. D. Cerón-Muñoz, and F. M. Catalano, *Aerodynamic Analysis Of High Rotation And Low Reynolds Number Propeller,* 48th AIAA/ASME/SAE/ASEE Joint Propulsion Conference and Exhibit 2012 , 1 (2012).

[24] B. Peerlings, *A review of aerodynamic flow models, solution methods and solvers and their applicability to aircraft conceptual design*, Ph.D. thesis, Delft University of Technology (2018).

[25] S. Kim and C. Lee, *A Review on Manufacturing and Application of Open-cell Metal Foam,* Procedia Materials Science **4**, 305 (2014).

[26] EnvisionTEC GmbH, *Htm 140 V2 Technical Datasheet,* (2018).

[27] M. Herr, K. S. Rossignol, J. Delfs, N. Lippitz, and M. Moßner, *Specification of Porous Materials for Low-Noise Trailing-Edge Applications,* in *20th AIAA/CEAS Aeroacoustics Conference* (2014) pp. 1–19.

[28] J. Kennedy, L. Flanagan, L. Dowling, G. J. Bennett, H. Rice, and D. Trimble, *The Influence of Additive Manufacturing Processes on the Performance of a Periodic Acoustic Metamaterial,* International Journal of Polymer Science **2019**, 1 (2019).

[29] P. Grathwohl, *Diffusion in Natural Porous Media: Contaminant Transport, Sorption/Desorption and Dissolution Kinetics*, 1st ed., Topics in Environmental Fluid Mechanics, Vol. 1 (Springer US, Boston, MA, 1998) p. 31.

[30] B. Tjaden, D. J. L. Brett, and P. R. Shearing, *Tortuosity in electrochemical devices: a review of calculation approaches,* International Materials Reviews **63**, 47 (2018).

[31] N. Epstein, *On tortuosity and the tortuosity factor in flow and diffusion through porous media,* Chemical Engineering Science **44**, 777 (1989).

[32] E. A. Codling, M. J. Plank, and S. Benhamou, *Random walk models in biology,* Journal of the Royal Society Interface **5**, 813 (2008).

[33] T. G. Tranter, M. D. Kok, M. Lam, and J. T. Gostick, *pytrax: A simple and efficient random walk implementation for calculating the directional tortuosity of images,* SoftwareX **10**, 100277 (2019).

[34] H. Iwai, N. Shikazono, T. Matsui, H. Teshima, M. Kishimoto, R. Kishida, D. Hayashi, K. Matsuzaki, D. Kanno, M. Saito, H. Muroyama, K. Eguchi, N. Kasagi, and H. Yoshida, *Quantification of Ni-YSZ anode microstructure based on dual beam FIB-SEM technique,* ECS Transactions **25**, 1819 (2009).

[35] J. M. Zalc, S. C. Reyes, and E. Iglesia, *The effects of diffusion mechanism and void structure on transport rates and tortuosity factors in complex porous structures,* Chemical Engineering Science **59**, 2947 (2004).

[36] P. Du Plessis, A. Montillet, J. Comiti, and J. Legrand, *Pressure drop prediction for flow through high porosity metallic foams,* Chemical Engineering Science **49**, 3545 (1994).

[37] B. Boudreau, *The diffusive tortuosity of fine-grained unlithified sediments,* Geochimica et Cosmochimica Acta **60**, 3139 (1996).

[38] K. K. Bodla, J. Y. Murthy, and S. V. Garimella, *Microtomography-based simulation of transport through open-cell metal foams,* Numerical Heat Transfer; Part A: Applications **58**, 527 (2010).

[39] D. Ingham and I. Pop, *Transport phenomena in porous media* (Pergamon, 1998) p. 446.

[40] E. Baril, A. Mostafid, L.-P. Lefebvre, and M. Medraj, *Experimental demonstration of entrance/exit effects on the permeability measurements of porous materials,* Advanced Engineering Materials **10**, 889 (2008).

[41] N. Dukhan and K. Patel, *Effect of sample's length on flow properties of open-cell metal foam and pressure-drop correlations,* Journal of Porous Materials **18**, 655 (2010).

[42] J. Despois and A. Mortensen, *Permeability of open-pore microcellular materials,* Acta Materialia **53**, 1381 (2005).

[43] J. P. Bonnet, F. Topin, and L. Tadrist, *Flow laws in metal foams: compressibility and pore size effects,* Transport in Porous Media **73**, 233 (2007).

[44] Y. Bae and Y. I. Kim, *Numerical modeling of anisotropic drag for a perforated plate with cylindrical holes,* Chemical Engineering Science **149**, 78 (2016).

[45] T. Geyer, E. Sarradj, and C. Fritzsche, *Porous airfoils: noise reduction and boundary layer effects,* in *15th AIAA/CEAS Aeroacoustics Conference* (American Institute of Aeronautics and Astronautics, 2009).

[46] T. Geyer, E. Sarradj, and C. Fritzsche, *Measurement of the noise generation at the trailing edge of porous airfoils,* Experiments in Fluids **48**, 291 (2010).

[47] A. Rubio Carpio, F. Avallone, D. Ragni, M. Snellen, and S. van ver Zwaag, *Mechanisms of broadband noise generation on metal foam edges,* Physics of Fluids **31** (2019), 10.1063/1.5121248.

[48] A. Rubio Carpio, R. Merino-Martínez, F. Avallone, D. Ragni, M. Snellen, and S. van der Zwaag, *Broadband trailing edge noise reduction using permeable metal foams,* 46th International Congress and Exposition of Noise Control Engineering, 27–30 August, 2017, Hong Kong , 4373 (2017).

[49] M. Raffel, C. E. Willert, and J. Kompenhans, *Particle Image Velocimetry* (Springer Berlin Heidelberg, 1998).

[50] J. Westerweel, *Fundamentals of digital particle image velocimetry,* Measurement Science and Technology **8**, 1379 (1997).

[51] S. Scharnowski and C. J. Kähler, *Particle image velocimetry - Classical operating rules from today's perspective,* Optics and Lasers in Engineering (2020), 10.1016/j.optlaseng.2020.106185.

[52] F. Scarano and M. Riethmuller, *Advances in Iterative multigrid PIV Image Processing,* Experiments in Fluids **29**, 51 (2000).

[53] F. Scarano, *Iterative image deformation methods in PIV,* Measurement Science and Technology **13**, R1 (2001).

[54] J. Westerweel and F. Scarano, *Universal outlier detection for PIV data,* Experiments in Fluids **39**, 1096 (2005).

[55] B. Wieneke, *PIV uncertainty quantification from correlation statistics,* Measurement Science and Technology **26**, 74002 (2015).

[56] F. E. Jorgensen, *How to measure turbulence with hot-wire anemometers - a practical guide*, Tech. Rep. (Dantec, 2002).

[57] J. D. Vagt, *Hot-Wire Probes in Low Speed Flow,* Aerospace **18**, 271 (1979).

[58] P. C. Stainback and K. A. Nagabushana, *Review of hot-wire anemometry techniques and the range of their applicability,* American Society of Mechanical Engineers, Fluids Engineering Division (Publication) FED **167**, 93 (1993).

[59] S. Pröbsting and S. Yarusevych, *Laminar separation bubble development on an airfoil emitting tonal noise,* Journal of Fluid Mechanics **780**, 167 (2015).

[60] S. Pröbsting, M. Tuinstra, and F. Scarano, *Trailing edge noise estimation by tomographic Particle Image Velocimetry,* Journal of Sound and Vibration **346**, 117 (2015).

[61] S. Luesutthiviboon, A. Malgoezar, M. Snellen, P. Sijtsma, and D. Simons, *Improving Source Discrimination Performance by Using an Optimized Acoustic Array and Adaptive High-Resolution CLEAN-SC Beamforming,* in *7th Berlin Beamforming Conference* (2018).

[62] P. Welch, *The use of fast Fourier transform for the estimation of power spectra: A method based on time averaging over short, modified periodograms,* IEEE Transactions on Audio and Electroacoustics **15**, 70 (1967).

[63] P. Sijtsma, *Phased Array Beamforming Applied to Wind Tunnel And Fly-Over Tests*, Tech. Rep. October (NLR, 2010).

[64] R. P. Dougherty, *Functional Beamforming,* in *5th Berlin Beamforming Conference* (Berlin, Germany, 2014).

[65] R. Merino-Martínez, P. Sijtsma, M. Snellen, T. Ahlefeldt, J. Antoni, C. J. Bahr, D. Blacodon, D. Ernst, A. Finez, S. Funke, T. F. Geyer, S. Haxter, G. Herold, X. Huang, W. M. Humphreys, Q. Leclère, A. Malgoezar, U. Michel, T. Padois, A. Pereira, C. Picard, E. Sarradj, H. Siller, D. G. Simons, and C. Spehr, *CEAS Aeronautical Journal*, Vol. 10 (Springer Vienna, 2019) pp. 197–230.

[66] P. Chiariotti, M. Martarelli, and P. Castellini, *Acoustic beamforming for noise source localization – Reviews, methodology and applications,* Mechanical Systems and Signal Processing **120**, 422 (2019).

[67] R. Merino-Martínez, P. Sijtsma, A. Rubio Carpio, R. Zamponi, S. Luesutthiviboon, A. M. N. Malgoezar, M. Snellen, C. Schram, and D. G. Simons, *Integration methods for distributed sound sources,* International Journal of Aeroacoustics (2019), 10.1177/1475472X19852945.

[68] S. Oerlemans and P. Migliore, *Aeroacoustic Wind Tunnel Tests of Wind Turbine Airfoils,* in *10th AIAA/CEAS Aeroacoustics Conference* (2004) pp. 1–18.

[69] E. Sarradj, G. Herold, P. Sijtsma, R. Merino Martinez, T. F. Geyer, C. J. Bahr, R. Porteous, D. Moreau, and C. J. Doolan, *A Microphone Array Method Benchmarking Exercise using Synthesized Input Data,* in *23rd AIAA/CEAS Aeroacoustics Conference* (2017) pp. 1–16.

[70] S. Oerlemans and P. Sijtsma, *Determination of Absolute Levels from Phased Array Measurements Using Spatial Source Coherence,* in *8th AIAA/CEAS Aeroacoustics Conference & Exhibit* (2002) pp. 1–12.

[71] M. Kamruzzaman, T. Lutz, E. Kraemer, and W. Wuerz, *On the Length Scales of Turbulence for Aeroacoustic Applications,* in *17th AIAA/CEAS Aeroacoustics Conference* (American Institute of Aeronautics and Astronautics, 2011).

[72] G. P. Romano, *Analysis of two-point velocity measurements in near-wall flows,* Experiments in Fluids **20**, 68 (1995).

[73] F. Avallone, S. Pröbsting, and D. Ragni, *Three-dimensional flow field over a trailing-edge serration and implications on broadband noise,* Physics of Fluids **28**, 117101 (2016).

[74] P. R. Spalart and J. H. Watmuff, *Experimental and numerical study of a turbulent boundary layer with pressure gradients,* Journal of Fluid Mechanics **249**, 337 (1993).

[75] R. Vinuesa, A. Bobke, R. Örlü, and P. Schlatter, *On determining characteristic length scales in pressure-gradient turbulent boundary layers,* Physics of Fluids **28** (2016), 10.1063/1.4947532.

[76] P. H. Alfredsson, A. Segalini, and R. Örlü, *A new scaling for the streamwise turbulence intensity in wall-bounded turbulent flows and what it tells us about the "outer" peak,* Physics of Fluids **23** (2011), 10.1063/1.3581074.

[77] B. André, T. Castelain, and C. Bailly, *Investigation of the mixing layer of underexpanded supersonic jets by particle image velocimetry,* International Journal of Heat and Fluid Flow **50**, 188 (2014).

[78] M. Kamruzzaman, T. Lutz, A. Ivanov, A. Herrig, W. Wuerz, and E. Kraemer, *Evaluation of Measured Anisotropic Turbulent Two-Point Correlation Data for the Accurate Prediction of the Turbulence Noise Sources,* in *15th AIAA/CEAS Aeroacoustics Conference (30th AIAA Aeroacoustics Conference)*, May (2009) pp. 11–13.

[79] M. Kamruzzaman, T. Lutz, A. Herrig, and E. Krämer, *Semi-Empirical Modeling of Turbulent Anisotropy for Airfoil Self-Noise Predictions,* AIAA Journal **50**, 46 (2012).

[80] M. Kamruzzaman, T. Lutz, W. Würz, W. Z. Shen, W. J. Zhu, M. O. L. Hansen, F. Bertagnolio, and H. A. Madsen, *Validations and improvements of airfoil trailing-edge noise prediction models using detailed experimental data,* Wind Energy **15**, 45 (2012).

[81] Y. Rozenberg, G. Robert, and S. Moreau, *Wall-pressure spectral model including the adverse pressure gradient effects,* AIAA Journal **50**, 2168 (2012).

[82] F. H. Clauser, *The turbulent boundary layer,* in *Advances in applied mechanics* (Elsevier, 1956) pp. 1–51.

[83] T. P. Chong and A. Vathylakis, *On the aeroacoustic and flow structures developed on a flat plate with a serrated sawtooth trailing edge,* Journal of Sound and Vibration **354**, 65 (2015).

[84] G. M. Corcos, *The structure of the turbulent pressure field in boundary-layer flows,* Journal of Fluid Mechanics **18**, 353 (1964).

[85] M. Roger and S. Moreau, *Trailing Edge Noise Measurements and Prediction for Subsonic Loaded Fan Blades,* in *8th AIAA/CEAS Aeroacoustics Conference & Exhibit,* Vol. 2460 (2002) pp. 1–15.

[86] O. Stalnov, P. Chaitanya, and P. F. Joseph, *Towards a non-empirical trailing edge noise prediction model,* Journal of Sound and Vibration **372**, 50 (2016).

[87] D. M. Chase, *Modeling the wavevector-frequency spectrum of turbulent boundary layer wall pressure,* Journal of Sound and Vibration **70**, 29 (1980).

[88] T. Brooks and T. Hodgson, *Trailing edge noise prediction from measured surface pressures,* Journal of Sound and Vibration **78**, 69 (1981).

[89] G. M. Corcos, *Resolution of Pressure in Turbulence,* The Journal of the Acoustical Society of America **35**, 192 (1963).

[90] B. Zang, Y. D. Mayer, and M. Azarpeyvand, *A note on the pressure–velocity correlation and coherence normalisation,* Experiments in Fluids **61**, 1 (2020).

4

FLOW FIELD OVER METAL FOAM TRAILING EDGES AND ACOUSTIC SCATTERING

"Aeronautics was neither an industry nor a science. It was a miracle."

Igor Sikorsky (1889-1972)

A full comprehension of the flow field in the vicinity of the trailing-edge is essential to understand changes in noise production. This chapter describes the velocity and surface-pressure fields above trailing edges manufactured with metallic foams. The effect of properties such as pore size and permeability on the flow field above the inserts, and the contribution of these changes to the acoustic scattering is assessed. Acoustic data show increasing low-frequency noise abatement for porous edges with higher permeability. Wall-pressure and kinematic data indicate two important changes in the flow field above metal foam inserts caused by roughness: a decrease in wall-pressure mean convection and mean flow velocity due to higher surface drag, and an increase in the energy of the turbulent flow field due to higher frictional forces. The comparison between far-field acoustic measurements and Amiet's analytical model predictions, that use as input wall-pressure data for solid and porous inserts, show that, contrarily to measured data, the model does not predict any degree of noise mitigation for none of the inserts, showing that the overall modification of the flow field does not contribute to noise mitigation.

Parts of this chapter have been published in the Journal of Sound and Vibration (2019) [1]

4.1. INTRODUCTION

As described in Chapter 2, the change of boundary layer properties nearby the trailing edge might be one of the reasons behind noise mitigation for partially porous airfoils. Recent research [2, 3] points out that the employment of porous materials entails a strong break down of the spanwise organization of the wall-pressure field in the vicinity of the edge, as well as a significant decrease in the mean convective velocity [4]. Following the analytical solution developed by Amiet [5] for solid wings, these two effects are in principle beneficial for noise mitigation purposes. With regard to the spectral energy of the turbulent field, i.e., the third flow quantity of relevance for noise production, other research [6–9] shows that an increase or a decrease with respect to a fully solid counterpart can be found depending on properties of the set-up such as airfoil loading or the type of porous material employed at the edge. Hence, the effect of the change in energy distribution to noise abatement remains unclear.

The purpose of this chapter is twofold. Firstly, it is intended to provide a comprehensive description of the far-field acoustic pressure scattered by porous inserts, as well as the flow field nearby the edges. Secondly, it aims at evaluating whether the general modification of the flow field in the vicinity of the porous edges contributes to noise abatement. To fulfil these aims, a selection of results obtained at no incidence and free-stream velocities ranging from 10 to 35 m/s (corresponding to Reynolds numbers based on the chord Re_c ranging from 1.32 to 4.63×10^5) is presented. Far-field noise, kinematic and wall-pressure data are investigated. These data are obtained with the NACA 0018 model and the 40×70 cm^2 nozzle exit detailed in Chapter 3. Porous inserts cover the last 20% of the chord, and are manufactured with metallic foams with cell diameters of 450 and 800 μm, and permeability values of 5×10^{-10} and 3.2×10^{-9} m^2 (a summary of the properties can be found in table 3.3). A fully solid insert is used as reference. Moreover, the latter objective is accomplished by using surface-pressure data obtained for solid and porous inserts as input in the analytical model for single line noise scattering described in Chapter 2, and comparing measurements and predictions.

The chapter is organized as follows. The far-field acoustic scattering is analysed in section 4.2.1. A description of velocity statistics and spectra on the basis of PIV and HWA data is included in section 4.2.2. The corresponding wall-pressure field beneath the turbulent boundary layer is described in section 4.2.3. Finally, measured and predicted far-field acoustic pressure are compared in section 4.2.4.

4.2. RESULTS AND DISCUSSION

4.2.1. FAR-FIELD ACOUSTIC PRESSURE

Trailing-edge noise data for the two porous inserts and the solid case measured at 20 m/s are presented in figure 4.1(a). Results are expressed in terms of Sound Pressure Level integrated in one-third octave bands $L_{p\ (1/3)}$ in decibels relative to $p_{\mathrm{ref}} = 20\ \mu$Pa, as a function of the Strouhal number St_c based on the chord and the free-stream velocity. It is interesting to note that the spectra show different slopes depending on the type of porous insert. This might be indicative of a modification of the noise source (turbulent flow) and/or the radiation efficiency of the edge, i.e., reduction in the acoustic impedance discontinuity at the edge. More in detail, up to $\mathrm{St}_c = 12.5$ the spectrum measured for the d_c = 450 μm metal foam insert has a similar slope to that of the baseline case, while the d_c = 800 μm insert shows a flatter slope. For the d_c = 450 μm case, the spectrum is shifted towards lower $L_{p(1/3)}$ values suggesting that the impedance discontinuity might not be strongly affected by the porous insert, but the energy of the source, i.e., turbulent fluctuations, decreases. Such a hypothesis is investigated in detail in the remainder of the chapter. Spectra for both porous treatments have similar slopes above St_c = 20, denoting that noise within this St_c range is related to the same phenomenon. This high-frequency excess noise has been already reported in previous experimental work involving porous trailing edges [6, 10, 11]. Due to its high-frequency nature, and the fact that higher noise levels are reported for materials with a larger pore size, it has been attributed to roughness induced noise [12].

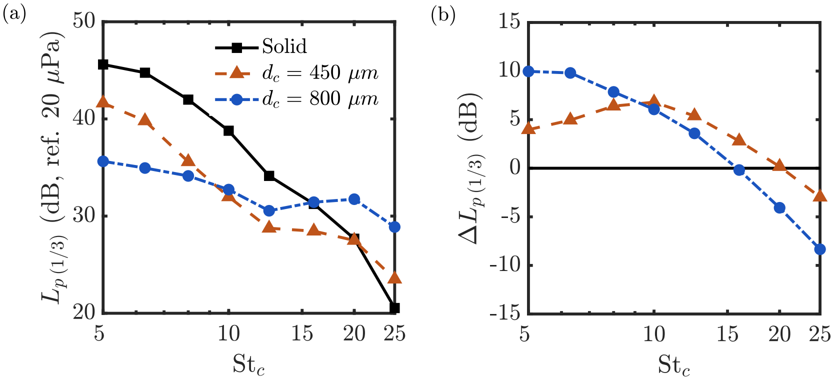

Figure 4.1: Sound Pressure Level L_p in one-third octave bands measured with the microphone phased array for solid and metal foam trailing-edge inserts. (a) Absolute values. (b) Relative values with respect to the solid case.

The difference between far-field noise for the solid insert with respect to the porous treatments $\Delta L_{p(1/3)} = L^{\mathrm{solid}}_{p(1/3)} - L^{\mathrm{porous}}_{p(1/3)}$ is shown in figure 4.1(b). It shows noise abatement below the cross-over St_c = 16 (1.6 kHz) and St_c = 20 (2 kHz) for metal foams with d_c = 800 μm and d_c = 450 μm, respectively. Noise abatement below St_c = 10 is larger for the d_c = 800 μm metal foam insert, with a maximum noise decrease of 10 dB at St_c = 5. On the other hand, the d_c = 450 μm metal foam treatment leads to a maximum noise attenuation of 7 dB at St_c = 10. The results confirm that the use of higher permeability metal foam treatments leads to a larger noise abatement, in agreement with previous research on porous trailing edges [13–15]; however, the frequency range where noise reduction is measured is smaller for foams with higher permeability. This observation also holds for data reported in Herr *et al.* [15], where a noise reduction up to 11 kHz was achieved with metal foams with variable flow resistivity (up to $R = 278\ \mathrm{k}Ns/m^4$ at $\mathrm{Re}_c = 1\times10^6$). Finally, noise increase with respect to the solid trailing edge is measured above the previously defined cross-over St_c. Maximum excess noise values of 3 and 8 dB are respectively found for metal foams with d_c = 450 μm and d_c = 800 μm metal foam inserts at St_c = 25.

4.2.2. VELOCITY FIELD

In this section, a description of the flow-field for the three measured test cases is presented. In order to investigate whether changes within the boundary layer due to porous inserts relate to changes in far-field noise production, the properties of the mean and turbulent flow field are further investigated and compared.

MEAN FLOW FIELD

The effect of employing porous materials on the mean flow field in the vicinity of the trailing-edge insert and the wake is analysed in the following. PIV data obtained for the solid and the d_c = 800 μm metal foam inserts at 35 m/s are described in figures 4.2 (a) and (b) respectively. Specifically, the mean streamwise velocity U/U_∞ is plotted. For the sake of clarity, the boundary layer and wake outer boundaries, computed as the location where the integral of the out-of-plane vorticity stabilizes [16] are also depicted as black solid lines. As expected, the boundary layer over the solid surface grows in the streamwise direction, and lower velocity regions are visible close to the surface towards the edge due to the presence of an adverse pressure gradient. A region with a streamwise velocity lower than $0.4U_\infty$ is found within the last 1% of the chord and the near wake (within a distance equal to 7% of the chord downstream the trailing edge). The mean flow field upstream of the solid-permeable junction is not affected by the porous surface. Yet, a region where the mean streamwise velocity is lower than $0.4U_\infty$, that for the solid case was only measured right above the edge, is now present above the entire porous insert. In other words, the use of porous materials entails a velocity deficit with respect to the solid surface. Such a phenomenon is localized to the near-wall region above the porous extent starting from the solid-permeable interface. Consequently, the wake is also slower than that of the baseline case. A velocity deficit is also reported in previous experiments on generic rough surfaces [17, 18] or porous trailing edges [6, 19] and it is attributed to higher surface drag caused by roughness.

This velocity deficit is further studied on the basis of HWA data measured for solid and metal foam inserts with d_c = 450 μm and d_c = 800 μm. Data, obtained at x/c = -0.08 and U_∞ = 20 m/s, are plotted in figure 4.3. Note that the analysis is performed in the x-y coordinate system, and that the wall-normal coordinate and the mean wall-parallel velocity are respectively normalized by the boundary layer thickness δ and the edge velocity U_e at that position. It is observed that the velocity profile measured above the metal foam insert with smaller pore size is similar to that of the reference case, and the velocity deficit is only noticeable below y/δ = 0.4. For the metal foam with d_c = 800 μm, a significant decrease in mean velocity is measured below 60% of the boundary layer. For a given height, a larger velocity deficit is consistently measured for foams with increasing pore size, and for data acquired closer to the wall. As a matter of fact, the largest changes (2 and 5 % of the edge velocity respectively for d_c = 450 μm and d_c = 800 μm foam) with respect to the smooth surface are measured at y/δ = 0.3 for both metal foam inserts. These observations are in line with the fact that the velocity deficit is caused by higher surface drag [8].

Following the theory for solid edge noise scattering detailed in Chapter 2, a decrease in the flow speed nearby the trailing edge is in principle beneficial for noise abatement purposes. As described in section 2.2.2, the effects are twofold: on the one hand, the

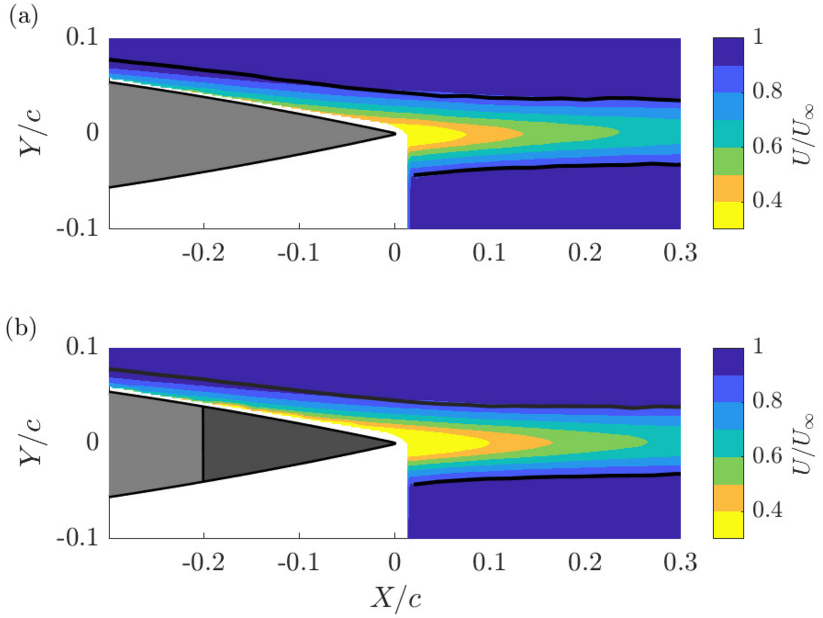

Figure 4.2: Mean streamwise velocity U/U_∞ field for the solid (a) and $d_c = 800$ μm metal foam (b) inserts at $U_\infty = 35$ m/s. The boundary layer thickness and wake outer boundaries, computed as the location where the integral of the out-of-plane vorticity stabilizes, are depicted as a black solid line. The airfoil aluminium body is depicted in lighter grey, and the metal foam insert in darker grey. Data obtained with PIV configuration D, detailed in table 3.4.

power of the acoustic source varies with a 5th or 6th power law with velocity (with the specific law depending on compactness effects); on the other hand, the frequency for maximum acoustic pressure scattered by the solid edge is moved towards lower frequencies. In this regard, the above described changes in the mean flow field due to roughness might contribute to a certain extent to the noise abatement levels described in 4.2.1, where lower noise scattering was reported for rougher surfaces. This hypothesis is further investigated in the following.

In figures 4.4 (a), (b) and (c), the change in boundary layer thickness δ, displacement thickness δ_* and momentum thickness θ along the wall are respectively analysed for the three trailing-edge inserts. PIV data ranging within $-0.1/ > x/c/ > 0$ and HWA data measured at $x/c = -0.08$ are included for completeness. Note that boundary layers over solid and permeable walls have different characteristics, i.e., the classic no-slip condition present at solid surfaces does not apply on permeable walls. In the present analysis, the same methodology employed to calculate δ, δ_* and θ over the solid surface is also applied on permeable walls for the sake of simplicity.

It is found that all the integral quantities have significantly larger values for the $d_c =$ 800 μm metal foam insert. Integral quantities measured above the $d_c = 450$ μm variant are in agreement within the uncertainty range (see section 3.4.1) with those computed

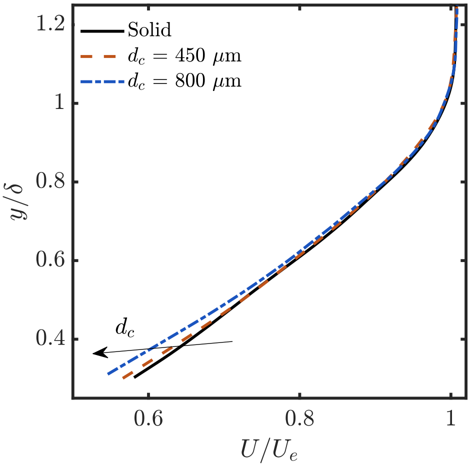

Figure 4.3: Mean wall-parallel velocity U/U_e variation along the wall-normal direction y/δ above the solid and metal foam inserts with $d_c = 450\ \mu$m and $d_c = 800\ \mu$m. Data measured employing HWA at $x/c = -0.08$ and $U_\infty = 20$ m/s.

above the solid insert. These results point out the dependence of the boundary layer topology on the characteristics of the metal foam. An increase of δ, δ_* and θ with pore size is reported in Geyer *et al.* [19] on fully porous airfoils. The fact that here the increase is measured only over one type of the metal foam might be explained by the shorter porous extension employed.

The increase of δ_* and θ for the $d_c = 800\ \mu$m metal foam insert with respect to the solid case is caused by the velocity deficit described previously, which leads to an increased mass and momentum deficit. Although the velocity deficit is also present above the $d_c = 450\ \mu$m metal foam insert, its magnitude is smaller. It can be concluded that only the $d_c = 800\ \mu$m porous treatment causes significant changes in the boundary layer topology with respect to the baseline case, whereas the $d_c = 450\ \mu$m and the solid insert lead to similar results. This result is in line with the noise reduction analysis described in section 4.2.1.

TURBULENT FLOW FIELD

The changes in the turbulent field due to the employment of porous treatments are investigated in the following. Streamwise turbulence intensity levels $\sqrt{\overline{u^2}}/U_\infty$ are firstly studied by means of the same PIV data-set. Specifically, turbulence intensity data measured at $U_\infty = 35$ m/s for the baseline case and the insert manufactured with the metal foam with $d_c = 800\ \mu$m are plotted in figures 4.5 (a) and (b), respectively. From these results, it follows that the use of porous materials provokes a significant increase in turbulence intensity levels close to the wall. As with the mean flow field, the effect of the porous surface takes place immediately downstream the solid-permeable junction, i.e., above the treated surface and within the wake. The origin and implications on noise production of this phenomenon are further detailed below.

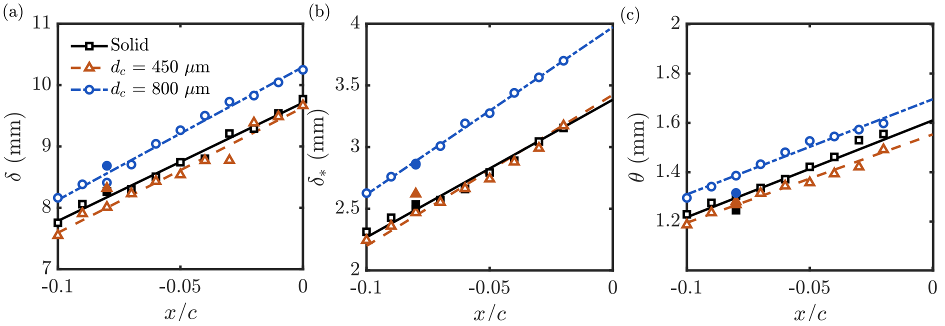

Figure 4.4: Boundary layer thickness δ (a), displacement thickness δ_* (b) and momentum thickness θ (c) variation with dimensionless streamwise coordinate x/c above solid and permeable trailing-edge inserts. Markers refer to measured data, and fitted lines are included to help the reader with the interpretation of results. Data represented with void and filled markers are obtained with PIV (configuration A) and HWA respectively.

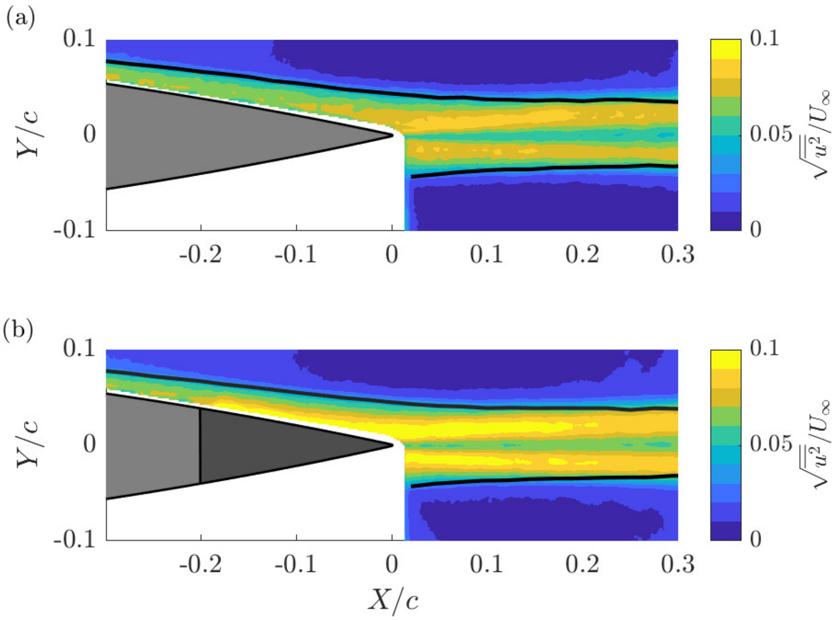

Figure 4.5: R.m.s. streamwise velocity $\sqrt{\overline{u^2}}/U_\infty$ field for the solid (a) and d_c = 800 μm metal foam inserts at U_∞ = 35 m/s. The boundary layer thickness and wake outer boundaries, computed as the location where the integral of the out-of-plane vorticity stabilizes, are depicted as a black solid line. The airfoil aluminium body is depicted in lighter grey, and the metal foam insert in darker grey. Data obtained with PIV configuration D.

In figure 4.6, profiles of the r.m.s. of the wall-parallel velocity measured with HWA above solid and metal foam inserts are plotted. As for the mean velocity profile, data are acquired at x/c = -0.08. In line with PIV results, HWA data for the porous inserts show an increase of turbulence intensity in the near-wall region (approximately below 50% of the boundary layer thickness). The extent of the boundary layer where the increase is measured is independent of the material. Conversely, higher maximum turbulence intensity levels are reported for metal foams with a larger pore size.

Similarly to the present results, an increase of turbulence intensity within the inner part of the boundary layer was also found by Ali *et al.* [8] employing a flat plate with a permeable extension manufactured with metal foams. In this case, the increase was attributed to the higher friction along the rough surface. Other experimental research involving partially porous asymmetric airfoils at incidence [19, 20] report an increase of the r.m.s. velocity fluctuations at the suction side within a larger extent of the boundary layer. In the latter studies, the imbalance of pressure between suction and pressure side of the trailing edge caused by the loading leads to a steady cross-flow, which is known to increase the turbulence intensity in boundary layers [21]. The absence of loading in the present set-up supports friction as the cause for the increase in turbulence intensity levels in these data.

Interestingly, metal foam inserts not only increase the energy of the turbulent fluctuations but also bring the location of maximum level of turbulence closer to the wall; employing theory for solid edge noise scattering, this is supposed to increase the scattering efficiency, hence far-field noise [22–24], in disagreement with results described in section 4.2.1.

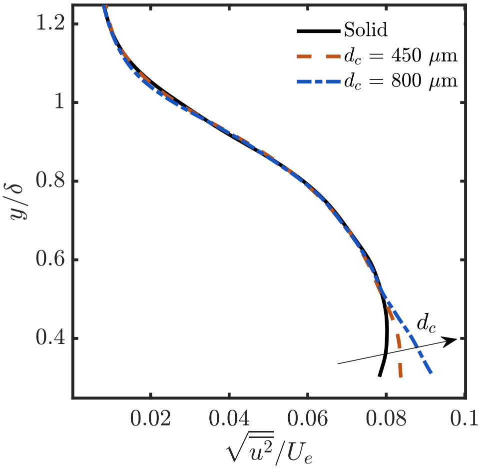

Figure 4.6: R.m.s. of the wall-parallel velocity $\sqrt{\overline{u^2}}/U_\infty$ variation along the wall-normal direction y/δ for solid and metal foam inserts at $x/c = -0.08$ and $U_\infty = 20$ m/s.

VELOCITY POWER SPECTRA

Considering the relevant differences in the turbulent field reported in section 4.2.2 and their implications on noise production, it is worthwhile to analyse the power spectra to determine which spectral range is affected by the porous treatments.

The power spectral density of the wall-parallel velocity fluctuations ϕ_u at $x/c = -0.08$ is shown in figure 4.7 for the three cases. Data correspond to a wall-normal location of $y/\delta = 0.3$, where the maximum increase of turbulent intensity was found. Results are consistent with the increase in $\sqrt{\overline{u^2}}/U_e$ with pore size described above: higher spectral levels are measured for rougher surfaces, with a significant increase being measured up to a St_c of 50 independently of the properties of the foam. The maximum increase with respect to the smooth surface is in the order of 1 and 2 dB for metal foams with $d_c = 450$ μm and $d_c = 800$ μm, respectively.

Assuming frozen turbulence, noise radiation at a certain frequency is only due to eddies being convected over the trailing edge with streamwise wavenumber $k_x = 2\pi f/U_c$ [25, 26]. Higher levels of ϕ_u within the low frequency range might be therefore linked to noise increase with respect to the solid edge. However, for the two porous inserts, larger low frequency noise attenuation is found for the metal foam insert with the largest pore size, in disagreement with the measured velocity fluctuation spectra. A hypothesis that would explain this inconclusive result is that the variation of turbulent energy within the boundary layer is only partially accountable for changes in noise emission, while other mechanisms such as the change in the impedance jump at the edge, i.e., the radiation efficiency arise. Another aspect of noise scattering by permeable inserts that remains unclear is the previously reported high frequency noise increase with respect to the baseline case; although the turbulent fluctuation levels increase with pore size, the magnitude of the increase is remarkably smaller than the one reported in the acoustic field, and such an increase is measured within the entire measured frequency range.

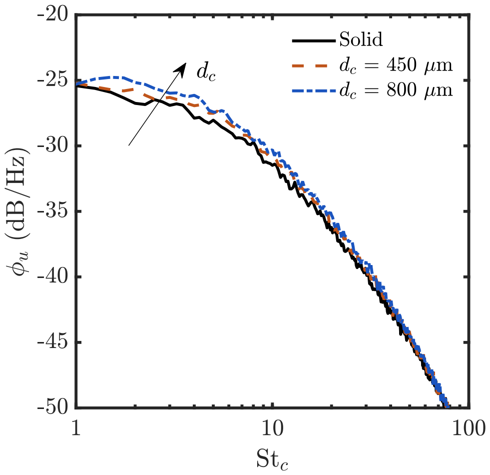

Figure 4.7: Power spectral density of the velocity fluctuations ϕ_u computed at a wall-normal distance $y/\delta = 0.3$. Data measured with HWA for solid and metal foam trailing edges at $U_\infty = 20$ m/s.

VERTICAL CORRELATION LENGTH

As seen in Chapter 2 (equation 2.43), the wall-normal correlation length can be employed to relate the size of turbulence structures with wall-pressure fluctuations above solid surfaces. For this reason, the wall-normal distribution of this quantity, normalized by the displacement thickness, $\Lambda_{v|y}/\delta_*$ is studied in the following. Specifically, data measured at $x/c = -0.02$ are respectively presented in figure 4.8. For the solid case, $\Lambda_{v|y}/\delta_*$ is between 1 and 2.5 times the displacement thickness, in line with values reported for previous trailing-edge noise research [27, 28].

For the porous inserts, a decrease of $\Lambda_{v|y}$ with respect to the baseline case is observed, with its magnitude depending on the type of metal foam. The $d_c = 800$ μm metal foam insert shows a reduction within the entire boundary layer, while results for the $d_c = 450$ μm insert indicate a decrease limited to the lower 60% of the boundary layer, approximately the same region where the increase in turbulence intensity was reported. At this streamwise position, a maximum relative reduction of 50% with respect to the solid case is measured above both porous materials. Given that $\Lambda_{v|y}$ is related to the largest wall-normal turbulence scale present within the boundary layer [29], the decrease of this quantity with increasing pore size indicates that porous treatments favour smaller in size, but more energetic turbulent motions closer to the wall. The fact that within this boundary layer region the wall-normal length scale decreases with the permeability of the insert suggests that such a change in the boundary layer organization might contribute to noise mitigation.

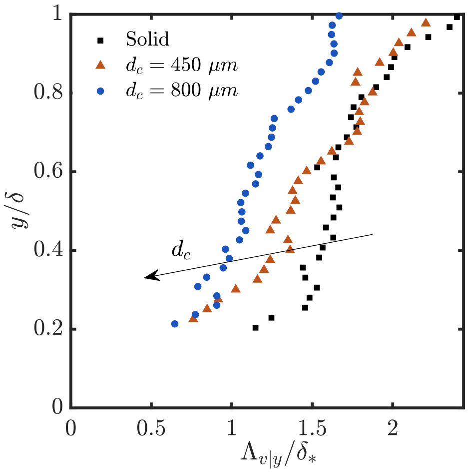

Figure 4.8: Variation of $\Lambda_{v|y}/\delta_*$ across the boundary layer at $U_\infty = 20$ m/s and $x/c = -0.02$. Data obtained with PIV configuration A.

CONVECTION VELOCITY

The last velocity-based turbulence quantity of relevance for noise generation that is addressed in the present chapter is the convection velocity U_c.

Figure 4.9 plots the convection velocity U_c/U_∞ profiles measured at $x/c = -0.02$. As for the mean velocity field, it is shown that permeable treatments produce a general decrease in the streamwise convection velocity, with stronger attenuation being measured for increasing pore size. As explained above, the reduction of the mean convective velocity might also contribute to noise abatement within the low frequency range. Interestingly, the maximum decrease in U_c/U_∞ and L_p is found over the same metal foam insert ($d_c = 800$ μm). However, given the small differences between U_c measured above both permeable inserts, it seems unlikely that such a change is able to explain alone the very different magnitude of low frequency noise abatement. This point is further addressed when discussing wall-pressure data measured for the same set of trailing-edge inserts.

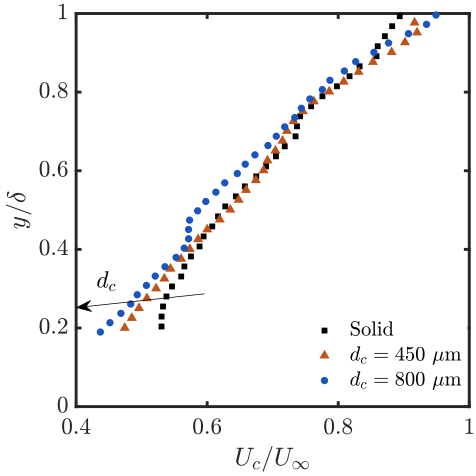

Figure 4.9: Wall-parallel convection velocity U_c/U_∞ at $x/c = -0.02$. Data obtained with PIV configuration A.

4.2.3. SURFACE PRESSURE

The surface-pressure field above the three trailing-edge inserts is measured employing the embedded transducer array described in Chapter 3. The quantities employed in the source term for noise production, i.e., the power spectra, the spanwise correlation length and the convection velocity of the pressure waves are analysed. Moreover, these are linked to the changes in the velocity field and noise generation described thus far.

SURFACE-PRESSURE POWER SPECTRA

Firstly, wall-pressure spectral data computed by averaging the signals acquired by the spanwisely distributed transducers that are located closest to the edge (x/c = -0.08) are analysed for the solid and porous inserts.

Spectra obtained at a flow speed U_∞ of 20 m/s are depicted in figure 4.10. The spectral energy distribution is similar to that measured with HWA, i.e., an overall increase in the energy of the pressure field is measured for increasing surface roughness. Similarly, changes in the pressure field can be ascribed to higher friction forces due to roughness.

These results are also in line with those reported in Showkat Ali *et al.* [3] based on wall-pressure data obtained above highly permeable metal foams.

The maximum increase in the energy of the pressure field is of the order of 3 and 6 dB for edges with increasing pore size, remarkably higher than the values found in the velocity spectra. This result might be explained employing the TNO-Blake model (equation 2.43). Following this analytical solution, the pressure field is contributed by eddies at different boundary layer regions, being particularly relevant those convecting closer to the wall. In other words, whereas HWA data describe the energy distribution at a single-point location within the boundary layer (figure 4.7), the pressure field accounts for the energy of all turbulent motions above the pressure transducer. Interestingly, the dimensionless frequency at which maxima are measured, namely $\mathrm{St}_c = 2$ and 15 for the $d_c = 800\ \mu\mathrm{m}$ and $d_c = 450\ \mu\mathrm{m}$ edges, are in line with those reported for the velocity field.

It is also interesting to note that the frequency range for the maximum increase in wall-pressure spectra is similar to the one where metal foams abate noise most efficiently. This apparent contradiction might be explained by a decrease in the spanwise organization or the convection velocity of the pressure waves, both results already anticipated by the analysis of the velocity field. If the modification of the flow field is the main driving factor for noise abatement, these should compensate for such a strong increase in the energy spectra. To assess it, these two variables are quantified in the following.

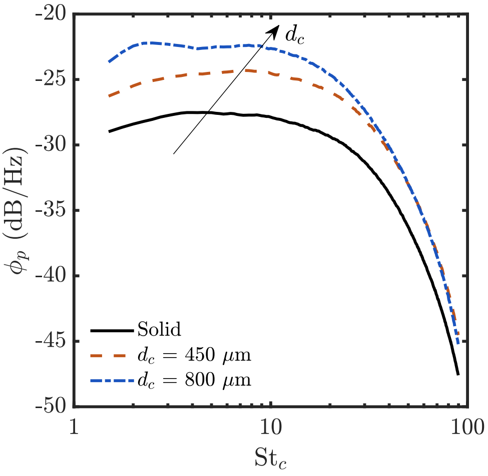

Figure 4.10: Power spectral density of surface pressure ϕ_p measured at a $U_\infty = 20$ m/s for solid and metal foam trailing edges.

SPANWISE CORRELATION LENGTH

The spatial organization of wall-pressure waves is now investigated in terms of the spanwise correlation length $\Lambda_{p|z}/\delta_*$ normalized by the displacement thickness. This quantity is plotted in figure 4.11 for data acquired at 20 m/s. Note that the measurement frequency range is limited by the finite distance between transducers; for these data, a significant level of coherence between the closest pair of microphones (ξ_z = 4 mm) is obtained up to St$_c$ = 15 (1.5 kHz).

Results show that, except within the very low frequency range, porous inserts reduce the correlation length with respect to the solid surface, with lower $\Lambda_{p|z}/\delta_*$ values being found for increasing pore size. Metal foam edges with d_c = 450 μm and d_c = 800 μm decrease significantly the spanwise organization of the surface-pressure field above St$_c$ = 2 and 3, respectively. For the latter, a correlation length peak around St$_c$ = 2 is measured, resulting in an increase with respect to the solid surface. Although not shown here for the sake of conciseness, the peak is noticeable even in the spectral cross-coherence of pressure signals acquired by transducers Z1 and Z5 (separated by 27 mm, i.e., more than three times the boundary layer size). As will be shown later in Chapter 6, this result is related to the appearance of large-scale vortex-shedding in edges with higher permeability.

Interestingly, porous edges break down the spanwise organization of the pressure waves within the frequency range where noise abatement is reported. Following theory for noise generation for solid edges, this result suggests that such a change in the flow field might contribute to the overall noise abatement. To support this, a lower correlation length is reported for porous edges with higher permeability, in agreement with the acoustic data.

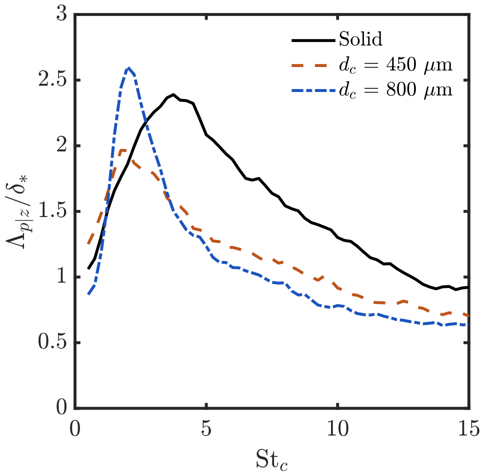

Figure 4.11: Spectral wall-pressure spanwise correlation length $\Lambda_{p|z}/\delta_*$ as a function of dimensionless frequency St$_c$ at a flow speed of and 20 m/s.

Data at different flow speeds are further computing the spanwise correlation length of the surface-pressure fluctuations $L_{p|z}$. As described in Chapter 3, this quantity is computed by integration of $\Lambda_{p|z}$ over the measured frequency range. In figure 4.12, $L_{p|z}$ data normalized by δ_* are plotted as a function of Re$_c$ for solid and metal foam inserts. Data measured at free-stream velocities ranging from 10 to 20 m/s, corresponding to Re$_c$ = 1.35×10^5 to 2.7×10^5, are shown.

In line with the wall-pressure data and the analysis of the wall-normal correlation length of the velocity fluctuations, metal foam inserts provoke an overall decrease of $L_{p|z}$ independently of the flow speed. In general, these changes agree with the relative reduction in $\Lambda_{p|z}$ of 60% reported by Bernicke *et al.* [2] on simulations of a NACA 0012 equipped with solid and porous edges at $\mathrm{Re}_c = 1\times10^6$. A similar feature is also reported in the numerical study of Ananthan *et al.* [4] for a (chambered) DLRF16 airfoil at the same Reynolds number. However, it seems unlikely that such a small difference in data measured for the two metal foam inserts is able to support the very different maximum noise attenuation levels reported in section 4.2.1.

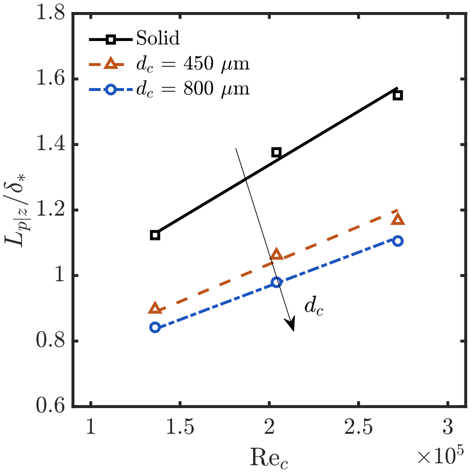

Figure 4.12: Change in wall-pressure spanwise correlation length $L_{p|z}$ with Re_c for solid and metal foam trailing edges. Markers refer to measured data, and fitted lines are included to help the reader with the interpretation of results.

CONVECTION VELOCITY

The last quantity of relevance for noise generation, i.e., the wall-pressure convection speed, is analysed below. The convection to free-stream velocity ratio U_c/U_∞ for metal foam and solid inserts is plotted in figure 4.13 as a function of Re_c for data obtained at free-stream velocities ranging from 10 to 20 m/s. For the solid case, an increase of U_c/U_∞ with Re_c is reported; specifically, a slight increase from $U_c/U_\infty = 0.54$ at $\mathrm{Re}_c = 1.35\times10^5$ to $U_c/U_\infty = 0.59$ at $\mathrm{Re}_c = 2.7\times10^5$ is measured. These U_c/U_∞ values are consistent with data reported by previous trailing-edge noise research on airfoils [25, 30, 31] and flat plates [32].

With regard to data obtained with the metal foam inserts, a decrease in the mean convection velocity with increasing pore size is found independently of Re_c. The agreement with mean flow field data described above suggests that such a phenomenon is due to the increase of frictional forces at the surface. A decrease in the mean convection velocity of the wall-pressure waves is also reported in Ananthan *et al.* [4], where it is deemed as a main driver for noise abatement. It is interesting to note that rough surfaces not only decrease the U_c/U_∞ ratio with respect to smooth surfaces but also inverse the dependence on Re_c. In other words, contrarily to the baseline case for metal foams U_c/U_∞ decreases with Re_c, and such a decrease is steeper for rougher surfaces.

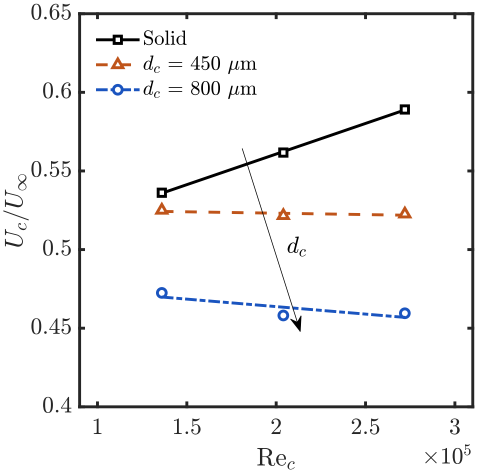

Figure 4.13: Change in surface-pressure mean convection speed to free-stream velocity ratio U_c/U_∞ with chord-based Reynolds number Re_c for solid and metal foam edges. Markers refer to measured data, and fitted lines are included to help the reader with the interpretation of results.

PRESSURE-VELOCITY CORRELATION

Finally, velocity and surface-pressure data described above are linked through the assessment of the coherence between velocity and pressure fluctuation data acquired synchronously. This analysis allows to gain understanding on how metal foams modify the interaction between turbulent eddies and the surface-pressure field beneath the boundary layer, responsible for noise generation.

Results are presented in figures 4.14 (a-c), where $\tilde{\gamma}^2_{u,p}$ is plotted as a function of distance to the wall y/δ and dimensionless frequency St_c for solid and metallic foam edges. Velocity-pressure coherence data for the baseline surface (figure 4.14 (a)) show strong coherence between flow structures within 30 and 50% of the boundary layer and pressure waves for the low frequency range (below $\mathrm{St}_c = 5$). For the same frequency range, moderate coherence values are also reported for turbulence motions further away from the wall ($0.5 \geq y/\delta \geq 0.8$). For higher dimensionless frequencies, significant coherence levels are measured exclusively below 50% of the boundary layer, i.e., only eddies closer to the wall contribute to the surface-pressure field. Such phenomena are in agreement with the interaction between eddies and wall-pressure fluctuations observed by Farabee [33].

For the metal foam insert with $d_c = 450\ \mu\mathrm{m}$ (figure 4.14 (b)) results are generally similar to those for the baseline case. However, the permeable wall seems to decouple smaller eddies closer to the wall ($y/\delta \leq 0.3$) from the pressure field, while enhancing the contribution of smaller eddies ($\mathrm{St}_c \leq 10$) around $y/\delta = 0.4$. For the metal foam insert with d_c = 800 μm (figure 4.14 (c)), a relevant loss of coherence is reported above 50% of the boundary layer, and generally lower coherence values are found below, i.e., the contribution of lower-frequency motions to the pressure field is greatly reduced. On the other hand, below y/δ = 0.5 high coherence peaks can also be noticed above St_c = 10.

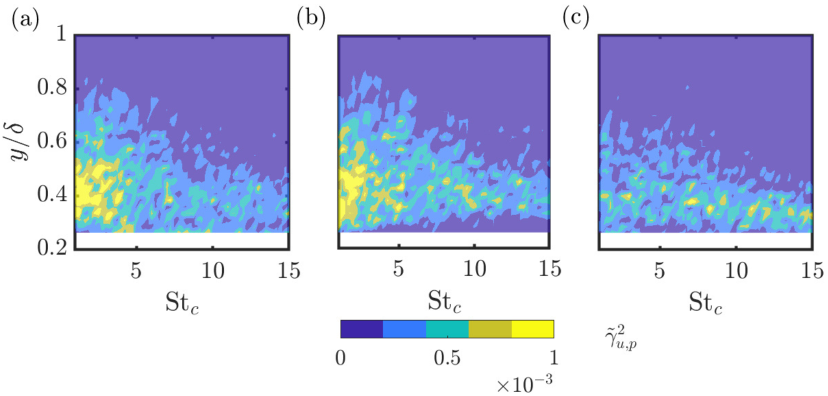

Figure 4.14: Magnitude-squared coherence of wall-pressure and velocity fluctuations $\tilde{\gamma}^2_{u,p}$ with distance from the wall y/δ and chord-based Strouhal number St_c for a free-stream velocity of 20 m/s. (a) Solid. (b) d_c = 450 μm. (c) d_c = 800 μm.

4.2.4. PREDICTION USING AMIET'S ANALYTICAL MODEL

All the velocity and pressure quantities of relevance for noise scattering at solid edges have been analysed thus far. Following the single line scattering analytical approach proposed by Amiet, the above-described changes in the hydrodynamic field due to the employment of porous edges with different properties might yield noise increase or mitigation with respect to the baseline configuration: on the one hand, the decrease in convection velocity and spanwise organization suggest that noise abatement might be contributed by such changes in the flow field; on the other hand, the significant increase in the spectral energy content for metal foam edges should result in larger noise scattering, suggesting that the employment of porous materials at the trailing edge entails intrinsic changes in noise production.

The comparison between predictions and measured far-field pressure is presented in figure 4.15 for data measured at 20 m/s. As in the analysis of the spanwise coherence, the frequency range for the predictions is limited by the finite distance between surface transducers. Moreover, it should be noted that predictions are compared to acoustic data obtained by averaging spectra obtained with the microphones closer to the center of the array to minimize directivity issues [34].

As expected, measured and predicted data for the baseline case agree well (within 3 dB). Yet, far-field noise predictions based on wall-pressure metal foam data differ significantly from measured data reported in section 4.2.1. Specifically, a noise increase with respect to the solid edge is predicted for both porous edges independently of the frequency, and higher noise levels are predicted for increasing pore size. The maximum in-

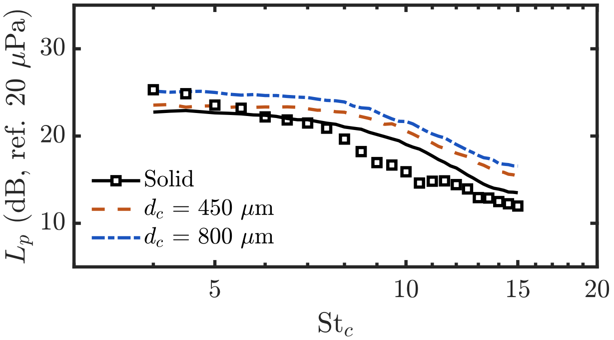

Figure 4.15: Comparison between measured far-field acoustic pressure and predictions using Amiet's model for data retrieved at 20 m/s. Markers and lines refer to measurements and predictions respectively. Acoustic pressure in 1 Hz bands.

crease is consistently measured at the highest reported frequency (St$_c$ = 15) and amounts to 2 and 3 dB respectively for metal foams with d_c = 450 μm and d_c = 800 μm. Predicted sound levels are therefore biased by the increase in wall-pressure/velocity spectral energy caused by friction. Such a disagreement between measurements and predictions suggests that, differently from solid edges, variations in the boundary layer properties play a limited role in the acoustic production of porous edges.

This might be explained by intrinsic changes in the noise production process for permeable edges anticipated in the simplified numerical simulations of Delfs *et al.* [35], namely a decrease in the acoustic impedance jump at the edge and the distribution of noise sources along the permeable surface. Such changes imply that analytical trailing-edge noise models developed for fully solid edges are not able to retrieve noise levels scattered by permeable edges accurately, and that even for lower permeability mock-ups a decrease in the scattering efficiency of the edge, as well as possible interference effects must be accounted for.

4.3. CONCLUSIONS

The flow field and acoustic scattering of a NACA 0018 airfoil with solid and trailing-edge inserts manufactured with metallic foams have been investigated. Acoustic data show increasing low-frequency noise abatement for porous edges with higher permeability. At higher frequencies, a noise increase with respect to the fully solid case due to roughness is reported. Wall-pressure and kinematic data show that the most relevant changes within the boundary layer are also due to surface roughness: higher surface drag decreases the wall-pressure mean convection and mean flow velocity, while higher frictional forces near the porous surface increment the power spectra of turbulent velocity and pressure fields. These effects are more significant for materials with larger pore size. It is also found that the use of porous edges strongly decreases the organization of pressure and velocity coherent motions within the boundary layer. Specifically, a strong decrease of the vertical length scale of the turbulent eddies, as well as in the spanwise correlation length of the pressure waves, is reported for materials with increasing pore size.

Following Amiet's theory for single line noise scattering, valid for solid edges, the increase in the spectral energy should be detrimental to noise abatement, while the loss of correlation, as well as the decrease in convection velocity might increase it. The comparison between far-field acoustic measurements and Amiet's analytical model predictions, that use wall-pressure data for solid and porous inserts as input, show that, contrarily to measured data, the model does not predict any degree of noise mitigation for none of the inserts, showing that the overall modification of the flow field does not contribute to noise mitigation, and suggesting that these porous edges alter the noise scattering process with respect to a fully solid variant. These changes will be further investigated in Chapter 5.

REFERENCES

[1] A. Rubio Carpio, R. Merino Martínez, F. Avallone, D. Ragni, M. Snellen, and S. van der Zwaag, *Experimental characterization of the turbulent boundary layer over a porous trailing edge for noise abatement,* Journal of Sound and Vibration **443**, 537 (2019).

[2] P. Bernicke, R. Akkermans, V. Ananthan, R. Ewert, J. Dierke, and L. Rossian, *A zonal noise prediction method for trailing-edge noise with a porous model,* International Journal of Heat and Fluid Flow **80**, 108469 (2019).

[3] S. A. Showkat Ali, M. Azarpeyvand, M. Szoke, and C. R. Ilário Da Silva, *Boundary layer flow interaction with a permeable wall,* Physics of Fluids **30** (2018), 10.1063/1.5043276.

[4] V. B. Ananthan, P. Bernicke, R. A. Akkermans, T. Hu, and P. Liu, *Effect of porous material on trailing edge sound sources of a lifting airfoil by zonal Overset-LES,* Journal of Sound and Vibration **480** (2020), 10.1016/j.jsv.2020.115386.

[5] R. K. Amiet, *Noise due to turbulent flow past a trailing edge,* Journal of Sound and Vibration **47**, 387 (1976).

[6] T. Geyer and E. Sarradj, *Trailing edge noise of partially porous airfoils,* 20th AIAA/CEAS Aeroacoustics Conference (2014), 10.2514/6.2014-3039.

[7] M. Mößner and R. Radespiel, *Flow simulations over porous media – Comparisons with experiments,* Computers and Fluids **154**, 358 (2017).

[8] S. A. S. Ali, M. Azarpeyvand, and C. R. I. Da Silva, *Trailing-edge flow and noise control using porous treatments,* Journal of Fluid Mechanics **850**, 83 (2018).

[9] M. Zhang and T. P. Chong, *Experimental investigation of the impact of porous parameters on trailing-edge noise,* Journal of Sound and Vibration , 115694 (2020).

[10] M. Herr and J. Reichenberger, *In Search of Airworthy Trailing-Edge Noise Reduction Means,* in *17th AIAA/CEAS Aeroacoustics Conference*, June (2011) pp. 1–25.

[11] T. Geyer, E. Sarradj, and C. Fritzsche, *Porous airfoils: noise reduction and boundary layer effects,* in *15th AIAA/CEAS Aeroacoustics Conference* (American Institute of Aeronautics and Astronautics, 2009).

[12] W. J. Devenport, D. L. Grissom, W. Nathan A., B. S. Smith, and S. A. L. Glegg, *Measurements of roughness noise,* Journal of Sound and Vibration **330**, 4250 (2011).

[13] T. Geyer, E. Sarradj, and C. Fritzsche, *Measurement of the noise generation at the trailing edge of porous airfoils,* Experiments in Fluids **48**, 291 (2010).

[14] E. Sarradj and T. Geyer, *Symbolic regression modeling of noise generation at porous airfoils,* Journal of Sound and Vibration **333**, 3189 (2014).

[15] M. Herr, K. S. Rossignol, J. Delfs, N. Lippitz, and M. Moßner, *Specification of Porous Materials for Low-Noise Trailing-Edge Applications,* in *20th AIAA/CEAS Aeroacoustics Conference* (2014) pp. 1–19.

[16] P. R. Spalart and J. H. Watmuff, *Experimental and numerical study of a turbulent boundary layer with pressure gradients,* Journal of Fluid Mechanics **249**, 337 (1993).

[17] P. Krogstad, R. A. Antonia, and L. W. B. Browne, *Comparison between rough- and smooth-wall turbulent boundary layers,* Journal of Fluid Mechanics **245**, 599 (1992).

[18] K. A. Flack and M. P. Schultz, *Roughness effects on wall-bounded turbulent flows,* Physics of Fluids **26**, 101305 (2014).

[19] T. Geyer, E. Sarradj, and C. Fritzsche, *Porous airfoils: noise reduction and boundary layer effects,* International Journal of Aeroacoustics **9**, 787 (2010).

[20] M. Moßner and R. Radespiel, *Flow simulations over porous media: comparisons with experiments,* Computers & Fluids **154**, 358 (2017).

[21] Y. Kametani, K. Fukagata, R. Örlü, and P. Schlatter, *Effect of uniform blowing/suction in a turbulent boundary layer at moderate {R}eynolds number,* International Journal of Heat and Fluid Flow **55**, 132 (2015).

[22] J. E. Ffowcs-Williams and L. H. Hall, *Aerodynamic sound generation by turbulent flow in the vicinity of a scattering half plane,* Journal of Fluid Mechanics **40**, 657 (1970).

[23] I. A. Clark, W. N. Alexander, W. Devenport, S. Glegg, J. W. Jaworski, C. Daly, and N. Peake, *Bioinspired trailing-edge noise control,* AIAA Journal **55**, 740 (2017).

[24] A. Afshari, M. Azarpeyvand, A. A. Dehghan, M. Szöke, and R. Maryami, *Trailing-edge flow manipulation using streamwise finlets,* Journal of Fluid Mechanics **870**, 617 (2019).

[25] O. Stalnov, P. Chaitanya, and P. F. Joseph, *Towards a non-empirical trailing edge noise prediction model,* Journal of Sound and Vibration **372**, 50 (2016).

[26] F. Bertagnolio, A. Fischer, and W. J. Zhu, *Tuning of turbulent boundary layer anisotropy for improved surface pressure and trailing-edge noise modeling,* Journal of Sound and Vibration **333**, 991 (2014).

[27] C. Arce León, R. Merino-Martínez, D. Ragni, F. Avallone, and M. Snellen, *Boundary layer characterization and acoustic measurements of flow-aligned trailing edge serrations,* Experiments in Fluids **57**, 182 (2016).

[28] M. Kamruzzaman, T. Lutz, A. Ivanov, A. Herrig, W. Wuerz, and E. Kraemer, *Evaluation of Measured Anisotropic Turbulent Two-Point Correlation Data for the Accurate Prediction of the Turbulence Noise Sources,* in *15th AIAA/CEAS Aeroacoustics Conference (30th AIAA Aeroacoustics Conference)*, May (2009) pp. 11–13.

[29] S. B. Pope, *Turbulent flows* (Cambridge University Press, 2000).

[30] M. Roger and S. Moreau, *Trailing Edge Noise Measurements and Prediction for Subsonic Loaded Fan Blades,* in *8th AIAA/CEAS Aeroacoustics Conference & Exhibit,* Vol. 2460 (2002) pp. 1–15.

[31] A. Garcia-Sagrado and T. Hynes, *Wall pressure sources near an airfoil trailing edge under turbulent boundary layers,* Journal of Fluids and Structures **30**, 3 (2012).

[32] G. M. Corcos, *The structure of the turbulent pressure field in boundary-layer flows,* Journal of Fluid Mechanics **18**, 353 (1964).

[33] T. M. Farabee, *An experimental investigation of wall pressure fluctuations beneath nonequilibrium turbulent flows,* The Journal of the Acoustical Society of America **80**, 1263 (1986).

[34] F. C. Hirono, P. F. Joseph, and F. Fazi, *Acoustic source distribution on aerofoils and its reconstruction from far-field array measurements,* Journal of Sound and Vibration , 115786 (2020).

[35] J. Delfs, B. Faßmann, N. Lippitz, M. Lummer, M. Mößner, L. Müller, K. Rurkowska, and S. Uphoff, *SFB 880: aeroacoustic research for low noise take-off and landing,* CEAS Aeronautical Journal **5**, 403 (2014).

5

MECHANISMS OF BROADBAND NOISE GENERATION ON METAL FOAM EDGES

"Measure what is measurable, and make measurable what is not so."

Galileo Galilei (1564-1642)

Four porous trailing edges, made of open-cell metal foams, are tested to evaluate the effects on far-field noise of the permeability of the material and of the hydrodynamic communication between the two sides of the airfoil. The latter is assessed by filling the symmetry plane of two of the porous trailing edges with a thin layer of adhesive that acts as a solid membrane. The porous inserts with an adhesive layer show no noise abatement in the low frequency range, but only a noise increase at higher frequency. The latter is, therefore, attributed to surface-roughness noise. Flow field measurements, carried out with time-resolved planar Particle Image Velocimetry, reveal correlation of near-wall velocity fluctuations between the two sides of the permeable trailing edges only within the frequency range where noise abatement is reported. This flow communication suggests that permeable treatments abate noise by distributing the impedance jump across the foam in the streamwise direction, promoting noise scattering from different chordwise locations along the inserts. This is further confirmed by noise source maps obtained from acoustic beamforming. For the frequency range where noise reduction is measured, the streamwise position of the main noise emission depends on the permeability of the insert. At higher frequencies, noise is scattered from upstream the trailing edge independently of the test case, in agreement with the roughness-generated noise assumption.

Parts of this chapter have been published in the proceedings of the 24th AIAA/CEAS Aeroacoustics Conference [1] and in Physics of Fluids (2019) [2].

5.1. INTRODUCTION

Recent analytical and numerical research show significant differences between the noise generation process for a solid and porous trailing edge. The analysis of the acoustic scattering of a gust convecting over a partially permeable airfoil [3] or a solid flat plate with porous extension [4] suggests that a secondary noise source appears at the discontinuity between the solid body and the porous treatment; in addition, noise scattering at the trailing edge is decreased by a pressure balance process, that lowers the magnitude of the acoustic impedance jump. These two results are in agreement with findings presented in Chapter 4, where it was shown that the noise scattering from porous edges cannot be computed employing flow field data measured in the vicinity of the edge using Amiet's model, or in other words, that analytical models for single line noise scattering are not directly applicable to a porous trailing edge.

This chapter is aimed at finding experimental evidence of the pressure balance process described by Delfs *et al.* [3]. Given that characterizing the flow inside metal foam inserts would compromise its nature, the study focuses on revealing the unsteady flow connection between the two sides of the airfoil through the permeable media. This will be referred to as cross-flow in the remainder of the chapter. To better describe the link between the flow within permeable trailing edges and the mitigation of the pressure jump at the edge (hence far-field noise emission), two sets of metal foam inserts and a baseline (solid) trailing edge are investigated. The first set consists of the two fully permeable inserts analysed in the previous chapter (see table 3.3 for further details on their properties), whilst the second one is obtained from the same materials by filling the symmetry plane with adhesive, thus avoiding flow communication between the two sides of the airfoil. The dominant noise sources are analyzed by using noise source imaging with acoustic beamforming and the turbulent boundary layer is characterized with PIV (set-up configuration B as defined in table 3.4), i.e. an optical non-intrusive method. Measurements are performed on the NACA 0018 airfoil at a chord-based Reynolds number Re_c of 2.63×10^5. To separate unsteady cross-flow effects from those derived by the presence of steady flow flowing through the foam inserts, the airfoil is set at zero degree angle of attack.

The remaining of the chapter is structured as follows. Changes in noise scattering and flow field derived from the blockage of the cross-flow are studied in sections 5.2.1 and 5.2.2 respectively. The appearance of correlation between unsteady flow features around porous inserts, as well as the implications on the scattered noise, are addressed in section 5.2.3. The change of position of dominant sound sources along the metal foam inserts is discussed in section 5.2.4. Finally, section 5.3 reports the conclusions of the chapter.

5.2. RESULTS

5.2.1. FAR-FIELD NOISE

Far-field acoustic scattering (figure 5.1 (a)) is presented in terms of Sound Pressure Level integrated in one-third octave bands $L_{p(1/3)}$ as a function of the Strouhal number based on the chord and the free-stream velocity St_c. For the sake of clarity, L_p values relative to the baseline case $\Delta L_p = L_p^{\mathrm{solid}} - L_p^{\mathrm{metal\ foam}}$ are also shown in figure 5.1 (b).

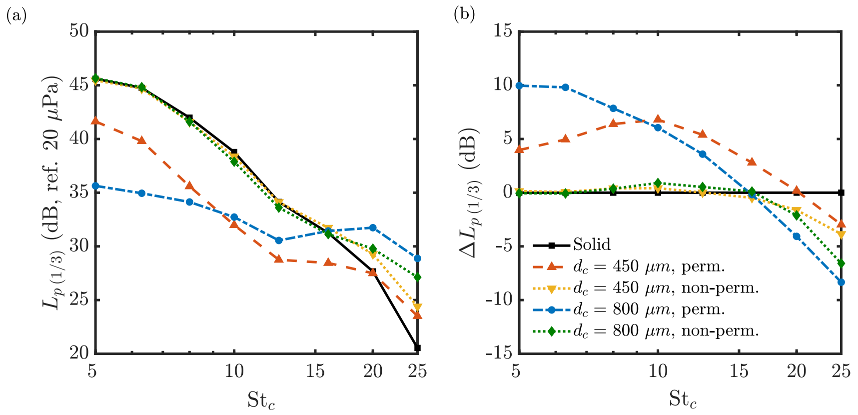

Figure 5.1: Far-field noise spectra. (a) Absolute $L_{p\,(1/3)}$ values. (b) Relative $L_{p\,(1/3)}$ values with respect to the baseline case.

Spectra plotted in figures 5.1 (a) and (b) show that in the low frequency range, fully permeable trailing edges show noise reduction with respect to the solid trailing edge, whilst avoiding flow communication between the two sides of the airfoil results in similar noise scattering as for the solid edge. Hence, for the present inserts, low-frequency noise reduction is solely caused by the permeability, with no significant effect due to the sound absorbing properties of these metal foams [5]. This result can be related to the presence of cross-flow, that will be further investigated in section 5.2.3.

At higher frequencies, a noise increase with respect to the baseline configuration is measured independently of the permeability of the insert. A cross-over $\mathrm{St}_c^* = 16$ (f_c = 1.6 kHz) is measured for the two non-permeable inserts and the permeable $d_c = 800$ μm foam insert, whilst for the permeable insert with $d_c = 450$ μm the St_c^* is equal to 20 ($f_c = 2$ kHz). The present results confirm that, as anticipated in Chapter 4, noise increase is indeed mostly due to the rough characteristics of the metal foam surface. Yet, the fact that permeable and non-permeable inserts manufactured with the same material generate slightly different excess noise levels suggests that additional aeroacoustic phenomena occur due to the permeability. This point will be also addressed below.

5.2.2. MEAN AND ROOT-MEAN-SQUARE VELOCITY

Velocity data measured for solid and metal foam trailing edges are studied in order to assess any effect of the cross-flow on the flow field surrounding the inserts. First, changes in the mean velocity field are analysed. Mean wall-parallel velocity U/U_∞ profiles above the trailing edge ($x/c = 0$) for metal foam and solid edges are shown in figure 5.2 (a). Below $y/\delta = 0.5$, lower velocity values are measured for metal foams with increasing pore size, while permeable and non-permeable counterparts of inserts manufactured with the same type of foam yield similar results. Hence, as suggested in Chapter 4, changes in the mean flow field are mainly influenced by higher surface drag caused by increased surface roughness, while the presence of flow communication between both sides of the airfoil does not affect the mean flow field.

R.m.s. wall-parallel velocity $\sqrt{\overline{u^2}}/U_\infty$ profiles for metal foam and solid inserts are shown in figure 5.2 (b). Significant changes with respect to the solid surface are only measured for porous inserts below $y/\delta = 0.5$. Within this region, an increase in turbulence intensity with pore size is found. As for mean velocity data, there is no relevant difference between data obtained for permeable and non-permeable variants manufactured with the same foam. This finding confirms that the increase in turbulence intensity close to the surface is caused by higher friction forces acting on the surface, and thus the magnitude of the increase is determined by the size of the pore.

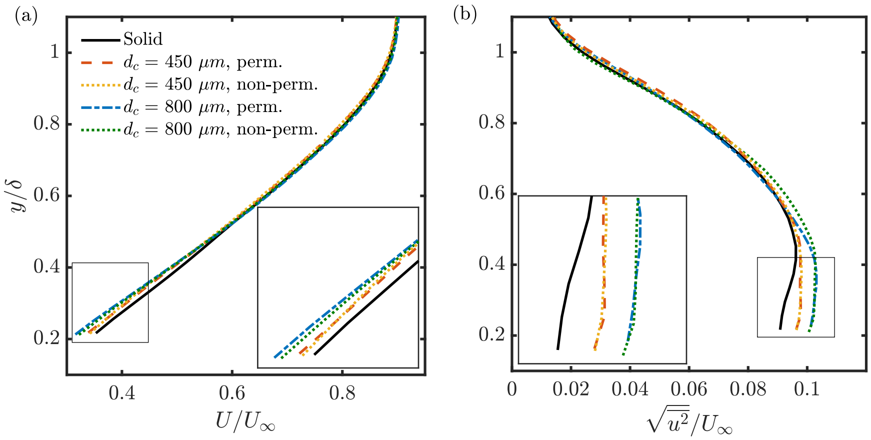

Figure 5.2: Mean flow field and statistics for solid and metal foam inserts at $x/c = 0$. (a) Mean wall-parallel velocity U/U_∞ profiles. (b) R.m.s. wall-parallel velocity $\sqrt{\overline{u^2}}/U_\infty$ profiles. Data measured at $U_\infty = 20$ m/s. A detailed view of data within 20% and 40% of the boundary layer is included in the bottom right (a) and bottom left (b) sub-figures.

It is interesting to note that, as shown in section 5.2.1, the low-frequency noise mitigation performance of a porous insert is affected by its flow permeability, i.e. only permeable inserts reduce noise scattering with respect to the solid trailing edge. Yet, the mean and turbulent flow field around the edge is mostly determined by roughness effects, hence its pore size. These results suggest that the open connection between the two sides of the airfoil through the metal foam alters significantly the mechanism of noise generation at the edge, eventually resulting in decreased noise scattering. This is further addressed in the following section, where the presence of flow communication through the porous medium is evaluated.

5.2.3. CORRELATION OF VELOCITY FLUCTUATIONS

In this section, correlation maps, as defined in section 3.5.1, are employed to assess the presence of cross-flow in the cases where noise reduction with respect to the baseline configuration is reported.

First, maps of the cross-correlation function as defined in equation 3.12 are plotted in

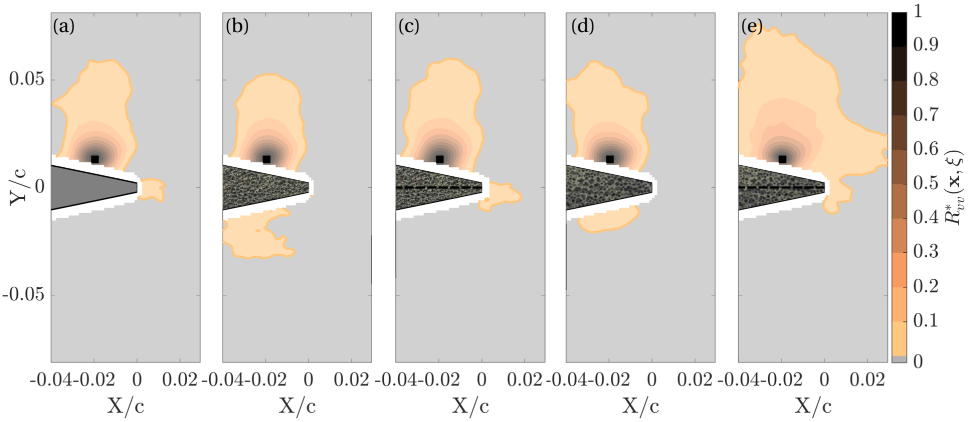

Figure 5.3: Low-frequency wall-normal velocity fluctuation correlation maps with reference point at $\mathbf{x}/c$ = (X/c , Y/c) = (-0.02, 0.013) (y/δ_{ref} = 0.15). (a) Solid. (b) Permeable d_c = 450 μm foam insert. (c) Non-permeable d_c = 450 μm foam insert. (d) Permeable d_c = 800 μm foam insert. (e) Non-permeable d_c = 800 μm foam insert.

figures 5.3 (a-e) for the five test cases. The maps depict only zones of positive correlation, whilst zones of negligible or negative correlation (R^*_{vv} < 0.02) are masked. The reference point, located at $\mathbf{x}/c$ = (X/c , Y/c) = (-0.02, 0.013), is marked with a black square. To link the presence of flow communication to the measured noise abatement, data are band-pass filtered within $\text{St}_c \in [4,16]$ for inserts manufactured with d_c = 800 μm foam and the non-permeable d_c = 450 μm foam insert, and $\text{St}_c \in [4,20]$ for the permeable d_c = 450 μm foam insert. Velocity fluctuations measured for the solid case are also band-pass filtered using the latter non-dimensional frequency range.

Figures 5.3 (a-e) show that the energy transfer from large coherent motions within the outer boundary layer to the near-wall region [6, 7] creates correlation zones surrounding the reference point, and elongated towards the wall-normal direction independently of the test case. For the solid and non-permeable metal foam cases (figures 5.3 (a), (c) and (e)), regions of high correlation only appear around the reference point or within the wake; wall-normal velocity fluctuations at upper and lower sides are not correlated, i.e. cross-flow is absent due to the presence of a solid boundary in between both sides. For the non-permeable d_c = 800 μm foam insert (figure 5.3 (e)), an increase of the streamwise extent of the correlation zone around the reference point is reported. Irregular rough surfaces usually introduce a certain degree of disorganization in the turbulent boundary layer, particularly in the flow direction, hence decreasing the associated length scales [8]. Ali *et al.* [9] reported the appearance of recirculation flow inside blunt trailing-edge permeable extensions; the streamwise enlargement of the correlation zone might be therefore related to this phenomenon. The lower permeability of the d_c = 450 μm foam insert (figures 5.3 (b) and (c)) might weaken or even fully prevent this flow feature, supporting the absence of significant differences between correlation zones surrounding the reference point for permeable and non-permeable configurations. Contrarily to the baseline and non-permeable inserts, for permeable inserts, a near-wall low-correlation ($0.02 < R^*_{vv} < 0.1$) region appears at the lower side regardless of the type of foam (figures 5.3 (b) and (d)); the presence of unsteady flow connection across the airfoil is thus confirmed.

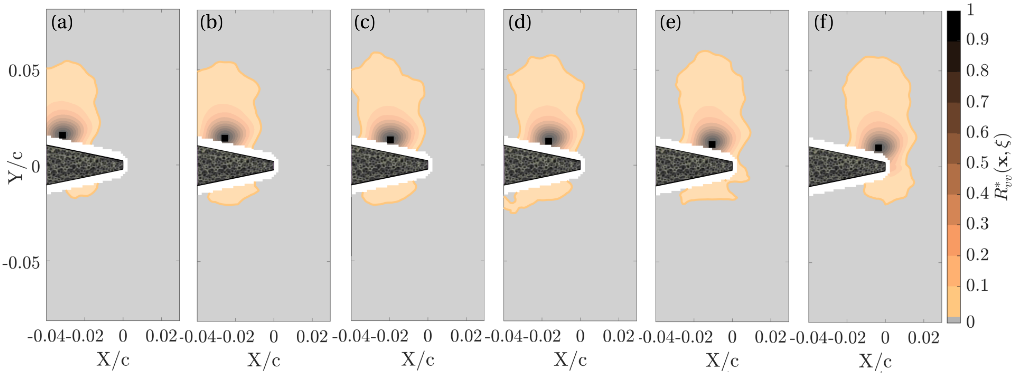

Figure 5.4: Low-frequency wall-normal velocity fluctuations correlation maps for the permeable $d_c = 800\ \mu$m foam insert with reference point at different streamwise locations. (a) $X/c = -0.032$, $Y/c = 0.016$ (b) $X/c = -0.026$, $Y/c = 0.014$ (c) $X/c = -0.020$, $Y/c = 0.013$ (d) $X/c = -0.016$, $Y/c = 0.012$ (e) $X/c = -0.011$, $Y/c = 0.011$ (f) $X/c = -0.004$, $Y/c = 0.01$

Before assessing the implications of these findings on noise generation, the size and extent of correlation regions found at both sides of the permeable trailing-edge mock-ups are addressed. Firstly, their appearance within the measured streamwise extent of permeable treatments is analysed. In figures 5.4 (a-f), it is shown that the appearance of correlation zones at the lower side of the $d_c = 800\ \mu$m insert is independent of the streamwise position of the reference point; this result evidences the presence of effective flow communication through the entire measured extension. The smaller correlation zone found when the reference point is moved upstream can be attributed to increased viscous and inertial losses due to the larger thickness of the insert [10].

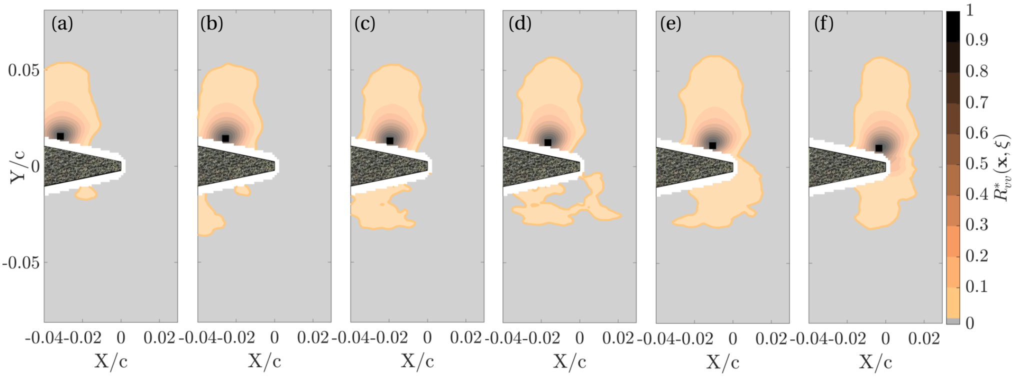

Figure 5.5: Low-frequency wall-normal velocity fluctuations correlation maps for the permeable $d_c = 450\ \mu$m foam insert with reference point at different streamwise locations. Locations are specified in the caption of figure 5.4.

It is also interesting to note that for the most upstream reference point location (figure 5.4 (a)) the correlation zone is located slightly downstream the reference point, indicating that flow communication through the foam occurs following preferred flow directions. Such a finding might be related to the presence of a pressure gradient between the two sides of the airfoil. Similar conclusions are also drawn for the least permeable foam (d_c = 450 μm) insert, shown in figures 5.5 (a-f).

The extension of the correlation zone in the opposite side is also strongly influenced by the distance between the reference point and the wall. In figures 5.6 (a-d), correlation maps for reference points ranging from $y/\delta_{\mathrm{ref}} = 0.15$ to $y/\delta_{\mathrm{ref}} = 0.25$ (where δ_{ref} is the boundary layer thickness at the trailing edge for the baseline case) at X/c = -0.02 are shown for the permeable d_c = 800 μm foam insert. It is found that correlated velocity fluctuations at the other side appear until a wall-normal distance of the reference point equal to 25 % of the boundary layer thickness; only near-wall turbulent motions are influenced by the absence of a solid boundary in between the upper and lower sides of the airfoil. As shown in section 5.2.2, this interaction is weak enough not to significantly affect the intensity of the velocity fluctuations. Yet, it strongly decreases acoustic scattering. Although this analysis is not shown for the permeable d_c = 450 μm foam insert for the sake of brevity, similar results are found.

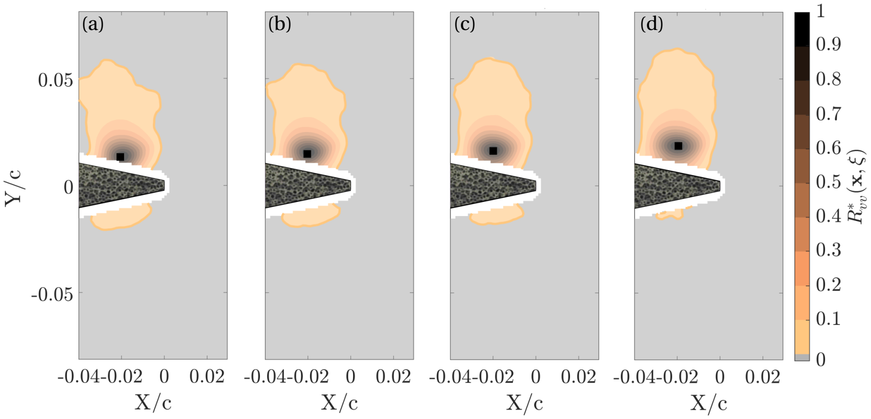

Figure 5.6: Low-frequency wall-normal velocity fluctuations correlation maps for the permeable d_c = 800 μm foam insert with reference point at different wall-normal locations. (a) $y/\delta_{ref} = 0.15$ (b) $y/\delta_{ref} = 0.18$ (c) $y/\delta_{ref} = 0.21$ (d) $y/\delta_{ref} = 0.25$

As explained above, the appearance of near-wall correlated flow regions implies the presence of cross-flow linking the suction and pressure sides of the airfoil within the permeable medium. This flow feature has direct implications on the edge noise generation of permeable lifting bodies: as reported by Delfs *et al.* [3], flow communication through the permeable inserts partially phases wall-pressure waves at both sides of the airfoil, hence decreasing the unsteady pressure mismatch at the edge. This process eventually results in far-field noise abatement within the frequency range where turbulent motions are phased, in agreement with results presented in section 5.2.1. As also pointed out by Kisil and Ayton [4], permeable materials might also trigger noise scattering from different streamwise positions, thus allowing constructive/destructive interference between noise sources arising along the insert. This point will be addressed in section 5.2.4, where the presence of different noise sources within the inserts for the five test cases is assessed.

To underline the link between cross-flow and noise abatement, the cross-correlation analysis is also applied to data-sets band-pass filtered using the frequency range where excess noise was previously reported. Specifically, wall-normal velocity fluctuations within $\mathrm{St}_c \in [16, 25]$ for inserts manufactured with $d_c = 800$ μm and the non-permeable $d_c = 450$ μm foam insert, and $\mathrm{St}_c \in [20, 25]$ for the permeable $d_c = 450$ μm foam insert are considered. Correlation maps computed on these data-sets are shown in figures 5.7 (a-e); results show no evidence of correlation regions on the complementary side of the airfoil, in line with results described in section 5.2.1.

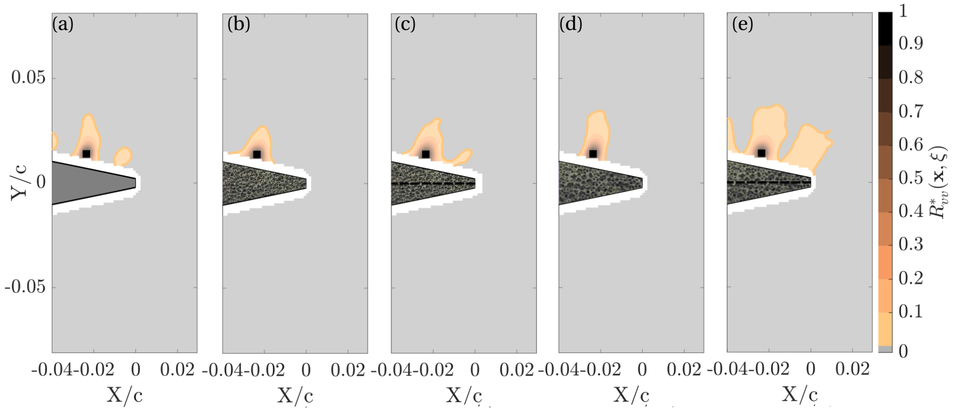

Figure 5.7: High-frequency wall-normal velocity fluctuation correlation maps with reference point at $\mathbf{x}/c = (X/c, Y/c) = (-0.02, 0.013)$ ($y/\delta_{\mathrm{ref}} = 0.15$). (a) Solid. (b) Permeable $d_c = 450$ μm foam insert. (c) Non-permeable $d_c = 450$ μm foam insert. (d) Permeable $d_c = 800$ μm foam insert. (e) Non-permeable $d_c = 800$ μm foam insert.

Further assessment is given in figures 5.8 (a-f), where correlation maps obtained by varying the streamwise position of the reference point are presented for the most permeable foam; it can be observed that no correlation at the lower side is found even when the point is placed above the trailing edge, where the thickness of the metal foam is minimal.

5.2.4. ACOUSTIC SOURCE MAPS

Noise source maps are analysed to verify any displacement of the predominant sound source detected by the microphone antenna. The current analysis is limited by the resolution of the antenna [11]; yet, it might allow to qualitatively identify different mechanisms involved in the process of sound generation for the test cases discussed.

Figures 5.9 (a-e) show acoustic source maps for $\mathrm{St}_c = 10$ ($f_c = 1$ kHz) for the five measured inserts. At this St_c, noise abatement with respect to the baseline configuration was reported only for permeable inserts in section 5.2.1. In the maps, the locations of maximum noise intensity within $-1 < Z/c < 1$ are indicated by a red dash-dotted line. For

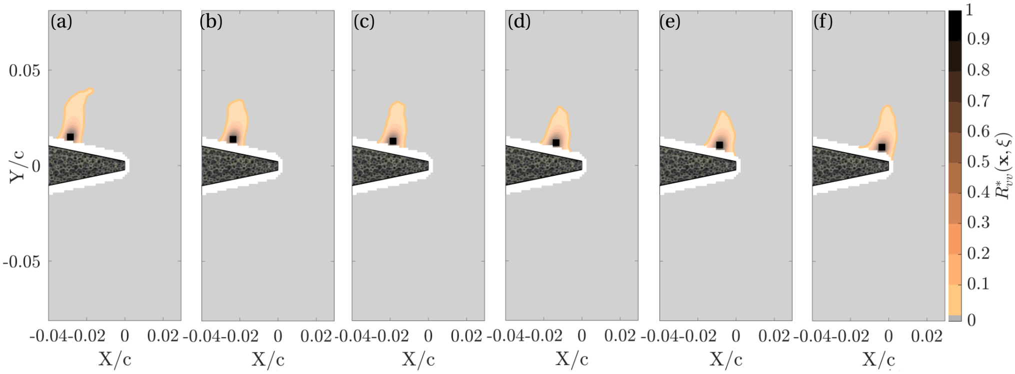

Figure 5.8: High-frequency wall-normal velocity fluctuations correlation maps for the permeable $d_c = 800$ μm foam insert with reference point at different streamwise locations. (a) X/c =-0.032, $Y/c = 0.016$ (b) X/c =-0.026, $Y/c = 0.014$ (c) X/c =-0.020, $Y/c = 0.013$ (d) X/c =-0.016, $Y/c = 0.012$ (e) X/c =-0.011, $Y/c = 0.011$ (f) X/c =-0.004, $Y/c = 0.01$

the solid case (figure 5.9 (a)), the red line is aligned with the trailing edge, as expected from the line source nature of broadband trailing-edge noise [12]. Similarly, for the non-permeable metal foam inserts (figures 5.9 (c) and (e)), noise is mainly scattered from the trailing edge and the intensity of the sound source is similar to the baseline case. Hence, within this frequency range, the location of the noise source is not altered by the presence of rougher surfaces, in agreement with results presented in section 5.2.1. For permeable inserts (figures 5.9 (b) and (d)), in addition to the reduction of the sound scattering caused by the mitigation of the pressure jump, it is also found that the maximum sound emission is located more upstream.

The employment of permeable materials thus promotes distributed noise scattering from different streamwise locations, in agreement with analytical models [4] and simplified numerical simulations [3]. This result, as well as the role of the cross-flow in the noise generation process, are confirmed by Teruna *et al.* [13], who numerically reproduced the permeable and blocked $d_c = 800$ μm foam test cases. A detailed analysis of the noise reduction mechanisms for the permeable variant points out that, besides a reduction of the scattering efficiency of the edge, the appearance of destructive interference among sources continuously distributed along the permeable surface also contributes significantly to noise abatement.

Acoustic source maps for $\mathrm{St}_c = 20$ ($f_c = 2$ kHz) are presented in figures 5.10 (a-e). Within this non-dimensional frequency band, noise increase due to roughness was found in section 5.2.1. For the baseline case, similarly to results obtained for lower frequencies, the dominant noise source is aligned with the trailing edge (figure 5.10 (a)). Conversely, for the porous configurations (figures 5.10 (b-e)), the location of maximum noise emission lies upstream the edge independently of the permeability. The noise source shift can be caused by the distributed nature of roughness noise, and confirms that this mechanism is mainly responsible for the excess noise reported in section 5.2.1. In figures 5.1 (a) and (b), it was observed that the permeable $d_c = 800$ μm metal foam mock-up produced higher excess noise levels than the non-permeable version whereas the $d_c = 450$

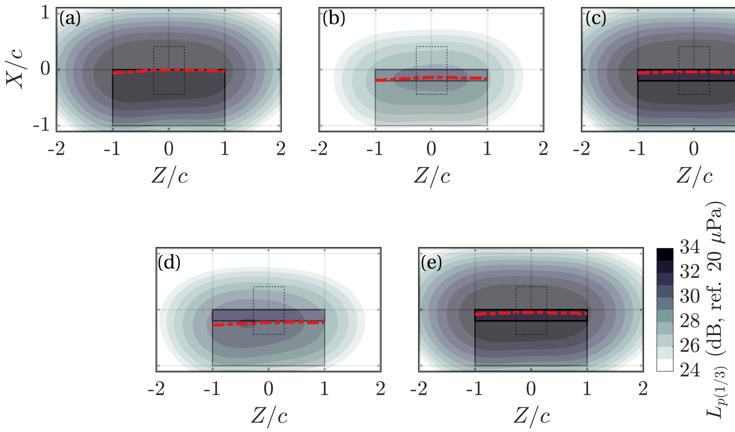

Figure 5.9: Source maps for the one-third octave band with f_c = 1000 Hz (St$_c$ = 10) for the measured test cases. (a) Solid. (b) Permeable d_c = 450 μm foam insert. (c) Non-permeable d_c = 450 μm foam insert. (d) Permeable d_c = 800 μm foam insert. (e) Non-permeable d_c = 800 μm foam insert. The airfoil is represented as a grey rectangle. Metal foam inserts are depicted with dark grey rectangles. Dashed area represents the region where the source power integration technique is applied. Red dash-dotted line marks streamwise $L_{p(1/3)}$ maxima within -1 < Z/c < 1.

μm inserts behaved oppositely. In agreement with Kisil and Ayton [4], this result points out that, apart from the roughness noise contribution, other noise generation mechanisms such as interference between sources distributed streamwisely along the insert or unsteady volume flow injection/ejection [14] due to permeability, might also be present.

The streamwise position of the maximum noise emission within the source maps normalized by the chord $X_{L^{\max}_{p(1/3)}}/c$ is plotted as a function of St$_c$ in figure 5.11 (a). Note that, as expected, at low St$_c$ the absolute location of the main noise emission is shifted upstream due to the low resolution of the array, and for the solid case the maximum noise emission is aligned with the trailing edge solely above St$_c$ = 10 (f_c = 1 kHz). However, it is considered that the shift affects every reported test case similarly; as a consequence, the analysis of the main source position relative to the solid edge $\Delta X_{L^{\max}_{p(1/3)}}/c = X^{\text{solid}}_{L^{\max}_{p(1/3)}}/c - X^{\text{metal foam}}_{L^{\max}_{p(1/3)}}/c$, reported in figure 5.11 (b), is expected to yield valuable insights on the nature of sound generation process present in metal foam inserts.

For the permeable d_c = 800 μm foam insert, the main noise source is upstream of the trailing edge; specifically, for the entire investigated frequency range, it is located approximately 4 cm (X/c = -0.2) upstream the position of the trailing edge (as retrieved for the solid case), lying near the solid-permeable junction position. In agreement with analytical [4] and numerical solutions [3], this finding suggests that the pressure jump at the trailing edge is decreased to the point that the one at the solid-permeable junction is larger. Hence, for highly enough permeable materials acoustic emission from other locations within the insert becomes a significant contributor to broadband self-noise. For its non-permeable counterpart the dominant source moves gradually from the trailing-edge position at low frequencies (St$_c$ < 12.5) towards more upstream positions at higher

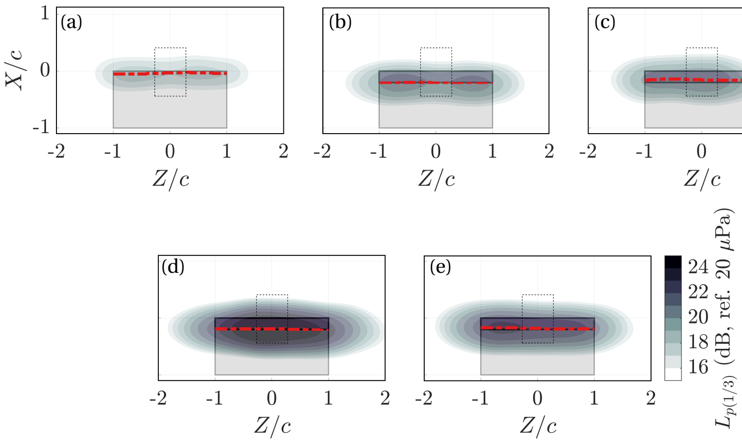

Figure 5.10: Source maps for the one-third octave band with $f_c = 2000$ Hz ($\mathrm{St}_c = 20$) for the three test cases. Legend as in figure 5.9.

frequencies. Interestingly, the transition from one location to another approximately coincides with the above-defined $\mathrm{St}_c^* = 16$. This points out that roughness noise exceeds the trailing-edge noise contribution from this non-dimensional frequency on, in agreement with results presented in section 5.2.1. At higher frequencies ($\mathrm{St}_c^* > 16$), the two inserts manufactured with $d_c = 800$ μm foam emit from similar locations. These findings also support roughness as the main cause for high-frequency excess noise, with other secondary mechanisms contributing to the small differences in the scattered sound levels.

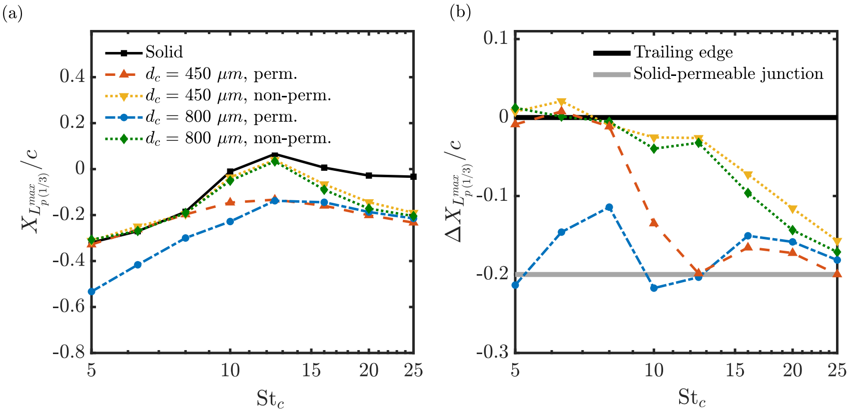

Figure 5.11: Streamwise location of the maximum $L_{p\,(1/3)}$ in the source maps with respect to the solid case. (a) Absolute coordinates. (b) Coordinates relative to the location of the solid edge.

For the permeable $d_c = 450$ μm foam insert, contrarily to the most permeable foam, dominant noise emission lies at the trailing edge up to $\mathrm{St}_c = 10$, where it moves upstream.

Discrepancies in the location of the main low-frequency emission between the two permeable treatments indicate that the permeability of a trailing-edge insert is indeed related to the impedance discontinuities created by the permeable treatment. It therefore seems that, for lower permeability materials, the actual edge scatters sound more efficiently than other regions along the insert, thus becoming the main contributor to the overall low-frequency noise emission; however, for higher permeability treatments the acoustic impedance jump created more upstream is larger.

5.3. CONCLUSION

Aerodynamic and acoustic measurements on a NACA 0018 airfoil with solid and porous trailing-edge inserts covering 20% of the chord length are carried out. Permeable porous inserts are manufactured by employing metal foams with different permeability values. To further assess the effect of the permeability, two non-permeable counterparts are also manufactured by applying a solid membrane in the symmetry plane. Noise source localization and far-field spectra measurements are performed by means of a phased microphone array. Time-resolved planar PIV measurements are performed to study the flow field around the inserts.

Far-field noise spectra show noise attenuation with respect to the solid trailing edge below St_c^* equal to 20 and 16 for inserts with increasing permeability. Conversely, non-permeable metal foam and solid inserts produce similar far-field noise scattering below St_c^*. Above the St_c^*, permeable and non-permeable treatments increase noise with respect to the baseline case, confirming that the excess noise is due to roughness. Yet, the most permeable insert generates slightly higher additional noise levels than its non-permeable equivalent, whereas the least permeable insert has an opposite behaviour.

The analysis of mean and r.m.s. velocity quantities computed above the trailing edge shows that permeable and non-permeable inserts manufactured with the same type of foam yield similar results. Hence, changes in the turbulent boundary layer with respect to the solid surface, i.e., the mean velocity deficit due to higher surface drag, as well as the increase in turbulence intensity due to higher friction forces, are driven by surface roughness and thus they are determined by the pore size.

The appearance of cross-flow is confirmed by the cross-correlation of low-frequency wall-normal velocity fluctuations within the measured domain; this analysis reveals near-wall regions of correlated flow at upper and lower sides of the airfoil only for the permeable inserts. This phenomenon evidences a communication process that affects flow at both sides of the trailing edge, reducing the acoustic impedance jump at the edge (hence sound generation). Contrarily, at higher frequencies, where noise increase with respect to the baseline configuration is reported, velocity fluctuations are not correlated.

This is reflected in changes in the dominant sound emission location within porous treatments are detected in the noise source maps. At lower frequencies the most permeable insert scatters noise mainly from upstream the trailing edge, whilst the least permeable insert emits from the edge. The permeability of the treatment thus determines the magnitude of the acoustic impedance jumps created along the metal foam treatment, defining where the scattering of wall-pressure waves into acoustic pressure perturbations is more efficient, in agreement with analytical models [4] and numerical results [3].

These findings demonstrate the significant role of the cross-flow for broadband self-noise attenuation using permeable materials at the trailing-edge. They suggest that permeable trailing-edge treatments with a simpler pore topology, e.g., straight channels connecting suction and pressure sides of the airfoil, would also abate noise. This aspect will be further addressed in Chapter 6. They also suggest that inserts with a streamwise permeability gradient might overcome the performance of homogeneous porous materials, in line with the optimized porous media proposed by Schulze and Sesterhenn [15]. This sort of permeable treatments, with a more gradual dampening of the pressure mismatch, might prevent the creation of coherent scattering regions within the permeable surface. This point will be further addressed in chapter 7, where perforated trailing-edge inserts with tailored permeability distributions along the chord are investigated.

REFERENCES

[1] A. Rubio Carpio, F. Avallone, and D. Ragni, *On the role of the flow permeability of metal foams on trailing edge noise reduction,* in *2018 AIAA/CEAS Aeroacoustics Conference* (American Institute of Aeronautics and Astronautics, 2018) pp. 1–18.

[2] A. Rubio Carpio, F. Avallone, D. Ragni, M. Snellen, and S. van der Zwaag, *Mechanisms of broadband noise generation on metal foam edges,* Physics of Fluids **31** (2019), 10.1063/1.5121248.

[3] J. Delfs, B. Faßmann, N. Lippitz, M. Lummer, M. Mößner, L. Müller, K. Rurkowska, and S. Uphoff, *SFB 880: aeroacoustic research for low noise take-off and landing,* CEAS Aeronautical Journal **5**, 403 (2014).

[4] A. Kisil and L. J. Ayton, *Aerodynamic noise from rigid trailing edges with finite porous extensions,* Journal of Fluid Mechanics **836**, 117 (2018).

[5] T. J. Lu, A. Hess, and M. F. Ashby, *Sound absorption in metallic foams,* Journal of Applied Physics **85**, 7528 (1999).

[6] P. Bradshaw, *'Inactive' motion and pressure fluctuations in turbulent boundary layers,* Journal of Fluid Mechanics **30**, 241 (1967).

[7] S. Hoyas and J. Jiménez, *Scaling of the velocity fluctuations in turbulent channels up to Re = 2003,* Physics of Fluids **18**, 10 (2006).

[8] Y. Wu and K. T. Christensen, *Spatial structure of a turbulent boundary layer with irregular surface roughness,* Journal of Fluid Mechanics **655**, 380 (2010).

[9] S. A. S. Ali, M. Azarpeyvand, and C. R. I. Da Silva, *Trailing-edge flow and noise control using porous treatments,* Journal of Fluid Mechanics **850**, 83 (2018).

[10] J. L. Lage, *The fundamental theory of flow through permeable media from Darcy to turbulence,* in *Transport Phenomena in Porous Media* (Elsevier, 1998) pp. 1–30.

[11] J. Hald and J. J. Christensen, *A novel beamformer array design for noise source location from intermediate measurement distances,* The Journal of the Acoustical Society of America **112**, 2448 (2002).

[12] T. F. Brooks, D. S. Pope, and M. A. Marcolini, *NASA Reference Publication*, Tech. Rep. (NASA Langley Research Center, 1989).

[13] C. Teruna, F. Manegar, F. Avallone, D. Ragni, D. Casalino, and T. Carolus, *Noise reduction mechanisms of an open-cell metal-foam trailing edge,* Journal of Fluid Mechanics **898**, 1 (2020).

[14] P. Nelson, *Noise Generated By Flow over perforated surfaces,* Journal of Sound and Vibration **83**, 11 (1982).

[15] J. Schulze and J. Sesterhenn, *Optimal distribution of porous media to reduce trailing edge noise,* Computers and Fluids **78**, 41 (2013).

6

NOISE MITIGATION WITH PERFORATED TRAILING EDGES

"Perfection is achieved, not when there is nothing more to add, but when there is nothing left to take away."

Antoine de Saint-Exupéry (1900-1944)

Noise emission from five 3D-printed perforated trailing-edge inserts, with straight cylindrical channels normal to the chord, is measured and is compared to that of inserts manufactured with metallic foams, with comparable flow permeability K but more tortuous pore paths. Scaling laws for noise mitigation ΔL_p*, computed as the difference between far-field noise scattering from solid and permeable edges, are presented. The analysis allows to identify the tortuosity of the permeable structure as an additional parameter (to the permeability) controlling noise attenuation. The effect of varying the overall porous extent on the noise mitigation performance is also studied. For the most permeable perforated insert, a tonal noise, provoked by the appearance of vortex-shedding in the wake of the model is reported. Since applying a larger permeable surface, or increasing the permeability at the trailing edge decreases the aerodynamic performance of the blade, an insert with permeable extension of only 5% of the chord, permeability of* 1×10^{-9} m^2 *and tortuosity of 1.15 is recommended to optimize broadband noise abatement and avoid shedding-related tones for the conditions explored in the current study.*

Parts of this chapter have been published in the Journal of Sound & Vibration (2020) [1].

6.1. INTRODUCTION

In Chapter 5 it was concluded that permeable inserts mitigate the impedance jump at the trailing edge, and promote noise scattering from the entire porous surface. Such a process is controlled by the local permeability of the material, that determines the intensity of the flow communication between both sides of the airfoil. Consequently, the employment of more permeable structures usually yields larger noise reduction.

Previous research on permeable trailing edges employed (open-cell) porous structures such as foams [2, 3], sintered granulates [4], fiber felts [5] or metal meshes [6]. Materials with such a complex pore arrangement often entail additional fluid-dynamic and acoustic features. For instance, hydrodynamically rough surfaces produce high-frequency excess noise and increased turbulence levels close to the wall [7, 8]; these effects might partially mask their acoustic benefits [9]. Additional aspects, such as the change of material properties when subjected to conventional machining processes (e.g., milling), alterations of the properties due to a modification of the manufacturing process over time (i.e., repeatability issues), or inhomogeneity issues also discourage their use for research [10]. Recently developed manufacturing techniques such as additive manufacturing [11] allow constructing permeable trailing edges with tailored micro-structures with low cost and high accuracy. Flow communication can be achieved with inserts with straight channels that connect suction and pressure sides of the airfoil, and their permeability can be tailored by varying hole size, shape or spatial density. Following the analysis of the process of noise scattering in permeable edges described above, these simplified perforated inserts should mimic the noise mitigation performance of those manufactured with metallic foam, with a much more complex pore arrangement.

In the current chapter, five different perforated trailing edges for a NACA 0018 airfoil are acoustically characterized at angles of attack α of 0.2 and 5.4 degrees and chord-based Reynolds numbers Re_c ranging between 1.8×10^5 and 4.5×10^5. These perforated inserts, whose properties are summarized in table 3.3, have cylindrical channels normal to the chord, and allow for flow communication between suction and pressure side along the last 20% of the airfoil. All five perforated inserts have the same hole diameter d_h = 0.8 mm, and different permeability K is obtained by homogeneously distributing holes within the insert with a fixed hole spacing l_h. Noise scattering of such perforated trailing edges, with a periodic channel arrangement, is compared to that of open-cell metal foam inserts, with different (random) micro-structure but similar macroscopic permeability. The comparison yields general topology and permeability criteria that might serve as guidelines for the design of future permeable trailing edges.

The current chapter is organized as follows. Firstly, scaling laws for noise mitigation with flow speed or material properties are presented in section 6.2.1; in section 6.2.2, the tortuosity of a permeable edge, i.e. a measure of how tortuous its pore paths are, is proposed as a parameter to further control and optimize noise abatement ; the scaling of far-field acoustic pressure with flow speed is reported in section 6.2.3; a brief analysis on the effect of varying the chordwise permeable length on noise mitigation is presented in section 6.2.4; finally, the appearance of tones in the spectra of perforated inserts with high permeability is addressed in section 6.2.5. To conclude, in section 6.3 a summary of the main findings is presented.

6.2. RESULTS

6.2.1. SCALING LAWS FOR NOISE MITIGATION

In figure 6.1 (a), far-field acoustic spectra for a free-stream velocity U_∞ = 20 m/s and α = 0.2 degrees are shown for inserts with homogeneous hole spacing l_h ranging from 1.5 to 5 mm. Data are presented in terms of Sound Pressure Level in one-third octave bands $L_{p\,(1/3)}$ (reference pressure: $p_{\mathrm{ref}} = 20\ \mu$Pa) as a function of the chord-based Strouhal number $\mathrm{St}_c = fc/U_\infty$. Relative levels $\Delta L_{p\,(1/3)} = L_{p(1/3),\,\mathrm{solid}} - L_{p(1/3),\,\mathrm{permeable}}$ with respect to the baseline configuration are shown in figure 6.1 (b), where positive values refer to noise abatement with respect to the fully solid airfoil.

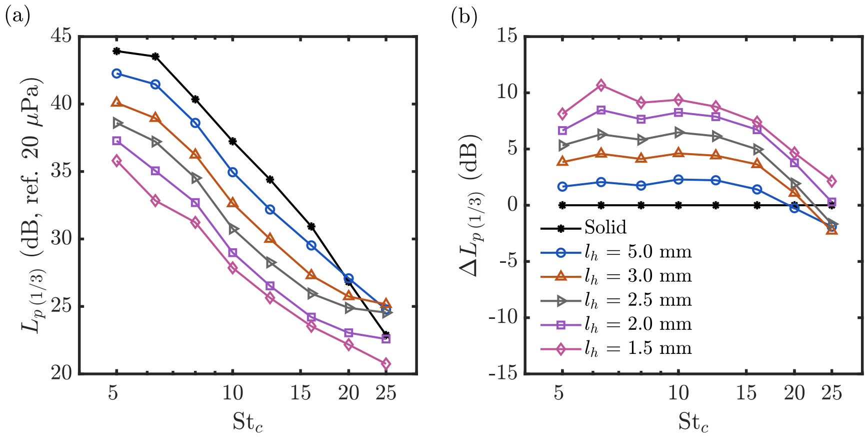

Figure 6.1: Far-field acoustic spectra for the perforated inserts (with $s/c = 0.2$) at U_∞ = 20 m/s and α = 0.2 degrees. (a) Absolute levels. (b) Relative levels with respect to the baseline configuration $\Delta L_{p(1/3)}$. Line colour and symbol coding as indicated in (b) also applies to (a).

Similarly to other flow permeable structures with a more complex and less regular pore arrangement, such as foams [7], sintered granulates [4] or felts [5, 6], perforated inserts yield low-frequency noise attenuation, with higher noise abatement being measured for inserts with higher flow permeability. Specifically, the largest noise attenuation (equal to 11 dB) is reported for the most permeable insert (l_h = 1.5 mm) at $\mathrm{St}_c = 6.3$. Also in line with other studies [7], acoustic spectra for permeable trailing edges show crossover Strouhal numbers St_c^*, which set the high-frequency bound for noise mitigation. St_c^* depends on the type of insert [1]. Specifically, a higher St_c^* is computed for perforated inserts with higher permeability, i.e. increasing the permeability of the trailing edge not only yields higher abatement but also extends the frequency range at which noise mitigation is observed. Contrarily, a decrease in St_c^* with increasing pore size, hence permeability, was reported in Chapter 5 for edges manufactured with metallic foams.

In figures 6.2 (a) and (b), far-field acoustic spectra for a free-stream velocity U_∞ = 20 m/s and α = 5.4 degrees are shown for the same set of inserts. Similarly to data for lower lift conditions (figures 6.1 (a) and (b)), perforated trailing edges with higher permeabil-

---

[1] Note that for the design with l_h = 1.5 mm, St_c^* is outside the measured frequency range.

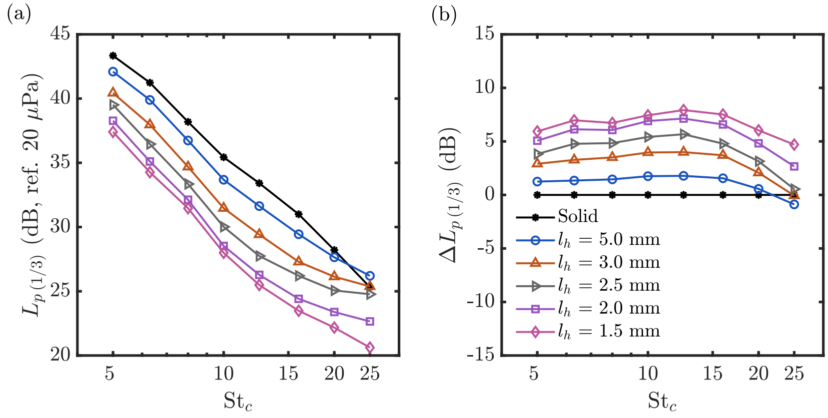

Figure 6.2: Far-field acoustic spectra for the perforated inserts (with $s/c = 0.2$) at $U_\infty = 20$ m/s and $\alpha = 5.4$ degrees. (a) Absolute levels. (b) Relative levels with respect to the baseline configuration $\Delta L_{p(1/3)}$. Line colour and symbol coding as indicated in (b) also applies to (a).

ity yield higher noise mitigation levels below St_c^*. Main differences with respect to data obtained at a lower angle of attack are a decrease of the highest noise abatement (for instance, the most permeable insert now yields $\Delta L_{p,(1/3)} = 8$ dB at $\mathrm{St}_c = 12.5$) and an overall increase of St_c^*.

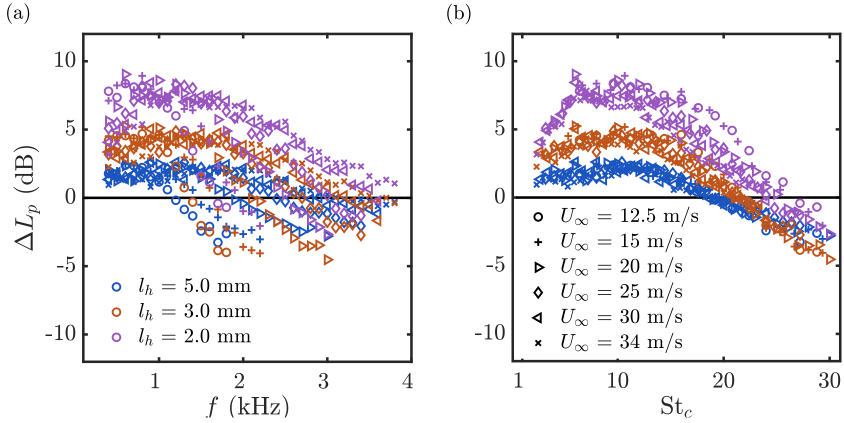

Figure 6.3: Collapse of noise attenuation ΔL_p for free-stream speeds ranging between 12.5 and 34 m/s and $\alpha = 0.2$ degrees for inserts with $l_h = 2$, 3 and 5 mm and $s/c = 0.2$. (a) ΔL_p as a function of f. (b) ΔL_p as a function of St_c. Colour and symbol coding apply to both figures.

In figure 6.3 (a), narrow-band noise attenuation data ΔL_p for U_∞ of 12.5, 15, 20, 25, 30 and 34 m/s are plotted as a function of f. Only data corresponding to inserts with $l_h = 2$, 3 and 5 mm are shown for the sake of clarity. For the same reason, only one out of ten points are depicted ($\Delta f = 100$ Hz). As seen in figure 6.3 (b), ΔL_p data measured for different free-stream velocities collapse onto each other when plotted as a function of St_c; for ΔL_p, the relationship between frequency and U_∞ is thus linear. For the current analysis, the chord is used as normalizing length scale for convenience. An attempt to further scale data for different inserts using length scales derived from the properties of the material ($\sqrt{K}$, $1/C$, $F = KC$) is presented in appendix C. After collapsing, data for inserts with different flow permeabilities yield curves that define the noise attenuation performance of each design independently of U_∞. In line with results presented above, characteristic curves for inserts with higher permeability allow for higher maximum noise attenuation and St_c^*.

This finding allows to predict the frequency for maximum noise attenuation, or the frequency range for noise reduction for different velocities. The same methodology yields a satisfactory collapse of data measured at $\alpha = 5.4$ degrees. These characteristic curves have also been compared to noise mitigation data predicted by the symbolic regression models described in Sarradj and Geyer [13]. However, the overall agreement is not satisfactory; there is no collapse of predicted noise mitigation data with St_c, and higher noise mitigation maxima are predicted for materials with decreasing permeability, contrarily to experimental data presented in this chapter. For the sake of brevity, the collapse of data measured with the model at incidence, and the comparison with symbolic regression models are not included here.

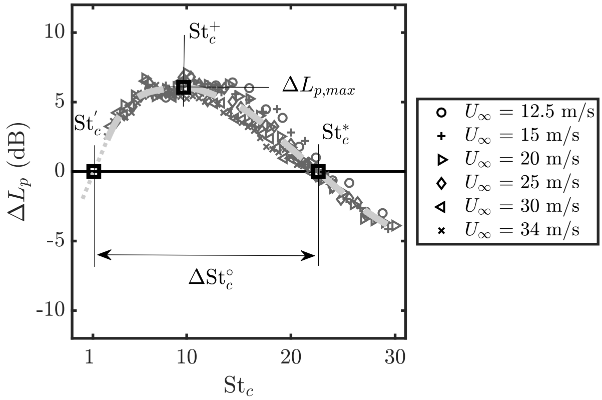

Figure 6.4: Sketch depicting collapsed ΔL_p data for the insert with $l_h = 2.5$ mm at $\alpha = 0.2$ degrees and free-stream speeds ranging from 12.5 to 34 m/s. The B-Spline fitted to experimental data is shown as a thick dashed line. In the sketch, low and high-bound cross-over Strouhal numbers $\mathrm{St}_c^{'}$ and St_c^*, the Strouhal number range for noise mitigation $\Delta\mathrm{St}^\circ = \mathrm{St}_c^*$-$\mathrm{St}_c^{'}$, the maximum noise attenuation $\Delta L_{p,\mathrm{max}}$ and its chord-based Strouhal number St_c^+ are also depicted. The thin dotted line indicates extrapolated data.

The characteristic curves shown above allow to study the change of relevant noise mitigation properties with the trailing edge permeability. Specifically, low $\mathrm{St}_c^{'}$ and high-bound St_c^* cross-over Strouhal numbers, the Strouhal number range for noise mitigation $\Delta\mathrm{St}_c^\circ = \mathrm{St}_c^*$-$\mathrm{St}_c^{'}$, the maximum noise mitigation $\Delta L_{p,\mathrm{max}}$ and the Strouhal number at which occurs St_c^+, as defined in figure 6.4, are analysed in the following. To compute these properties, cubic B-splines [14] with 8 knots and C2 continuity [15] are fitted to experimental data. In the test cases where $\mathrm{St}_c^{'}$ or St_c^* are not present within the measured St_c range, the spline is extended with constant slope, as shown in figure 6.4 (thin dotted line).

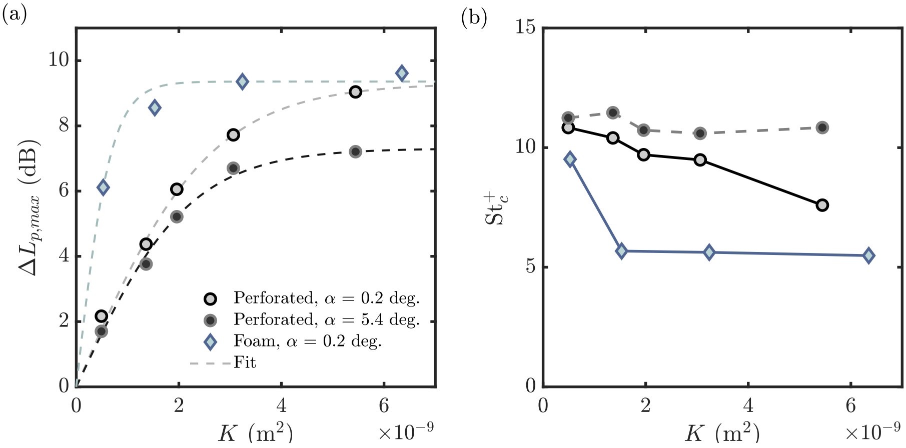

Figure 6.5: Change in maximum noise mitigation with permeability for perforated and metal foam inserts at $\alpha = 0.2$ and 5.4 degrees. (a) $\Delta L_{p,\max}$. (b) St_c^+.

Firstly, the change in maximum noise attenuation $\Delta L_{p,\max}$ with permeability K, shown in figure 6.5 (a), is analysed. $\Delta L_{p,\max}$ data for metal foam trailing edges, which also collapse with St_c are also presented for comparison. To facilitate the interpretation of results, $\Delta L_{p,\max}$ data are fitted with a hyperbolic tangent function, as defined in equation 6.1

$$\Delta L_{p,\max} = \gamma_1 \tanh\left(\gamma_2 K\right) \tag{6.1}$$

where γ_1 defines the asymptotic $\Delta L_{p,\max}$ value and γ_2 the slope of the function within the low permeability range. The coefficients for the fit of experimental data to equation 6.1 are presented in table 6.1, together with the coefficient of determination R^2, that gives a measure of the goodness of the fit. The reasons to choose this function are twofold: firstly, it adequately mimics the asymptotic character of experimental data for increasing permeability of the edges; secondly, it passes through the point $K = 0$ m^2, $\Delta L_{p,\max} = 0$ dB, and properly describes baseline data.

Case	γ_1 (dB)	$\gamma_2 \times 10^{-9}$ (m^{-2})	R^2
Perforated, $\alpha = 0.2$ deg.	9.311±0.984	0.388±0.084	0.995
Perforated, $\alpha = 5.4$ deg.	7.310±0.699	0.456±0.098	0.988
Metal Foam, $\alpha = 0.2$ deg	9.358±1.221	1.484±0.779	0.943

Table 6.1: Coefficients (γ_1, γ_2) (with 95% confidence bounds) and correlation coefficient R^2 for the fit of experimental $\Delta L_{p,\max}$ and permeability K data to equation 6.1

These curves yield valuable information on the type of microstructure that maximizes noise mitigation. It is observed that, for perforated inserts at $\alpha = 0.2$ degrees, increasing the permeability to 3.5×10^{-9} m^2 causes up to 8.3 dB noise mitigation. Further increasing the permeability of the insert brings small additional noise attenuation benefits (approximately 1 dB more, up to an asymptotic value of 9.3 dB at $K = 6\times10^{-9}$ m^2). Furthermore, increasing α to 5.4 degrees penalizes noise mitigation: $\Delta L_{p,\max}$ values measured at a higher-lift condition are lower than those computed at 0.2 degrees independently of the permeability. Interestingly, lower-permeability variants are less sensitive to a change in α: for instance, for the least permeable perforated insert (l_h = 5 mm) increasing α yields a $\Delta L_{p,\max}$ loss equal to 0.5 dB, whilst for the most permeable insert (l_h = 1.5 mm) the decrease is equal to 2 dB. Given the lift decrease and drag increase when employing inserts with higher permeability [5, 16], as well as their higher sensitivity to changes in α, the employment of perforated inserts with moderate flow permeability (below a threshold of $K = 3.5\times10^{-9}$ m^2) is recommended.

For inserts manufactured with metal foams, similar features are found: maximum noise attenuation increases rapidly with permeability up to approximately 8.4 dB (for a K threshold of 1×10^{-9} m^2, less than one third of the value reported for perforated pores); further increasing K only yields a 1 dB gain in $\Delta L_{p,\max}$, up to a maximum noise mitigation of 9.4 dB. Both metal foam and perforated trailing edges share a high bound for $\Delta L_{p,\max}$ of 9.3-9.4 dB; yet, for a given K (below 6×10^{-9} m^2) an additional increase of up to 4 dB (for edges with K between 0.5 and 2×10^{-9} m^2) can be achieved by employing a random pore arrangement. Similarly, to obtain similar $\Delta L_{p,\max}$ levels, perforated inserts must be more permeable than metal foam trailing edges. In view of these findings, the permeability of the trailing edge can be therefore considered as a good first order indicator for noise mitigation effectiveness, but it is insufficient to fully characterize the noise scattering potential of trailing edges with significant micro structural differences. Other parameters describing the different pore organization of permeable materials, such as tortuosity, need to be considered to fully characterize the noise scattering. This analysis will be presented in section 6.2.2.

In figure 6.5 (b), the chord-based Strouhal number at which $\Delta L_{p,\max}$ occurs, St_c^+, is shown for perforated inserts at $\alpha = 0.2$ and 5.4 degrees, and metal foam inserts at $\alpha = 0.2$ degrees as a function of K. For perforated inserts at $\alpha = 0.2$ degrees, an approximately linear decrease of St_c^+ with K is measured: the least permeable insert produces maximum noise attenuation at $\mathrm{St}_c^+ = 11$, while the most permeable insert yields $\mathrm{St}_c^+ = 7.5$. Therefore, perforated trailing edges with increasing permeability not only yield higher $\Delta L_{p,\max}$ but also mitigate low-frequency noise more efficiently. Increasing the angle of attack to $\alpha = 5.4$ degrees leads to a constant St_c^+ value of 11 for all K; similarly to $\Delta L_{p,\max}$, inserts with higher flow permeability are more sensitive to a change in α. Regarding metal foams, low-permeability inserts ($K = 0.5\times10^{-9}$ m^2) yield maximum noise attenuation at $\mathrm{St}_c^+ = 9.5$, close to the value for perforated edges. However, increasing K to 1.5×10^{-9} m^2 rapidly brings St_c^+ to 5.7; for higher flow permeability St_c^+ is approximately constant. Therefore, the choice of an adequate pore arrangement allows not only to obtain different maximum noise attenuation levels (below a certain K threshold), but also to target specific frequencies.

In figure 6.6, the lower-bound cross-over Strouhal numbers $\mathrm{St}_c^{'}$, computed for perforated and metal foam inserts at $\alpha = 0.2$ and 5.4 degrees, are plotted as a function of K. For perforated inserts at $\alpha = 0.2$ degrees, $\mathrm{St}_c^{'}$ increases from 0.04 to 2.44 within the measured permeability range. Increasing the angle of attack, or employing inserts with random pore distribution (i.e. metal foams) yield higher $\mathrm{St}_c^{'}$; specifically, $\mathrm{St}_c^{'}$ values between 0.96

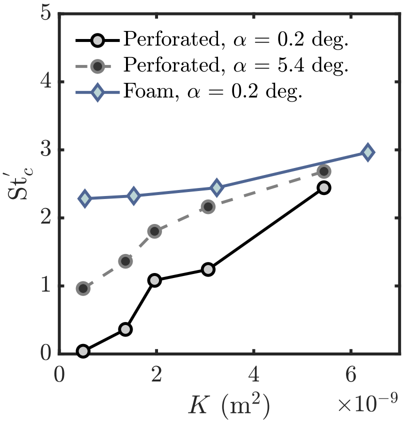

Figure 6.6: Change in $\mathrm{St}_c^{'}$ with permeability for perforated and metal foam inserts at $\alpha = 0.2$ and 5.4 degrees.

and 2.68 are measured for the former case, and between 2.28 and 2.96 for the latter. It can be therefore concluded that to guarantee noise mitigation within the very low frequency range one must employ edges with low permeability and ordered pore arrangement.

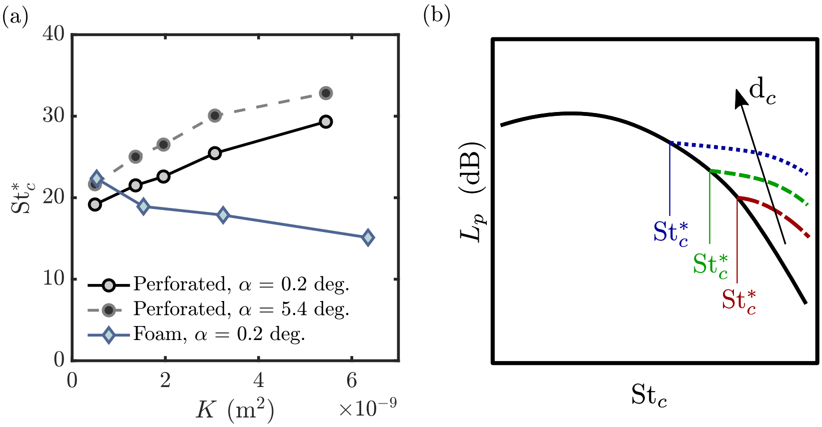

Figure 6.7: (a) Change in St_c^* with permeability for perforated and metal foam inserts at $\alpha = 0.2$ and 5.4 degrees. (b) Sketch depicting typical roughness noise features for porous edges. Black line represents baseline (smooth surface) trailing-edge noise. Dashed lines illustrate roughness noise contributions for increasing pore size d_c, i.e. higher roughness.

In figure 6.7 (a), high-bound cross-over Strouhal number St_c^* data are presented. For this quantity, a linear-like increase of St_c^* with K is measured for perforated inserts at $\alpha = 0.2$ degrees. Therefore, besides higher noise attenuation, inserts with higher permeability also mitigate noise up to higher frequencies (in line with results shown in figures 6.1 (a) and (b)). Additionally, increasing the angle of attack to $\alpha = 5.4$ degrees further increments St_c^*. For metal foams edges, a different trend is reported: a lower St_c^* is measured for increasing permeability of the insert. As reported in Chapter 5, high-frequency excess noise is caused by surface roughness [7, 9]. For this type of inserts, it has been previously shown that a larger pore size, that often translates in larger K, generates higher noise and becomes more relevant at lower frequencies (see the sketch shown in figure 6.7 (b)), in agreement with results in figure 6.7 (a). As will be shown in Chapter 7, the opposite trends for the variation of St_c^* with K in perforated and metal foam edges is determined by the fact that the former type allows to obtain different flow permeabilities with a constant pore size. It is also important to remark that, for the present data-set, peaks are only observed in the acoustic spectra of the most permeable perforated insert; however, the low-frequency nature of these tones suggests that they are not driven by roughness. These will be addressed in detail in section 6.2.5.

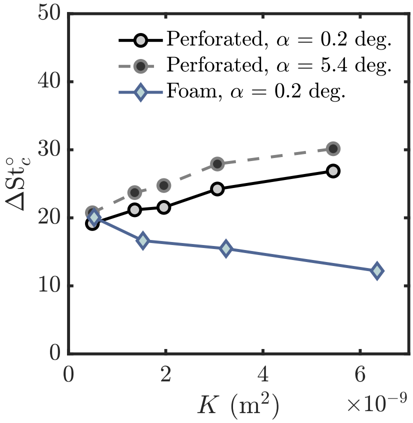

Figure 6.8: Change in $\Delta\mathrm{St}_c^\circ$ with permeability for perforated and metal foam inserts at $\alpha = 0.2$ and 5.4 degrees.

The resulting St_c range for noise abatement $\Delta\mathrm{St}^\circ = \mathrm{St}_c^*\text{-}\mathrm{St}_c^{'}$, measured for perforated and metal foam inserts at angles of attack of 0.2 and 5.4 degrees, is shown in figure 6.8. Results are similar to those found for St_c^*, i.e., perforated edges with higher permeability yield acoustic benefits within a wider frequency range, and increasing α further extends it (approximately an increase of $\Delta\mathrm{St}^\circ = 4$ with α is measured independently of K). For metal foam edges, a decrease in $\Delta\mathrm{St}^\circ$ with K is observed instead; hence, contrarily to perforated edges, more permeable metal foam edges yield noise mitigation within a smaller frequency range. The similarity between figure 6.7 (a) and figure 6.8 suggests that $\Delta\mathrm{St}^\circ$ is particularly sensitive to the appearance of noise generation mechanisms other than edge noise, that generate high-frequency excess noise.

6.2.2. EFFECT OF TORTUOSITY ON NOISE MITIGATION

Following the discussion in section 6.2.1, the tortuosity τ_Y as defined in section 3.3.3. is proposed, in addition to K, as an additional indicator for the noise mitigation capabilities of permeable trailing edges. In figure 6.9, $\Delta L_{p,\mathrm{max}}$ data are plotted as a function of flow permeability and tortuosity for perforated and metal foam trailing edges.

It is observed that, for a given permeability, micro-structures with more tortuous

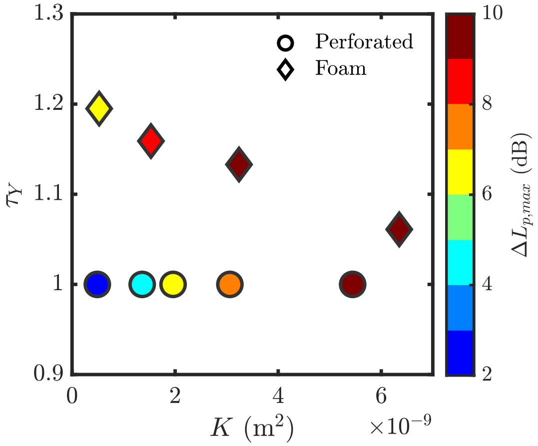

Figure 6.9: Maximum noise attenuation $\Delta L_{p,\mathrm{max}}$ as a function of permeability K and tortuosity τ_Y for $\alpha = 0.2$ deg.

pore paths, i.e. foams, gain up to 4 dB noise attenuation with respect to straight channelled inserts. To this end, highly tortuous pore arrangements, such as those derived from sintering [17] or casting around space-holders [18] manufacturing processes, might yield additional benefits for low-noise applications. For the current experimental set-up, a trailing edge with a permeability of $K = 1\times10^{-9}$ m^2 and tortuosity $\tau_Y \simeq 1.15$ is a good trade-off between aerodynamic and broadband acoustic performance.

6.2.3. SCALING OF FAR-FIELD ACOUSTIC PRESSURE WITH FREE-STREAM VELOCITY

The exponent m for the scaling of far-field mean-squared acoustic pressure with free-stream velocity is now analysed. This quantity is computed fitting the Overall Sound Pressure Level (OSPL) [19], calculated as

$$\mathrm{OSPL} = 10\,\log_{10}\sum_{f_c} 10^{L_{p(1/3)}/10\,\mathrm{dB}} \tag{6.2}$$

to experimental data measured at different speeds. To isolate broadband noise mitigation, only frequency bands where noise abatement with respect to the baseline configuration is measured are considered. For the same reason, the most permeable perforated ($l_h = 1.5$ mm) and metal foam ($d_c = 1200$ μm) inserts are excluded from the analysis because, as will be seen in section 6.2.5, acoustic spectra for the former contain tones; for the latter, a low-frequency broadband hump is measured. The fit of experimental OSPL data to U_∞ is performed employing

$$\mathrm{OSPL} = m10\log_{10}\left(\frac{U_\infty}{U_{\mathrm{ref}}}\right)+\eta \tag{6.3}$$

with η being an additional fit coefficient and $U_{\mathrm{ref}} = 1$ m/s for convenience.

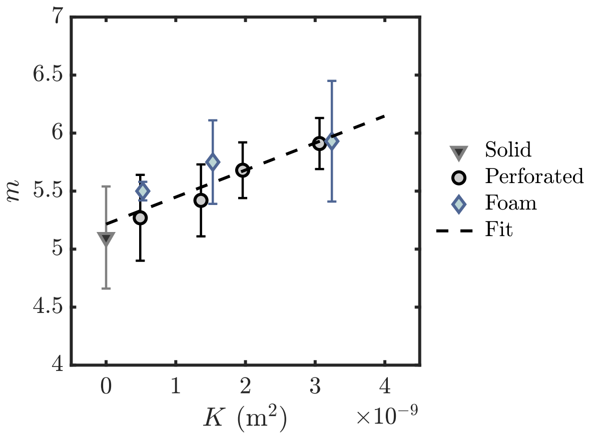

Figure 6.10: Analysis of the exponent m of the scaling low of the far-field acoustic pressure with free-stream velocity U_∞. Change in m with permeability K for metal foam and perforated inserts at $\alpha = 0.2$ degrees.

For the fully solid insert, the fit yields $m = 5.1$, in line with theoretical [20, 21] and experimental results [22]. The computed exponent m is plotted (together with the uncertainty, estimated as the 95% confidence bounds of the fit) as a function of K in figure 6.10 for perforated and metal foam inserts at $\alpha = 0.2$ degrees. In spite of the many spectral differences described above, exponents m for micro-structures with similar flow permeability are comparable (within their uncertainty range) independently of the pore arrangement. This result suggests that although specific noise mitigation features ($\mathrm{St}_c^{'}$, St_c^{*}, $\Delta L_{p,\max}$, etc.) for permeable inserts rely on certain topological properties, they all act upon noise generation through the same mechanism, i.e. decreasing the pressure mismatch at the edge and creating distributed noise scattering. Data for both perforated and metal foam edges increase linearly from $m = 5.1$ (at $K = 0$ m^2, solid case) to $m = 5.9$ (at $K = 3 \times 10^{-9}$ m^2). Consequently, m values are fitted (fit coefficients are reported in table 6.2) to a line, defined as follows

$$m = \chi_1 K + \chi_2 \tag{6.4}$$

The linear increase suggests intrinsic changes in the noise source nature (from a dipole over a non-compact to a compact surface), and might be explained by a more effective distribution of noise sources along the permeable extent for increasing K, that decreases the ratio of effective chord length to noise source extension, i.e., it promotes the compactness of the airfoil.

χ_1 $\times 10^{-9}$ (m^{-2})	χ_2 (-)	R^2
23.306±7.535	5.215±0.142	0.8575

Table 6.2: Coefficients (χ_1, χ_2) (with 95% confidence bounds) and correlation coefficient R^2 for the fit of experimental m and K data to equation 6.4.

6.2.4. EFFECT OF THE RELATIVE PERMEABLE CHORD LENGTH ON NOISE ABATEMENT

Tests are carried out to assess the effect of the permeable chordwise extent s on noise mitigation. To this aim, besides data gathered for $s/c = 0.2$ (40 mm), additional experiments are carried out for perforated inserts with l_h = 2 and 5 mm; specifically, these inserts are taped at both sides, leaving only $s/c = 0.1$ (20 mm) and $s/c = 0.05$ (10 mm) exposed to the flow. As seen in figures 6.11 (a) and (b), noise mitigation data for varying U_∞ also collapse when non-dimensionalizing the frequency as Strouhal number, yielding the curves already described in section 6.2.1. Similarly, relevant parameters such as $\mathrm{St}_c^{'}$, St_c^{*}, $\Delta\mathrm{St}^\circ$, $\Delta L_{p,\max}$ and St_c^{+} are computed fitting experimental data with a spline. For data corresponding to shorter permeable lengths, the lower-bound cross-over Strouhal number $\mathrm{St}_c^{'}$, is directly computed from measured data, i.e., no data extrapolation is required.

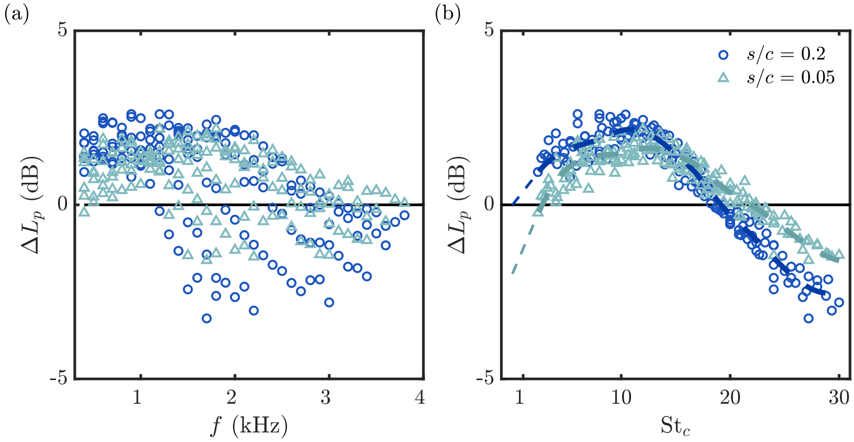

Figure 6.11: Collapse of ΔL_p with St_c for perforated inserts with l_h = 5 mm and permeable extent $s/c = 0.2$ and $s/c = 0.05$. Data are measured at U_∞ ranging from 12.5 to 34 m/s and $\alpha = 0.2$ degrees. Dashed lines represent the B-Spline fitted to experimental data. Thick dashed lines indicate interpolated data. Thin dashed lines indicate extrapolated values.

Results are shown in figures 6.12 (a) and (b), where $\mathrm{St}_c^{'}$, St_c^{*}, $\Delta L_{p,\max}$ and St_c^{+} are plotted as a function of the permeable length to chord ratio s/c for perforated inserts with l_h = 5 and 2 mm respectively. For the perforated insert with l_h = 5 mm, an overall decrease in all St-based parameters for increasing s/c is found (figures 6.12 (a)); hence, a longer permeable insert with this pore arrangement does not broaden the frequency range of noise abatement, but is beneficial to tackle lower frequencies. Data for the perforated insert with l_h = 2 mm show a decrease of $\mathrm{St}_c^{'}$ with s/c; yet, St_c^{*} has an approximately constant value of 25 for all s/c. Consequently, for this insert the noise mitigation range is extended for increasing s/c.

These findings are analysed more in detail in figure 6.13 (a), where the frequency range for noise mitigation $\Delta\mathrm{St}_c^\circ$ is plotted as a function of s/c. For the perforated insert with l_h = 5 mm, increasing s/c yields few additional benefits in $\Delta\mathrm{St}_c^\circ$; for the one with l_h

= 2 mm, a slight extension of the frequency range (from 23 at $s/c = 0.05$ to 24.5 at $s/c = 0.2$) is reported instead. This result evidences that increasing s/c is not a convenient way to achieve noise mitigation throughout a wider frequency range (to this end, increasing K is more effective), but rather to enhance abatement upon lower frequencies.

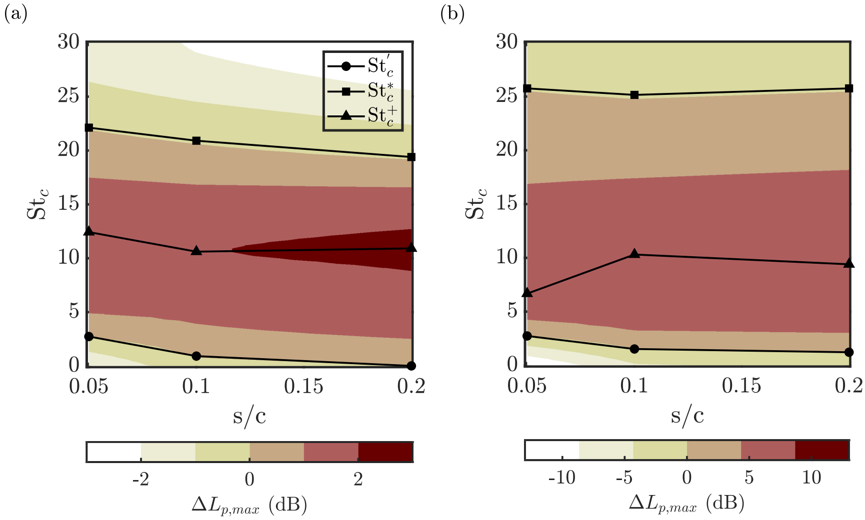

Figure 6.12: Change in maximum noise attenuation $\Delta L_{p,\max}$ with permeable chordwise length s/c and chord-based Strouhal number St$_c$ for perforated inserts with $l_h = 5$ (a) and 2 mm (b) at $\alpha = 0.2$ degrees.

Finally, maximum noise abatement $\Delta L_{p,\max}$ data are plotted in figure 6.13 (b). As in section 6.2.1, experimental data are fitted (fitting coefficients are reported in table 6.3) with

$$\Delta L_{p,\max} = \xi_1 \tanh\left(\xi_2 \frac{s}{c}\right) \tag{6.5}$$

Results show that with $s/c = 0.05$, inserts with $l_h = 2$ mm and 5 mm abate up to 1.6 and 6.7 dB respectively. Further increasing s/c yields negligible additional noise abatement (less than 1 dB). Since a longer permeable extent would decrease lift and increase drag, this value represents a good trade-off between noise mitigation and aerodynamic performance. It is interesting to note that for the $s/c = 0.05$ configuration the permeable extent approximately coincides with the boundary layer thickness at the trailing edge for the baseline configuration; whether this observation can be generalized or is merely a coincidence for the current experimental set-up will be addressed in future research.

Case	ξ_1 (dB)	ξ_2 (-)	R^2
$l_h = 5$ mm ($K = 5\times10^{-10}$ m^2)	2.117±0.964	19.834±32.040	0.945
$l_h = 2$ mm ($K = 31\times10^{-10}$ m^2)	7.553±2.513	27.923±50.391	0.869

Table 6.3: Coefficients (ξ_1, ξ_2) (with 95% confidence bounds) and correlation coefficient R^2 for the fit of experimental $\Delta L_{p,\max}$ and s/c data to equation 6.5

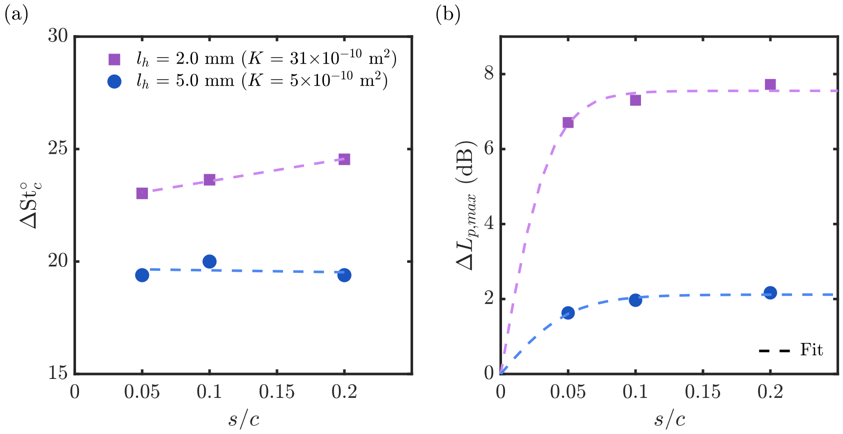

Figure 6.13: Change in the frequency range for noise mitigation $\Delta\mathrm{St}_c^\circ$ (a) and maximum noise attenuation $\Delta L_{p,\mathrm{max}}$ (b) with permeable chordwise length s/c for perforated inserts with l_h = 2 and 5 mm (α = 0.2 deg.).

It is also interesting to note that some of the features derived from decreasing the length of the permeable insert, such as the decrease in $\Delta L_{p,\mathrm{max}}$, or the increase in St_c^*, are in line with those reported in section 6.2.1 for increasing α. This might be related to the passage of steady flow through permeable media due to a pressure imbalance between pressure and suction side, illustrated, for instance, by Mößner and Radespiel [23], that decreases the effective length of the permeable extent.

6.2.5. APPEARANCE OF SHEDDING-RELATED TONES

In spite of the just reported benefits regarding broadband noise mitigation, for permeable inserts with periodic arrangement of the channels and high flow permeability, an undesired tone is measured independently of the angle of attack. Specifically, such a feature is found in far-field acoustic spectra for the most permeable perforated insert (l_h = 1.5 mm).

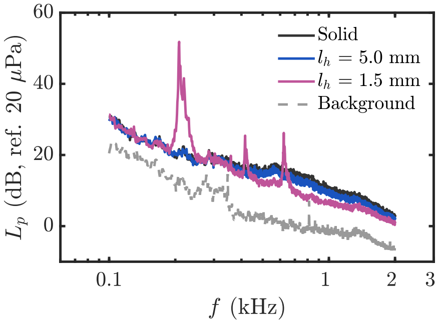

Figure 6.14: Narrow band far-field acoustic spectra for the solid and perforated inserts with l_h = 5 mm and l_h = 1.5 mm at U_∞ = 25 m/s and α = 0.2 deg.

In figure 6.14, narrow band acoustic measurements for a free-stream velocity of 25 m/s and an angle of attack of 0.2 degrees are presented, together with background noise measurements and data for the l_h = 5 mm and reference configurations. A strong (+30 dB over broadband noise levels) tonal component is measured at a frequency of 208 Hz, with harmonics at 416 and 624 Hz.

In figure 6.15 (a), narrow-band spectra for the l_h = 1.5 mm insert at U_∞ = 15, 20, 25, 30 and 35 m/s are shown. Only at U_∞ = 15 m/s no tones are observed within the measured frequency range. When f is scaled employing the thickness of the airfoil at the solid-permeable junction h = 15.7 mm and the free-stream velocity, all tones collapse (figure 6.15 (b)). The analysis yields a fundamental tone at $\mathrm{St}_{h,1}$ = 0.13, with visible harmonics up to $\mathrm{St}_{h,i}$ = 0.91. Such values are in line with those found for blunt trailing-edge noise (of $\mathrm{St}_{h,1}$ = 0.2; see figures 6.15 (c) and (d)), in which a similar peak arises due to shedding from the blunt trailing edge [22].

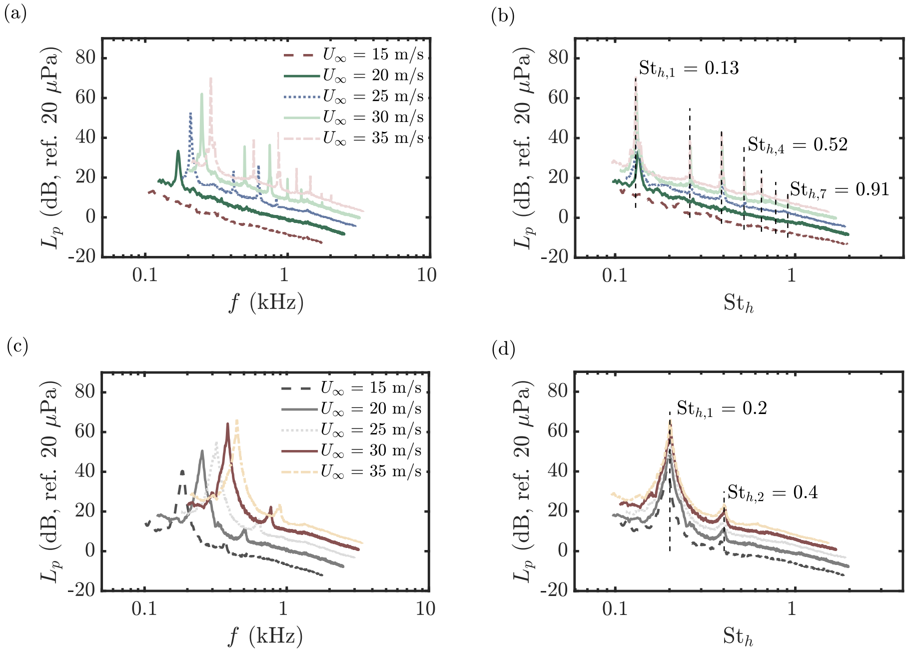

Figure 6.15: Collapse of tonal noise with St_h for the perforated insert with l_h = 1.5 mm (a, b) and the airfoil with blunt trailing edge at 80% of the chord (c, d). Data measured at free-stream velocities ranging from 15 to 35 m/s and α = 0.2 deg. (a, c) Far-field acoustic spectra as a function of f. (b, d) Far-field acoustic spectra as a function of St_h.

The nature of this tone seems therefore to be related to the appearance of periodic flow phenomena, i.e. vortex shedding at the wake of the perforated mock-up, due to the high permeability and periodic pore arrangement of the insert. It is interesting to note that the metal foam with d_c = 1200 μm and the perforated insert with l_h = 1.5 mm have comparable flow permeability ($K \simeq 6\times10^{-9}$ m^2); yet, tones are solely reported for the latter insert. The introduction of a certain degree of randomness in the pore distribution prevents the appearance of strong tones. The change in fundamental frequency between fully blunt and perforated edges, as well as the absence of tones for inserts with lower permeability and/or random pore distribution suggest that the vortex organization and periodicity are highly sensitive to the characteristics of the permeable trailing edge. This point is further addressed below with the analysis of instantaneous PIV data.

Instantaneous PIV realizations for the blunt model and the perforated insert with l_h = 1.5 mm are respectively plotted in figures 6.16 (a) and (b). Contours of the out-of-plane vorticity $\omega c/U_\infty$ are shown together with the instantaneous velocity field. The vortex identification method described in Graftieaux *et al.* [24], based on the separation of large swirling motions and small-scale turbulence via Proper Orthogonal Decomposition (POD), is applied, and the center of the shed vortices are marked with red crosses.

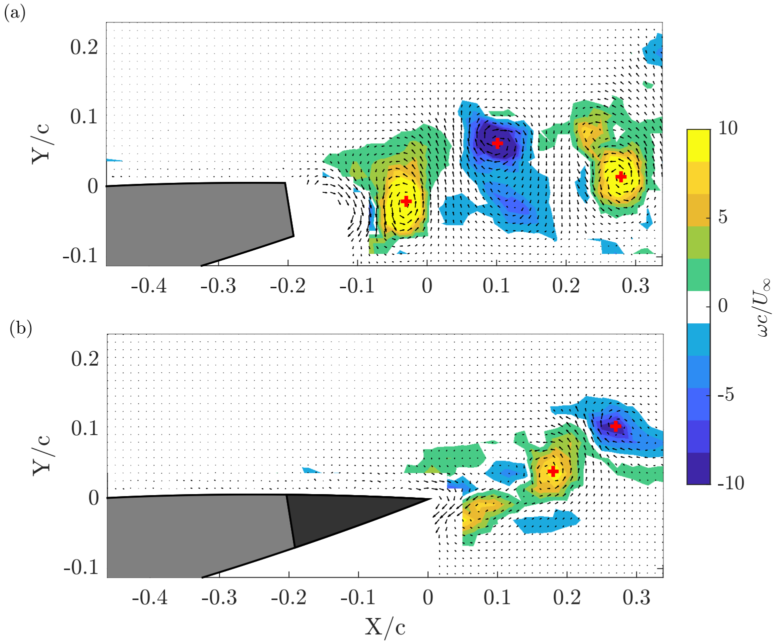

Figure 6.16: Instantaneous velocity field for the model with blunt trailing edge at 80% of the chord (a) and perforated insert with l_h = 1.5 mm (b). The velocity vector field is shown together with background vorticity $\omega c U_\infty$ isocontours. The center of the large scale vortices present at the wake of the model are marked with red crosses. The aluminium body of the airfoil and the permeable insert are indicated as light and dark gray regions respectively. Data measured at a free-stream velocity of 55 m/s.

For the blunt edge (figure 6.16 (a)), the boundary layers at suction and pressure sides of the airfoil separate at the trailing edge and produce pairs of counter-rotating vortices that travel further downstream, forming a Von Kármán vortex street [25, 26]. Similarly, large-scale swirling motions are also present in the wake of the model equipped with the perforated insert (figure 6.16 (b)); the shedding-nature of the tone is therefore confirmed. Yet, the presence of the permeable mock-up alters the topology of the vortices, i.e., the separation between vortices decreases, and these are weaker than for the blunt case. For fully solid blunt trailing edges such changes in the hydrodynamic field usually entail quieter and higher-frequency tones [27, 28]. However, the frequency of the acoustic peak reported for the perforated insert is actually lower, and from 25 m/s on the fundamental peaks for both perforated and blunt edges are of similar magnitude. Such inconsistencies with theory for vortex-shedding trailing-edge noise suggest that, as for broadband noise scattering, the presence of a permeable surface alters the process of noise generation. To further investigate this aspect, the preliminary analysis reported here will be extended in future research.

6.3. CONCLUSIONS

In this chapter, acoustic measurements on a NACA 0018 airfoil (with chord $c = 0.2$ m) equipped with solid and permeable trailing-edge inserts are performed. To obtain criteria for maximizing noise abatement while limiting changes in aerodynamic performance, trailing edges with straight open channels that link suction and pressure sides are manufactured. For comparison, trailing-edge inserts manufactured with open-cell metal foams, with comparable flow permeability but random pore distribution, are also analysed.

Far-field noise spectra reveal the collapse of ΔL_p, defined as the difference between noise scattering from solid and permeable edges, when nondimensionalizing frequency with chord and free-stream velocity. Collapsed data produce sine-like ΔL_p curves that define the acoustic benefits of each trailing edge independently of flow speed. From this analysis, it stems that the change in maximum noise mitigation $\Delta L_{p,\max}$ with permeability K can be accurately described with a hyperbolic tangent ($\Delta L_{p,\max} = \gamma_1 \tanh\left(\gamma_2 K\right)$, where γ_1 and γ_2 are fitting coefficients), i.e. significant noise mitigation can be achieved with moderate K, but it saturates above certain K thresholds, that depend on the type of edge employed. Specifically, permeability thresholds of 3.5×10^{-9} and 1×10^{-9} m^2 are respectively obtained for perforated and metal foam inserts. The employment of edges with permeability equal to these thresholds is therefore recommended to minimize aerodynamic penalty due to the use of permeable materials in lifting devices, to maximize the frequency range for noise mitigation, and to prevent an excessive downgrade of the acoustic benefits when increasing the angle of attack. Furthermore, the tortuosity of the trailing edge is proposed to account for differences in noise mitigation reported for edges with similar permeability but different pore arrangement. This study also stresses that increasing the chordwise extent of the permeable region s beyond $s/c = 0.05$ does not extend the frequency range for noise mitigation, nor increases its magnitude significantly. Finally, it is also confirmed that inserts with high permeability and an ordered pore arrangement produce extremely loud tones, which are caused by vortex-shedding.

Taken together, these findings suggest that a permeable trailing edge insert with permeability equal to 1×10^{-9} m^2, with a tortuosity of 1.15 (which is in turn beneficial to avoid tones) and with $s/c = 0.05$ yields the best trade-off between broadband noise mitigation and aerodynamic loss. Future work will address optimal trailing-edge properties for more realistic conditions, i.e., cambered airfoils with longer chord, as well as the definition of the micro-structural and fluid features necessary to prevent shedding from permeable edges.

REFERENCES

[1] A. Rubio Carpio, F. Avallone, D. Ragni, M. Snellen, and S. van der Zwaag, *Quantitative criteria to design optimal permeable trailing edges for noise abatement,* Journal of Sound and Vibration **485**, 115596 (2020).

[2] A. Rubio Carpio, R. Merino Martínez, F. Avallone, D. Ragni, M. Snellen, and S. van der Zwaag, *Experimental characterization of the turbulent boundary layer over a porous trailing edge for noise abatement,* Journal of Sound and Vibration **443**, 537 (2019).

[3] T. F. Geyer and E. Sarradj, *Self Noise Reduction and Aerodynamics of Airfoils With Porous Trailing Edges,* Acoustics **1**, 393 (2019).

[4] T. Geyer, E. Sarradj, and C. Fritzsche, *Porous airfoils: noise reduction and boundary layer effects,* International Journal of Aeroacoustics **9**, 787 (2010).

[5] T. Geyer, E. Sarradj, and C. Fritzsche, *Measurement of the noise generation at the trailing edge of porous airfoils,* Experiments in Fluids **48**, 291 (2010).

[6] M. Herr and J. Reichenberger, *In Search of Airworthy Trailing-Edge Noise Reduction Means,* in *17th AIAA/CEAS Aeroacoustics Conference*, June (2011) pp. 1–25.

[7] M. Herr, K. S. Rossignol, J. Delfs, N. Lippitz, and M. Moßner, *Specification of Porous Materials for Low-Noise Trailing-Edge Applications,* in *20th AIAA/CEAS Aeroacoustics Conference* (2014) pp. 1–19.

[8] S. A. S. Ali, M. Azarpeyvand, and C. R. I. Da Silva, *Trailing-edge flow and noise control using porous treatments,* Journal of Fluid Mechanics **850**, 83 (2018).

[9] A. Rubio Carpio, F. Avallone, D. Ragni, M. Snellen, and S. van der Zwaag, *Mechanisms of broadband noise generation on metal foam edges,* Physics of Fluids **31** (2019), 10.1063/1.5121248.

[10] K. S. Rossignol, A. Suryadi, M. Herr, J. Schmidt, and J. Tychsen, *Experimental investigation of porous materials for trailing-edge noise reduction,* International Journal of Aeroacoustics **19**, 365 (2020).

[11] I. Gibson, D. Rosen, and B. Stucker, *Additive Manufacturing Technologies* (Springer New York, New York, NY, 2015).

[12] C. Jiang, D. Moreau, Y. Yauwenas, J. R. Fischer, C. J. Doolan, J. Gao, W. Jiang, R. McKay, and M. Kingan, *Control of rotor trailing edge noise using porous additively manufactured blades,* in *2018 AIAA/CEAS Aeroacoustics Conference* (2018) pp. 1–24.

[13] E. Sarradj and T. Geyer, *Symbolic regression modeling of noise generation at porous airfoils,* Journal of Sound and Vibration **333**, 3189 (2014).

[14] C. de Boor, *A Practical Guide to Splines.*, Vol. 27 (Springer-Verlag New York, 1978) p. 348.

[15] B. A. Barsky and T. D. DeRose, *Geometric continuity of parametric curves: three equivalent characterizations,* IEEE Computer Graphics and Applications **9**, 60 (1989).

[16] M. Aldheeb, W. Asrar, E. Sulaeman, and A. A. Omar, *Aerodynamics of porous airfoils and wings,* Acta Mechanica **229**, 3915 (2018).

[17] H. Gao, Y. H. He, J. Zou, N. P. Xu, and C. T. Liu, *Tortuosity factor for porous FeAl intermetallics fabricated by reactive synthesis,* Transactions of Nonferrous Metals Society of China **22**, 2179 (2012).

[18] S. Pardo-Alonso, J. Vicente, E. Solórzano, M. A. Rodriguez-Perez, and D. Lehmhus, *Geometrical Tortuosity 3D Calculations in Infiltrated Aluminium Cellular Materials,* Procedia Materials Science **4**, 145 (2014).

[19] B. Moore, *Hearing* (Elsevier Science, 1995).

[20] J. E. Ffowcs-Williams and L. H. Hall, *Aerodynamic sound generation by turbulent flow in the vicinity of a scattering half plane,* Journal of Fluid Mechanics **40**, 657 (1970).

[21] M. S. Howe, *Aerodynamic noise of a serrated trailing edge,* Journal of Fluids and Structures **5**, 33 (1991).

[22] T. F. Brooks, D. S. Pope, and M. A. Marcolini, *NASA Reference Publication*, Tech. Rep. (NASA Langley Research Center, 1989).

[23] M. Mößner and R. Radespiel, *Flow simulations over porous media – Comparisons with experiments,* Computers and Fluids **154**, 358 (2017).

[24] L. Graftieaux, M. Michard, and G. Nathalie, *Combining PIV, POD and vortex identification algorithms for the study of unsteady turbulent swirling flows,* Measurement Science and Technology **12**, 1422 (2001).

[25] J. F. Nash, *A Review of Research on Two-Dimensional Base Flow,* Aeronautical Research Council Reports and Memoranda **3323**, 1 (1963).

[26] D. Krentel and W. Nitsche, *Investigation of the near and far wake of a bluff airfoil model with trailing edge modifications using time-resolved particle image velocimetry,* Experiments in Fluids **54** (2013).

[27] D. W. Shannon, S. C. Morris, and T. J. Mueller, *Radiated sound and turbulent motions in a blunt trailing edge flow field,* International Journal of Heat and Fluid Flow **27**, 730 (2006).

[28] S. Pröbsting, M. Zamponi, S. Ronconi, Y. Guan, S. C. Morris, and F. Scarano, *Vortex shedding noise from a beveled trailing edge,* International Journal of Aeroacoustics **15**, 712 (2016).

7

INSERTS WITH TAILORED PERMEABILITY GRADIENTS FOR NOISE MITIGATION

"The whole is greater than the sum of its parts.”

Aristotle (384–322 BC)

This chapter presents a methodology to create trailing edges with tailored permeability gradients. The permeability of the trailing edges is varied by changing the hole spacing along the streamwise direction, while the hole size is constant. The methodology is applied to two different airfoil models, namely a NACA 0018 and a NACA 63018, and the acoustic scattering at trailing edges with different types of gradients is analysed. For the sets of inserts tested in the NACA 0018 model, it is found that the magnitude of the noise abatement within the lower frequency range can be incremented with inserts with higher permeability at the solid-permeable interface. The graded insert employed in the NACA 63018 airfoil produces higher broadband noise mitigation than its homogeneous counterpart. All the graded variants suppress the strong acoustic tones present for their fully homogeneous counterparts. It is also observed that non-uniform inserts might prevent from the downgrade of the acoustic performance with increasing angles of attack previously reported for fully homogeneous inserts.

Parts of this chapter have been submitted to the Aerospace Science and Technology journal

7.1. INTRODUCTION

In Chapter 5, it was shown that the employment of permeable trailing-edge inserts distributes the acoustic impedance jump along the entire permeable surface, creating additional noise sources with decreased radiation efficiency. For highly permeable inserts, the solid-permeable junction is the region with the largest impedance discontinuity, hence it becomes the most significant contributor to the overall far-field noise, exceeding the emission at the actual trailing edge. Such a result suggests that the noise attenuation performance of this noise control strategy could be further improved with trailing-edge inserts containing a streamwise permeability gradient.

Graded trailing-edge inserts might therefore minimize strong, coherent scattering regions. This hypothesis is supported by the numerical study of Schulze and Sesterhenn [1], that concludes that a permeable edge optimized for noise mitigation should contain a wide range of permeabilities, ranging from fully solid at the solid-permeable interface to fully permeable at the actual edge. More recent optimization studies [2, 3] also point out that in order to maximize trailing-edge noise mitigation, trailing edges that continuously increase their permeability along the chord are beneficial. In this context, the numerical investigation reported in Rossian *et al.* [4] shows that a NACA 0012 with a trailing edge with linearly increasing permeability minimizes noise scattering at both the solid-permeable interface and the edge.

Furthermore, the application of permeable materials within a lifting surface causes a reduction of the aerodynamic performance, i.e. a loss in lift and an increase in drag [5, 6]; besides a greater noise mitigation performance, graded variants might alleviate these significant drawbacks by confining regions of higher permeability to the very aft end of the airfoil.

Given the great potential of this type of solutions, experimental efforts to demonstrate the concept have been recently pursued. Rossignol *et al.* [7] describe the acoustic scattering of a DLR F16 airfoil equipped with graded trailing-edge inserts manufactured by cold rolling of homogeneous metal foams [8]. Inserts with two gradient slopes are obtained by applying different compression rates to a baseline metal foam block. However, as pointed out by the authors, due to the manufacturing process the flow permeability of graded samples cannot be accurately quantified, preventing from comparison with subsequent research. In comparison with fully homogeneous permeable inserts, graded materials yield additional noise mitigation at very low frequencies (below 1.25 kHz, i.e. $\mathrm{St}_c = 7.5$) and above 2 kHz ($\mathrm{St}_c = 12$). Within these frequency bounds, homogeneous inserts perform better. Yet, the comparison of the acoustic scattering of inserts with different gradient slopes does not yield any evident relationship between gradient and noise mitigation performance.

This chapter describes research to create and test perforated trailing-edge inserts with tailored permeability distributions. The methodology is applied to manufacture ten different graded inserts. Additionally, four homogeneous inserts are manufactured and employed as reference. The effect of aspects such as type of gradient or the magnitude permeability jump on the noise abatement performance are investigated. Extensive experimental data are obtained at chord-based Reynolds numbers ranging between 2×10^5 and 4.7×10^5 and geometrical angles of attack ranging between of 0 and 12 degrees.

The current chapter is organized as follows. First, the algorithm and the trailing-edge inserts are described in section 7.2. Then, far-field noise results are discussed in section 7.3. Finally, a summary of the main findings is presented in section 7.4.

7.2. TRAILING-EDGE INSERTS WITH STREAMWISE PERMEABILITY GRADIENTS

Graded trailing-edge inserts for the two airfoil models described in Chapter 3, i.e. NACA 0018 and NACA 63018, are manufactured. All trailing-edge inserts have a total permeable extension of s = 40 mm ($s/c = 0.2$) independently of the airfoil. As in Chapter 6, flow communication between both sides of the airfoil is allowed with cylindrical channels normal to the chord. The hole size is fixed, and customized gradients are obtained by varying the hole density along the chord. The trailing-edge inserts are created using additive manufacturing. This process has three fundamental advantages against grading materials with randomly distributed pores, e.g., metal foams: (i) it allows to impose permeability gradients in a fully controlled manner; (ii) it minimizes repeatability issues derived from changes in the manufacturing process; (iii) lower cost and shorter manufacturing periods.

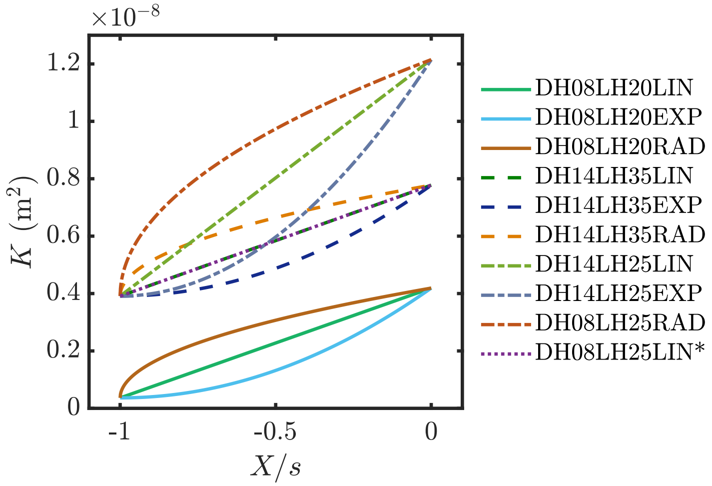

Figure 7.1: Imposed permeability distributions along the chord of the flow permeable trailing-edge inserts. Sample code with "*" refers to NACA 63018, others to NACA 0018.

In order to minimize the discontinuity at the junction, graded inserts have lower permeability at the solid-permeable interface (hereon referred to as the "root" of the insert) and monotonically increase their permeability towards the actual trailing edge (i.e. the "tip" of the insert). In other words, the streamwise permeability gradient is always positive along the streamwise direction ($dK/dX > 0$). The change in permeability along the chord is described by the following functions:

$$K_{\text{lin}} = K_{\text{root}} + (K_{\text{tip}} - K_{\text{root}})(X/s), \tag{7.1a}$$

$$K_{\text{exp}} = K_{\text{root}} + (K_{\text{tip}} - K_{\text{root}})(X/s)^2, \tag{7.1b}$$

$$K_{\text{rad}} = K_{\text{root}} + (K_{\text{tip}} - K_{\text{root}})(X/s)^{\frac{1}{2}} \tag{7.1c}$$

where $K_{\text{root}} = K(X/s = -1)$ and $K_{\text{tip}} = K(X/s = 0)$ refer to the permeability at the root and the tip of the inserts respectively. The distributions defined in equations 7.1 (a), (b) and (c) impose a linear, exponential and radical growth of the permeability with X, hence they are denoted as "linear", "exponential" and "radical".

A total of 10 graded trailing-edge inserts are manufactured. Three different subsets of inserts are created for the NACA 0018 airfoil: each one imposes all three linear, radical and exponential permeability growths with different values of K_{root} and K_{tip}. Hence, there are 9 graded inserts for this model. Only one linearly graded insert with the same permeability distribution as one of the NACA 0018 inserts was made for the NACA 63018 airfoil (dotted line in figure 7.1). The first subset (solid lines in figure 7.1) has a fixed hole size of d_h = 0.8 mm, similarly to the homogeneous counterparts described in the previous chapter. The permeability bounds, detailed in table 7.1 for all the inserts, are determined from manufacturing constraints, i.e., the minimum allowable wall thickness is equal to 0.4 mm. The second subset (dashed lines in figure 7.1) has a constant hole diameter of d_h = 1.4 mm, and the magnitude of the permeability change across the insert is similar to the previous one, but the inserts are generally more permeable. Hence, this subset creates a larger discontinuity at the solid-permeable interface and a milder one at the tip. The last subset (dash-dotted lines in figure 7.1) has also a hole diameter of d_h = 1.4 mm, and poses the lowest impedance jump between trailing edge and air.

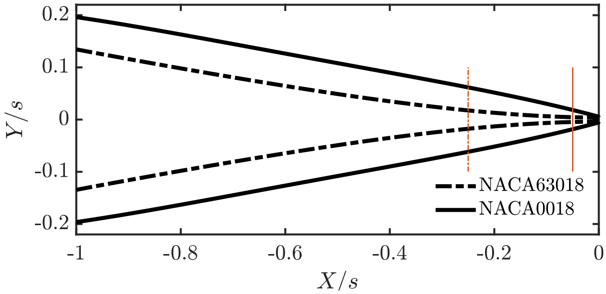

Figure 7.2: Contours of the permeable inserts manufactured for the NACA 63018 (dash-dotted line) and NACA 0018 (solid line) models. The vertical lines indicate the downstream bound for the validity of equations 3.7 (a) and (b), i.e. the positions where the thickness of the inserts is equal to the largest hole diameter (d_h/s = 0.04) employed in the present investigation.

The graded inserts are hereafter labelled as "DHnnLHnnlll", where "n" is a digit and "l" is a letter. The two digits behind "DH" specify the hole size (e.g. a hole size of 1.4 mm is labelled as DH14), and the last two digits refer to the hole spacing at the tip (e.g. an insert with hole spacing at the tip of 2.5 mm is labelled as LH25). The last three letters specify the type of permeability distribution (e.g. "LIN" for linear, "RAD" for radical and "EXP" for exponential). The homogeneous inserts are in turn labelled as "DHnnL-HnnHOM".

The above-described permeability distributions are translated into varying hole densities employing the empirical relations 3.7 (a) and (b), that relate the permeability of a perforated plate to its geometry. The original fitting coefficients proposed by Bae and Kim [9] are employed. These equations are derived on the basis of data obtained for samples with thicknesses of up to one hole diameter. For the largest hole size employed in this investigation ($d_h = 1.4$ mm) they hold up to 75% of the NACA 63018 inserts, and up to 95% of the NACA 0018 inserts (figure 7.2).

Discrete hole spacings are computed as follows: the initial hole spacing $l_{h,1} = l_h(X_1/s)$ is located at $X_1/s = -0.99$ for the set with $d_h = 0.8$ mm and $l_{h,1} = l_h(X_1/s = -0.97)$ for those with $d_h = 1.4$ mm; these spacings allow to maintain the minimum wall thickness at 0.4 mm at the solid-permeable junction. Holes are then consecutively allocated at $X_{i+1}/s = X_i/s + l_{h,i}/s$ with $l_{h,i+1} = l_h(X_{i+1}/s)$, and spanwisely distributed employing the resulting hole separation computed at each streamwise position.

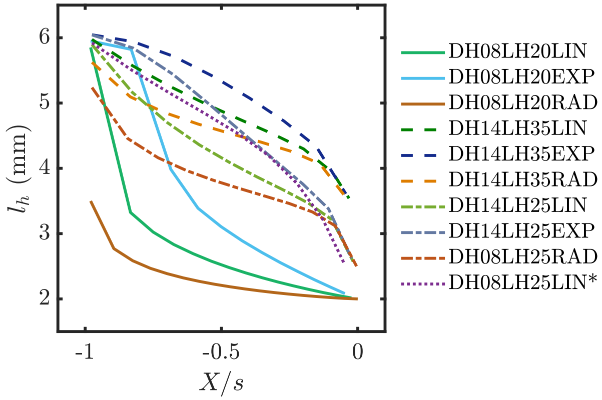

Figure 7.3: Imposed hole spacing distributions along the chord of the flow permeable trailing-edge inserts. Sample code with "*" refers to NACA 63018, others to NACA 0018.

The resulting hole spacing distributions are plotted in figure 7.3, and the values at the root and the tip can be found in table 7.1. The subset with $d_h = 0.8$ mm (solid lines) has a hole spacing at the tip $l_{h,\text{tip}}$ of approximately 2 mm independently of the type of permeability distribution (i.e. linear, exponential or radical). The second subset (with $d_h = 1.4$ mm; dash-dotted lines) has a $l_{h,\text{tip}}$ of 3.5 mm. The NACA 63018 insert with the same linear permeability variation has the same $l_{h,\text{root}}$ but a smaller $l_{h,\text{tip}}$ (equal to 2.5 mm). This variation is due to the fact that the NACA 63018 airfoil insert is thinner; hence, a higher hole density is necessary to achieve the same permeability. Finally, the third subset ($d_h = 1.4$ mm; dashed lines) has a $l_{h,\text{tip}}$ of 2.5 mm. For comparison, four trailing-edge inserts with constant hole spacing are also manufactured. These have the same hole diameter, and the hole spacing at the tip of each subset is applied homogeneously within the entire permeable extension.

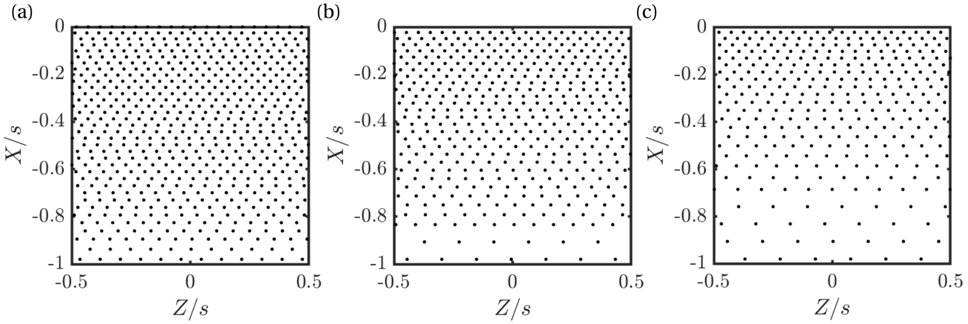

Figure 7.4: Hole patterns for radical (a), linear (b) and exponential (c) permeability gradients. The hole patterns correspond to the inserts with hole diameter of 0.8 mm and hole spacing at the tip of 2 mm.

The hole distribution around the midspan of the DH08LH6020LIN, DH08LH6020EXP and DH08LH6020RAD inserts are respectively plotted in figures 7.4 (a), (b) and (c). It can be observed that in order to impose a linear permeability growth, the hole density increases gradually towards the tip. The insert with exponential permeability distribution has a lower hole density up to approximately 50% of the permeable extension, and at this point the hole density increases rapidly. The radical distribution has a lower density exclusively close to the root, with smaller hole spacing throughout most of the insert. CAD depictions of these inserts are shown in figures 7.5 (a-c) for exponential, linear and radical permeability distributions. For comparison, the variants with d_h = 1.4 mm and $l_{h,\mathrm{tip}}$ = 2.5 mm are plotted in figures 7.5 (d-f)

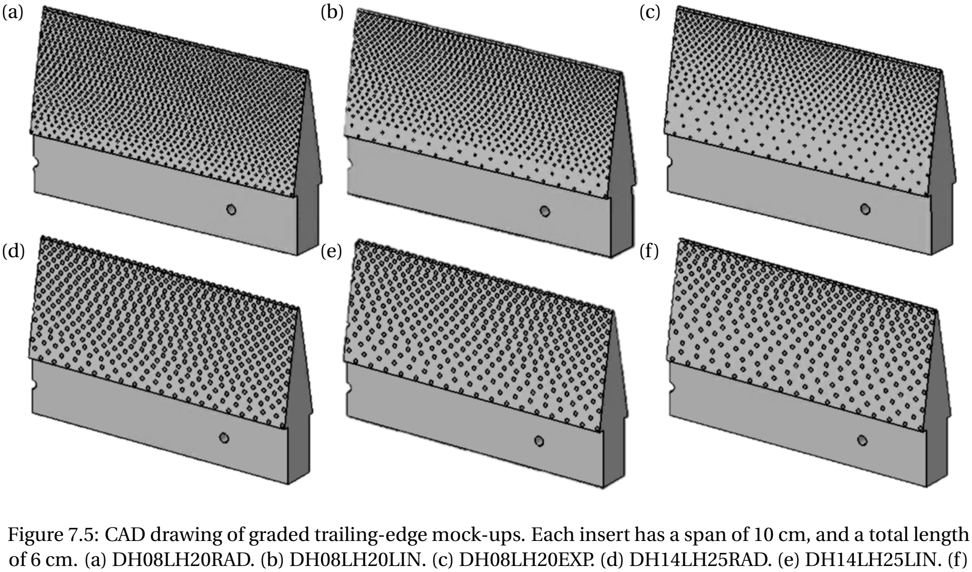

Figure 7.5: CAD drawing of graded trailing-edge mock-ups. Each insert has a span of 10 cm, and a total length of 6 cm. (a) DH08LH20RAD. (b) DH08LH20LIN. (c) DH08LH20EXP. (d) DH14LH25RAD. (e) DH14LH25LIN. (f) DH14LH25EXP.

The average permeability of the insert, computed as

$$K_{\mathbf{avg}} = \left| \frac{1}{s} \int_{-s}^{0} K \, dX \right| \tag{7.2}$$

is also included in table 7.1 for completeness. This quantity gives a sense of the overall permeability of the insert. As could be inferred from figure 7.1, within each subset the most permeable insert is the one with radical permeability growth, while the exponential variant is the least permeable one.

Nomenclature	Model	Type	d_h (mm)	$l_{h,\mathrm{root}}$ (mm)	$l_{h,\mathrm{tip}}$ (mm)	K_{root} (m^2)	K_{tip} (m^2)	K_{avg} (m^2)
DH08LH20HOM	NACA0018	Hom.	0.8	2	2	42×10^{-10}	40×10^{-10}	41×10^{-10}
DH08LH20LIN	NACA0018	Linear	0.8	5.9	2	4×10^{-10}	40×10^{-10}	23×10^{-10}
DH08LH20EXP	NACA0018	Exp.	0.8	6	2	4×10^{-10}	40×10^{-10}	21×10^{-10}
DH08LH20RAD	NACA0018	Radical	0.8	3.5	2	13×10^{-10}	40×10^{-10}	26×10^{-10}
DH14LH35HOM	NACA0018	Hom.	1.4	3.5	3.5	117×10^{-10}	78×10^{-10}	109×10^{-10}
DH14LH35LIN	NACA0018	Linear	1.4	6	3.5	39×10^{-10}	78×10^{-10}	58×10^{-10}
DH14LH35EXP	NACA0018	Exp.	1.4	6	3.5	39×10^{-10}	78×10^{-10}	52×10^{-10}
DH14LH35RAD	NACA0018	Radical	1.4	5.6	3.5	46×10^{-10}	78×10^{-10}	65×10^{-10}
DH14LH25HOM	NACA63018	Hom.	1.4	2.5	2.5	225×10^{-10}	78×10^{-10}	186×10^{-10}
DH14LH25LIN	NACA63018	Linear	1.4	5.9	2.5	40×10^{-10}	78×10^{-10}	58×10^{-10}
DH14LH25HOM	NACA0018	Hom.	1.4	2.5	2.5	229×10^{-10}	121×10^{-10}	214×10^{-10}
DH14LH25LIN	NACA0018	Linear	1.4	5.9	2.5	41×10^{-10}	121×10^{-10}	80×10^{-10}
DH14LH25EXP	NACA0018	Exp.	1.4	6	2.5	39×10^{-10}	121×10^{-10}	67×10^{-10}
DH14LH25RAD	NACA0018	Radical	1.4	5.2	2.5	53×10^{-10}	121×10^{-10}	94×10^{-10}

Table 7.1: Properties of the trailing-edge inserts.

7.3. RESULTS

7.3.1. INFLUENCE OF THE PERMEABILITY GRADIENT ON NOISE SCATTERING

Acoustic spectra are analysed in the following. Results are presented in terms of Sound Pressure Level L_p as a function of the Strouhal number based on the chord St_c. Absolute values for the least permeable set DH08LH20 are shown in figure 7.6 (a), and relative values with respect to the solid case are plotted in 7.6 (b). Data are obtained with the NACA 0018 model at no incidence and $U_\infty = 30$ m/s. For the sake of clarity, figure 7.1 is included in the bottom left corner of the absolute spectra, and the permeability distribution corresponding to the set of graded inserts is highlighted.

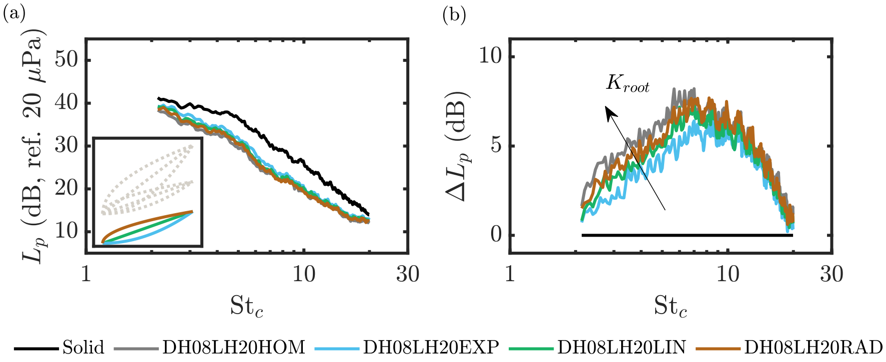

Figure 7.6: Acoustic spectra measured for the set of permeable inserts with hole diameter $d_h = 0.8$ mm and hole spacing at the tip $l_{h,\mathrm{tip}} = 2$ mm. Data measured at a free-stream velocity of 30 m/s with the NACA 0018 model at no incidence. (a) Absolute spectra. The permeability distribution of the graded inserts is highlighted in the left bottom corner plot. (b) Relative spectra with respect to the baseline case.

Results show that, independently of the type of permeability distribution, all the inserts abate noise with respect the solid configuration within the entire measured frequency range. Moreover, no tonal noise is observed for this set. Above a $\mathrm{St}_c = 10$, all inserts yield similar noise attenuation levels, while below this value the magnitude of the noise mitigation depends on the permeability at the root of the insert, with higher abatement levels found for variants with higher K_{root}. Although the differences in ΔL_p between permeable inserts are small, these are more evident at lower frequencies. At the frequency of maximum noise abatement ($\mathrm{St}_c = 7$) the homogeneous insert mitigates up to 2 dB more than the DH08LH20EXP variant (i.e. the one with the lowest K_{root}), while at a $\mathrm{St}_c = 3$ the difference amounts to 3 dB. This result is in line with data analysed in Chapter 6 for inserts with varying permeable extension s, where it was found that longer permeable mock-ups abated noise within a lower frequency range. Therefore, the extension of the permeable insert seems to affect the range of frequencies for noise abatement, while K_{root} controls the magnitude within lower frequencies. This result suggests that a specific degree of noise mitigation can be accomplished within a target frequency range with tailored permeability distributions.

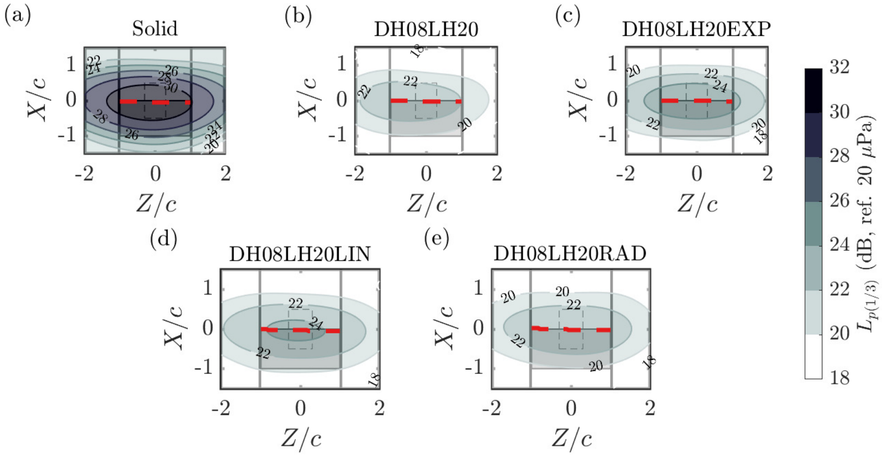

Figure 7.7: Source maps for f = 1000 Hz (St_c = 7) for the NACA 0018 trailing-edge inserts with l_h = 0.8 mm and $l_{h,\mathrm{tip}}$ = 2 mm. (a) Solid. (b) DH08LH20HOM. (c) DH08LH20EXP. (d) DH08LH20LIN. (e) DH08LH20RAD. The airfoil is represented as a gray rectangle. Dashed area represents the region where the source power integration technique is applied. Red dashed-dotted line marks streamwise L_p maxima within $-1 < Z/c < 1$.

For the present set of trailing-edge inserts, the graded variants do not produce any additional advantage in terms of noise attenuation with respect to the fully homogeneous one. Furthermore, acoustic source maps at the dimensionless frequency of maximum noise mitigation ($\mathrm{St}_c = 7$), plotted in figures 7.7 (a-e), show that the maximum noise emission for the permeable inserts is aligned with the trailing edge, similarly to the fully solid case. Hence, the radiation efficiency of the main scattering location seems to be mainly influenced by the permeability at the tip, which is similar for all the permeable variants. In this context, the small differences between homogeneous and graded inserts might be provoked by the interaction between noise sources distributed along the insert, as detailed in Teruna *et al.* [10]. To support this, the mitigation of the impedance jump at the root, hence the presence of strong scattering at this location, deteriorates the overall acoustic performance of the insert. These results underscore the relevance of the employed permeability distribution. These effects are further studied in the following with the analysis of results for the other sets of graded inserts.

Results for all DH14LH35 trailing-edge inserts, that have higher permeability than the DH08LH20 set but an equal difference in root and tip permeability, are presented in figures 7.8 (a) and (b), where absolute and relative spectra are respectively plotted. As for the previous data, these are measured at 30 m/s and with the model at no incidence. For comparison, figure 7.1 is also included in the bottom left corner of the absolute spectra. With respect to the previous ensemble, these mock-ups impose a higher acoustic impedance jump at the root of the insert, and a milder one at the tip. Moreover, in spite of being generally more permeable (i.e. the K_{avg} is higher), the overall permeability change across the inserts is exactly of the same magnitude as in the previous set.

Acoustic data for this set also show similar maximum broadband noise attenuation levels independently of the type of grading, with slight differences being found within the

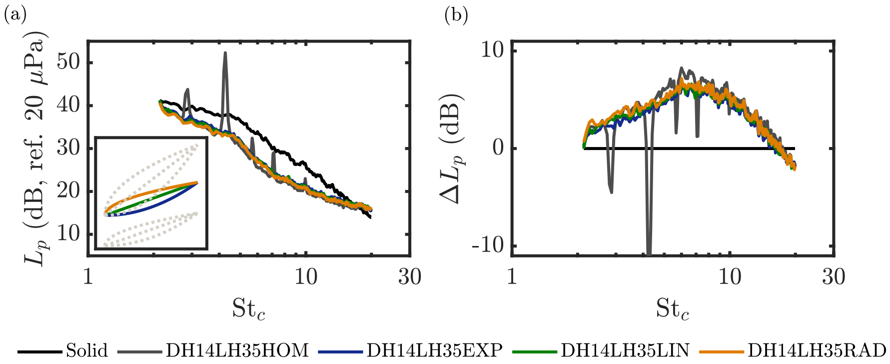

Figure 7.8: Acoustic spectra at a free-stream velocity of 30 m/s with the NACA 0018 model at no incidence. Set of permeable inserts with hole diameter d_h = 1.4 mm and hole spacing at the tip $l_{h,\text{tip}}$ = 3.5 mm. (a) Absolute levels. The permeability distribution of the graded inserts is highlighted in the left bottom corner plot. (b) Relative spectra with respect to the solid case.

very low frequency range (below St$_c$ = 4). As in the previous case, the noise mitigation for the insert with the highest K_{avg} (radical distribution) is only 1 dB higher than the one with the lowest one (exponential distribution). Similarly, this result suggests that in spite of the higher permeability jump at the root of the insert, the main noise emission region is still nearby the actual trailing edge, hence noise abatement levels are mainly determined by K_{tip}. Although not shown here for the sake of conciseness, source maps for this set confirm this point.

In this configuration, the homogeneous insert provokes strong peaks with fundamental frequency of St$_c$ = 1.42[1]. Contrarily, there are no tones in the spectra of the graded inserts. Hence, regardless of the limited benefits in terms of broadband noise mitigation, all the graded inserts have a greater overall performance as they minimize the presence of loud tones. As these tones are generated by the material itself, graded inserts represent a self-solution for large permeability treatments.

The employment of graded variants thus prevents the appearance of the large vortical structures described in Chapter 6. This feature might be contributed by the fact that homogeneous inserts are highly permeable at the solid-permeable interface, where the ratio of blunt-edge thickness to displacement thickness h/δ_* is high, while graded variants restrict the highly permeable region to the very aft end. Another advantage might stem from the design strategy adopted in the current investigation, i.e. inserts with varying permeability introduce a certain degree of misalignment between consecutive holes distributed streamwisely. In the previous chapter it was shown that materials with a random pore distribution require a much higher permeability to trigger vortex-shedding. Hence, the disordered hole allocation employed in the graded inserts might also contribute to minimize shedding.

---

[1] As for the tonal analysis presented in Chapter 6, the fundamental frequency is of low-frequency nature, and it falls outside of the measured frequency range. In this case, only the second to seventh harmonics are present in the measured spectra.

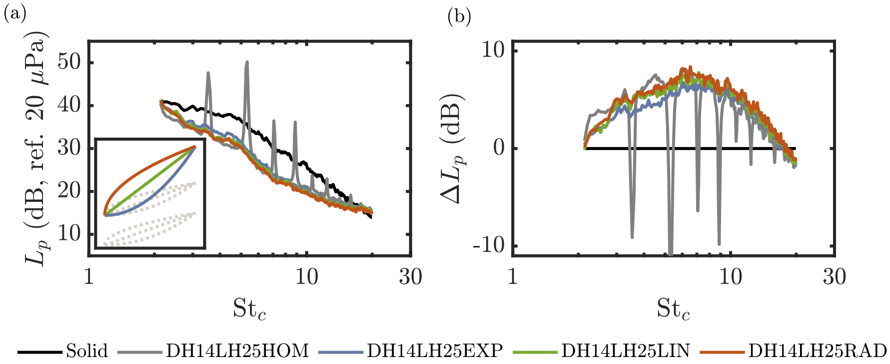

Figure 7.9: Acoustic spectra at a free-stream velocity of 30 m/s with the NACA 0018 model at no incidence. Set of permeable inserts with hole diameter d_h = 1.4 mm and hole spacing at the tip $l_{h,\text{tip}}$ = 2.5 mm. (a) Absolute levels. The permeability distribution of the graded inserts is highlighted in the left bottom corner plot. (b) Relative spectra with respect to the solid case.

Similar features are found in the acoustic spectra of the last subset of inserts manufactured for the NACA 0018 model (DH14LH25), that have the highest permeability at the tip (figures 7.9 (a) and (b)). As in the previous case, graded inserts do not yield additional broadband noise mitigation with respect to the homogeneous counterpart, but prevent the appearance of loud tones within the measured acoustic spectra. These are present only for the homogeneous insert at a fundamental dimensionless frequency of St$_c$ = 1.77. In spite of the steeper growth of permeability across these variants, the location of noise emission is still aligned with the actual trailing edge, i.e. the acoustic impedance jump upstream the edge is not large enough.

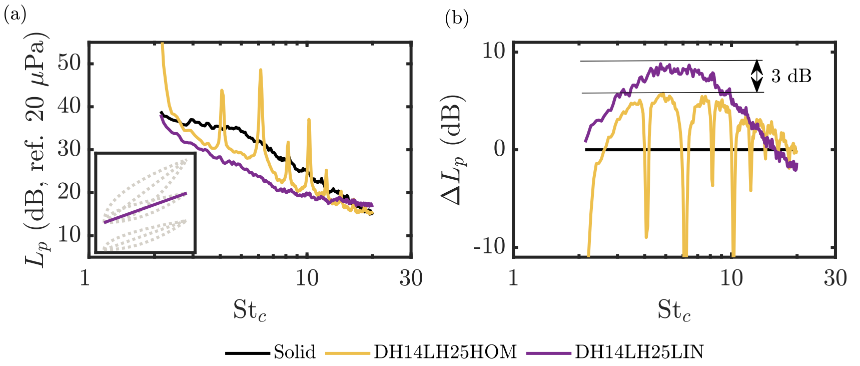

Figure 7.10: Acoustic spectra measured for the set of permeable inserts with hole diameter d_h = 1.4 mm and hole spacing at the tip $l_{h,\text{tip}}$ = 2.5 mm. Data measured at a free-stream velocity of 30 m/s with the NACA 63018 model at no incidence. (a) Absolute spectra. The permeability distribution of the graded insert is highlighted in the left bottom corner plot. (b) Relative spectra with respect to the baseline case.

In figures 7.10 (a) and (b), the acoustic spectra for the set of trailing-edge inserts manufactured for the NACA 63018 model (d_h = 1.4 mm; $l_{h,\mathrm{tip}}$ = 2.5 mm) are plotted. In this case, the homogeneous insert again produces loud tones with a fundamental frequency of $\mathrm{St}_c = 2.1$, and a maximum broadband noise mitigation of 6 dB around a $\mathrm{St}_c = 5$. Interestingly, in this case the graded insert not only removes the presence of tones but also presents a significantly higher broadband noise attenuation performance. This variant causes a maximum noise attenuation of 9 dB around a dimensionless frequency of St_c = 6, i.e. the use of a linear permeability distribution provokes an additional noise attenuation of 3 dB with respect to the fully homogeneous counterpart. This result indicates the high noise mitigation potential of this class of solutions.

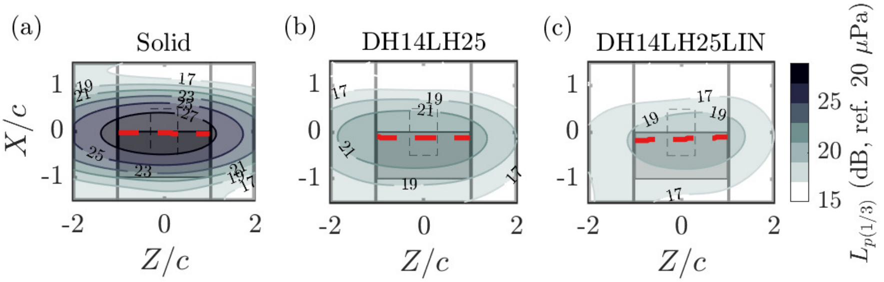

Figure 7.11: Source maps for f = 900 Hz (St_c = 6) for the NACA 63018 trailing-edge inserts with l_h = 1.4 mm and $l_{h,\mathrm{tip}}$ = 2 mm. (a) Solid. (b) DH14LH25HOM. (c) DH14LH25LIN. The airfoil is represented as a gray rectangle. Dashed area represents the region where the source power integration technique is applied. Red dashed-dotted line marks streamwise L_p maxima within $-1 < Z/c < 1$.

In figures 7.11 (a-c), acoustic source maps for solid and permeable inserts at the frequency of maximum noise mitigation are plotted. It is shown that, differently from the inserts described above, the maximum noise emission for the permeable mock-ups is moved towards more upstream positions with respect to the solid case. Therefore, the higher potential of the graded insert seems to be related to the capability to distribute noise sources along the permeable extension. It must be noted that the use of the same type of permeability distribution in the NACA 0018 model did not entail any additional benefit in terms of broadband noise attenuation, i.e. tailored permeability distributions are required depending on the model and, besides the permeability, other properties such as the thickness of the model must be accounted for.

7.3.2. CHANGE IN NOISE MITIGATION PERFORMANCE WITH REYNOLDS NUMBER AND LOADING

In this section, the change in noise mitigation performance with Reynolds numbers and angles of attack for the trailing-edge inserts described above is analysed. To this aim, the OSPL, as defined in equation 6.2, is computed based on data measured at free-stream velocities ranging from 15 to 35 m/s (corresponding to Re_c ranging from 2×10^5 to 4.7×10^5) and geometrical angles of attack ranging from 0 to 12 degrees.

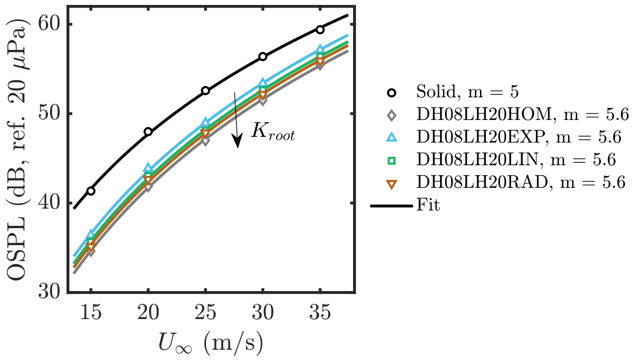

Figure 7.12: Change in OSPL with free-stream velocity for the set of permeable inserts with hole diameter d_h = 0.8 mm and hole spacing at the tip $l_{h,\text{tip}}$ = 2 mm. Data measured at a free-stream velocity of 15 to 35 m/s with the NACA 0018 model at no incidence. Markers represent measured data; lines depict fitted data employing the equation 6.3.

In figure 7.12, OSPL data for the DH08LH20 inserts are plotted as a function of the free-stream velocity. Measured data are plotted as markers, and fitted data (employing equation 6.3) are represented as lines. In line with results presented in figure 7.6, graded inserts with higher K_{root} have a slightly better noise attenuation performance, i.e. the OSPL curves are shifted towards lower values. Yet, the computed exponent m is equal to 5.6 for all the permeable inserts. Hence, the use of different permeability distributions does not alter the nature of the acoustic scattering mechanisms. Similar results are found for data measured on the remaining graded inserts.

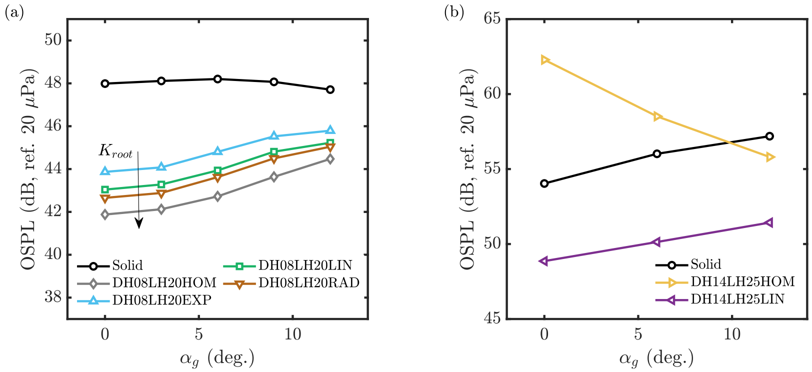

Figure 7.13: Change in OSPL with geometric angle of attack. (a) Set of permeable inserts with hole diameter d_h = 1.4 mm and hole spacing at the tip $l_{h,\text{tip}}$ = 3.5 mm. Data measured at a free-stream velocity of 30 m/s with the NACA 0018 model. (b) Set of permeable inserts with hole diameter d_h = 1.4 mm and hole spacing at the tip $l_{h,\text{tip}}$ = 2.5 mm. Data measured at a free-stream velocity of 20 m/s.

In figure 7.13 (a), experimental OSPL data for the same set of NACA 0018 inserts are plotted as a function of the geometric angle of attack α_g. In line with data analysed above, noise attenuation levels increase with K_{root} independently of α_g. As with homogeneous inserts, the noise mitigation performance of graded inserts also decreases with the angle of attack. For instance, for the DH08LH20EXP insert a decrease in OSPL with respect to the solid case of 4 dB is measured at $\alpha_g = 0$ degrees, and of only 2 dB at $\alpha_g = 12$ degrees.

However, for the graded insert manufactured for the NACA 63018 airfoil (figure 7.13 (b)), a constant reduction in OSPL of 5 dB is observed independently of the angle of attack. Hence, the selection of an optimal permeability distribution can also minimize the downgrade in acoustic performance found at high loading conditions. It is also interesting to note that the fully homogeneous insert produces decreasing OSPL levels for increasing angles of attack. This is due to the fact that strong tones are only present for spectra measured with the model at no incidence; as with models with a fully blunt trailing edge, the peak decreases for increasing angles of attack due to the suppression of vortex-shedding [11].

7.3.3. REMARKS ON ROUGHNESS NOISE

Roughness noise, described in Chapter 5 for metal foam inserts, is further investigated in this section for homogeneous and graded perforated inserts. To this aim, acoustic spectra in one-third octave bands are analysed. Data are measured at a free-stream velocity of 20 m/s and an angle of attack of 0 degrees.

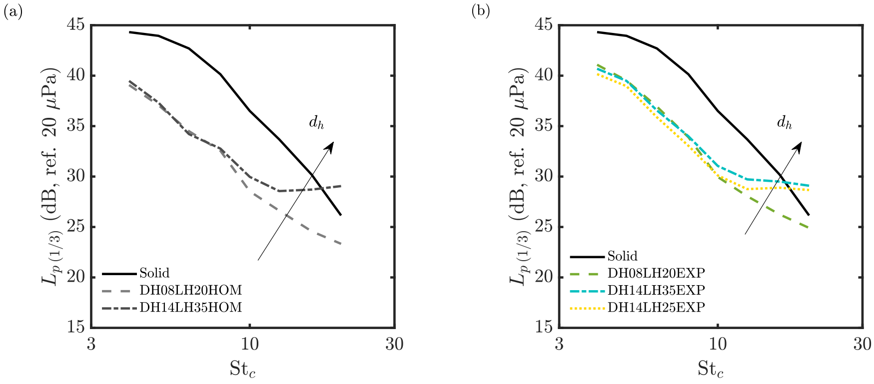

Figure 7.14: Acoustic spectra in one-third octave bands $L_{p(1/3)}$ for perforated trailing-edge inserts. (a) Homogeneous inserts. (b) Graded inserts. Data measured at a free-stream velocity of 20 m/s with the NACA 0018 model at no incidence.

Results for inserts with a homogeneous hole spacing, i.e. the DH08LH20HOM and DH14LH35HOM inserts, are plotted in figure 7.14 (a). Data for the DH14LH25HOM variant are not shown due to the presence of tones within the measured spectra. As shown in the previous section, for the two trailing-edge variants the region of maximum noise scattering is aligned with the tip of the insert. The two inserts have a K_{tip} above the threshold of 35×10^{-10} m^2 defined in Chapter 6. From this value on, the relationship between maximum noise mitigation and permeability flattens. Hence, although the

DH14LH35HOM mock-up is twice as permeable as the DH08LH20HOM insert within the tip, below a $\mathrm{St}_c = 8$ both inserts yield similar noise scattering, with a maximum noise attenuation with respect to the baseline case of 9 dB at $\mathrm{St}_c = 6.3$.

Above $\mathrm{St}_c = 8$, the DH14LH35HOM insert yields significantly higher noise levels, with the maximum difference (of 6 dB) being found at the highest measured $\mathrm{St}_c = 20$. Hence, as with metal foam inserts, roughness noise is higher for inserts with larger hole size. Such a result suggests that in order to optimize the acoustic performance of perforated inserts, i.e. to maximize low-frequency abatement and minimize roughness noise, it is preferable to use small holes while increasing the hole density. This supports data presented in Rossignol *et al.* [7] and Luesutthiviboon *et al.* [12], where it is shown that the use of hydraulically smooth surfaces at the trailing-edge minimizes high-frequency excess noise.

These observations also hold for graded inserts, i.e. in figure 7.14 (b), where data for inserts with an exponential permeability distribution, above a $\mathrm{St}_c = 10$ the two inserts with larger hole size (DH14LH35EXP and DH1425EXP) are louder than the DH08LH20EXP counterpart. As for homogeneous inserts, noise levels below $\mathrm{St}_c = 10$ are similar as they all have a K_{tip} above the afore defined threshold. Although spectra for inserts with radical and linear permeability distributions are not shown here for the sake of brevity, similar conclusions can be drawn from them.

7.4. CONCLUSIONS

In the current chapter, a methodology to create trailing-edge inserts with customized permeability distributions along the chord is presented. The methodology allows to impose permeability gradients in a fully controlled manner by varying the hole density along the insert, while keeping the hole size constant. Ten graded inserts are designed by changing the permeability at the root and the tip of the inserts, as well as the type of distribution, i.e. linear, radical and exponential increase. There are nine variants for a NACA 0018 airfoil, and one for a NACA 63018 airfoil. The inserts are then fabricated with additive manufacturing. Four homogeneous mock-ups with the same permeability at the tip of the insert, and a fully solid insert are employed as reference.

Acoustic data obtained with the NACA 0018 airfoil show that the magnitude of the noise abatement within the lower frequency range can be increased by employing inserts with higher permeability at the solid-permeable junction. Consequently, homogeneous inserts yield maximum noise attenuation below a $\mathrm{St}_c = 7$. Contrarily, the graded insert employed in the NACA 63018 airfoil produces higher broadband noise mitigation than its homogeneous counterpart. Source maps for this case show a displacement of the location of maximum noise emission with respect to the solid case, suggesting that the higher potential of graded inserts is linked to their capability to distribute the impedance jump uniformly along the permeable surface. This result also confirms that the acoustic performance of a graded insert not only depends on the permeability but also on the airfoil.

Independently of the type of grading or airfoil, all the non-uniform variants present significant advantages in terms of tonal noise reduction. Strong tones appearing for homogeneous inserts are suppressed with the employment of graded mock-ups. This is likely due to the confinement of the highly permeable region to the very aft end of the insert, as well as the current design methodology, that promotes a certain degree of misalignment between holes distributed streamwisely.

Results obtained at different flow speeds and angles of attack show that the nature of the acoustic source is determined by parameters such as the permeability at the tip and the extension of the permeable surface, but it does not depend on the specific permeability distribution employed along the insert, and that graded inserts might prevent from the downgrade of the acoustic performance with increasing angles of attack previously reported for fully homogeneous inserts.

Finally, as with inserts manufactured with metallic foams, higher roughness noise levels are observed for perforated inserts with larger holes, independently of their distribution, i.e. homogeneous or graded. Hence, the employment of inserts with small holes and high hole density is recommended to maximize low-frequency abatement and minimize this high-frequency excess noise contribution.

Present results confirm the potential of graded trailing-edge inserts against fully homogeneous solutions. Future work will further address the type of grading necessary to achieve an optimal acoustic performance in airfoils with different size and shape, as well as the acoustic scattering of heterogeneous inserts with pore topologies different from straight holes.

REFERENCES

[1] J. Schulze and J. Sesterhenn, *Optimal distribution of porous media to reduce trailing edge noise,* Computers and Fluids **78**, 41 (2013).

[2] H. Liu, N. Chen, and Z. Hu, *Effects of non-uniform permeability on vortex shedding and noise control of blunt trailing edge,* AIP Advances **9**, 1 (2019).

[3] S. R. Koh, B. Zhou, M. Meinke, N. Gauger, and W. Schröder, *Numerical analysis of the impact of variable porosity on trailing-edge noise,* Computers and Fluids **167**, 66 (2018).

[4] L. Rossian, R. Ewert, and J. Delfs, *Prediction of airfoil trailing edge noise reduction by application of complex porous material,* Notes on Numerical Fluid Mechanics and Multidisciplinary Design **136** (2018), 10.1007/978-3-319-64519-358.

[5] M. Aldheeb, W. Asrar, E. Sulaeman, and A. A. Omar, *Aerodynamics of porous airfoils and wings,* Acta Mechanica **229**, 3915 (2018).

[6] F. Wienke, A. Dillmann, and M. Raffel, *Experimental Investigation of the Influence of Permeability on Finite Wing Lift and Drag,* in *New Results in Numerical and Experimental Fluid Mechanics XII* (Springer International Publishing, 2020) 1st ed., pp. 716–725.

[7] K. S. Rossignol, A. Suryadi, M. Herr, J. Schmidt, and J. Tychsen, *Experimental investigation of porous materials for trailing-edge noise reduction,* International Journal of Aeroacoustics **19**, 365 (2020).

[8] J. Tychsen, N. Lippitz, and J. Rösler, *Modification of Porous Aluminum by Cold Rolling for Low-Noise Trailing Edge Applications,* Metals **8**, 1 (2018).

[9] Y. Bae and Y. I. Kim, *Numerical modeling of anisotropic drag for a perforated plate with cylindrical holes,* Chemical Engineering Science **149**, 78 (2016).

[10] C. Teruna, F. Manegar, F. Avallone, D. Ragni, D. Casalino, and T. Carolus, *Noise reduction mechanisms of an open-cell metal-foam trailing edge,* Journal of Fluid Mechanics **898**, 1 (2020).

[11] W. J. Zhu, W. Z. Shen, J. N. Sørensen, and G. Leloudas, *Improvement of airfoil trailing edge bluntness noise model,* Advances in Mechanical Engineering **8**, 1 (2016).

[12] S. Luesutthiviboon, D. Ragni, F. Avallone, and M. Snellen, *An alternative permeable topology design space for trailing edge-noise attenuation,* International Journal of Aeroacoustics (2020).

8

CONCLUSIONS AND RECOMMENDATIONS

8.1. CONCLUSIONS

The goal of the research described in this thesis is twofold: i) to advance towards a more complete understanding of the underlying physical mechanisms behind sound production in permeable edges; and ii) to explore the design and 3D-printing of porous materials with optimized meso-structures that yield optimal noise abatement over a wide frequency range, while minimizing the lack of repeatability and inhomogeneity problems often present in conventional, commercially available cellular materials.

To accomplish these objectives the flow field and acoustic scattering of airfoils with solid and permeable trailing-edge inserts with different pore topologies are extensively characterized utilizing state-of-the-art experimental techniques such as acoustic beamforming, HWA, unsteady wall-pressure transducers and PIV.

In Chapter 4, flow field and far-field noise of a NACA 0018 airfoil equipped with solid and metal foam inserts manufactured with metallic foams with varying permeability and pore size are investigated.

Acoustic data show substantial low-frequency noise abatement for porous edges with larger permeability. At higher frequencies, a noise increase with respect to the fully solid case is reported, with higher noise levels being observed for materials with larger pore size.

Wall-pressure and kinematic data show significant changes within the boundary layer due to the use of porous inserts: a higher surface drag decreases the wall-pressure mean convection and mean flow velocity, while higher frictional forces near the porous surface increase the power spectra of the turbulent velocity and pressure fields. These effects are more significant for materials with larger pore size, hence they are attributed to roughness. It is also found that the use of porous edges strongly decreases the organization of turbulent flow structures within the boundary layer: a significant decrease of the vertical length scale of the turbulent eddies, as well as in the spanwise correlation length of the wall-pressure fluctuations, are reported for materials with increasing pore size. Moreover, Amiet's theory for single line noise scattering, conceived for solid edges, is employed to prove that the overall modification of the flow field above the metal foam inserts does not contribute to noise mitigation, which suggests that these porous edges intrinsically alter the noise scattering process with respect to a fully solid variant.

This hypothesis is confirmed in Chapter 5, where two non-permeable counterparts of the metal foam inserts investigated in the previous chapter, manufactured by applying a solid membrane in the symmetry plane of the insert, are studied.

Acoustic data show that porous non-permeable and solid inserts produce similar far-field noise scattering in the range of frequencies where the fully permeable variants abate noise. The very different acoustic performance of permeable and blocked inserts manufactured with the same type of metal foam is explained by the appearance of cross-flow, revealed by the presence of near-wall regions of correlated flow at upper and lower sides of the permeable inserts. This phenomenon evidences a communication process that affects flow at both sides of the trailing edge, reducing the pressure mismatch at the edge, hence decreasing sound generation.

This process provokes changes in the dominant sound emission location along porous treatments. In the range of frequencies where noise mitigation is observed, the most permeable metal foam insert scatters noise mainly from upstream the trailing edge, whilst the least permeable insert emits from the actual edge. The permeability of the insert thus determines the magnitude of the acoustic impedance discontinuities created along the metal foam surface, defining where the scattering of wall-pressure fluctuations into acoustic pressure perturbations is more efficient.

Moreover, far-field noise spectra show that permeable and non-permeable cellular inserts increase high-frequency noise with respect to the baseline case similarly, confirming that the previously described excess noise is indeed due to roughness.

These findings suggest that trailing-edge inserts would abate noise provided that flow communication between the two sides of the model is allowed. Hence, perforated trailing-edge inserts, with a simpler pore topology, i.e., straight channels perpendicular to the chord, are 3D-printed. This part of the research is described in Chapter 6, where the acoustic scattering of the same NACA 0018 airfoil equipped with solid and perforated trailing-edge inserts is investigated. The comparison between noise scattering from perforated and metal foam inserts yield scaling laws for noise abatement, and criteria for maximizing noise mitigation while limiting the downgrade in aerodynamic performance stemming from the use of permeable materials in lifting devices.

Specifically, it is found that the range of frequencies for noise mitigation scales linearly with the free-stream velocity. Scaled noise mitigation data allows to define permeability thresholds of 3.5×10^{-9} and 1×10^{-9} m^2 for perforated and metal foam inserts respectively. Below these thresholds, an increment of the permeability of the insert provokes a significant increase of maximum noise mitigation; further increasing the permeability does not entail any significant advantage in terms of acoustic performance.

The fact that porous materials with similar permeability but different pore topologies yield different acoustic scattering suggests that the former quantity alone is insufficient to fully control noise mitigation; to this aim, the tortuosity of the trailing edge is proposed in addition to the permeability. Moreover, it is stressed that increasing the chordwise extent of the permeable region beyond 5% of the total chord does not increase noise mitigation significantly, and it is also reported that inserts with high permeability and an ordered pore arrangement trigger vortex-shedding, that produces extremely loud acoustic tones.

A permeable trailing edge insert with permeability equal to 1×10^{-9} m^2, with a tortuosity of 1.15 (which is in turn beneficial to avoid tones) and with a permeable extent of 5% of the total chord is therefore recommended to minimize the aerodynamic penalty while maximizing noise abatement.

Results in Chapter 5 also suggest that inserts with a streamwise permeability gradient might surpass the performance of homogeneous porous materials, as this sort of variants might minimize the creation of strong coherent scattering regions within the permeable surface. This point is assessed in Chapter 7, where perforated trailing-edge inserts with tailored permeability distributions along the chord are investigated. A methodology to create perforated trailing-edge inserts with customized permeability distributions along the chord is described. This methodology allows to impose permeability gradients in a fully controlled manner by varying the hole density along the graded insert, while keeping the hole size constant. Different inserts are created by changing the permeability at the root and the tip of the inserts, as well as the type of permeability increase along the chord, i.e. linear, radical and exponential. Variants with the same permeability distribution for a NACA 0018 airfoil, and for a NACA 63018 airfoil are also manufactured to assess the effect of the type of airfoil on the performance of the insert.

Results show that the magnitude of the noise abatement within the lower frequency range can be increased by employing inserts with higher permeability at the solid permeable interface. The graded insert employed in the NACA 63018 airfoil produces higher broadband noise mitigation than its fully homogeneous counterpart, and also features a weaker decrease in acoustic performance with increasing angles of attack. These results confirm the great potential of graded trailing-edge inserts against fully homogeneous solutions. Independently of the type of grading or airfoil, all the non-uniform variants present great advantages in terms of tonal noise reduction.

As for inserts manufactured with metallic foams, higher roughness-induced noise levels are observed for perforated inserts with larger holes, independently of their distribution, i.e. homogeneous or graded. Hence, the employment of inserts with small holes and high hole density is recommended to maximize low-frequency abatement and minimize this high-frequency excess noise contribution.

8.2. RECOMMENDATIONS

This doctoral work has successfully given insights on the mechanisms of noise generation present at permeable trailing edges. Moreover, it has also defined criteria to 3D-print homogeneous permeable edges that represent an optimal trade-off between aerodynamic and aeroacoustic performance. Moreover, it has proposed a methodology to design and manufacture permeable trailing edges with tailored permeability gradients along the chord in a fully controlled manner, and has also demonstrated the noise mitigation potential of this class of solutions.

Future work should aim to further understand and minimize some of the detrimental side-effects of using permeable materials at the trailing edge of a lifting surface, such as the appearance of vortex-shedding or the overall decrease in aerodynamic performance. It should also address strategies to optimize noise abatement for specific airfoils and design conditions. A more detailed list of recommendations for future research activities is presented below:

- In the framework of this thesis (Chapter 6) it has been shown that, as for fully blunt models, the use of permeable trailing-edge inserts might trigger vortex-shedding, hence yielding loud acoustic tones. This phenomenon poses a serious threat to a successful industrial application of permeable materials for noise mitigation as tonal components are extremely penalized by environmental regulations. For this reason, the set of parameters and conditions where shedding at permeable edges appears should be accurately defined. These include material properties such as permeability, form coefficient and tortuosity; geometric effects such as the type of airfoil and permeable extent; and loading, i.e., Reynolds number and angle of attack.

- As shown in Chapter 6, for a given permeability, trailing-edge inserts with interconnected pores that have some degree of tortuosity yield better noise mitigation performance than simply perforated ones. Given that the permeability controls the downgrade in aerodynamic performance of the airfoil, the design of new non-uniform porous trailing-edge inserts whose unit-cell allows for interconnection between tortuous pore paths might be yield better results than perforated ones both in terms of acoustics and aerodynamics.

- In Chapter 7, it is shown that the application of the same permeability distribution on different airfoils yields very different noise scattering. Numerical tools could give further insight into this result; in particular, the change in noise source distribution along the permeable inserts, as well as their interaction when specific permeability gradients are applied to different airfoil models, should be studied.

- For aircraft applications, trailing-edge noise is of major concern only during landing. Using permeable materials in an aircraft wing as a passive noise control strategy would result in noise mitigation during cruise, where airframe noise does not jeopardize cabin comfort, thus unnecessarily increasing drag and fuel consumption. For this reason, aircraft applications would be better suited by an actively controlled use of permeable materials for noise mitigation. To this aim, one could think of a hydrodynamically smooth permeable trailing-edge insert with a movable solid obstacle in the symmetry plane; such a device could be activated to effectively block flow communication during specific operating conditions. Preliminary work in this direction is described in the MSc thesis of Y. Khan "Design of actively controlled semi-permeable trailing edge inserts for aeroacoustic noise reduction" *(TU Delft, 2020).*

ACKNOWLEDGEMENTS

There are many people that deserve credit for the work described in this thesis. First of all, I would like to thank my four supervisors, namely Francesco Avallone, Daniele Ragni, Mirjam Snellen and Sybrand van der Zwaag for their infinite patience, and for providing trust, confidence and critical insight. I am glad I owe them successfully becoming a scientist.

I would also like to thank the many colleagues from the two excellent research groups I shared the PhD road with: Ana, Timo, Tannaz, Salil, Colin, Christopher, Edo, Livia, Leandro, Tercio, Hugo, and many more. Special gratitude to Roberto, who has always been willing to give me a hand, a beer, or share a 3000 km road-trip in the American South.

Outside academia, the Netherlands proved to be a wonderful place to meet equally wonderful people. I had the pleasure to get to know really well three beautiful cities within the dutch Randstad, each one with a different soul. The first one was Utrecht, where I was lucky to make some very good and life-lasting friends: Costa, Gaghi, Renato, Kiraz, Leone, Guido, greek Costa, Caragh, David, Sophie and Charlie. The second one was Amsterdam, where I enjoyed some of the funniest moments of my life with Esther and Plaza. The last city I enjoyed was Rotterdam, where I shared the anxiety of going through the last year of the PhD together with Beatriz.

During these years, I was always keen to coming back to Spain for holidays, as I knew I would be spending quite some time with my friends from the university (Diego, Miqui, Clara, Cele, Andrea) or high-school (Rubén, Andrea, Álex, David, Jordi, Leticia). I would also like to thank them for making me feel home when we were together.

I cannot forget my parents, Carmen and Julián, who always fought so I could have every opportunity, and my sister Maria, who has always been there to support me and give me best advice. I would also like to thank my two nephews, Guillem and Lluc, born while I was completing the thesis; playing with them has somehow reminded me how fun was being a child.

Last but not least, I would like to thank my life partner Cos. I will always remember our time together in Utrecht as one of the happiest periods of my life. When you had to leave, even though we were 2000 km away from each other, you have been always there to guide me through moments of darkness.

A

ACOUSTICS: DEFINITIONS

Sound is a local deviation p' from the ambient pressure that propagates as a wave in a medium [5]. Acoustic waves propagate at the speed of sound c_0; in dry air at 20 Celsius degrees $c_0 = \sqrt{\gamma RT} = 343$ m/s, where R is the ideal gas constant (equal to 287.6 J/(K Kg) for dry air), γ is the heat capacity ratio and T the ambient temperature. The human hear can typically detect pressure waves within 20 Hz $< f <$ 20,000 Hz, thus corresponding to acoustic wavelengths $\lambda_0 = c_0/f$ of 17 m and 1.7 cm, respectively.

On a daily basis, human beings perceive sounds whose amplitudes differ by several orders of magnitude. For instance:

- In a quiet library, an observer receives pressure disturbances with an amplitude of 0.003 Pa.
- An observer placed 50 m away from a jet aircraft will typically perceive pressure disturbances with an amplitude of 300 Pa.

For this reason, acoustic pressure levels are commonly reported in terms of Sound Pressure Level L_p expressed in decibels (dB).

$$L_p = 10\log_{10}\left(\frac{\overline{p'^2}}{p_{ref}^2}\right) \tag{A.1}$$

where $p_{ref} = 20$ μPa (for air) represents the threshold of audibility of the human ear at 1 kHz. The sound intensity I is then defined as the energy flux (Watt per unit area) due to the sound wave propagation. Far-away from the source the intensity is related to the acoustic pressure by the acoustic impedance of the medium $\rho_0 c_0$

$$I = \frac{\overline{p'^2}}{\rho_0 c_0} \tag{A.2}$$

and the corresponding Sound Intensity Level L_I is defined as

$$L_I = 10\log_{10}\left(\frac{I}{I_{ref}}\right) \tag{A.3}$$

with $I_{ref} = 10^{-12}$ W/m^2. So far, noise metrics L_p and L_I refer to noise levels as perceived by the observer, i.e. they change with the distance between source and observer r. The acoustic power of a source W can be estimated by integration of the sound intensity along a surface S enclosing the source.

$$W = \int_S \boldsymbol{I} \cdot \boldsymbol{n} dS \tag{A.4}$$

For a source suspended in the far-field, this reads $W = 4\pi r^2 I$, where $4\pi r^2$ is the surface area of a sphere of radius r. The Sound Power Level L_W can then be computed as

$$L_W = 10\log_{10}\left(\frac{W}{W_{ref}}\right) \tag{A.5}$$

with $W_{ref} = 10^{-12}$ W.

B

SCHWARZSCHILD'S SOLUTION

Schwarzschild's solution [23] is a theorem derived by physicist Karl Schwarzschild at the beginning of the 20th century to solve the scattering of a electromagnetic wave by the edge of a semi-infinite plate. It reads as follows. Let ϕ be a two-dimensional scalar field, solution of the Helmhotz equation

$$\frac{\partial^2\phi}{\partial x^2} + \frac{\partial^2\phi}{\partial y^2} + \mu^2\phi = 0 \tag{B.1}$$

with boundary conditions

$$\phi(x,0) = F(x), \quad x \geq 0 \tag{B.2a}$$

$$\frac{\partial\phi}{\partial y}(x,0) = 0, \quad x < 0 \tag{B.2b}$$

where $F(x)$ is known. Then for $x < 0$, the solution on $y = 0$ is

$$\phi(x,0) = \frac{1}{\pi}\int_{\infty}^{0}\sqrt{\frac{-x}{\xi}}\,\frac{e^{i\mu(\xi - x)}}{\xi - x}F(\xi)\,d\xi \tag{B.3}$$

Note that the theorem does not yield a solution for the entire scalar field, but its trace on the surface along the plate.

C

ADDITIONAL SCALING LAWS

In Section 6.2.1, the collapse of noise mitigation data for different free-stream velocities when plotted as a function of St_c is shown. In the analysis, the chord of the airfoil is employed as length scale for the sake of simplicity. However, an attempt to collapse data for different permeable inserts employing length scales based on hydraulic properties, such as $\sqrt{K}$, $1/C$ or $F = KC$ was also performed.

Results are shown in figures C.1 (a), (b) and (c), where cross-over Strouhal numbers based on these quantities $\mathrm{St}^*_{\sqrt{K}}$, $\mathrm{St}^*_{1/C}$ and St^*_F are respectively depicted as a function of the corresponding hydraulic property for perforated and metal foam inserts at α = 0.2 and 5.4 degrees. As seen in these plots, employing hydraulic properties does not remove the dependency of St^* on these quantities neither for perforated nor metal foam inserts. Yet, for all three properties the relation seems to be linear. Interestingly, for the collapse with $1/C$ as length scale, all data seem to collapse in a line independently of hole arrangement or lifting condition.

Similar phenomena are found for the analysis of the Strouhal number for maximum

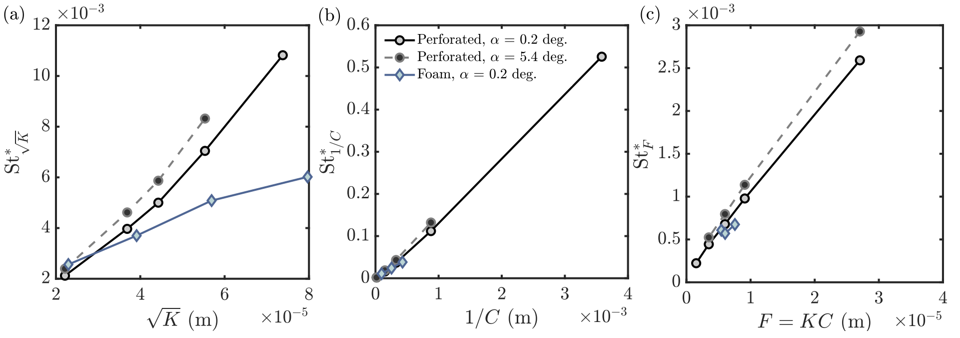

Figure C.1: Scaling of St^*_c with length scales derived from the permeability characterization. (a) $\sqrt{K}$. (b) $1/C$. (c) $F = KC$.

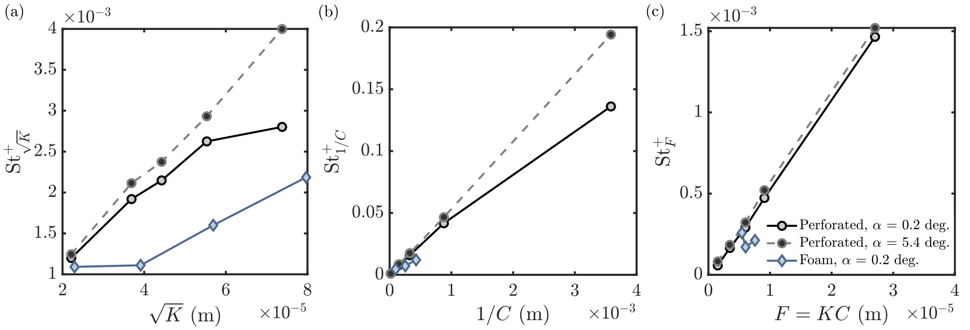

Figure C.2: Scaling of St^+ with length scales derived from the permeability characterization. (a) $\sqrt{K}$. (b) $1/C$. (c) $F = KC$.

noise attenuation St^+. In figures C.2 (a), (b) and (c), $\mathrm{St}^+_{\sqrt{K}}$, $\mathrm{St}^+_{1/C}$ and St^+_F are respectively plotted as a function of hydraulic properties.

CURRICULUM VITÆ

Alejandro RUBIO CARPIO

03-11-1991 Born in Valencia, Spain.

EDUCATION

2007–2009 Bachillerato de Ciencias. *Cum Laude*
Pureza de Maria, Valencia

2009–2012 Bachelor of Science (BSc). Aerospace Engineering
Polytechnic University of Valencia, Valencia, Spain

2012–2015 Master of Science (MSc). Aerodynamics & Structures
Polytechnic University of Valencia, Valencia, Spain
Sapienza University of Rome, Rome, Italy (2014–2015)
Thesis: Experimental Methodology for Heat Transfer Characterization in a Centrifugal Compressor
Promotor: Prof. dr. J.R. Serrano Cruz
Supervisor: dr. A. Dombrovsky

2015–2016 Research Master. Fluid Dynamics *Excellence in Experimental Research Prize*
von Kármán Institute for Fluid Dynamics, Rhode-Saint-Genése, Belgium
Thesis: Experimental Investigation of Shock-Cell Noise on a Supersonic Coaxial Jet
Promotor: Prof. dr. C. Schram
Supervisor: dr. D. Guariglia

2016–2021 PhD. Aeroacoustics
Delft University of Technology, Delft, the Netherlands
Thesis: Innovative Permeable Materials for Broadband Noise Mitigation
Promotor: dr. D. Ragni
Promotor: Prof. dr. M. Snellen
Supervisor: dr. F. Avallone

LIST OF PUBLICATIONS

JOURNAL ARTICLES

11. **A. Rubio Carpio**, F. Avallone, D. Ragni, M. Snellen, S. van der Zwaag, *3D-Printed Trailing Edges with Tailored Permeability Gradients for Noise Mitigation*, Aerospace Science and Technology, *under consideration* (2021).

10. C. Teruna, F. Avallone, D. Ragni, **A. Rubio Carpio**, D. Casalino, *Numerical analysis of a 3D-printed porous trailing edge for broadband noise reduction*, Journal of Fluid Mechanics, *under consideration* (2021).

9. R. Merino Martínez, **A. Rubio Carpio**, L.T. Lima Pereira, S. van Herk, F. Avallone, D. Ragni, M. Kotsonis, *Aeroacoustic design and characterization of the 3D-printed, open-jet, anechoic wind tunnel of Delft University of Technology*, Applied Acoustics **170**:107504 (2020).

8. **A. Rubio Carpio**, F. Avallone, D. Ragni, M. Snellen, S. van der Zwaag, *Quantitative criteria to design optimal permeable trailing edges for noise abatement*, Journal of Sound and Vibration **485**:115596 (2020).

7. R. Merino Martínez, S. Luesutthiviboon, R. Zamponi, **A. Rubio Carpio**, D. Ragni, P. Sijtsma, M. Snellen, C. Schram, *Assessment of the accuracy of microphone array methods for aeroacoustic measurements*, Journal of Sound and Vibration **470**:115176 (2020).

6. **A. Rubio Carpio**, F. Avallone, D. Ragni, M. Snellen, S. van der Zwaag, *Mechanisms of broadband noise generation on metal foam edges*, Physics of Fluids **31**(10):105110 (2019).

5. J. Mayer, **A. Rubio Carpio**, D. Ragni, *Temperature-activated change of permeable material properties for low-noise trailing edge applications*, Applied Sciences **9**(15):3119 (2019).

4. R. Merino Martínez, P. Sijtsma, **A. Rubio Carpio**, R. Zamponi, S. Luesutthiviboon, A. Malgoezar, M. Snellen, C. Schram, D.G. Simons *Integration methods for distributed sound sources*, International Journal of Aeroacoustics **18**(4-5):444-469 (2019).

3. R. Hedayati, **A. Rubio Carpio**, S. Luesutthiviboon, D. Ragni, F. Avallone, D. Casalino, S. van der Zwaag, *Role of polymeric coating on metallic foams to control the aeroacoustic noise reduction of airfoils with permeable trailing edges*, Materials **12**(7):1087 (2019).

2. **A. Rubio Carpio**, R. Merino Martínez, F. Avallone, D. Ragni, M. Snellen, S. van der Zwaag, *Experimental characterization of the turbulent boundary layer over a porous trailing edge for noise abatement*, Journal of Sound and Vibration **443**:537-558 (2018).

1. D. Guariglia, **A. Rubio Carpio**, C. Schram, *Design of a facility for studying shock-Cell noise on single and coaxial jets*, Aerospace **5**(1):25 (2018).

CONFERENCE PROCEEDINGS

7. E. Arcondoulis, D. Ragni, **A. Rubio Carpio**, F. Avallone, Y. Liu, Y. Yang, Z. Li, *The internal and external flow fields of a structured porous coated cylinder and implications on flow-induced noise*, 2019 AIAA/CEAS Aeroacoustics Conference, Delft, Netherlands (2019).

6. C. Teruna, F. A. Manegar, F. Avallone, D. Casalino, D. Ragni, **A. Rubio Carpio**, T. Carolus, *Numerical analysis of metal-foam application for trailing edge noise reduction*, 2019 AIAA/CEAS Aeroacoustics Conference, Delft, Netherlands (2019).

5. **A. Rubio Carpio**, F. Avallone, D. Ragni, M. Snellen, S. van der Zwaag, *3D-printed perforated trailing edges for broadband noise abatement*, 2019 AIAA/CEAS Aeroacoustics Conference, Delft, Netherlands (2019).

4. F. A. Manegar, C. Teruna, F. Avallone, W. van der Velden, D. Casalino, T. Carolus, D. Ragni, **A. Rubio Carpio**, *Numerical investigation of the porous trailing edge noise reduction mechanism using the Lattice- Boltzmann method*, 8th International Conference on Wind Turbine Noise, Lisbon, Portugal (2019).

3. **A. Rubio Carpio**, F. Avallone, D. Ragni, *On the role of the flow permeability of metal foams on trailing edge noise reduction*, 2018 AIAA/CEAS Aeroacoustics Conference, Atlanta, USA (2018).

2. **A. Rubio Carpio**, R. Merino Martínez, F. Avallone, D. Ragni, M. Snellen, S. van der Zwaag, *Broadband trailing edge noise reduction using Permeable metal foams*, 46th International Congress and Exposition on Noise Control Engineering (Inter-Noise), Hong Kong, China (2017).

1. D. Guariglia, **A. Rubio Carpio**, C. Schram, *Design of a facility for shock-cells noise experimental investigation on a subsonic/supersonic coaxial jet*, 2016 AIAA/CEAS Aeroacoustics Conference, Lyon, France (2016).